# Controlled Precipitation of Energetic Van Allen Belt Protons by Electromagnetic Ion Cyclotron (EMIC) Waves: Scientific and Engineering Implications

by

Maria de Soria-Santacruz Pich

Submitted to the Department of Aeronautics and Astronautics
in partial fulfillment of the requirements for the degree of

Doctor of Philosophy

at the

MASSACHUSETTS INSTITUTE OF TECHNOLOGY

February 2014



Author .....
Department of Aeronautics and Astronautics
January 15, 2014

Certified by .....
Manuel Martinez-Sanchez
Professor of Aeronautics and Astronautics
Thesis Committee Chair

Certified by .....
David W. Miller
Hunsaker Professor of Aeronautics and Astronautics

Certified by .....
Jeffrey A. Hoffman
Professor of Aeronautics and Astronautics

Certified by .....
Kerri Cahoy
Assistant Professor of Aeronautics and Astronautics

Certified by .....
Gregory P. Ginet
Senior Staff, MIT Lincoln Laboratory

Accepted by .....
Paulo C. Lozano
Associate Professor of Aeronautics and Astronautics
Chair, Graduate Program Committee

**Controlled Precipitation of Energetic Van Allen Belt Protons by Electromagnetic Ion Cyclotron (EMIC) Waves: Scientific and Engineering Implications**

by

Maria de Soria-Santacruz Pich

Submitted to the Department of Aeronautics and Astronautics
on January 15, 2014, in partial fulfillment of the
requirements for the degree of
Doctor of Philosophy

## Abstract

The inner Van Allen radiation belt traps highly energetic protons sourced from solar storms, cosmic rays and other processes. These particles can rapidly damage the space systems orbiting the inner region, limiting access to Low Earth Orbit (LEO). Decades of modeling and observations, however, show that naturally generated ULF/VLF waves have the capability of precipitating energetic trapped electrons and protons. This fact suggests that there could be human control over the stable inner belt proton population by artificially transmitting Electromagnetic Ion Cyclotron (EMIC) waves from space-based antennas (named *remediation*). These waves are naturally generated by equatorial ring current ions in the outer belt region, which explains the absence of EMIC waves at lower altitudes. Consequently, the precipitation of high-energy protons requires artificial generation of EMIC waves into the inner zone. The controlled removal of energetic outer belt electrons by man-made whistler waves has been widely studied, and a space test of a linear antenna for this purpose is in preparation. Contrarily, the interaction between inner belt protons and EMIC waves from in-situ transmitters is an unexplored solution to the radiation environment that should be addressed given its relevance to the scientific and engineering communities. This dissertation focuses on four interconnected research efforts in this direction, which are (1) the radiation of EMIC waves from a space-based antenna, (2) the propagation of these waves in the inner radiation belt, (3) the wave-particle interactions with energetic trapped protons and (4) the feasibility of a mission capable of significantly reducing this hazardous radiation. Our analyses show that a DC rotating coil antenna would be capable of radiating EMIC waves into space. Magnetic dipoles, however, have a very small radiation resistance. Additionally, the interaction between these waves and energetic protons is very inefficient. Our simulations show that, with the current technology, it is not engineeringly feasible to clean up the proton belt using space-based transmitters. A mission scaled down to detectability of the precipitating protons, however, could be launched easily and would allow us to better understand the science and test the technology involved in the concept of remediation.

Thesis Supervisor: Manuel Martinez-Sanchez
Title: Professor of Aeronautics and Astronautics
Thesis Committee Chair

Thesis Supervisor: David W. Miller
Title: Hunsaker Professor of Aeronautics and Astronautics

Thesis Supervisor: Jeffrey A. Hoffman
Title: Professor of Aeronautics and Astronautics

Thesis Supervisor: Kerri Cahoy
Title: Assistant Professor of Aeronautics and Astronautics

Thesis Supervisor: Gregory P. Ginet
Title: Senior Staff, MIT Lincoln Laboratory

## Acknowledgments

During my time at MIT I have had the support of many people. They made these four years and a half some of the best ones of my life, and they certainly contributed to this work in one way or another.

Mom and Dad, you have undoubtably contributed to all my achievements so far – and I'll continue in Catalan because this paragraph is for them. Isabel i Joan Carles, gràcies per ser-hi sempre, pels vostres consells, crítiques constructives, les hores feliçes d'Skype i les no tan feliçes. La vostra manera de fer és el millor recolzament possible, i és responsable del que fins ara ha estat una trajectòria exitosa des del Ferran i Clua fins al MIT. Us estimo molt i us dono les gràcies.

Mike, you have been the greatest motivation to get to this point. You know what MIT is about, thank you for always being supportive and encouraging. I love you and I can't wait for this flight to LA.

I have been excited about work for the past four years and my advisor, Prof. Martinez-Sanchez, definitely contributed to my enthusiasm. Manuel, thank you for your guidance and support, for your smart questions and suggestions, for being encouraging with all my academic steps. Not only you are one of the smartest professors in the Department, but also a great advisor.

I would also like to thank the rest of my Committee – Prof. Miller, Prof. Hoffman, Dr. Ginet and Prof. Cahoy –, as well as Dr. Minervini in the PSFC, Prof. Lorenzini from the University of Padova, and my readers Prof. Shprits and Dr. Lunjin Chen. Thank you for your advice and for sharing your knowledge and experience with me.

Additionally, I have been lucky to meet the best experts in my field from other institutions. To the VLF Group at Stanford, than you for your guidance on what is your field of expertise. Maria Spasojevic, it was a pleasure to write my very first paper with you, you are a great scientist and a wonderful person. Forrest and David Lauben, thank you for your patience. And thank you Nansen, I don't know where would I be now without your 26 nodes and all your RAM. Also Jacob Bortnik, Richard Thorne and Ksenia Orlova at UCLA, and Jay Albert at AFRL. For more exciting discussions to come.

These years have been way more enjoyable because of Dani, Carlos, Maite, Ana, Ale, Jorge, Fer, Ada, MJ and Bruno. Thank you for the happy times, you've made me laugh a lot. Also thank you for those not that happy ones, you have always been there whenever I needed it. We said at least annual meetings, right?

I would also like to thank my career-promising UROP Guillermo Bautista, as well as all my fellow graduate students, professors and friends in the SPL and SSL – Paulo, Carla, Carmen, Louis, Chase, Gwen... – for being so nice to me and helpful at all times.

Finally, I am very grateful to my sponsors Obra Social La Caixa, Fundación Caja Madrid and the Air Force Office of Scientific Research (AFOSR) for making this work possible.

# Contents

# List of Figures

# List of Tables

# Chapter 1

# Introduction

## 1.1 Motivation and Purpose

The inner Van Allen radiation belt traps highly energetic protons up to 300 MeV originating from solar storms, cosmic rays and other processes. These particles can rapidly damage solar panels, electronics and other components of the space systems orbiting the inner region, limiting access to Low and Medium Earth Orbits (LEO/MEO) [*Baker*, 2000, 2001]. Shielding against this radiation is extremely expensive and even with hardening measures the lifetime and reliability of space systems is limited by degradation caused by trapped energetic particles. Years of modeling and observations, however, show that naturally generated ULF/VLF waves can produce pitch-angle scattering of the energetic trapped particles, causing a portion of them to get lost into the atmosphere [e.g. *Abel and Thorne*, 1998; *Albert*, 1999; *Jordanova et al.*, 2001; *Loto'aniu et al.*, 2006]. These observations show that whistler waves (in the VLF range, typically in the tens of kHz) can precipitate energetic trapped electrons, while left-hand polarized (L-mode) Electromagnetic Ion Cyclotron (EMIC) waves (in the ULF range, typically less than 10 Hz) are capable of interacting with both energetic electrons and protons. This fact suggests that there could be human control over the stable inner belt proton population by artificially transmitting EMIC waves from space-based antennas. These waves are naturally generated by the cyclotron instability of

ring current ions of tens of keV located at $L > 3^*$ [*Meredith et al.*, 2003], which explains the absence of EMIC power at lower $L$-shells. Consequently, the precipitation of MeV protons requires artificial generation of EMIC waves into the inner zone.

The initial research efforts on controlled removal techniques [*Inan et al.*, 1984, 2003; *Kulkarni et al.*, 2008] have been directed to the energetic electron population because the injection of these particles is the preponderant effect of high-altitude nuclear explosions (HANEs) [*Brown and Gabbe*, 1963; *Mozer et al.*, 1963; *Pieper*, 1963]. On the other hand, it is well known that geomagnetic storms cause large-scale injections of both protons and electrons into the belts, which can increase the quiet-time fluxes by more than two orders of magnitude. The naturally occurring radiation belts, which by themselves constitute a large hazard to spacecraft, contain both electrons and ions (protons mainly), with similar deleterious effects. For this reason, the interaction between inner belt protons and EMIC waves radiated from in-situ transmitters is an unexplored solution to the radiation environment that should be addressed given its relevance to the scientific and engineering communities.

The purpose of this dissertation is to reveal the physics and engineering implications involved in the idea of controlled precipitation (commonly referred as mitigation) of energetic radiation belt protons by EMIC waves, as well as to determine the feasibility of a mission based on in-situ transmitters capable of depleting the inner Van Allen belt of these energetic particles. More specifically, this thesis aims at understanding the physics behind the radiation of EMIC waves from a space-based antenna, their propagation in the magnetosphere and their interaction with the energetic inner belt proton population. The mechanical, thermal and electrical implications of an antenna capable of radiating EMIC waves are also discussed. It must be emphasized that this dissertation analyzes the feasibility of the remediation concept based on EMIC waves radiated from space-based transmitters; other methods of generation of EMIC waves are outside the scope of this thesis. The scientific and engineering studies are finally combined to determine if it is feasible to clean up the inner Van Allen belt from energetic protons using Electromagnetic Ion Cyclotron waves. Additionally, a scientific mission is also outlined, which would be able to test and demonstrate some of the ideas investigated in this dissertation.

* The $L$ parameter or $L$-shell is used to characterize the Earth's geomagnetic field lines. A particular $L$-shell value corresponds to the field line that crosses the magnetic equator at the number of Earth's radii given by the $L$ parameter.

## 1.2 Scientific Background

The radiation belts constitute the portion of the space environment that governs the outcomes of this work. The dissertation builds up on the concept proposed to mitigate the negative effects of this environment on spacecraft. In the following, we summarize the magnetosphere structure and conditions, its harmful interaction with satellites and the mitigation ideas proposed to solve the problem.

### 1.2.1 The Magnetosphere and Radiation Belts

The magnetosphere is the region of space where plasma is controlled by the Earth's magnetic field. In the inner magnetosphere ($L \lesssim 6$), the geomagnetic field is accurately represented by a dipole model; this approximation, however, fails with larger $L$-shells due to the distortion introduced by the solar wind coming from the Sun. The Earth's magnetosphere is shown in Figure 1-1. The solar wind compresses the Earth's field on the day-side, and it generates a tail (known as magnetotail) on the night-side. The boundary of the magnetosphere is known as magnetopause, which is located around $L \approx 10$ on the day-side and stretches to $L \gtrsim 60$ on the tail-side. Another boundary, the plasmapause, separates the *frozen-in* plasma corotating with the Earth from the convecting plasma ~~constantly streaming from~~ the Sun. The location of the plasmapause is strongly influenced by the geomagnetic activity and varies between $L \approx 3 - 7$.

The Van Allen radiation belts are concentrations of high-energy charged particles coming from cosmic rays, solar storms, and other processes. Their existence was confirmed by the Explorer 1 and Explorer 3 missions in 1958, under Dr. James Van Allen from the University of Iowa [*Van Allen et al.*, 1958]. These particles are trapped in the plasmasphere by the Earth's magnetic field, and they rapidly bounce back and forth between mirror points above the atmosphere. The altitude of their mirror point depends upon the pitch angle of their velocity vector with respect to the magnetic field line direction. Particles with pitch angles greater than a certain value are trapped, while those with lower pitch angles have their mirror point in a denser region where collisions with atmospheric species effectively remove them from the radiation belts. The density of this hot population is very low ($<1$ el/cm$^3$) and it concentrates on two major belts represented in Figure 1-2 together with the Van Allen

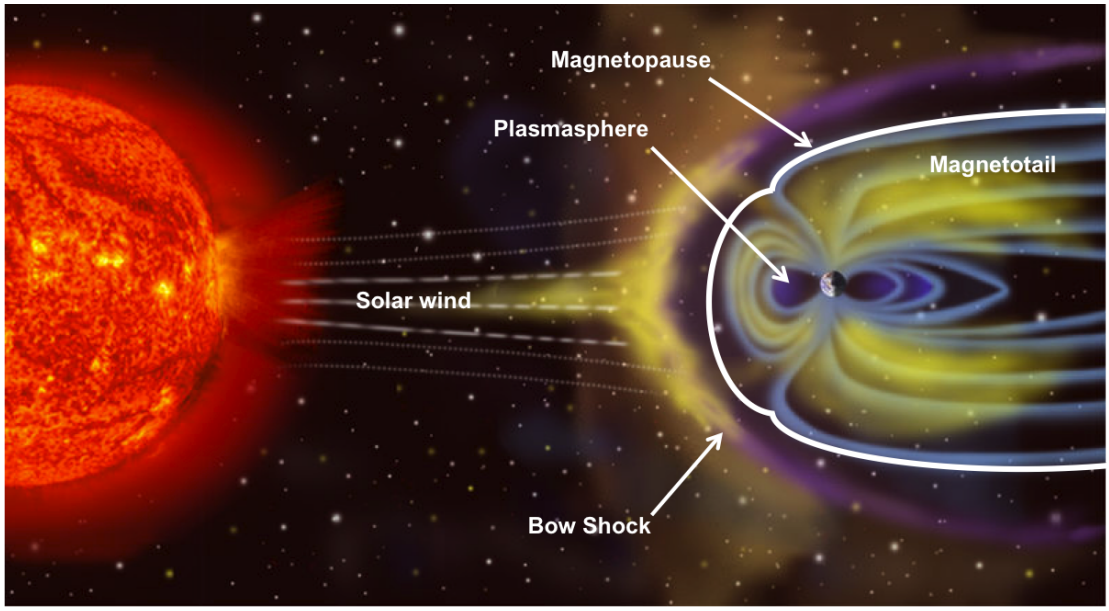


Figure 1-1: Schematic of the magnetosphere

Probes[†]: a broad inner belt between $L \approx 1.2-2$ with particles' energies up to ~~400~~ 1 MeV for protons and 1 MeV for electrons, and an outer electron belt between $L \approx 3-5$ with energies around 0.1-10 MeV. The belts extend about 65° from the celestial equator. The existence of a safe-gap between the inner and outer belts indicates that there are certain $L$-shells that do not trap significant amount of energetic particles for long periods of time or, equivalently, that natural precipitation mechanisms are stronger in this region. In addition, there exists a quasi-neutral background plasma, which is much denser than the hot population of the radiation belts but much less energetic.

The present work focuses on the inner Van Allen belt and its energetic proton population. Within this region, the Earth's magnetic field can be accurately represented using a dipole field model, and the bulk plasma can be considered cold and collisionless.

[†] One of the greatest discoveries in space physics this year has been the work published by *Baker et al.* [2013], which shows the formation of a third isolated ring, of electron energies >2 MeV located between $L = 3-5$. The ring was detected by the Van Allen Probes; it formed on 2 September 2012, persisted unchanged for over four weeks, and suddenly disappeared during the passage of a powerful interplanetary shock wave.

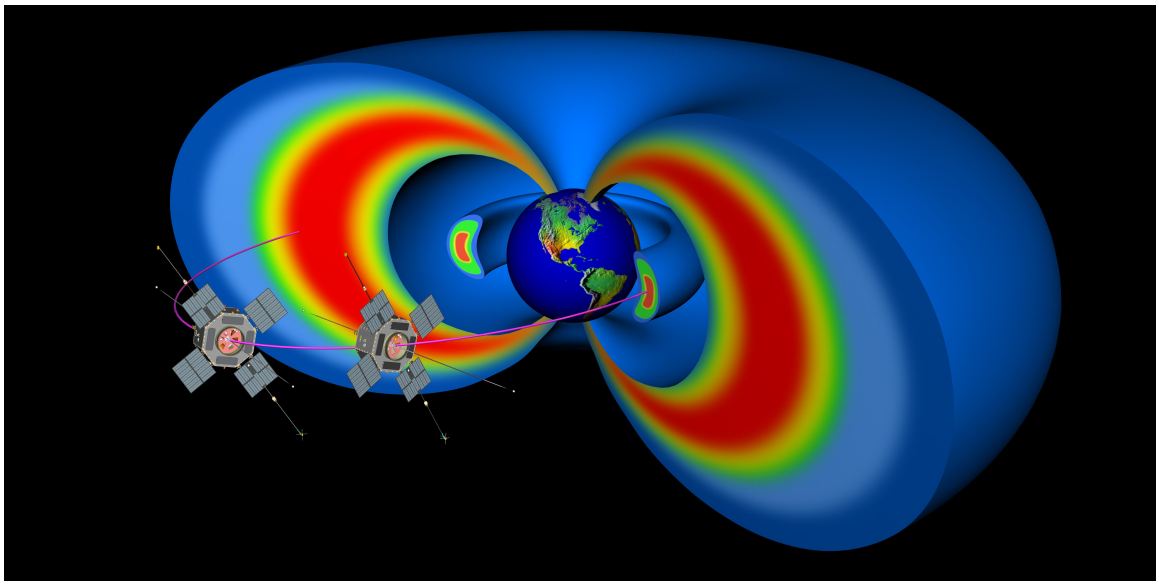

Figure 1-2: Van Allen Probes orbiting in the radiation belts

### 1.2.2 The Concept of Radiation Belt Remediation (RBR)

The high fluxes of energetic particles in the radiation belts rapidly damage electronic and biological systems, and they limit long-duration manned missions to operation below 1200 km of altitude. *Abel and Thorne* [1998] showed that wave-particle interactions with ULF/VLF waves may dominate losses in the radiation belts. This fact suggests that, if the power requirements allow, it could be possible to have human control on the belts to protect the orbiting systems from energetic particles' injections. The idea of controlled removal of high-energy particles was called Radiation Belt Remediation (RBR). VLF transmitters on the Earth's surface could be used for this purpose, as can antennas mounted on space-based platforms. While ground based transmitters have been used to test the concept in the whistler band [*Imhof et al.*, 1983; *Inan et al.*, 1984], the radiation of EMIC waves from ground is much more complicated. Magnetospheric coupling of EMIC waves would require multi-km horizontal linear antennas, which are very inefficient because the ground is a very good conductor; the ground has an opposite image current that cancels out the antenna current and the radiated fields (Section 3.1). For this reason, the approach presented in this thesis uses space-based antennas to inject ULF/VLF waves into the magnetosphere. Space-based sources, however, only radiate effectively at very oblique wave normal angles, which will inevitably translate into efficiency considerations. In this dissertation we attempt

to determine the degree to which space-based transmitters are a feasible way of achieving controlled precipitation of inner belt protons. The possible utilization of whistler waves for precipitation of high-energy trapped electrons has been studied extensively, and a space test of a linear antenna for this purpose is in preparation [*Spanjers et al.*, 2006; *Scherbarth et al.*, 2009]. The lower electromagnetic ion cyclotron (EMIC) frequency band has also been studied in the context of natural emissions and their interaction with energetic electrons, but much less work has been devoted to the use of the left-hand polarized EMIC branch for inner belt proton scattering, which is the purpose of the present work.

### 1.2.3 Trapped Particles' Dynamics

In the absence of waves, trapped energetic particles perform three basic motions: gyromotion around the magnetic lines, bounce motion along them and drift motion around the Earth. Figure 1-3 shows a simulation of the bounce and drift motions of a 100 MeV proton. When the variation of the geomagnetic field with position and time is sufficiently slow, there is an adiabatic invariant associated with each of these motions. These conservation laws lead to retention of the particles in the field. In this section we summarize the basic physics behind the adiabatic motions of this trapped radiation.

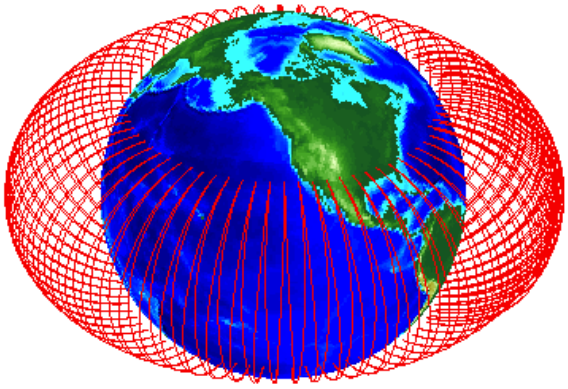

Figure 1-3: Bounce and drift motion of a 100 MeV proton at $L$=1.5. The bounce period is $\tau_b = 0.3$ s and the drift period is $\tau_d = 20$ s.

In a magnetic field with small spatial and temporal variations compared to the particle's radius and period of gyration the particle describes approximately a circle with center moving along the line of force and slowly drifting at right angles to that line. The motion along the local $\vec{B}$-field is given by

$$\left\langle \frac{dp_{\parallel}}{dt} \right\rangle = -\frac{\mu}{\gamma}\frac{\partial B}{\partial s} + qE_{\parallel} \tag{1.1}$$

where $B$ and $E$ are magnetic and electric fields, respectively. $p_{II}$ and $p_{\perp}$ are the momentum components parallel and perpendicular to the external magnetic field, $\alpha = atan\left(p_{\perp}/p_{II}\right)$ is the particle's pitch angle, $\gamma$ is the relativistic factor, $s$ is the distance along the line of force and $\mu$ is the magnetic moment given by

$$\mu = \frac{p_{\perp}^2}{2mB} \tag{1.2}$$

The drifting motion that moves the guiding center to a neighboring line is given by

$$\vec{v}_d = \frac{\hat{n}}{B} \times \left( -\vec{E} + \frac{\mu}{\gamma q}\nabla B + \frac{p_{II}^2}{\gamma q m}\frac{\partial \hat{n}}{\partial s} \right) \tag{1.3}$$

where $\hat{n}$ is the unit vector along the Earth's magnetic field direction. The first term in the right side of equation (1.3) is the $\vec{E} \times \vec{B}$ drift, which is in the same direction for both electrons and protons. The second term is the grad-$B$ drift due to the variation of the magnetic field over a gyroperiod, and the third term corresponds to the curvature drift due to the centrifugal force over a particle with parallel velocity $v_{II}$. This equation is valid if its right-hand side is small compared to the velocity of the particle. Grad-$B$ and curvature drifts give an azimuthal current, with electrons moving eastward and positive ions drifting westward. In addition, in the absence of azimuthal symmetry we could also have drifts in the radial direction.

The magnetic moment, $\mu$, introduced in equation (1.2) constitutes the first adiabatic invariant. The magnetic moment is a conserved quantity in the inner magnetosphere because the gyroradius of the high-energy particles is much smaller than the variation length-scale of the magnetic field. Invariance of $\mu$ implies that a particle will bounce back at the point where the Earth's magnetic field equals $B_{TP} = p^2/\left(2\mu m\right)$, which corresponds to $v_{\parallel TP} = 0$. Conserving energy along a magnetic field line we can write that

$$\frac{B_0}{B_{TP}} = \frac{p_{\perp 0}^2}{p^2} = \frac{p_{\perp 0}^2}{p_0^2} = sin^2\alpha_0 \tag{1.4}$$

where the subscript 0 represents a point along that line. The expression above shows that the turning point is independent of momentum and charge. In addition, in the absence of electric fields the kinetic energy remains constant and the particle always bounces at a point with the same magnetic field magnitude. In the presence of a parallel electric field, the total energy is then a constant. Equation (1.2) can be rewritten as follows

$$\frac{p_{\perp}^2}{B} = \frac{p^2 sin^2\alpha}{B} = constant \tag{1.5}$$

which allows to compute the pitch angle at any point along the trajectory, provided $B$ at that position is known. In terms of the equatorial values, the pitch angle can be expressed as follows

$$sin\alpha\,(s) = \sqrt{\frac{B\,(s)}{B_{eq}}}sin\alpha_{eq} \tag{1.6}$$

If we define $B_a$ as the magnetic field intensity at the border of the sensible atmosphere ($\sim$100 km), particles with $\alpha < \alpha_{lc} = 1/sin\left(\sqrt{B/B_a}\right)$ will be removed from the trapped configuration by collisions in the atmosphere. The pitch angle $\alpha_{lc}$ is referred as the bounce loss cone of the particles.

The second or longitudinal invariant, $J$, is given by

$$J = \oint p_{II} ds \tag{1.7}$$

where $ds$ is the element of length of the line of force, and the integral is over a complete oscillation along that line. The second adiabatic invariant is associated with the bounce motion between two mirror points in a magnetic line, and it is only constant provided that the geomagnetic field and the drift velocity $\vec{v}_d$ vary on time-scales much longer than the bounce period; this is not a particularly demanding constraint because the bounce time for MeV protons and electrons is a few seconds at most. The bounce period in a dipole magnetic field can be calculated as follows

Table 1.1: Energetic particles' characteristic periods

| | 100 MeV protons | 1 MeV electrons | |
|---|---|---|---|
| | $L$=1.5 | $L$=1.5 | $L$=4.5 |
| Gyroperiod [s] | $10^{-2}$ | $5{\cdot}10^{-6}$ | $3{\cdot}10^{-4}$ |
| Bounce period [s] | 0.3 | 0.1 | 0.5 |
| Drift period [s] | 20 | 3000 | 1200 |

$$\tau_b\left(\alpha_{eq}\right) = \frac{4\gamma m L R_E}{p} \int_0^{\lambda_m(\alpha_{eq})} \frac{cos\lambda\left(4 - 3cos^2\lambda\right) d\lambda}{\left[1 - \frac{sin^2\alpha_{eq}}{cos^6\lambda}\left(4 - 3cos^2\lambda\right)^{1/2}\right]^{1/2}} \tag{1.8}$$

where $R_E$ is the radius of the Earth and $\lambda_m$ is the magnetic latitude of the mirror point, which depends on the equatorial pitch angle $\alpha_{eq}$. A fair approximation to the expression above in a dipole magnetic field was calculated by *Lenchek et al.* [1961]

$$\tau_b\left(\alpha_{eq}\right) \approx \frac{4\gamma m L R_E}{p}\left[1.3802 - 0.3198\left(sin\alpha_{eq} + \sqrt{sin\alpha_{eq}}\right)\right] \tag{1.9}$$

The third adiabatic invariant is the magnetic flux inside the invariant surface enclosed by the particle's drift path. This invariant is associated with the precession of particles around the Earth. The third adiabatic invariant is conserved provided that the Earth's magnetic field varies on time-scales much longer than the drift period, which is only likely to be the case when the magnetosphere is relatively quiescent. In a dipole magnetic field, the drift period can be approximated by the following formula [*Davidson*, 1977]

$$\tau_d \approx \frac{1.43 K_t}{L\gamma\left(v/c\right)^2\left(1 + 0.42 sin\alpha_{eq}\right)} \tag{1.10}$$

where $K_t = 1.0308 \cdot 10^4$ seconds for electrons, and $K_t = 5.655$ seconds for protons.

Table 1.1 presents typical gyro, bounce and drift periods of particles trapped in the inner and outer radiation belts.

According to adiabatic theory, the energetic particles in the radiation belts would remain indefinitely trapped in the geomagnetic field. During geomagnetic storms, however, particles diffuse from one invariant surface to another and may eventually get lost away from the

Earth or down into the atmosphere. In addition, precipitation induced by wave-particle interactions is one of the major loss processes of radiation belt particles [*Abel and Thorne*, 1998]. The following sections will show how waves are capable of perturbing the adiabatic motion and precipitating energetic radiation belt particles.

### 1.2.4 What are EMIC Waves?

Electromagnetic Ion Cyclotron (EMIC) waves are plasma waves that propagate below the proton gyrofrequency, $\Omega_{H^+}$, given by

$$\omega < \Omega_{H^+} = \frac{qB_0}{m_H} \tag{1.11}$$

where $\omega$ is the frequency of the wave, $q$ is the electron charge, $B_0$ is the external magnetic field and $m_H$ is the proton mass. While whistler-type emissions are capable of precipitating energetic trapped electrons [*Imhof et al.*, 1983; *Inan et al.*, 1984, 2003; *Kulkarni et al.*, 2008], EMIC frequencies are appropriate for interaction with the energetic protons of the inner belt. EMIC waves appear in multiple frequency bands due to the presence of heavy ions, which strongly modify wave propagation characteristics.

Observations of naturally generated EMIC waves have been reported from ground and space [*Anderson*, 1996; *Fraser et al.*, 1992, 1996; *Loto'aniu et al.*, 2005]. These waves are most frequent and most intense during geomagnetic storms. Evidence shows that naturally occurring EMIC waves can precipitate both energetic ring current protons [*Erlandson and Ukhorskiy*, 2001; *Young et al.*, 1981] and electrons [*Lorentzen et al.*, 2000; *Meredith et al.*, 2003; *Miyoshi et al.*, 2008; *Rodger et al.*, 2008], which supports the concept of man-made intervention if the energies and power involved are reasonable.

L-mode EMIC waves are naturally generated by ion cyclotron instability of ring current ions (10-200 keV), whose temperature anisotropy provides the free energy required for wave growth [*de Soria-Santacruz et al.*, 2013a]. The ring current is located in the equatorial plane at a distance of 3-5 $R_E$, which explains the lack of EMIC wave power at low L-shells and the stability of the inner proton belt. Consequently, the precipitation of energetic trapped protons requires the in-situ radiation of L-mode EMIC waves at low L-shells, which is a broad unexplored problem and it is addressed in this dissertation.

## 1.3 Review of Past Work

The propagation and emission of ULF and VLF waves from orbiting antennas is a problem of growing interest to the scientific, engineering and defense community, largely motivated by their potential application for artificial modification of the high-energy particle radiation environment, both natural and man-made. These emissions will create a pitch angle scattering of the energetic particles. A portion of the particles may be scattered into the loss cone, lowering the altitude of their mirror point such that they are absorbed by the atmosphere.

The propagation of whistler and EMIC waves has been studied through observations and ray tracing simulations. The wave number vector of EMIC waves tends to become oblique due to the curvature and gradient of the Earth's magnetic field as the waves propagate away from the equator [*Thorne et al.*, 2006], but the group velocity vector remains field aligned except ~~in the vicinity of~~ the bi-ion frequency, which is a mixed resonance between two ion species. At frequencies above the bi-ion frequency, EMIC waves exhibit a resonance cone that prevents them from bouncing, thus wave reflection cannot occur until they propagate to higher latitudes and the local bi-ion frequency increases above the wave frequency [*Thorne and Horne*, 1993]. At the bi-ion frequency the wave normal angle equals $\theta = 90°$, the parallel group velocity is zero and the wave could be reflected [*Rauch and Roux*, 1982], which is analogous to the reflection of whisters at the lower hybrid frequency [*Thorne and Kennel*, 1967]. There is no observational evidence, however, showing that EMIC waves are capable of bouncing back from high latitudes [*Loto'aniu et al.*, 2005]. Ray tracing codes, which use the eikonal approximation of geometrical optics [*Budden*, 1966] to follow the wave group velocity for given magnetic field and plasma density models, have been developed to study the propagation of EMIC waves in the context of in situ observations. *Rauch and Roux* [1982] developed a three-dimensional ray tracing code for ULF waves propagating in an $He^+$-rich plasma, and *Gomberoff and Neira* [1983] added a third cold ion species ($O^+$) and showed that it can affect the growth rate of parallel propagating EMIC waves below the $He^+$ cyclotron frequency. Further studies [*Dobes*, 1970; *Ludlow*, 1989] added a finite parallel electric field and perpendicular wave number that allows Landau damping effects to take place. The 3D ray tracer developed by the VLF Group at Stanford University [*Golden et al.*, 2010] has been widely used to model the remediation ideas, and it was the predecessor of the

HOTRAY ray tracing code [*Horne and Thorne*, 1993] capable of computing propagation, growth and absorption of EMIC waves.

Evidence of energetic particles' precipitation mediated by interactions with ULF/VLF waves has renewed interest in the analysis of wave-particle interactions. Two different approaches exist to model the problem. The first approach consists of finding diffusion coefficients, and using them to solve the pitch angle diffusion equation (Fokker-Planck equation) for the distribution function of energetic particles perturbed by the waves. This methodology assumes broad-band incoherent waves, which results in pitch angle diffusion and precipitation. *Kennel and Engelmann* [1966] were the first to derive the general quasi-linear pitch angle diffusion equation, and based on their formulation *Lyons and Thorne* [1972], *Lyons et al.* [1972], *Lyons* [1974a] and *Lyons* [1974b] derived general expressions for the particle quasi-linear diffusion coefficients in both pitch angle and energy in an electron-proton medium. *Albert* [1999] introduced relativistic effects to the quasi-linear analysis of either electrons or protons interacting with oblique whistler or ion cyclotron waves in an hydrogen plasma, and in a later publication [*Albert*, 2003] he studied the diffusion coefficients of oblique EMIC waves interacting with electrons in a multi-species plasma. *Jordanova et al.* [1996, 1997, 1998, 2001] introduced heavy ion species in the calculation of diffusion coefficients for incoherent EMIC waves interacting with protons. *Loto'aniu et al.* [2005] modeled the electron pitch angle scattering due to the field-aligned EMIC waves observed by the CRRES spacecraft using multi-ion diffusion coefficients, and later, *Li et al.* [2007] examined the pitch angle scattering of electrons by field-aligned EMIC and hiss waves during the main and recovery phases of a storm. The recent study by *Shao et al.* [2009] derived diffusion coefficients for field-aligned shear Alfvén waves interacting with inner belt energetic protons. For the whistler regime, *Abel and Thorne* [1998] calculated the diffusion coefficients and precipitated fluxes of energetic electrons due to natural phenomena and whistler emissions, and *Horne and Thorne* [2003] introduced ray tracing to the analysis. *Inan et al.* [2003] used power scaling from Abel and Thorne's results to compare scattering of electrons due to whistler emissions from space-based versus ground-based transmitters. *Glauert and Horne* [2005] and *Albert* [2005] developed relativistic computer codes that efficiently calculate the quasi-linear diffusion coefficients, and *Summers* [2005] provided exact closed-form analytical expressions of the diffusion coefficients for field-aligned electromagnetic waves.

The second approach involves a test particle simulation of the non-linear equations of motion of energetic particles interacting with the waves. Compared to the diffusion approach, this formulation is capable of modeling coherent and narrow-band waves that more accurately reproduce the effect of in-situ transmitters. Moreover, test particle simulations are capable of capturing non-linear as well as off-resonant interactions between particles and waves. The test particle formulation was initially proposed by *Inan et al.* [1978], who described the non-linear steady interaction between coherent field-aligned whistlers and energetic electrons. The model was further extended to include short-duration whistler pulses [*Chang and Inan*, 1983; *Inan et al.*, 1982], relativistic effects [*Chang and Inan*, 1983, 1985a,b], and obliquely propagating whistlers [*Bell*, 1984; *Inan and Bell*, 1991; *Ristic-Djurovic et al.*, 1992, 1998; *Tao and Bortnik*, 2010]. Recently, *Bortnik et al.* [2006] introduced ray tracing and Landau damping to study the precipitation of radiation belt electrons driven by lightning generated whistlers, and *Kulkarni et al.* [2008] modeled the effect of space-based VLF transmitters operating in the whistler band. This methodology has always been applied to whistler emissions and their effect on energetic electrons; however, there are no studies related to the interaction between narrow-band EMIC waves and radiation belt particles.

The precipitation of energetic inner belt protons requires the in-situ radiation of EMIC waves at low $L$-shells, which is a prominent problem among the at-least-partially unsolved questions related to remediation. The impedance of an electric dipole transmitting in the ULF/VLF regime in a magnetoplasma has been determined in the absence of the plasma sheath [*Balmain*, 1964; *Wang and Bell*, 1969, 1970, 1972a], and its current distribution has been analyzed under the same assumption [*Bell et al.*, 2006; *Chevalier et al.*, 2008]. More specifically, the quasi-electrostatic approximation of *Balmain* [1964] for the far-field is valid for any antenna orientation with respect to the Earth's magnetic field lines. This approximation only involves the longitudinal electric field, which correctly captures the antenna radiation resistance; the imaginary part of the impedance, however, is not well reproduced by Balmain's method because it neglects the divergence of the plasma current due to the transverse electric field. Additional methods have been developed describing the linear propagation in the far-field region [*de Soria-Santacruz*, 2011; *Takiguchi*, 2009]. In particular, we have in hand full-wave calculation methods for both whistler and EMIC waves, and we have calibrated them with previous work [*Kuehl*, 1962; *Wang and Bell*, 1972a; *Stenzel*, 1976] and with Balmain's approximation. For many plasma waves like

EMIC waves, resonances occur where the index of refraction approaches infinity for some special directions; it is in the vicinity of these directions that most of the radiated power propagates, thus the quasi-electrostatic approximation can be expected to have a wide range of validity in the calculation of the radiation resistance [*Wang and Bell*, 1969]. For an electrical dipole antenna, however, the plasma involves the formation of a thick oscillatory sheath [*Chevalier et al.*, 2010; *Song et al.*, 2007; *Tu et al.*, 2008], the concentration of power around resonance cones, with potential for wave ducting [*Stenzel*, 1975], and the effects of this highly perturbed plasma region on the radiation impedance and on the self-consistent current distribution along the antenna. For non-capacitive loop antennae only linear far-field analyses of single loops exist [*Wang and Bell*, 1972b, 1973]; their implementation was attempted once with the Soviet Active mission (Intercosmos 24) [*NASA Data Center National Space Science*, 2012], which failed in its attempt to deploy a VLF magnetic loop with the objective to understand its radiation properties and triggered particle precipitation. Most of the work above addressed the radiation of whistlers from space-based transmitters, but the emission of the very low EMIC band entails additional complexity as we will see in this dissertation. The problem of in-situ radiation of EMIC waves requires more attention, and it will be addressed in the present work.

Many civil and military missions have tried to characterize the Van Allen belts and the wave-particle interactions that take place there, but none has been designed and launched with the objective to demonstrate the feasibility of the RBR concept yet. The Dynamics Explorer (DE) launched in 1981, the Combined Release and Radiation Effects Satellite (CRRES) in 1990, the Imager for Magnetopause-to-Aurora Global Exploration (IMAGE) in 2000 or the Van Allen Probes launched in August 2012 are examples of the first kind of spacecraft. The only effort so far to test the RBR concept is the Demonstration and Science Experiments (DSX) from the Air Force Research Laboratory (AFRL) [*Scherbarth et al.*, 2009], which is scheduled to be launched in 2015. The satellite features 14 payloads, grouped under three main experiments: the Wave Particle Interaction Experiment (WPIx), the Space Weather Experiment (SWx) and the Space Environmental Effects Experiment (SFx). WPIx aims at radiating whistler waves from an 80 meter-long dipole antenna and characterizing its feasibility to precipitate energetic trapped electrons. The Loss Cone Imager (LCI) [*Voss et al.*, 2009] is an electron loss cone particle detector that will provide 3D measurements of energetic particle distributions, and the High Sensitivity Telescope (HST) is a separate solid

state detector telescope required to obtain fluxes of energetic electrons along the field lines. While DSX is testing the efficacy of whistler waves to alter the high-energy electrons of the radiation belts, this dissertation provides a preliminary assessment of the specifications required by a space-based system capable of precipitating the extremely energetic proton population of the inner radiation belt.

## 1.4 Thesis Statement, Objectives and Approach

The previous sections described the fundamental terms and ideas behind the concept of controlled precipitation of energetic trapped particles. These notions allow us to introduce the thesis statement, objectives and approach, which are presented below.

### 1.4.1 Thesis Statement and Objectives

This dissertation aims to characterize the ability of Electromagnetic Ion Cyclotron (EMIC) waves radiated from space-based transmitters to precipitate the energetic protons trapped in the inner Van Allen belt, as well as to determine the feasibility and engineering implications of a space-based antenna capable of significantly reducing this energetic radiation.

The following objectives have been defined in order to fulfill the thesis statement presented above:

- Investigate if it is possible to radiate EMIC waves from a space-based antenna. Determine the type of transmitter (if any) and the effect of the plasma on its radiation characteristics, i.e. its radiation impedance and radiation pattern.
- Study the cold plasma wave propagation in the magnetosphere of the EMIC waves radiated from a space-based transmitter.
- Analyze and understand the distribution and dynamics of the energetic protons trapped in the inner Van Allen belt.
- Characterize the interaction of these energetic protons (20-300 MeV) with man-made EMIC waves.

- Calculate the new lifetimes of the energetic inner belt protons due to their interaction with the EMIC waves radiated from space-based transmitters, and compare these lifetimes with the natural precipitation mechanisms.

- Analyze the mechanical, thermal and electrical implications of a space-based antenna capable of radiating EMIC waves in the magnetosphere.

- Characterize the feasibility of a space-based transmitter(s) able to significantly reduce the amount of trapped energetic protons. More specifically, we have called *remediation* to the fact of reducing the natural residence time of the energetic protons by a factor of 10 over the entire inner belt.

Additionally, at the end of the thesis we also outline a scientific mission scaled down to detectability of the proton precipitation induced by the antenna, which would serve to test the theory and technology involved in the controlled removal of energetic particles.

### 1.4.2 Approach

The approach adopted in this thesis is based on theory, modeling, and design. Two distinct areas can be easily identified: one analyzing the scientific aspects of the problem and another dealing with the engineering implications with the purpose of determining the feasibility of the concept. Both domains are dependent on each other and they share inputs/outputs.

The scientific studies involve theoretical work, which finally translates into three core simulations: (1) radiation, (2) wave propagation and damping, and (3) wave-particle interaction simulations. The engineering work is also based on modeling and design involving mechanical, thermal and electrical considerations. Figure 1-4 aims at describing the approach followed in this dissertation. The big pink box includes geomagnetic field, energetic trapped protons, cold plasma and hot plasma models, which represent the magnetospheric conditions. These models are input to all the simulations in this dissertation. The analyses represented in the radiation module aim to determine the type of antenna capable of radiating EMIC waves and the effect of the plasma on its radiation. The wave propagation, damping and wave-particle interaction simulations (the science module in the figure) take radiation model results as inputs. Similarly, the outputs from the science module are used

by the engineering module to determine the transmitter's capability of depleting the inner Van Allen belt of energetic protons. The engineering implications of such a transmitter, however, have the capability of modifying the radiation models, which introduces coupling between the different simulations.

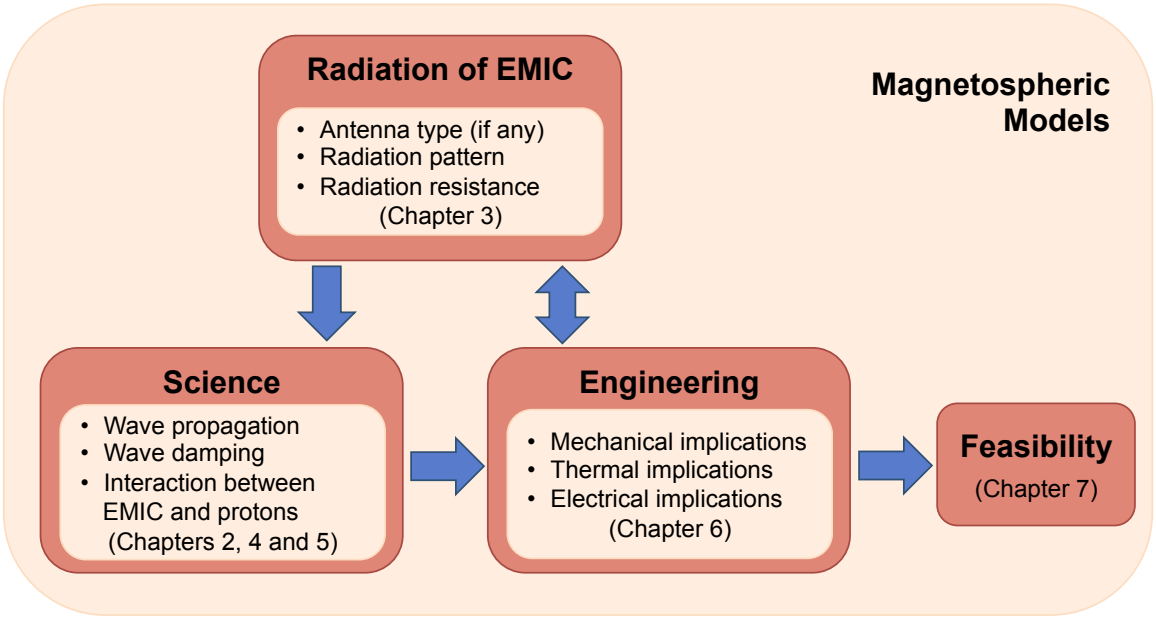


Figure 1-4: Schematic illustrating the approach followed in this thesis

## 1.5 Thesis Organization

In the present chapter we provided the motivation for this dissertation, scientific background, literature review, objectives and approach. Chapters 2 to 5 focus on the science behind the concept of remediation, while Chapters 6 and 7 use the physics to derive engineering implications. More specifically, Chapter 2 describes and formulates the basic physics behind the propagation and damping of EMIC waves, and their interaction with highly energetic protons. Chapter 3 identifies a potential antenna configuration capable of radiating EMIC waves and focuses on the effect of the plasma on its radiation characteristics. Chapter 4 calculates the propagation and damping of EMIC waves in the magnetosphere radiated from such an antenna, and in Chapter 5 we use these propagation results to calculate the wave-particle interaction between energetic inner belt protons and EMIC waves. We first characterize the behavior of individual particles and we next study the interaction with the

whole inner belt proton population to calculate precipitating fluxes and time evolution of the distribution. Chapter 6 analyzes the mechanical, thermal and electrical implications of the proposed antenna configuration, including a preliminary sizing, a study of its thermal control system and an estimation of its performance. Chapter 7 analyzes the feasibility of a mission capable of depleting the inner Van Allen belt of energetic protons, and outlines a scientific mission scaled down to detectability of the proton precipitating fluxes. To conclude, Chapter 8 provides a summary and discussion, contributions of this dissertation and suggestions for future work.

# Chapter 2

# Theoretical Formulation and Definition of Mission Parameters

This chapter describes and formulates the basic physics behind the propagation and damping of EMIC waves, and their interaction with highly energetic protons.

## 2.1 Electromagnetic Ion Cyclotron (EMIC) Waves

Electromagnetic Ion Cyclotron (EMIC) waves are plasma waves that propagate below the proton gyrofrequency, $\Omega_{H^+}$. In vacuum, the wavelength is constant for a fixed frequency. Contrarily, plasmas are dispersive, that is, the wavelength is a function of ~~the direction of propagation~~. The dispersion relationship of a given plasma wave mode relates its frequency to the refractive index and propagation angle. The presence of heavy ions strongly modifies EMIC propagation characteristics. The EMIC dispersion in a $H^+$-$He^+$-$O^+$ plasma was analyzed by *Ludlow* [1989] and *Albert* [2003], and we summarize their findings using cold plasma theory as a first approximation.

The general dispersion relationship in a cold plasma for any wave mode can be expressed as follows [*Stix*, 1992]

$$An^4 - Bn^2 + C = 0 \tag{2.1}$$

where $n = c|\vec{k}|/\omega$ is the index of refraction, $\vec{k}$ is the wave number vector, $c$ is the speed of light and

$$A = Ssin^2\theta + Pcos^2\theta \tag{2.2}$$

$$B = RLsin^2\theta + PS\left(1 + cos^2\theta\right) \tag{2.3}$$

$$C = PRL \tag{2.4}$$

where $\theta$ is the angle between the external magnetic field and the wave normal direction, and the wave coefficients are given by

$$R = 1 - \sum_l \frac{\omega_{pl}^2}{\omega^2} \frac{\omega}{\omega + \Omega_l} \tag{2.5}$$

$$L = 1 - \sum_l \frac{\omega_{pl}^2}{\omega^2} \frac{\omega}{\omega - \Omega_l} \tag{2.6}$$

$$P = 1 - \sum_l \frac{\omega_{pl}^2}{\omega^2} \tag{2.7}$$

$$S = \frac{R + L}{2} \tag{2.8}$$

$$D = \frac{R - L}{2} \tag{2.9}$$

the summations are over all species including electrons. The plasma frequency $\omega_{pl}$, and the cyclotron frequency $\Omega_l$ are defined as follows

$$\omega_{pl} = \sqrt{\frac{q_l^2 n_l}{m_l \epsilon_0}} \tag{2.10}$$

$$\Omega_l = \frac{q_l B_0}{m_l} \tag{2.11}$$

where $n_l$, $m_l$ and $q_l$ are the density, mass and charge of the $l$-species, respectively. Rearranging equation (2.1) we get

$$n^2 = \frac{2PRL}{(RL - PS)\, sin^2\theta + 2PS \pm \sqrt{(RL - PS)^2\, sin^4\theta + 4P^2D^2cos^2\theta}} \tag{2.12}$$

The summations in equations (2.5) to (2.7) are much larger than one because the frequencies under consideration are such that $\omega/\left|\Omega_e\right| << \omega_{pe}^2/\Omega_e^2$. With this approximation and normalizing with $\omega_{pe}^2/\Omega_e^2$ (i.e. $\overline{R} = R\ \Omega_e^2/\omega_{pe}^2$, etc.), the coefficients can be expressed as [*Albert*, 2003; *Jordanova et al.*, 1996]

$$\overline{R} = -\frac{1}{MY}\left[\frac{1}{MY - 1} + \sum_i \frac{\gamma_i Z_i}{\beta_i Y/Z_i + 1}\right] \tag{2.13}$$

$$\overline{L} = -\frac{1}{MY}\left[\frac{1}{MY + 1} + \sum_i \frac{\gamma_i Z_i}{\beta_i Y/Z_i - 1}\right] \tag{2.14}$$

$$\overline{P} = -\left(\frac{1}{MY}\right)^2\left[1 + M\sum_i \frac{\gamma_i Z_i^2}{\beta_i}\right] \tag{2.15}$$

$$\overline{S} = \frac{\overline{R} + \overline{L}}{2} \tag{2.16}$$

$$\overline{D} = \frac{\overline{R} - \overline{L}}{2} \tag{2.17}$$

where the summations are now over all ion species and $\gamma_i = n_i/n_e$, $Z_i = q_i/e$, $M = m_e/m_H$, $\beta_i = m_i/m_H$ and $Y = \omega/\Omega_{H^+}$. With these assumptions, the cold plasma dispersion relationship can be expressed as follows

$$n^2 = \frac{\omega_{pe}^2}{\Omega_e^2}\Psi^{-1} \tag{2.18}$$

where

$$\Psi = \frac{\left(\overline{RL} - \overline{PS}\right) sin^2\theta + 2\overline{PS} \pm \sqrt{\left(\overline{RL} - \overline{PS}\right)^2 sin^4\theta + 4\overline{P}^2\overline{D}^2 cos^2\theta}}{2\overline{PRL}} \tag{2.19}$$

Waves only propagate for $\Psi > 0$. For a given frequency, ~~the EMIC dispersion has two solutions or branches, one with left-hand (L-mode) and another with right-hand (R-mode) polarizations.~~ This thesis focuses on L-mode EMIC waves by analogy with the ones that are naturally generated in the magnetosphere, and that have been shown to precipitate ring current protons. At a particular wave normal angle in cold plasma theory, the refractive index of L-mode EMIC waves tends to infinity, i.e. a resonance occurs. For the EMIC band, the resonant wave normal angle is almost perpendicular to the external magnetic field; the group velocity, however, typically stays aligned with the external magnetic field direction due to the flat shape of the EMIC dispersion relationship. From equation (2.1) it can be observed that resonances ($n \to \infty$) occur when $A = 0$, or equivalently

$$tan^2\theta_{res} = -P/S \tag{2.20}$$

The bi-ion frequencies are mixed resonances between two ion species. At the bi-ion frequency ($S = 0$) the wave-normal angle equals $\theta = 90°$, the parallel group velocity is zero and the wave is reflected and/or absorbed [*Rauch and Roux*, 1982]. For frequencies above the bi-ion frequency, EMIC waves exhibit a resonance cone that prevents them from getting perpendicular to the geomagnetic field, thus wave reflection/absorption occurs when they propagate to higher latitudes and the local bi-ion frequency increases above the wave frequency [*Thorne and Horne*, 1993]. At the cyclotron frequencies of each ion species ($L \to \infty$, $S \to \infty$), the resonance occurs for parallel propagation ($\theta = 0$). Cutoffs occur whenever $n \to 0$, which corresponds to $RPL = 0$. Heavy ions also introduce stop bands in the EMIC dispersion relationship; the propagation of the L-mode is interrupted between the ~~resonance~~ and the cutoff frequency of each ion species. In addition, changes of polarization in a multi-ion plasma can happen when $D = 0$, which corresponds to crossover frequencies. At the crossover frequencies a particular branch changes from R to L mode through linear polarization, and vice versa.

Figure 2-1 summarizes the dispersion properties of EMIC waves in a cold plasma with

77% $H^+$, 20% $He^+$ and 3% $O^+$. Figure 2-1 (a) plots the non-dimensional wave frequency, $Y=\omega/\Omega_{H^+}$, as a function of the magnitude of the wave number vector for waves propagating at $\theta = 45°$ with respect to the external magnetic field direction. We clearly observe the effect of heavy ions, which introduce L-mode resonances ($Y_{resO^+}$, $Y_{resHe^+}$, $Y_{resH^+}$) where the cold plasma refraction index tends to infinity, L-mode stop bands bounded by resonant and cutoff frequencies ($Y_{cfO^+}$, $Y_{cfHe^+}$, $Y_{cfH^+}$), and crossover frequencies ($Y_{crO^+}$, $Y_{crHe^+}$, $Y_{crH^+}$) where the dispersion branches change polarization. Figure 2-1 (b) also plots the dispersion relation of L-mode EMIC waves but in another format. The parallel and perpendicular components of the wave number vector are represented for different normalized wave frequencies. It can be observed that, for a fixed wave frequency, the wave number vector can be very sensitive to the direction of propagation. Some of the curves are open, which correspond to the branches with asymptotes in Figure 2-1 (a). Other branches, however, are closed and mostly isotropic in wave number magnitude, which correspond to the frequency ranges between cutoffs and crossovers in Figure 2-1 (a).

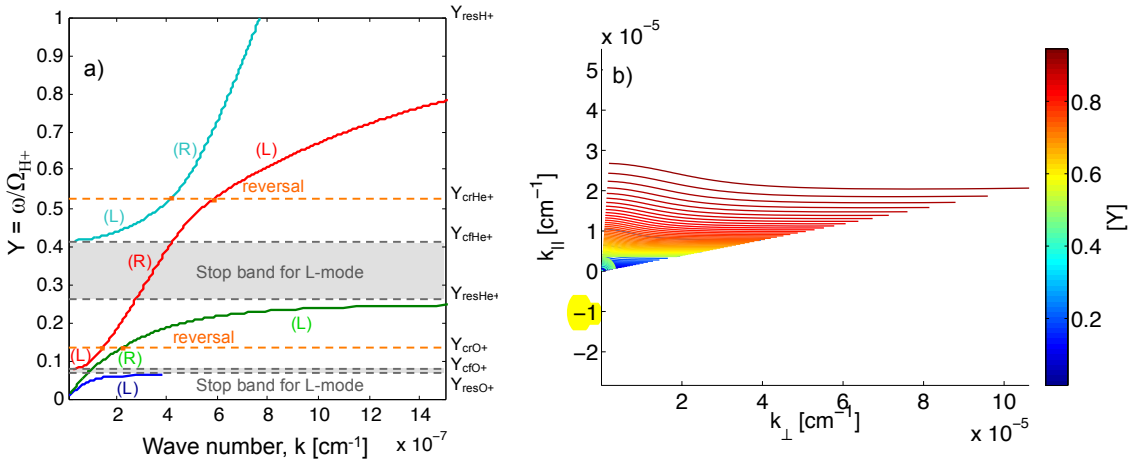


Figure 2-1: Dispersion relation of EMIC waves in a cold plasma with 77% $H^+$, 20% $He^+$ and 3% $O^+$. (a) Non-dimensional wave frequency, $Y=\omega/\Omega_{H^+}$, as a function of the magnitude of the wave number vector for $\theta = 45°$. (b) L-mode parallel and perpendicular components of the wave number vector for different normalized wave frequencies.

## 2.2 Wave Propagation

The sections below present the formulation that describes the propagation and damping of EMIC waves in the magnetosphere, which will be used in the following chapters.

### 2.2.1 Ray Tracing Methodology

The magnetosphere is an inhomogeneous and anisotropic medium. The variation of the geomagnetic field and plasma density with location modifies the propagation of EMIC waves in the radiation belts. In such a medium, the phase and group velocities of the waves are generally different in magnitude and direction. The trajectory of the wave energy is called ray path, and it is always perpendicular to the refraction index surface.

If the properties of the medium vary slowly within one wavelength, then geometrical optics gives a good approximation of the ray path trajectory. Geometrical optics assumes that, within a given slab, the properties of the medium are locally constant and change slowly as the ray propagates to the next slab; this can be interpreted as successive applications of Snell's Law. Ray tracing uses the geometrical optics approximation to determine the trajectory of the ray path and assumes that the plasma is cold, i.e. the thermal velocity of the particles is smaller than the wave phase velocity. For a fixed frequency wave, ray tracing allows us to calculate the wave normal angle and the group time along the ray path, while the power density has to be inferred from the ray path divergence and from Landau and cyclotron damping calculations. The ray tracing equations were first derived by *Haselgrove* [1955] and they are a set of closed first order differential equations that can be integrated numerically. In the following chapters we solve the full three dimensional differential equations, which are given by [*Kimura*, 1966]

$$\frac{dr}{dt} = \frac{1}{n^2}\left(\rho_r - n\frac{\partial n}{\partial \rho_r}\right) \tag{2.21}$$

$$\frac{d\varphi}{dt} = \frac{1}{rn^2}\left(\rho_\varphi - n\frac{\partial n}{\partial \rho_\varphi}\right) \tag{2.22}$$

$$\frac{d\phi}{dt} = \frac{1}{rn^2\sin\varphi}\left(\rho_\phi - n\frac{\partial n}{\partial \rho_\phi}\right) \tag{2.23}$$

$$\frac{d\rho_r}{dt} = \frac{1}{n}\frac{\partial n}{\partial r} + \rho_\varphi\frac{d\varphi}{dt} + \rho_\phi\frac{d\phi}{dt}\sin\varphi \tag{2.24}$$

$$\frac{d\rho_\varphi}{dt} = \frac{1}{r}\left(\frac{1}{n}\frac{\partial n}{\partial \varphi} - \rho_\varphi \frac{dr}{dt} + r\rho_\phi \frac{d\phi}{dt}\cos\varphi\right) \tag{2.25}$$

$$\frac{d\rho_\phi}{dt} = \frac{1}{r\sin\varphi}\left(\frac{1}{n}\frac{\partial n}{\partial \phi} - \rho_\phi \frac{dr}{dt}\sin\varphi - r\rho_\phi \frac{d\varphi}{dt}\cos\varphi\right) \tag{2.26}$$

where $r$, $\varphi$ and $\phi$ are the geocentric distance, zenith angle and longitude, respectively. $\rho_r$, $\rho_\varphi$ and $\rho_\phi$ are the radial, colatitude and longitude components of the refractive index vector (parallel to $\vec{k}$ with length $n$) and $t$ is the integration variable which has units of distance ($t$ = phase time $\times$ speed of light). It must be noted that the properties of the medium appear only through the refractive index $n$ and its components. Given a set of initial values of ray position and wave normal vector, the integration of the ray tracing equations determines the variation of the these quantities within the magnetosphere.

### 2.2.2 Landau/Cyclotron Damping and Power Flux Divergence

Ray tracing provides wave normal vectors and plasma properties along the ray path, but it is not able to determine the behavior of the wave power along that path. The wave power can be modified by collisionless damping mechanisms named Landau and cyclotron damping. Landau and cyclotron damping happen due to resonant interaction between the wave and charged particles. More specifically, Landau damping is a resonant interaction that occurs between waves and thermal electrons that travel with parallel velocity close to the wave phase velocity, ~~i.e. electrons' thermal velocity along the wave propagation direction has to be non-zero~~. In the presence of a parallel wave electric field, these resonant electrons see this field as static, which accelerates or decelerates them. If the electron moves slower (faster) than the wave, the particle is accelerated (decelerated) and the wave loses (gains) energy. The wave is damped over time if there are more electrons with slower than larger velocities compared to the wave phase speed; this is the case for the Maxwellian distribution represented in Figure 2-2, as well as for any other electron distribution that monotonically decreases with increasing energy. The shadowed area in Figure 2-2 represents the range of resonant velocities; since there are more resonant particles with slower than larger velocities compared to the wave phase speed, these particles will gain energy from the wave and the latter will be damped.

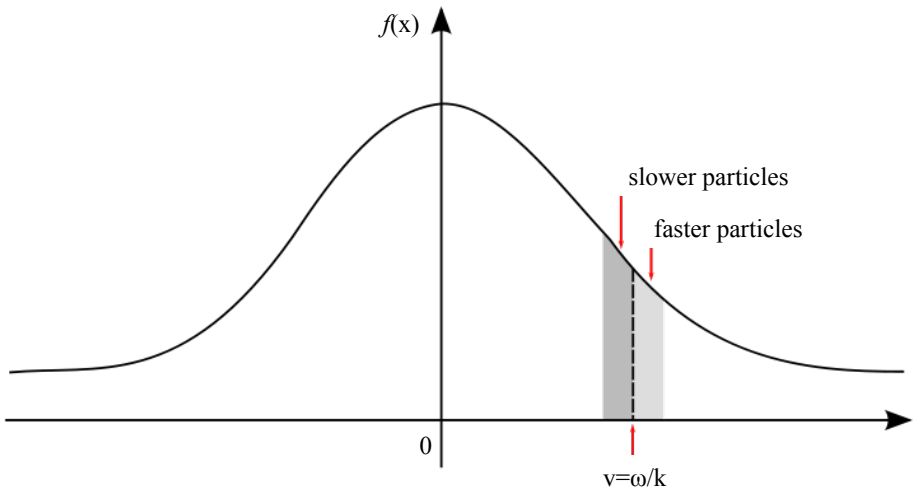


Figure 2-2: Maxwellian distribution function of energetic particles required by Landau damping

The growth/damping rate of EMIC waves due to Landau and cyclotron interaction, $\gamma$, calculated at each location along the ray path can be expressed as follows [*Chen et al.*, 2010, equation (2)]

$$\begin{aligned}
\gamma_l \;=\; & 2\pi^2 \frac{\omega_{pl}^2}{\omega \left|k_{\|}\right| \frac{\partial D^{(0)}}{\partial \omega}} \int_0^{\infty} v_{\perp} dv_{\perp} \int_{-\infty}^{\infty} dv_{\|} \sum_m \delta\left(v_{\|} - \frac{\omega - m\Omega_l}{k_{\|}}\right) \left[G_{1l}\left(\left(P - n^2 sin^2\theta\right)\right.\right. \\
& \left[2\left(L - n^2\right) v_{\perp} J_{m+1}^2 + 2v_{\perp}\left(R - n^2\right) J_{m-1}^2 + n^2 sin^2\theta v_{\perp}\left(J_{m+1} - J_{m-1}\right)^2\right] \\
& -n^2 cos\theta sin\theta \left[2v_{\|} J_m \left(J_{m+1}\left(R - n^2\right) + J_{m-1}\left(L - n^2\right)\right)\right. \\
& \left.\left. +n^2 cos\theta sin\theta v_{\perp}\left(J_{m+1} - J_{m-1}\right)^2\right]\right) \\
& +G_{2l}\left(4v_{\|} J_m \left[\left(L - n^2\right)\left(R - n^2\right) + n^2 sin^2\theta\left(S - n^2\right)\right]\right. \\
& \left. -2n^2 cos\theta sin\theta \left[\left(R - n^2\right) v_{\perp} J_{m-1} + \left(L - n^2\right) v_{\perp} J_{m+1}\right]\right)\Big] \qquad (2.27)
\end{aligned}$$

where the subscript $l$ refers to each different charged species (the total growth rate is the sum of the growth rates of all resonant species), $m$ is the resonant harmonic number, $D^{(0)}$ is the determinant from the cold dispersion relation, R, L, S and P are the Stix parameters [*Stix*, 1992], $\theta$ is the wave normal angle, $\omega$ is the wave frequency, $\Omega$ is the cyclotron frequency including the charge of the particle, $\omega_p$ is the plasma frequency, $n$ is the refractive index, $k$ is the wave number vector, $J_m$ is the Bessel function of order $m$ and argument $k_{\perp} v_{\perp} / \Omega_l$,

and $G_{1l}$ and $G_{2l}$ are defined as follows

$$G_{1l} = \frac{\partial F_l}{\partial v_\perp} - \frac{k_\parallel}{\omega}\left(v_\parallel \frac{\partial F_l}{\partial v_\perp} - v_\perp \frac{\partial F_l}{\partial v_\parallel}\right) \tag{2.28}$$

$$G_{2l} = J_m\left[\frac{\partial F_l}{\partial v_\parallel} + \frac{m\Omega_l}{\omega v_\perp}\left(v_\parallel \frac{\partial F_l}{\partial v_\perp} - v_\perp \frac{\partial F_l}{\partial v_\parallel}\right)\right] \tag{2.29}$$

where $F_l$ is the normalized distribution function of species $l$.

Finally, the path-integrated gain can be found by integrating the local growth rate in equation (2.27) along the ray path [*Chen et al.*, 2010, equation (5)]

$$Gain\ [dB] = 20\, log_{10}\left[exp\left(\int \gamma dt\right)\right] = \frac{20}{2.3}\int \gamma dt \tag{2.30}$$

Similarly, ray tracing does not directly capture the power flux divergence of a monochromatic wave. This change in wave power density is associated with the change in geometrical cross-sectional area as the wave propagates along its energy "corridor", and its calculation is detailed in Section 4.2.

## 2.3 Oblique Wave-particle Interactions

In the absence of waves, trapped energetic particles perform their adiabatic motion. The relativistic equations of motion of a charged particle can be written as follows

$$\dot{\vec{p}} = \frac{\vec{p}}{\gamma m} \times \vec{B}_0 \tag{2.31}$$

In the presence of waves, their effect adds to the adiabatic motion as follows

$$\dot{\vec{p}} = q\left[\vec{E}^w + \frac{\vec{p}}{\gamma m} \times \left(\vec{B}^w + \vec{B}_0\right)\right] \tag{2.32}$$

where $\vec{E}^w$ and $\vec{B}^w$ are the electric and magnetic fields of the wave, respectively.

In the case of resonant interactions, waves effectively introduce cumulative change of energy

or momentum with charged particles when the wave vectors as seen by the particle remain stationary or periodic for a significant length of time, or in other words, when the Doppler shifted frequency as seen by the particle equals its cyclotron frequency or a multiple of it

$$\omega - \vec{k} \cdot \vec{v} = l\frac{\Omega}{\gamma} \tag{2.33}$$

where $\vec{k}$ is the wavenumber vector, $\vec{v}$ is the particle's velocity vector, and $l$ is the harmonic number. Equation (2.33) describes the cyclotron resonance condition and it will be further discussed in Chapter 5. Cyclotron resonance between L-mode EMIC waves and energetic protons requires that waves and particles move in opposite directions (i.e. $\vec{k} \cdot \vec{v} < 0$) causing an upward shift in frequency. On the other hand, electrons (with $\Omega < 0$) must overtake the wave to reverse the apparent sense of polarization to R-mode with a velocity sufficient to Doppler shift the wave frequency to the relativistic electron gyrofrequency. In Chapter 5, however, we will see that not only resonant but also off-resonant interactions are capable of introducing pitch angle scattering of the particles.

Section 3.4.6 describes the radiation of EMIC waves from space-based transmitters, which results in very oblique wave normal angles with respect to the geomagnetic field direction. Equation (2.34) describes these fields, radiated at a wave normal angle $\theta$ with respect to the external magnetic field direction (-z-axis) and with a wave number vector located in the x-z plane [*Bell*, 1984]. The situation is represented in Figure 2-3. The wave fields can be written in the form

$$\begin{aligned} \vec{B}^w &= \hat{B}_x^w cos\Phi\, \hat{e}_x + \hat{B}_y^w sin\Phi\, \hat{e}_y - \hat{B}_z^w cos\Phi\, \hat{e}_z \\ \vec{E}^w &= -\hat{E}_x^w sin\Phi\, \hat{e}_x + \hat{E}_y^w cos\Phi\, \hat{e}_y - \hat{E}_z^w sin\Phi\, \hat{e}_z \end{aligned} \tag{2.34}$$

where $\hat{B}_j^w$ and $\hat{E}_j^w$ are the Fourier components of the fields and $\Phi$ is the wave phase defined as follows

$$\Phi = \int \omega dt - \int \vec{k} \cdot \vec{dr} \tag{2.35}$$

The magnitude of the wave polarization ratios can be found from Maxwell's equations and are given by

$$\frac{\hat{E}_x^w}{\hat{E}_y^w} = \frac{S - n^2}{D} \tag{2.36}$$

$$\frac{\hat{E}_z^w}{\hat{E}_y^w} = \frac{\left(S - n^2\right) n^2 sin\theta cos\theta}{D\left(n^2 sin^2\theta - P\right)} \tag{2.37}$$

$$\frac{\hat{B}_x^w}{\hat{B}_y^w} = -\frac{D\left(n^2 sin^2\theta - P\right)}{P\left(S - n^2\right)} \tag{2.38}$$

$$\frac{\hat{B}_z^w}{\hat{B}_y^w} = -tan\theta \frac{D\left(n^2 sin^2\theta - P\right)}{P\left(S - n^2\right)} \tag{2.39}$$

where $n$ is the refractive index given by equation (2.18), and P, S and D are the Stix parameters defined in (2.15)-(2.17).

Following *Ristic-Djurovic* [1993], *Bortnik* [2004] and others, the Poynting flux at a particular location, $\vec{S}^w$, is related to the wave fields as follows

$$|\hat{B}_y^w|^2 = \frac{2\mu_0 \left(\frac{\hat{E}_x^w}{\hat{E}_y^w}\right)^2 X^2 \, n \cos\theta |\vec{S}^w|}{c\sqrt{\left(\tan\theta - \frac{\hat{E}_x^w}{\hat{E}_y^w}\frac{\hat{E}_z^w}{\hat{E}_y^w} X\right)^2 + \left(1 + \left(\frac{\hat{E}_x^w}{\hat{E}_y^w}\right)^2 X\right)^2}} \tag{2.40}$$

where

$$X = \frac{P}{P - n^2 \sin^2\theta} \tag{2.41}$$

The wave fields can be expressed as a sum of right and left circularly polarized components

$$\vec{B}^w = \vec{B}_R + \vec{B}_L - \hat{e}_z \hat{B}_z^w cos\Phi \tag{2.42}$$

where

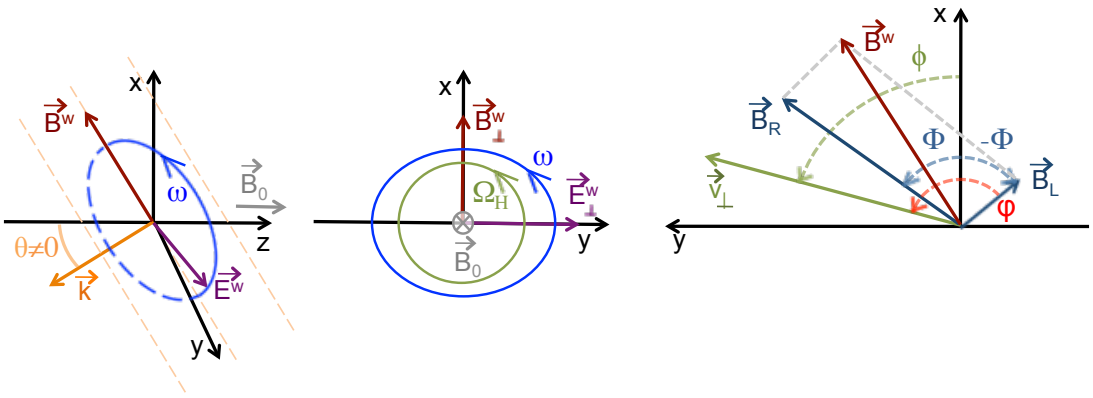


Figure 2-3: Wave-particle interaction schematics. The waves are considered oblique, and therefore with elliptical polarization.

$$\vec{B}_R = \frac{\hat{B}^w_x + \hat{B}^w_y}{2} \left(\hat{e}_x cos\Phi + \hat{e}_y sin\Phi\right) \tag{2.43}$$

$$\vec{B}_L = \frac{\hat{B}^w_x - \hat{B}^w_y}{2} \left(\hat{e}_x cos\Phi - \hat{e}_y sin\Phi\right) \tag{2.44}$$

At a fixed point in space, $\vec{B}_R$ rotates counterclockwise about $\vec{B}_0$ with angular velocity $\omega$, while $\vec{B}_L$ rotates clockwise.

The Earth's magnetic field is assumed to be locally parallel to the z-axis and vary slowly along it as follows

$$\vec{B}_0\left(\vec{r}\right) = \vec{B}_{0z}\left(z\right) + \vec{B}_{0\perp}\left(x, y, z\right) \tag{2.45}$$

where $\vec{B}_{0\perp}$ is zero at $z = 0$, and for a dipole model it can be evaluated using a Taylor expansion in x and y

$$\vec{B}_{0\perp}\left(x, y, z\right) = -\left(\hat{e}_x cos\xi + \hat{e}_y sin\xi\right)\left(x\, cos\xi + y\, \hat{e}_y sin\xi\right) \frac{\partial B_{0z}}{\partial z} \tag{2.46}$$

where $\xi$ is the angle between the magnetic meridional plane and the x-z plane.

Substituting these expressions into the Lorentz force equation (2.32) the scalar equations of motion of protons interacting with EMIC waves can be expressed as follows

$$\dot{p}_x = -q\hat{E}_x^w sin\Phi + \frac{q}{m_H\gamma}\left[p_y\left(-\hat{B}_z^w cos\Phi + B_{0z}\right) - p_z\left(\hat{B}_y^w sin\Phi + B_{0\perp y}\right)\right] \tag{2.47}$$

$$\dot{p}_y = q\hat{E}_y^w cos\Phi + \frac{q}{m_H\gamma}\left[-p_x\left(-\hat{B}_z^w cos\Phi + B_{0z}\right) + p_z\left(\hat{B}_x^w cos\Phi + B_{0\perp x}\right)\right] \tag{2.48}$$

$$\dot{p}_z = -q\hat{E}_z^w sin\Phi + \frac{q}{m_H\gamma}\left[p_x\left(\hat{B}_y^w sin\Phi + B_{0\perp y}\right) - p_y\left(\hat{B}_x^w cos\Phi + B_{0\perp x}\right)\right] \tag{2.49}$$

The equations above can be expressed in terms of parallel and perpendicular momentum to the Earth's magnetic field. The angle between $\vec{B}_L$ and $\vec{p}_\perp$, $\varphi$, is selected as the third coordinate in this derivation because the resonant interaction between energetic protons and EMIC waves occurs for particle's gyration in phase with the left-hand polarized component of the wave magnetic field. This angle is represented in Figure 2-3. The equations of motion in the new coordinates are

$$\dot{\varphi} = \dot{\phi} + \dot{\Phi} = -\frac{\Omega_{cH^+}}{\gamma} + \omega + v_x k_x + v_z k_z + \frac{C_1}{\gamma} \tag{2.50}$$

$$\dot{p}_z = -q\hat{E}_z^w sin\Phi - \frac{1}{\gamma}\omega_1 p_\perp sin\left(\varphi - 2\Phi\right) - \frac{1}{\gamma}\omega_2 p_\perp sin\varphi + C_2 \tag{2.51}$$

$$\dot{p}_\perp = \omega_1\left(\frac{p_z}{\gamma} + R_1 m_H\right) sin\left(\varphi - 2\Phi\right) + \omega_2\left(\frac{p_z}{\gamma} - R_2 m_H\right) sin\varphi + C_3 \tag{2.52}$$

where

$$p_x = p_\perp cos\phi \quad , \quad p_y = p_\perp sin\phi \tag{2.53}$$

$$\phi = \varphi - \Phi \tag{2.54}$$

$$\dot{\Phi} = \omega - \vec{v}\cdot\vec{k} = \omega + v_x k_x + v_z k_z \tag{2.55}$$

$$\omega_1 = \frac{q}{m_H}\frac{\hat{B}_x^w + \hat{B}_y^w}{2} \quad , \quad \omega_2 = \frac{q}{m_H}\frac{\hat{B}_x^w - \hat{B}_y^w}{2} \tag{2.56}$$

$$R_1 = \frac{\hat{E}_x^w + \hat{E}_y^w}{\hat{B}_x^w + \hat{B}_y^w} \quad , \quad R_2 = \frac{\hat{E}_x^w - \hat{E}_y^w}{\hat{B}_x^w - \hat{B}_y^w} \tag{2.57}$$

$$C_1 = \frac{q}{m_H}\frac{p_z}{p_\perp}\left[B_{0\perp x} cos\left(\varphi - \Phi\right) + B_{0\perp y} sin\left(\varphi - \Phi\right)\right] \tag{2.58}$$

$$C_2 = \frac{q}{m_H \gamma} p_\perp \left[B_{0\perp y} cos\left(\varphi - \Phi\right) - B_{0\perp x} sin\left(\varphi - \Phi\right)\right] \tag{2.59}$$

$$C_3 = \frac{q}{m_H \gamma} p_z \left[B_{0\perp x} sin\left(\varphi - \Phi\right) - B_{0\perp y} cos\left(\varphi - \Phi\right)\right] \tag{2.60}$$

where the different quantities refer to their magnitudes since the signs have already been taken into account. The equations above will be used in Chapter 5 to solve for the off-resonant interaction between waves and particles. In the hypothetical case of waves spread over a broad range of MLTs, the equations above can be simplified by taking the average over the particle's gyroperiod. This approximation can be done when the proton's gyroperiod is short compared to the time scale for wave-particle interactions, which is commonly the case when dealing with natural phenomena. Following Ristic's formulation [*Ristic-Djurovic*, 1993] and introducing three new variables

$$\chi = \int k_x dx \quad \Rightarrow \quad \dot{\chi} = k_x v_x \tag{2.61}$$

$$\varphi = \eta + \chi \quad \Rightarrow \quad \dot{\varphi} = \dot{\eta} + \dot{\chi} \tag{2.62}$$

$$\dot{\varphi} = -\frac{\Omega_{H^+}}{\gamma} + \omega + v_x k_x + v_z k_z \quad \Rightarrow \quad \varphi = -\frac{\Omega_{H^+}}{\gamma} t + \Phi + \Phi_0 - \varphi_0 \tag{2.63}$$

$$\Phi = \frac{\Omega_{H^+}}{\gamma} t + \phi_0 + \varphi = \sigma + \varphi = \sigma + \eta + \chi \tag{2.64}$$

$$\sigma = \frac{\Omega_{H^+}}{\gamma} t + \phi_0 \ , \ \ \phi_0 = \varphi_0 - \Phi_0 \tag{2.65}$$

Substituting into (2.50)-(2.52), the equations of motion can be rewritten as follows

$$\dot{\eta} = -\frac{\Omega_{H^+}}{\gamma} + \omega + v_z k_z + \frac{C_1}{\gamma} \tag{2.66}$$

$$\dot{p}_z = \omega_{\tau 0}^2 \frac{1}{k_z} \left[ -\alpha_1 sin\left(\eta + \chi\right) - \gamma \alpha_2 sin\left(\sigma + \eta + \chi\right) + sin\left(2\sigma + \eta + \chi\right) \right] + C_2 \tag{2.67}$$

$$\dot{p}_\perp = -\omega_1 \left( \frac{p_z}{\gamma} + R_1 m_p \right) sin\left(2\sigma + \eta + \chi\right) + \omega_2 \left( \frac{p_z}{\gamma} - R_2 m_p \right) sin\left(\eta + \chi\right) + C_3 \tag{2.68}$$

where

$$\omega_{\tau 0}^2 = \frac{\omega_1 k_z p_\perp}{\gamma} \ \ , \ \ \alpha_1 = \frac{\omega_2}{\omega_1} \ \ , \ \ \alpha_2 = \frac{q \hat{E}_z^w}{\omega_1 p_\perp} \tag{2.69}$$

Using the fact that

$$\chi = \int k_x dx = k_x v_\perp \int cos\left(\varphi - \Phi\right) dt = k_x v_\perp \int cos\left(\sigma\right) dt = \beta \, sin\sigma \tag{2.70}$$

where $\beta = \gamma k_x v_\perp / \Omega_{H^+}$, and taking into account that

$$e^{i\beta sin\sigma} = \sum_{l=-\infty}^{l=\infty} J_l\left(\beta\right) e^{il\sigma} \tag{2.71}$$

the gyroaveraged equations of motion can be expressed as follows

$$\dot{\eta} = -l\frac{\Omega_{H^+}}{\gamma} + \omega + v_z k_z + \frac{\overline{\overline{C_1}}}{\gamma} \tag{2.72}$$

$$\dot{p}_z = \omega_{\tau 0}^2 \frac{1}{k_z} \left[ -\alpha_1 J_{l-1}(\beta) + \gamma \alpha_2 J_l(\beta) + J_{l+1}(\beta) \right] sin\eta + \underline{C_2} \tag{2.73}$$

$$\dot{p}_\perp = \left[ -\omega_1 \left( \frac{p_z}{\gamma} + R_1 m_H \right) J_{l+1}(\beta) + \omega_2 \left( \frac{p_z}{\gamma} - R_2 m_H \right) J_{l-1}(\beta) \right] sin\eta + \underline{C_3} \tag{2.74}$$

where $l$ represents the harmonic number, $J_\nu(\beta)$ are the Bessel functions of order $\nu$ and argument $\beta$, and

$$\underline{C_1} = 0 \ , \ \underline{C_2} = -\frac{1}{\gamma m_H} \frac{p_\perp^2}{2\Omega_{H^+}} \frac{\partial \Omega_{H^+}}{\partial z} \ , \ \underline{C_3} = \frac{1}{\gamma m_H} \frac{p_\perp p_z}{2\Omega_{H^+}} \frac{\partial \Omega_{H^+}}{\partial z} \tag{2.75}$$

The total scattering will be the summation of the scattering from each harmonic number. From these expressions it can be observed that $\eta \approx \underline{\eta}$, which can be interpreted as the value of $\varphi$ averaged over one gyroperiod. The non-linear terms $\underline{C_2}$ and $\underline{C_3}$ in equations (2.73) and (2.74) describe the adiabatic motion due to the Earth's slowly varying magnetic field. The rest of the terms in $\dot{p}_z$ and $\dot{p}_\perp$ are generated by the wave, which are non-linear due to the $p_z$ term in the equation for $\dot{\eta}$. If $\dot{\eta}$ were a constant, the $\sin \eta$ would be linear with time and so too would the wave contribution. The $p_z$ term in $\dot{\eta}$, however, introduces a non-linearity for wave fields that are large compared to the geomagnetic field inhomogeneity. The integration of equations (2.72)-(2.74) over time determines the velocity space trajectories of individual protons under the influence of coherent waves propagating in the magnetosphere. Chapter 5 with further discuss the formulation above and will analyze the applicability of both the gyroaveraged and non-gyroaveraged set of equations.

# Chapter 3

# Radiation of EMIC Waves from a Space-based Antenna

This chapter identifies a potential antenna capable of radiating EMIC waves and focuses on the effect of the plasma on its radiation characteristics. In the following sections we develop models that describe the radiation pattern and radiation resistance of the antenna, which are input to the wave propagation and wave-particle interaction simulations. Further electrical implications not due to the plasma but to the antenna physical characteristics are addressed in Chapter 6.

## 3.1 Space-based versus Ground-based Transmitters

In principle, both ground and space-based transmitters could be used to couple wave power into the inner radiation belt. ULF/VLF waves, however, are very difficult to generate from the ground for the purpose of remediation experiments. Electrically short antennas on ground (antenna length much smaller than the wavelength) have a very small radiation resistance and their reactance dominates, that is, very little power is radiated [*Cohen*, 2009]. To try to solve this problem, transmitters at frequencies above 20 kHz are oriented vertically; this configuration has a matching circuitry that cancels out the reactance of the antenna, but this can only be achieved over a narrow frequency range (M. Cohen, personal communication, August 2012). In addition, voltages need to be very high, which causes

engineering problems. An example of this antenna type is the NAA transmitter in Cutler, ME, presented in Figure 3-1 (a).

Below 10 kHz, the radiation resistance of a ground-based transmitter becomes too small (proportional to length/$\lambda$), and the residual resistance of the matching circuitry dominates; the only practical solution at low frequencies consists of increasing the length of the antenna and, consequently, laying it out horizontally. The ground, however, is a very good conductor and generates an image charge that cancels out the antenna potential. Several horizontal transmitters do, nevertheless, exist, like the 150 km ELF antenna in Wisconsin and Michigan, which only managed to radiate about 10 W at 76 Hz. Another example is the Siple Station in Antartica, which is lifted about 2 km above the ground by a thick layer of ice but only has an efficiency of a few percent in the 1-10 kHz range [*Raghuram et al.*, 1974].

Not only ground-based antennas are very inefficient, but they are very expensive to build, they operate at a fixed frequency with no directional control and they cannot be moved.

Another concept consists of coupling power from ground to the magnetosphere by turning the lower ionosphere into a radiating source. This is achieved with intense Radio Frequency (RF) directed to the ionosphere that modulates its conductivity; in the presence of natural ionospheric currents this conductivity also modulates those currents. An example of natural current system is the auroral electrojet, and the High Frequency Active Auroral Research Program (HAARP) (Figure 3-1 (b)) in Gakona, AK, is one of the few RF heating facilities on Earth that aims at modulating that current system. Nevertheless, the utilization of this technique is not feasible to couple power into to the inner belt because there are no strong ionospheric currents at low $L$-shells. Consequently, the precipitation of energetic inner belt trapped protons requires the artificial injection of EMIC waves at low $L$-shells using space-based transmitters.

Space-based ULF/VLF antennas radiate directly into the magnetosphere, thus avoiding the inefficiencies associated with ionospheric coupling and ground effects. Even so, these transmitters are immersed in a magnetoplasma which dramatically modifies their radiation characteristics. ULF/VLF in-situ sources only radiate at wave normal angles close to perpendicular to the geomagnetic field lines, which constrains illumination to a very narrow range of $L$-shells and will inevitably translate into efficiency considerations. In this dis-

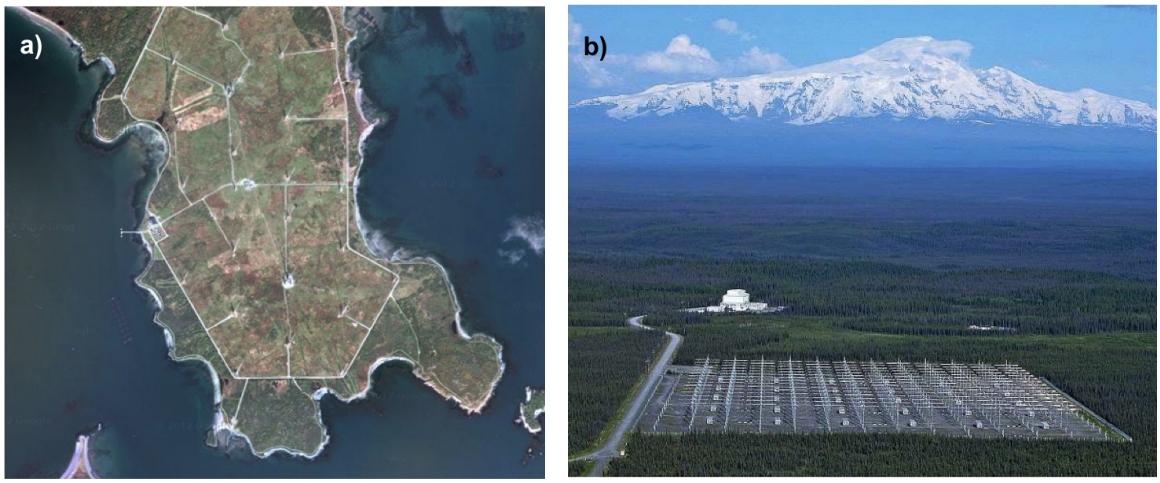


Figure 3-1: (a) NAA transmitter in Cutler, ME. (b) High Frequency Active Auroral Research Program (HAARP) experiment in Gakona, AK.

sertation we determine the degree to which space-based transmitters are a feasible way of achieving controlled precipitation of inner belt protons.

## 3.2 Equivalent Circuit of a Space-based EMIC Transmitter

The plasma surrounding a space-based transmitter strongly modifies its radiation characteristics compared to free space. Figure 3-2 represents the equivalent circuit of a space-based antenna (or antenna-sheath-plasma system) operating at ULF/VLF frequencies. The physical antenna is enclosed in a green box and consists of an AC source, a resistor that accounts for ohmic losses and the self-reactance of the transmitter. In the case of a linear antenna, the accumulation of charge on its surface also involves the formation of a thick oscillatory sheath around the transmitter, which is due to the different response time of electrons and protons to the fields generated by the antenna; the sheath is a region of non-neutrality that shields the fields generated by the source and limits their coupling to the plasma. The fourth component is the plasma impedance connected to the antenna; the real part of this impedance is the radiation resistance responsible for radiation, while the wave energy is stored as reactive power due to the radiation reactance (imaginary part). Sheath and plasma impedances are enclosed in the pink box of Figure 3-2, which represents the effect of the plasma. High system performance requires large radiation resistance and minimization of any system reactance. This chapter focuses on the pink box, i.e. the effect of the plasma

on the radiation. The sizing of the antenna determines its physical electrical characteristics (green box), which will be addressed in Chapter 6.

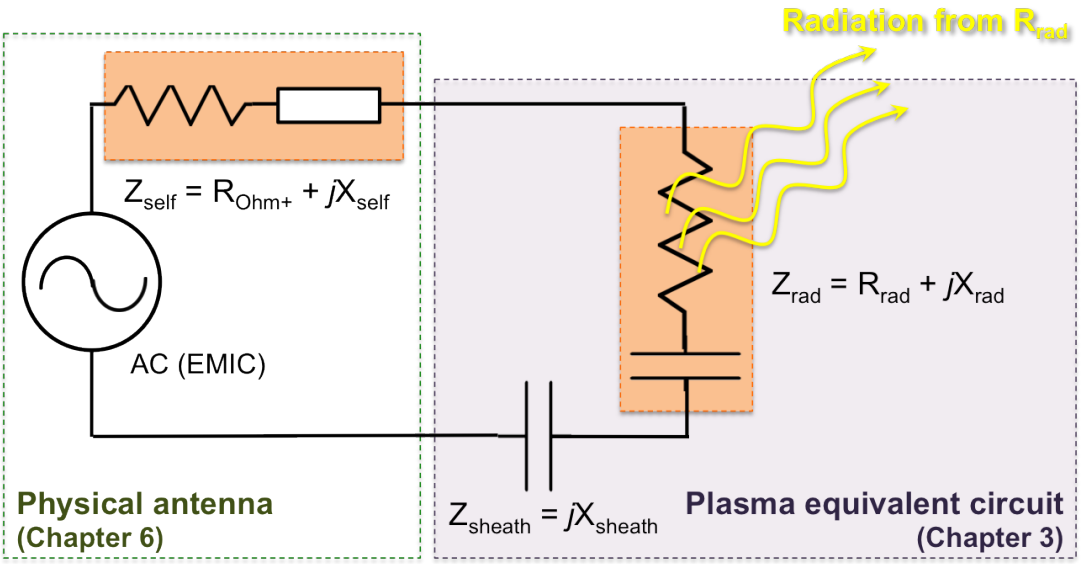


Figure 3-2: Antenna-sheath-plasma system

The emission of the EMIC band entails additional complexity compared to the higher frequencies of whistlers. The sheath around a space-based electric dipole is very thick, and so its capacitance is very small and dominates. The sheath capacitance in an electric dipole is nearly independent of the frequency and proportional to the transmitter length [*Song et al.*, 2007]

$$C_{sh} = \frac{\pi L_a \epsilon_0}{Ln\left(\frac{r_{sh}}{R_a} - \frac{1}{2}\right)} \tag{3.1}$$

which resembles the vacuum capacitance given by

$$C_{vac} = \frac{\pi L_a \epsilon_0}{Ln\left(\frac{L_a}{2R_a}\right)} \tag{3.2}$$

where $r_{sh}$ is the sheaths radius, and $L_a$ and $R_a$ are the antenna length and radius, respectively. $r_{sh}$ can be estimated from *Song et al.* [2007].

The radiation resistance of an electric dipole perpendicular to the Earth's magnetic field and immersed in a magnetoplasma was derived by *Balmain* [1964] under the quasi-static

approximation, which neglects the electric field induced by time-dependent magnetic fields. This far-field approximation is valid in our case and whenever the gradient distances are relatively small, as in the vicinity of the resonance cones. Balmain's radiation resistance of an electric dipole is given by

$$R_{rad} = \frac{2\,|p|}{\pi\omega\epsilon_0 S L_a}\left[Ln\left(\frac{L_a}{2R_a}\right) - 1 - Ln\left(\frac{\sqrt{1+p^2}}{2}\right)\right] \tag{3.3}$$

where $p^2 = S/P$, and S and P are given by equations (2.8) and (2.7). The imaginary part of the radiation impedance, however, is not correctly reproduced by Balmain's method because it neglects the divergence of the plasma current due to the transverse electric field. This reactance is very small compared to the sheath contribution and can therefore be neglected.

The sheath capacitance of an 80-meter electric dipole at 10 kHz (whistler band) and equatorial altitude of 12,000 km is 35 nF, only 1.5 times larger than the sheath's capacitance. The corresponding ratio of reactance to radiation resistance is $X_{sh}/R_{rad} \approx 10^3$, which slightly improves (decreases) with increasing antenna length. This system would require an inductor of 1 H to compensate for plasma capacitive effects, which is within the realm of engineering feasibility. On the other hand, for a transmitter operating in the EMIC band, this ratio would be around $X_{sh}/R_{rad} \approx 10^5$; the system would require an inductor of 2 MH for circuit compensation, which is far beyond what could reasonably be launched. The associated reactance in the EMIC band is extremely high even for a multi-km transmitter, to the point that it is not realistically possible to use an electric dipole to radiate these waves. From these expressions we observe that a short antenna would be ideal in terms of radiation resistance because the relevant wavelengths (those near the resonance cone) are indeed very short. Unfortunately, it is the ratio of $X_{sh}/R_{rad}$ that matters for antenna design, and that ratio only presents a small logarithmic dependence on $L_a$; even a multi-km antenna would have too much reactance compared to radiation resistance in the EMIC regime. A hopeful solution to this problem has been identified, which involves the use of magnetic loop antennas.

## 3.3 The Magnetic Loop as an EMIC Transmitter

The most promising solution to the problem identified above consists of a DC rotating coil operating as an EMIC transmitter. As we will see in Chapter 6, a plasma sheath will most likely appear around an static AC coil due to its excessive self-inductance introduced by the large dimensions and circulating current required by the system, which translates into huge voltages across the coil and the potential for sheath formation. For this reason, instead of an alternating current circulating around a static coil, we propose a direct current driven around a rotating coil. The current is DC, thus the only reactance that remains is the one associated with the plasma currents. Both DC and AC options, however, can be equivalently modeled in terms of radiation characteristics, since the dipole component of the rotating DC antenna is equivalent to two AC static orthogonal coils.

The radiation resistance of magnetic dipoles, however, is several orders of magnitude smaller compared to the one of electric dipoles. *Bell and Wang* [1971] and *Wang and Bell* [1972c] provided a quasi-static analytical approximation to the radiation impedance of a small filamentary ULF/VLF loop antenna immersed in a cold magnetoplasma*

$$X_{rad} \approx \frac{\omega}{c} R_a Z_0 \left( log \frac{8R_a}{\xi} - \frac{1}{2} \right), \ \frac{R_a}{\xi} \lll 1 \tag{3.4}$$

$$R_{rad} \approx -\frac{\pi}{2} D_0 \frac{I\left(\theta_r, \psi\right)}{\sqrt{S\left(S-P\right)}} \tag{3.5}$$

where $\psi$ is the angle between the loop axis and the Earth's magnetic field direction, $\theta_r$ is the angle of the resonance cone defined in equation (2.20), $Z_0 \approx 377\ \Omega$, $R_a$ is the antenna radius, $\xi$ is the wire radius and

$$D_0 = \frac{8}{3\pi^2} \left( R_a \frac{\omega}{c} \right)^3 Z_0 R L \tag{3.6}$$

* These expressions imply $P/S < 0$, which corresponds to the EMIC band being analyzed in this dissertation.

$$I(\theta,\psi) = \sin\tau\left[1 + A\left(1+\cos^2\theta\right)E(\chi) - A\left(1-\chi^2\right)K(\chi) + \cos\theta\cos\psi\left(1 - A\sin^2\theta\right)K(\chi)\,Z(\sigma,\chi)\right] \tag{3.7}$$

$$A = \frac{PS - RL}{RL} \tag{3.8}$$

where $R, L, P, S$ and $D$ are the Stix parameters defined in equations (2.5) to (2.9), $\theta$ is the wave normal angle, $K(\chi)$ and $E(\chi)$ are the complete elliptic integrals of first and second kinds and modulus $\chi$, respectively. $Z(\sigma,\chi)$ is defined as $Z(\sigma,\chi) = E(\sigma,\chi) - K^{-1}(\chi)\,E(\chi)\,F(\sigma,\chi)$, where $F(\sigma,\chi)$ and $E(\sigma,\chi)$ are the incomplete elliptic integrals of first and second kinds of argument $\sigma$ and modulus $\chi$, respectively. Other definitions are $\tau = \psi$ and $\chi = \sin\theta/\sin\psi$ for $\theta \leq \psi$, while $\tau = \theta$ and $\chi = \sin\psi/\sin\theta$ for $\theta \geq \psi$; $\sigma = \sin^{-1}(\cos\psi/\cos\theta)$ for $\theta \leq \psi$, while $\sigma = \sin^{-1}(\cos\theta/\cos\phi)$ for $\theta \geq \psi$. Due to the linearity of the problem the radiation resistance at any orientation can be easily calculated from the parallel and perpendicular results as follows

$$R_{rad} = R_{\parallel}\cos^2\psi + R_{\perp}\sin^2\psi \tag{3.9}$$

Figure 3-3 shows the radiation resistance as a function of the angle of orientation of the loop axis with respect to the geomagnetic field. The figure is for a single turn loop with $R_a = 15$ m at $L = 1.5$, and for four different normalized frequencies. The expressions from *Bell and Wang* [1971] and *Wang and Bell* [1972c] have been used in the plots. It can be observed that the radiation resistance is fairly independent of the orientation angle except very close to the parallel direction, where it suddenly drops off. From this figure we can clearly see that the perpendicular orientation is preferred since it gives the larger radiation resistance possible.

Similarly, Figure 3-4 shows the radiation impedance of a single loop as a function of its major radius and the normalized driving frequency. The figure is for a wire radius of $\xi$ =0.5 mm, at $L = 1.5$ and for a loop axis orientation perpendicular to the external magnetic field. It can be observed that the radiation resistance, $R_{rad}$, scales with the cube of the radius

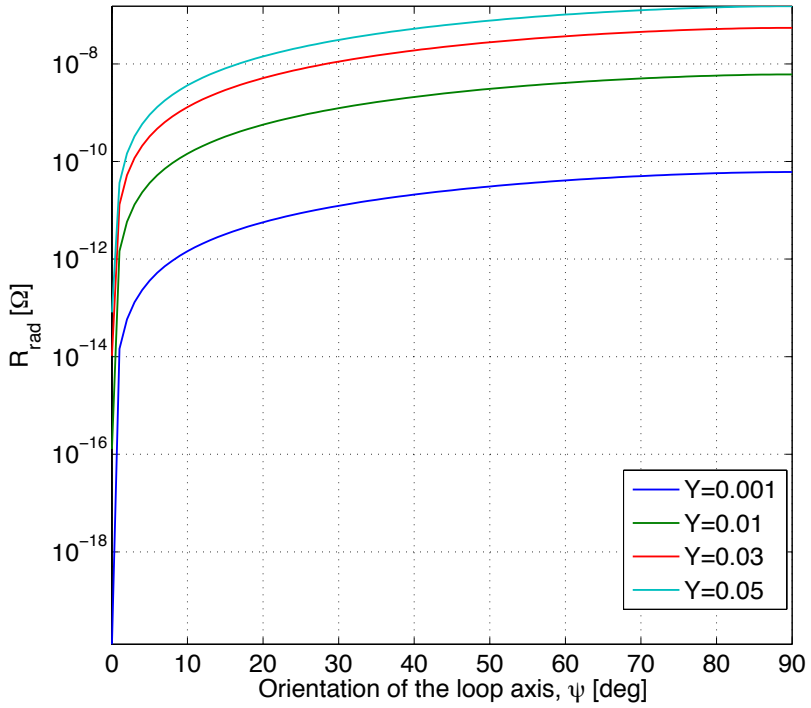


Figure 3-3: Radiation resistance of a single turn loop antenna as a function of the orientation of the loop axis with respect to the geomagnetic field. The plot is for $R_a = 15$ m at $L = 1.5$, and for four different normalized frequencies.

and the square of the frequency. Contrarily, the radiation reactance (inductive), $X_{rad}$, is mostly linear with both radius and frequency. For these reasons, the higher the frequency and the radius the better in terms of radiation resistance.

Figure 3-4 shows that the values of the radiation resistance are extremely small. According to expressions (3.4)-(3.5), we would require a loop radius of 220 meters and an input current of 4.5 kA to obtain a radiated power of 100 W at a frequency of 2 Hz. This design corresponds to a radiation resistance of $R_{rad} = 10^{-5}$ Ω as given by equation (3.5). The required large input current and the need for small ohmic losses can be handled by taking advantage of superconducting materials. In addition, multiple loop turn arrangements and large coil radius have to be considered in order to increase the radiation resistance of these antenna types. The design and performance of a superconducting magnetic coil antenna with these characteristics is described in Chapter 6. In the present chapter, we focus on the effect of the plasma on the radiation characteristics, or in other words, the calculation of the radiation pattern and radiation resistance. In the next section we present the far-field radiation pattern of an EMIC magnetic loop using a linear full-wave cold plasma model, and

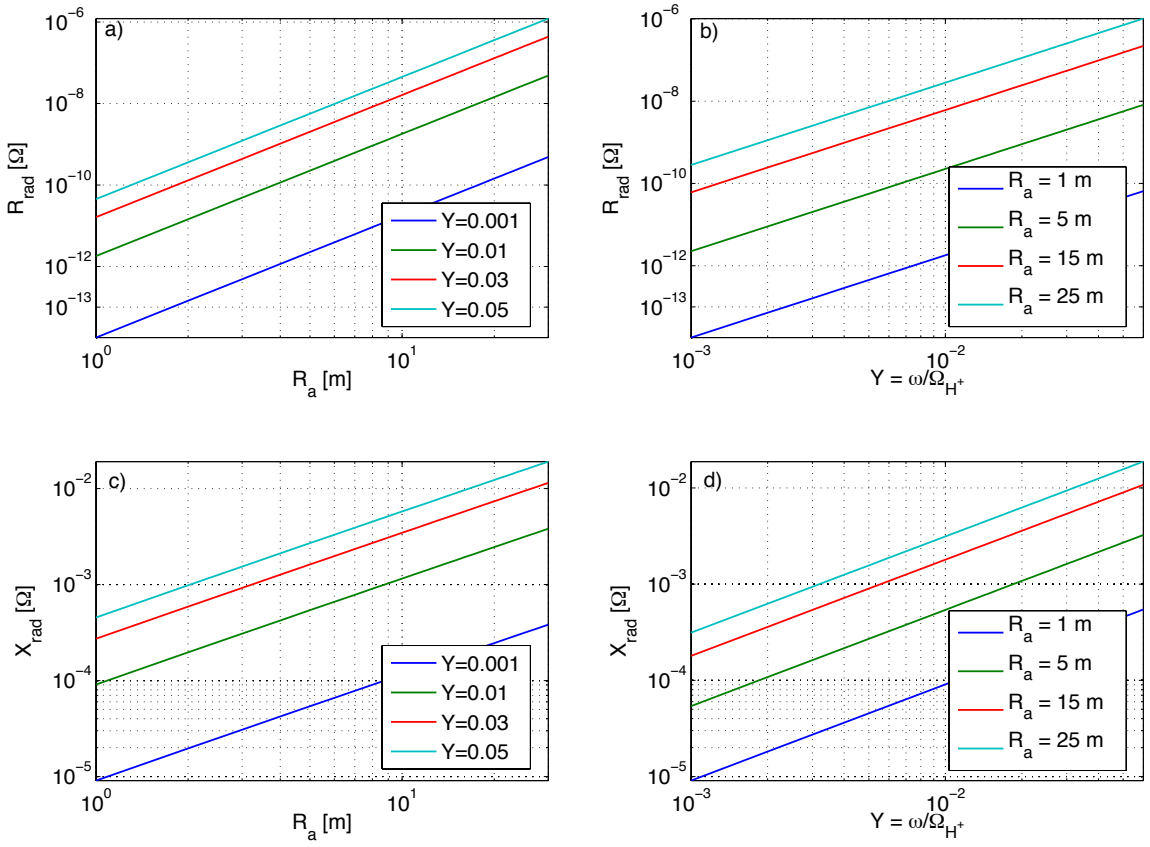


Figure 3-4: (a) Radiation resistance of a single loop as a function of major radius for different normalized driving frequencies. (b) Radiation resistance as a function normalized driving frequency for different loop radii. (c) Radiation reactance (inductive) as a function of loop radius for different normalized driving frequencies. (d) Radiation reactance (inductive) as a function normalized driving frequency for different loop radii. The plots are for a wire radius of $\xi$ =1 mm, at $L = 1.5$ and for a loop axis orientation perpendicular to the external magnetic field.

we compare the results with the quasi-static solution of *Bell and Wang* [1971] and *Wang and Bell* [1973] presented above.

## 3.4 Radiation Pattern Calculation

A full-wave model of the radiation pattern of a coil antenna operating in the EMIC band is presented next. The plasma is assumed cold and only electrons and protons are considered. The transmitter is immersed in a magnetoplasma, which strongly modifies its radiation characteristics compared to free space. In vacuum, the wavelength is a constant for a fixed frequency; contrarily, plasmas are dispersive, i.e. the wavelength is a function of the

direction of propagation. A linear analysis is presented to calculate the fields and power in the far-field region radiated by the transmitter. The theory below is based on a single coil antenna; the case of two phased orthogonal antennas, which is equivalent to the DC rotating coil introduced in the previous section, is easily derived from the single coil theory and it is also discussed at the end of the section.

### 3.4.1 Radiated Fields in the Fourier Domain

Ampère's law with a source (antenna) current density $\vec{j_s}$ can be written as follows

$$\nabla \times \vec{B} = \mu_0 q n_0 (\vec{v}_p - \vec{v}_e) + \mu_0 \vec{j_s} \tag{3.10}$$

where $n_0$ is the plasma density, and $\vec{v_p}$ and $\vec{v_e}$ are the proton and electron velocities, respectively. Combining Ampère's and Faraday's law

$$\nabla \times \nabla \times \vec{E} = -\frac{\partial}{\partial t}\left[\mu_0 e n_0 (\vec{v}_p - \vec{v}_e) + \mu_0 \vec{j_s}\right] \tag{3.11}$$

Assuming a dependence of the type $Re\left[e^{i(\vec{k}\cdot\vec{x}-\omega t)}\right]$, the equation above can be linearized as follows

$$\vec{k} \times \vec{k} \times \vec{\hat{E}} = -i\omega\left[\mu_0 e n_0 (\hat{\vec{v}}_p - \hat{\vec{v}}_e) + \mu_0 \vec{\hat{J}_s}\right] \tag{3.12}$$

where $\vec{\hat{E}}$ and $\vec{\hat{J}_s}$ are the Fourier transform of the wave electric field and the source current density, respectively. The particles' velocities can be found from their momentum equations

$$m_e \frac{\partial \vec{v}_e}{\partial t} = -q(\vec{E} + \vec{v}_e \times \vec{B}_0) \tag{3.13}$$

$$m_H \frac{\partial \vec{v}_p}{\partial t} = q(\vec{E} + \vec{v}_p \times \vec{B}_0) \tag{3.14}$$

The external magnetic field $\vec{B}_0$ is taken along the z-axis and the wave number vector $\vec{k}$ is located at an angle $\theta$ with respect to $\vec{B}_0$ in the X-Z plane. Taking $\vec{B} = B_0\vec{e_z} + \vec{B}$ and

$\vec{k} = \vec{k}_\perp + k_\parallel \vec{e}_z = k\, sin\theta\, \vec{e}_\perp + k\, cos\theta\, \vec{e_z}$, the particles' velocity can be written as follows

$$\hat{v}_{ex} = \frac{1}{B_0} \frac{i\frac{\omega}{\Omega_e}\hat{E}_x + \hat{E}_y}{1 - \frac{\omega^2}{\Omega_e^2}} \quad \hat{v}_{ey} = \frac{1}{B_0} \frac{-\hat{E}_x + i\frac{\omega}{\Omega_e}\hat{E}_y}{1 - \frac{\omega^2}{\Omega_e^2}} \quad \hat{v}_{ez} = -i\frac{q}{\omega m_e}\hat{E}_z \tag{3.15}$$

$$\hat{v}_{px} = \frac{1}{B_0} \frac{-i\frac{\omega}{\omega_{ci}}\hat{E}_x + \hat{E}_y}{1 - \frac{\omega^2}{\Omega_{H^+}^2}} \quad \hat{v}_{py} = \frac{1}{B_0} \frac{-\hat{E}_x - i\frac{\omega}{\Omega_{H^+}}\hat{E}_y}{1 - \frac{\omega^2}{\Omega_{H^+}^2}} \quad \hat{v}_{pz} = i\frac{q}{\omega m_H}\hat{E}_z \tag{3.16}$$

Introducing these velocities into equation (3.12), the linearized Ohm's law takes the following form

$$[A] \cdot \vec{\hat{E}} = \frac{1}{\sigma_{cp}} \vec{\hat{J}}_s \tag{3.17}$$

where $\sigma_{cp}$ is the Hall conductivity of the plasma

$$\sigma_{cp} = \frac{q^2 n_0}{\Omega_{H^+} m_H} = \frac{q n_0}{B_0} \tag{3.18}$$

and $[A]$ is the the tensor

$$[A] = \begin{bmatrix} i\left(\frac{Y}{1-Y^2} - \frac{K^2 cos^2\theta}{Y}\right) & -\frac{Y^2}{1-Y^2} & i\frac{K^2 sin\theta cos\theta}{Y} \\ \frac{Y^2}{1-Y^2} & i\left(\frac{Y}{1-Y^2} - \frac{K^2}{Y}\right) & 0 \\ i\frac{K^2 sin\theta cos\theta}{Y} & 0 & -\frac{i}{Y}\left(K^2 sin^2\theta + M\right) \end{bmatrix}$$

where $Y = \frac{\omega}{\Omega_{H^+}}$, $M = \frac{m_H}{m_e}$ and

$$K = k\Lambda, \quad \Lambda^2 = \frac{m_H}{q^2 \mu_0 n_0} \tag{3.19}$$

Inverting matrix $[A]$, the electric field in the Fourier domain can be expressed as

$$\vec{\hat{E}}(\vec{k}) = \frac{1}{\sigma_{cp}} [Z]\, \vec{\hat{J}}_s \tag{3.20}$$

where $[Z]$ is the impedance matrix in the $\vec{k}$-related axes

$$[Z] = \frac{1}{\Delta} \left[ \begin{array}{c} i\left(K^2 sin^2\theta + M\right)\left(Y^2 - K^2 + K^2Y^2\right) \\ -Y^3\left(K^2 sin^2\theta + M\right) \\ iK^2 sin\theta cos\theta\left(Y^2 - K^2 + K^2Y^2\right) \end{array} \right.$$

$$\begin{array}{c} Y^3\left(K^2 sin^2\theta + M\right) \\ i\left(Y^2K^2 sin^2\theta + Y^2M - K^2 M cos^2\theta + K^2Y^2 M cos^2\theta\right) \\ K^2Y^3 sin\theta cos\theta \end{array}$$

$$\left. \begin{array}{c} iK^2 sin\theta cos\theta\left(Y^2 - K^2 + K^2Y^2\right) \\ -K^2Y^3 sin\theta cos\theta \\ i\left(-Y^4 + K^2Y^2 + K^2Y^2 cos^2\theta + K^4Y^2 cos^2\theta - K^4 cos^2\theta\right) \end{array} \right] \tag{3.21}$$

$$\Delta = -\frac{Y^3 M}{K_p^2 K_e^2}\left(K^2 - K_p^2\right)\left(K^2 - K_e^2\right) \tag{3.22}$$

where $K_p^2$ and $K_e^2$ are the left and right-hand polarized solutions of the dispersion relation, respectively.

The Fourier transform of the electric field needs to be expressed in antenna-related axes rather than $\vec{k}$-related axes. Subsequently, the coordinates will not change during the computation of the inverse Fourier transform. The antenna axes are represented in Figure 3-5; the coil axis is at an angle $\psi$ with respect to $\vec{B}_0$ (along the $z_A$-axis), and at an angle $\zeta$ with respect to the $x_A$-axis. $\vec{k}$ is oriented according to the polar angles ($\theta$, $\phi$). A $-\phi$ rotation around $z_A$ is required to change from $\vec{k}$ axes to antenna axes

$$\vec{\tilde{E}}_A(\vec{k}) = \frac{1}{\sigma_{cp}}\left[Z_A\right]\vec{J}_A \tag{3.23}$$

where

$$[Z_A] = [R]^T\,[Z]\,[R]\ ,\ [R] = \left[ \begin{array}{ccc} cos\phi & sin\phi & 0 \\ -sin\phi & cos\phi & 0 \\ 0 & 0 & 1 \end{array} \right] \tag{3.24}$$

$$\vec{\hat{J}}_A = [A_{\psi\zeta}]\,\vec{\hat{J}}_s = \begin{bmatrix} \cos\zeta\cos\psi & -\sin\zeta & \cos\zeta\sin\psi \\ \sin\zeta\cos\psi & \cos\zeta & \sin\zeta\sin\psi \\ -sin\psi & 0 & cos\psi \end{bmatrix} \vec{\hat{J}}_s \tag{3.25}$$

and the transformed magnetic field is given by

$$\vec{\hat{B}} = \frac{\vec{k} \times \vec{\hat{E}}}{\omega} \tag{3.26}$$

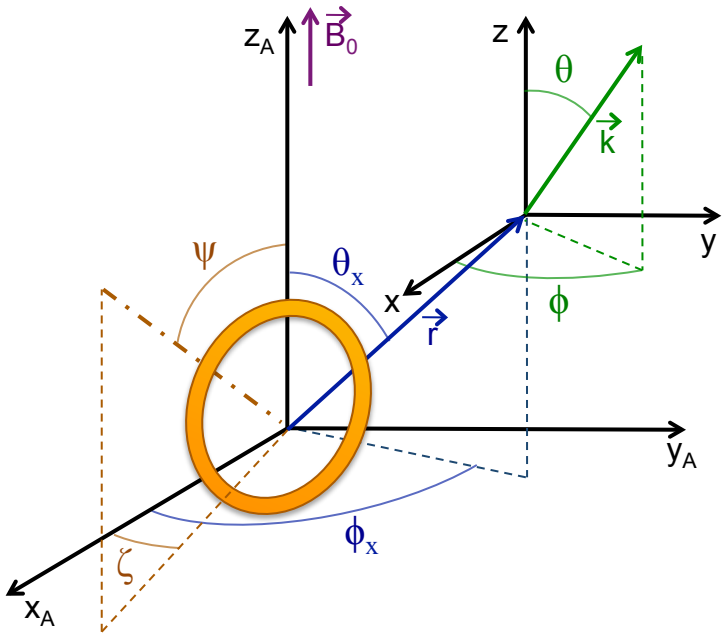


Figure 3-5: Antenna-related axes

### 3.4.2 Source Current Distribution

The antenna current distribution of a magnetic loop in a magnetoplasma can be considered constant along the loop, but varying sinusoidally in time (Section 3.3). The antenna source current density can then be expressed as follows

$$\vec{j_s}\,(\vec{\rho},\,t) = R_a I_0 \frac{\delta(\rho - R_a)\delta(z)}{\rho} cos\,(\omega_0 t)\,\hat{\phi} \tag{3.27}$$

where $R_a$ is the antenna radius, $I_0$ is the current amplitude, $\rho$ is the position vector of the

loop in cylindrical coordinates $(\rho, \phi, z)$, and $\hat{\phi}$ is a unit vector in the positive $\phi$ direction. The Fourier transform of the source current density can be easily calculated

$$\vec{\hat{J}}_s(\vec{k},\, \omega) = -i\frac{I_0 R_a}{8\pi^2} J_1(k_\perp R_a)\delta(\omega - \omega_0)\,(-sin\chi, cos\chi, 0) \tag{3.28}$$

where $\chi$ is contained in the plane of the loop and is the angle between the reference origin and the projection of $\vec{k}$ in that plane. The relationship between $\chi$, $\theta$, $\phi$, $\psi$ and $\zeta$ is as follows

$$\tan\chi = \frac{\cos\zeta\sin\theta\sin\phi - \sin\zeta\sin\theta\cos\phi}{\cos\zeta\cos\psi\sin\theta\cos\phi + \sin\zeta\cos\psi\sin\theta\sin\phi - \sin\psi\cos\theta} \tag{3.29}$$

### 3.4.3 Inverse Fourier Transform of the Radiated Fields

The inverse Fourier transform of the radiated fields can be calculated as follows

$$\vec{E}(\vec{r}, t) = \iiiint \frac{1}{\sigma_{cp}\Lambda^3}\,[Z_A]\,\vec{\hat{J}}_A e^{i(\vec{k}\cdot\vec{x}-\omega t)} K^2 sin\theta\, dK d\phi d\theta d\omega \tag{3.30}$$

$$\vec{B}(\vec{r}, t) = \iiiint \frac{1}{\sigma_{cp}\Lambda^3}\frac{\vec{k}}{\omega} \times [Z_A]\,\vec{\hat{J}}_A e^{i(\vec{k}\cdot\vec{x}-\omega t)} K^2 sin\theta\, dK d\phi d\theta d\omega \tag{3.31}$$

where it has been used that $d^3k = k^2 sin\theta\, dk\, d\phi\, d\theta$. The integration above was previously described by *de Soria-Santacruz* [2011] and it is briefly summarized next. The process involves three steps

1. Integration over $\omega$
2. Cauchy's Residue Theorem for $K$ integration, fixed $\theta$ and $\phi$
3. Stationary Phase Method for $\theta, \phi$ integration

The integration over $\omega$ is straightforward and gives

$$\vec{E}(\vec{r}, t) = \vec{E}(\vec{r})\Big|_{\omega=\omega_0} e^{-i\omega_0 t} \tag{3.32}$$

where $\omega_0$ is the antenna driving frequency.

The integration over $K$ is performed in the complex plane using Cauchy's Residue Theorem. The closing of the integration path must be done in the half plane where $e^{i\vec{k}\cdot\vec{x}}$ does not diverge, i.e. the imaginary part of $\vec{k}\cdot\vec{x}$ must be positive. This phase can be written as follows

$$i\vec{k}\cdot\vec{x} = i\frac{r}{\Lambda}K\left[sin\theta sin\theta_x cos(\phi-\phi_x) + cos\theta cos\theta_x\right] = i\frac{r}{\Lambda}Kcos\gamma \tag{3.33}$$

where $\gamma$ is the angle between $\vec{k}$ and $\vec{x}$, $(\theta,\phi)$ are the coordinates of the wave number vector and $(\theta_x,\phi_x)$ are the coordinates of the observation point. The K-integration in the complex plane gives the following result

$$\vec{E}(\vec{r}) = \frac{2\pi i}{\Lambda\sigma_{cp}}\iint\limits_{\phi\theta}\sum Res\left\{\left[Z_A\right]\vec{\hat{J}}_A e^{i\vec{k}\cdot\vec{x}}\left(\frac{K}{\Lambda}\right)^2\right\}sin\theta\, d\phi d\theta \tag{3.34}$$

where

$$\sum Res\left(\left[Z_A\right]\vec{\hat{J}}_A e^{i\vec{k}\cdot\vec{x}}k^2\right) = \left(-\frac{K_i^2K_e^2}{Y^3M}\right)\frac{\triangle\left[Z_A\right]\vec{\hat{J}}_A e^{i\vec{k}\cdot\vec{x}}\left(\frac{K}{\Lambda}\right)^2}{\left(K^2-K_i^2\right)\left(K+K_e\right)}\Bigg|_{K_e} \tag{3.35}$$

$$+\left(-\frac{K_i^2K_e^2}{Y^3M}\right)\frac{\triangle\left[Z_A\right]\vec{\hat{J}}_A e^{i\vec{k}\cdot\vec{x}}\left(\frac{K}{\Lambda}\right)^2}{\left(K^2-K_e^2\right)\left(K+K_i\right)}\Bigg|_{K_i} \tag{3.36}$$

and the $\Delta$ term is given in equation (3.22).

The Stationary Phase Method is finally used to integrate over $\theta$ and $\phi$ when the observation point is in the far field region. In the far-field region the parameter $r/\Lambda$ is large, and the exponential term $e^{i\vec{k}\cdot\vec{x}}$ oscillates much faster than the other terms. At the so called stationary points ($\theta_S$, $\phi_S$), however, the exponential term does not vary rapidly. Near the stationary points it is possible to take the other terms out of the integral and only integrate the exponential. Since it is only the vicinity of the stationary points that contributes, the exponent can be expanded in Taylor series about these points. The phase can be written as follows

$$i\vec{k}\cdot\vec{x} = i\frac{r}{\Lambda}K\left[sin\theta sin\theta_x cos(\phi-\phi_x) + cos\theta cos\theta_x\right] = i\frac{r}{\Lambda}Y\Phi \tag{3.37}$$

where the dispersion relation in an electron-proton plasma has been used to substitute $K$. The phase $\Phi$ then is given by

$$\Phi(\theta,\phi,\theta_x,\phi_x) = \frac{sin\theta sin\theta_x cos(\phi-\phi_x) + cos\theta cos\theta_x}{\sqrt{\frac{1+cos^2\theta}{2} - \frac{Y^2 sin^2\theta}{2M} \pm \sqrt{\frac{sin^4\theta}{4}\left(1+\frac{Y^2}{M}\right)^2 + Y^2 cos^2\theta}}} \tag{3.38}$$

where the positive and negative signs correspond to the right and left-hand polarized solutions of the dispersion relationship, respectively.

The stationary points ($\theta_S$, $\phi_S$) can be found by imposing $\frac{\partial\Phi}{\partial\phi} = 0$ and $\frac{\partial\Phi}{\partial\theta} = 0$, which are detailed in Appendix A. The integration reduces to a summation over these points

$$\begin{aligned}\vec{E}(\vec{r}) \;=\; & \frac{2\pi i}{\Lambda\sigma_{cp}}\sum Res\left\{\sum_{Stationary\,Points}\left[sin\theta_s\left[Z_A(\theta_s)\right]\vec{J}_A\left(\theta_S\right)\left(\frac{K(\theta_s)}{\Lambda}\right)^2 e^{i\frac{r}{\Lambda}Y\Phi\left(\theta_{S_j},\phi_{S_j}\right)}\right.\right. \\ & \left.\left.\iint_{\phi\theta} e^{i\frac{r}{\Lambda}Y\left[\frac{1}{2}\frac{\partial^2\Phi}{\partial\theta^2}\Big|_{S_j}\left(\theta-\theta_{S_j}\right)^2+\frac{1}{2}\frac{\partial^2\Phi}{\partial\phi^2}\Big|_{S_j}\left(\phi-\phi_{S_j}\right)^2\right]}d\theta d\phi\right]\right\}\end{aligned} \tag{3.39}$$

The exponential term can be integrated using normalized Fresnel Integrals, which are defined as follows

$$C(x) = \int_0^x cos\left(\frac{\pi}{2}t^2\right)dt, \qquad S(x) = \int_0^x sin\left(\frac{\pi}{2}t^2\right)dt \tag{3.40}$$

and integration of the exponential term can then be exactly calculated using the following expressions

$$I_1 = \int_{\phi=0}^{2\pi} e^{i\frac{1}{2}\frac{r}{\Lambda}Y\frac{\partial^2\Phi}{\partial\phi^2}\Big|_{S_j}\left(\phi-\phi_{S_j}\right)^2} d\phi = \sqrt{\frac{\pi}{2A_\phi}}\left\{-\left[C\left(-\sqrt{\frac{2A_\phi}{\pi}}\phi_{S_j}\right) \pm iS\left(-\sqrt{\frac{2A_\phi}{\pi}}\phi_{S_j}\right)\right] + \left[C\left(\sqrt{\frac{2A_\phi}{\pi}}\left(2\pi-\phi_{S_j}\right)\right) \pm iS\left(\sqrt{\frac{2A_\phi}{\pi}}\left(2\pi-\phi_{S_j}\right)\right)\right]\right\} \quad (3.41)$$

$$I_2 = \int_{\theta=0}^{\pi} e^{i\frac{1}{2}\frac{r}{\Lambda}Y\frac{\partial^2\Phi}{\partial\theta^2}\Big|_{S_j}\left(\theta-\theta_{S_j}\right)^2} d\theta = \sqrt{\frac{\pi}{2A_\theta}}\left\{-\left[C\left(-\sqrt{\frac{2A_\theta}{\pi}}\theta_{S_j}\right) \pm iS\left(-\sqrt{\frac{2A_\theta}{\pi}}\theta_{S_j}\right)\right] + \left[C\left(\sqrt{\frac{2A_\theta}{\pi}}\left(\pi-\theta_{S_j}\right)\right) \pm iS\left(\sqrt{\frac{2A_\theta}{\pi}}\left(\pi-\theta_{S_j}\right)\right)\right]\right\} \quad (3.42)$$

where $A_\zeta = \frac{1}{2}\frac{r}{\Lambda}Y\frac{\partial^2\Phi}{\partial\zeta^2}$. The expressions with the plus sign correspond to $\frac{\partial^2\Phi}{\partial\zeta^2} > 0$ and the minus sign to $\frac{\partial^2\Phi}{\partial\zeta^2} < 0$.

Finally, the integration of the wave fields using the Cauchy's Residue Theorem and the Stationary Phase Method gives the following result

$$\vec{E}(\vec{r}) = \frac{2\pi i}{\Lambda\sigma_{ci}}\sum Res\left\{\sum_{Stationary\,Points}\left[sin\theta_S\left[Z_B(\theta_S)\right]\vec{J}_B(\theta_S)\left(\frac{K(\theta_S)}{\Lambda}\right)^2 e^{i\frac{r}{\Lambda}Y\Phi(\theta_S,\phi_S)}I_1I_2\right]\right\} \quad (3.43)$$

$$\vec{B}(\vec{r}) = \frac{2\pi i}{\Lambda\sigma_{ci}}\frac{1}{Y\omega_{ci}}\sum Res\left\{\sum_{Stationary\,Points}\left[sin\theta_S\vec{k}(\theta_S)\times\left[Z_B(\theta_S)\right]\vec{J}_B(\theta_S)\left(\frac{K(\theta_S)}{\Lambda}\right)^2 e^{i\frac{r}{\Lambda}Y\Phi(\theta_S,\phi_S)}I_1I_2\right]\right\} \quad (3.44)$$

where it can be observed that the wave fields decay like $1/r$, thus the Poynting flux goes like $1/r^2$.

### 3.4.4 Calculation of the Poynting Flux and Radiated Power

The Poynting vector $\vec{S}$ represents the instantaneous energy flux $\left[W/m^2\right]$ of the wave at a given point. Consistent with the definition of the group velocity, the Poynting vector must be along the radial direction to the observation point. The time-averaged Poynting vector can be calculated as follows

$$\left\langle \vec{S} \right\rangle = \frac{1}{\mu_0} \left\langle \vec{E} \times \vec{B} \right\rangle \tag{3.45}$$

The radiated power can be found by integrating the equation above over a spherical shell around the antenna

$$P = \int_0^{\pi} \int_0^{2\pi} \left( \hat{r} \cdot \left\langle \vec{S} \right\rangle \right) r^2 sin\theta_x d\theta_x d\phi_x = 2 \int_0^{\pi/2} \int_0^{2\pi} \left( \hat{r} \cdot \left\langle \vec{S} \right\rangle \right) r^2 sin\theta_x d\theta_x d\phi_x \tag{3.46}$$

and the radiation resistance $R$ follows immediately from the power

$$R = \frac{2P}{I_0^2} \tag{3.47}$$

The Poynting flux around the resonance cone diverges like $K \propto (cos\theta - cos\theta_{res})^{-1/2}$; this is an integrable singularity, i.e. the radiated power in equation (3.46) does not diverge.

### 3.4.5 Fields and Power from a Two-coil Configuration

The formulation of the fields above is applicable to a single AC coil with arbitrary axis' orientation given by ($\zeta$, $\psi$), as indicated in Figure 3-6 (a). In Chapter 6 we will see, however, that an AC static coil has a too large self-inductance due to the large coil dimensions and circulating current, which translates into huge voltages across the coil and the potential for sheath formation. For this reason, a DC rotating coil idea is proposed as a more feasible option, which complexity is not electrical but mechanical.

The dipole component of a DC coil rotating at the EMIC frequencies ($< 2$ Hz) is equivalent to two AC static orthogonal coils with axes given by ($\zeta_1$, $\psi_1$) and ($\zeta_2$, $\psi_2$), as illustrated

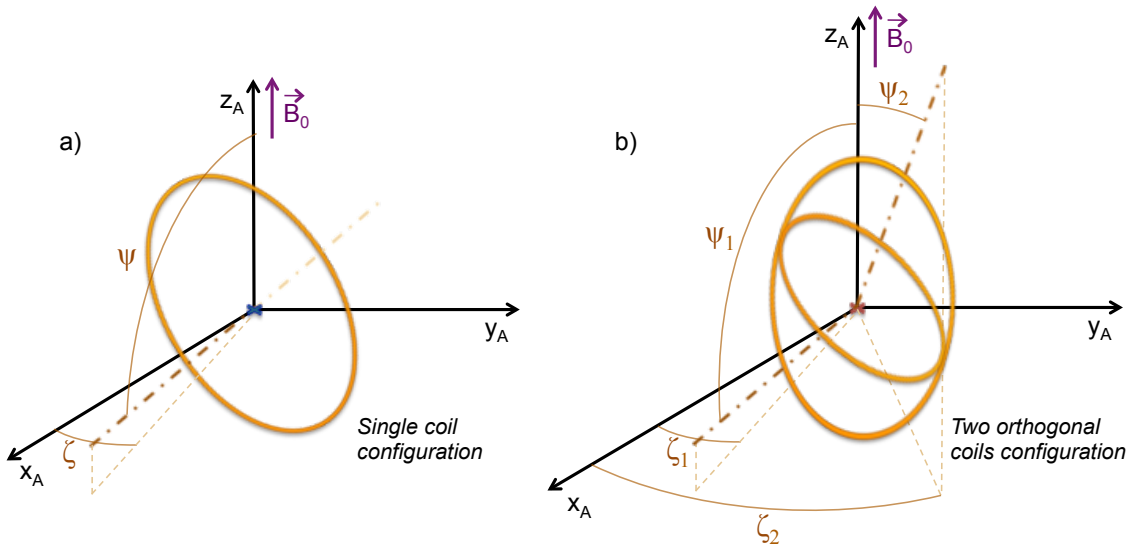


Figure 3-6: (a) Single AC coil configuration. (b) Two orthogonal AC coils, equivalent to a DC rotating coil.

in Figure 3-6 (b). The radiation energy eventually comes from the kinetic energy of the rotating antenna. We should note that in this thesis we are not addressing the origin of the radiation power; we believe that the *radiation drag* will impart a steady torque on the coil, which would have to be compensated and should be carefully studied in future efforts.

The radiation pattern of the two orthogonal coils can be easily calculated from the expressions above for a single coil antenna. The fields of the two-coil setting will be the composition (the sum) of the fields from a coil at $(\zeta_1, \psi_1)$ plus the fields from a second coil at $(\zeta_2, \psi_2)$, the latter perpendicular to the first and also displaced in time by 90° (i.e. multiply the fields by the complex number $i$). Once we calculate both fields, we only have to add them up, and cross multiply the electric and magnetic contributions to find the Poynting flux. The current is DC, thus the only reactance that remains is the one associated with the plasma currents, which is considered small and will be neglected. The Poynting flux and radiation resistance of both configurations in Figure 3-6 are detailed in the following section.

### 3.4.6 Results: Radiation Pattern and Radiation Resistance

The Poynting flux from a magnetic coil antenna calculated with the full-wave analysis described above is presented in Figure 3-7, which corresponds to the parameters detailed

in Table 3.1 and a frequency of Y = 0.02. Figure 3-7 considers three different loop radii, $R_a$, for parallel ($\psi = 0°$) and perpendicular ($\psi = 90°$) antenna orientations. It must be noted that the results are for $\phi_x$=0°; the radiation pattern, however, does not depend on the azimuthal angle of the observation direction because the power is concentrated in a very small cone and does not distinguish between different $\phi_x$. It can be observed that the perpendicular orientation is preferred in terms of radiation efficiency because the Poynting flux is up to eight orders of magnitude larger compared to the parallel case, which was also noted by *Wang and Bell* [1972c]. For this reason, the antenna axis should be oriented around the perpendicular direction with respect to the Earth's magnetic field lines.

Table 3.1: Environmental and antenna parameters

| | |
|---|---|
| Antenna location | $L$=1.5, equatorial |
| r distance | 5000 km |
| $n_{eq}$ | $3.05{\cdot}10^4$ cm$^{-3}$ |
| $B_{0eq}$ | $0.89{\cdot}10^{-5}$ T |
| Composition | Electron-proton plasma |
| Antenna current | 300 A |
| # turns | 106 |
| Wire radius, $\xi$ | 0.5 mm |

By definition, power flows in the direction of the group velocity, $v_g$, which is almost perpendicular to the phase velocity direction. This fact is exemplified in Figure 3-8 (a). The schematic is a qualitative representation of the wave number dispersion surface of L-mode EMIC waves, $\vec{k}(\theta)$, which is perpendicular to the direction of $\vec{v}_g(\theta_x)$ for every wave normal angle, then $\theta_x = f(\theta)$. The actual dispersion surface of EMIC waves with frequencies much below the proton gyrofrequency is almost flat, i.e. power always propagates field-aligned independently of the wave number vectors being coupled to the plasma.

Figure 3-7 shows that power propagates very close to field-aligned, in a small cone around the magnetic direction defined by the resonance cone of EMIC waves in equation (2.20). For the environmental parameters in Table 3.1, $\theta_{res} = 89.97°$ and $\theta_x|_{res} = 0.0267°$, which is the angle observed in Figure 3-7[†]. The wave normal vectors that correspond to this radiation

[†] This fact could seem to violate the diffraction limit because the power is being naturally focused to an angle much smaller than $\lambda/R_a$. This focusing effect is possible because EMIC are plasma waves that propagate in a magnetized plasma, which completely changes wave propagation characteristics compared to vacuum (M. Porkolab, personal communication, April 2013; W. Gekelman, personal communication, April 2013)

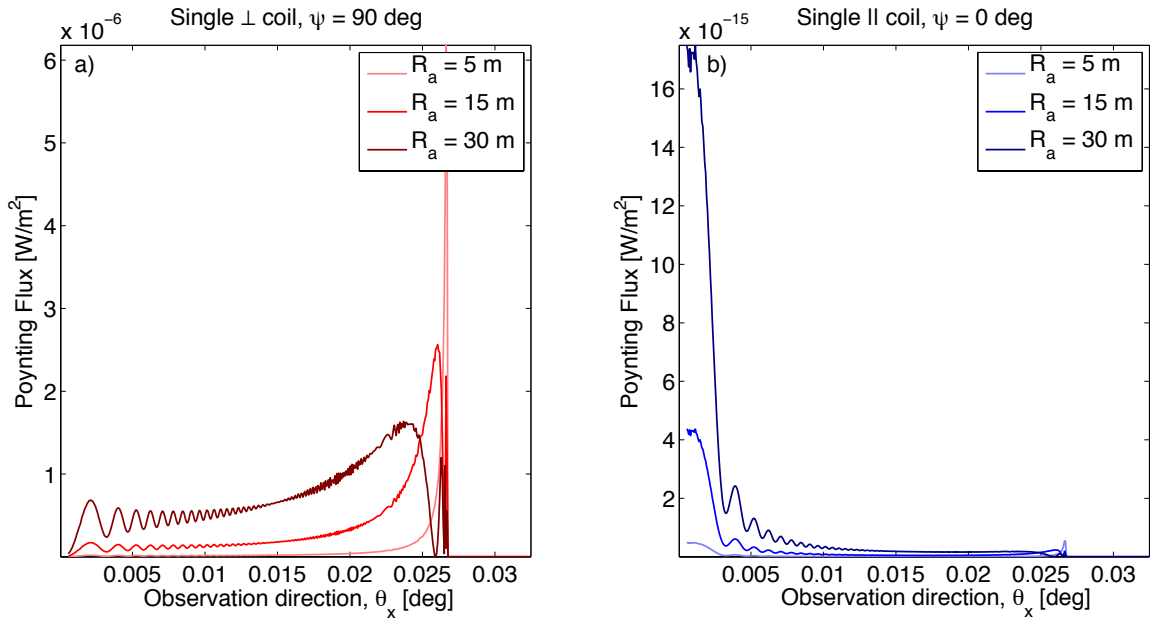


Figure 3-7: Poynting flux from a space-based magnetic coil antenna for the parameters given in Table 3.1, a frequency of Y = 0.02, and for (a) perpendicular and (b) parallel orientations with respect to the Earth's magnetic field. The plots are for $\phi_x = 0°$, but they do not depend on the azimuthal angle of the observation direction due to the smallness of $\pi/2 - \theta_{res}$.

pattern are close to perpendicular. The Poynting flux in Figure 3-7 is characteristic of any space-based transmitter in the EMIC band and it is controlled by the surrounding plasma environment. In addition, we observe that increasing the loop radius has the effect of filling up the resonance cone, while the power concentrates on the surface of the cone for the smaller radius values. This happens because larger $R_a$ couples to larger wavelengths, i.e. smaller $\vec{k}$'s. For the larger $R_a$ values, the wave normal vector slightly moves away from the resonance cone towards larger wavelengths. This corresponds to smaller $\theta_x$ because the wave normal is moving towards the minimum of the dispersion surface (which is indeed almost unperceivable). The dependence of the resonance cone angle on frequency calculated using equation (2.20) is presented in Figure 3-8 (b) for the parameters in Table 3.1, which is linear in frequency and always smaller than 1°.

The power and the radiation resistance can be found by integrating the Poynting flux over a spherical shell around the antenna (equation (3.46)). Figure 3-9 (a) compares the radiation resistance of a perpendicular coil antenna calculated using the full-wave model derived above with the analytical expressions from *Bell and Wang* [1971] presented in equations (3.5)-(3.8).

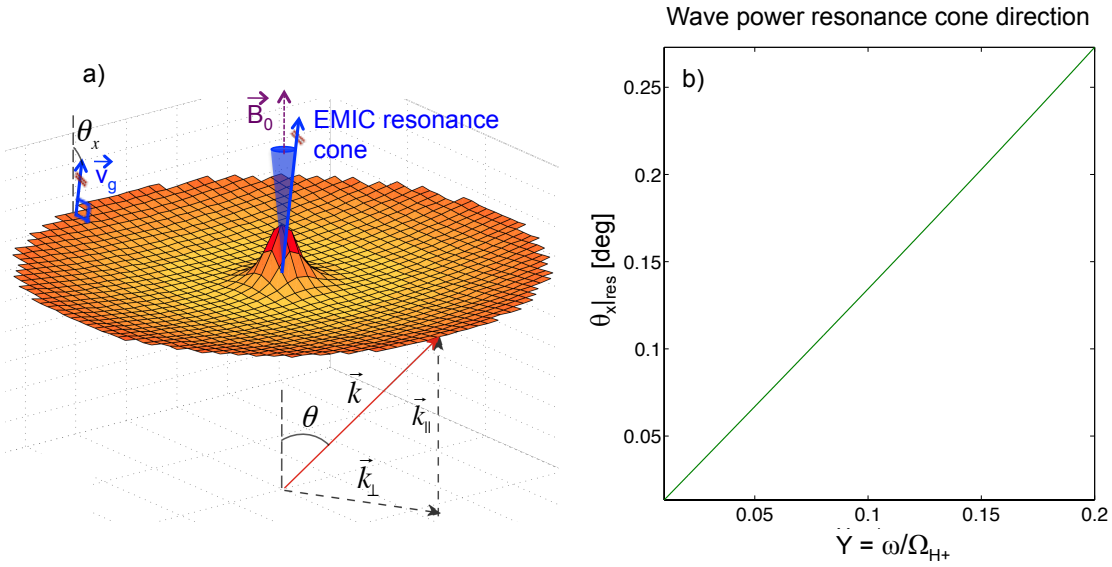


Figure 3-8: (a) Qualitative representation of the dispersion surface of an L-mode EMIC wave. (b) Wave power resonance cone direction, $\theta_x|_{res}$, as a function of non-dimensional frequency, $Y = \omega/\Omega_{H+}$

Even though their expressions are taken in the limit of the quasi-static approximation, they are in very good agreement with our full-wave solution. For a fixed frequency of Y = 0.02, Figure 3-9 (b) shows that the radiation resistance decreases with increasing $L$-shell of operation.

Finally, Figure 3-10 presents the Poynting flux and the radiation resistance of a two orthogonal coil configuration calculated with our full-wave model. The radiation pattern in the figure is equivalent to that of a DC rotating coil with axis always perpendicular to the Earth's magnetic field, that is, $\psi_1 = \psi_2 = 90°$, $\zeta_1 = 0°$ and $\zeta_2 = 90°$ in Figure 3-6 (b). The radiation pattern in Figure 3-10 (a) has been calculated for the parameters in Table 3.1, a frequency of Y = 0.02, a coil radius of $R_a$ =15 m and for $\phi_x = 0°$. In the figure we observe the same features as in the radiation pattern of a single coil described above. Similarly, the radiation resistance in Figure 3-10 (b) also presents the same trends that the results for a single perpendicular coil antenna, with the exception that the values of the resistance are slightly higher, by no more than a factor of 3. Table 3.2 depicts the values of the radiation resistance of the curves in Figure 3-10 (a) for three different coil radii. As expected, the larger the coil the better, since the radiation resistance scales with the cube of the loop radius. The mechanical considerations of such a big structure are discussed in Chapter 6.

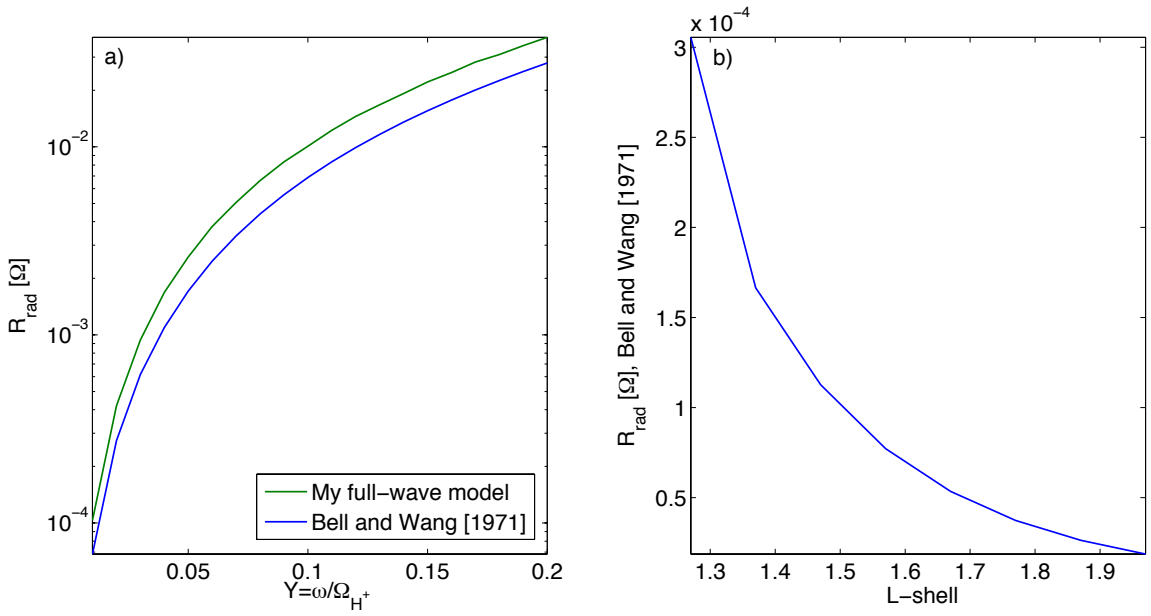


Figure 3-9: (a) Comparison between the radiation resistance given by the model derived in Sections 3.4.3 and 3.4.4 and the analytical expressions of *Bell and Wang* [1971]. (b) Radiation resistance from *Bell and Wang* [1971] versus $L$-shell for Y = 0.02.

Table 3.2: Radiation resistance of the two-orthogonal loop configurations corresponding to Figure 3-10 (a). The values are for a frequency of Y = 0.02.

| $R_a$ [m] | $R_{rad}$ [Ω] |
|---|---|
| 5 | $3.7{\cdot}10^{-5}$ |
| 15 | $8.4{\cdot}10^{-4}$ |
| 30 | $5.3{\cdot}10^{-3}$ |

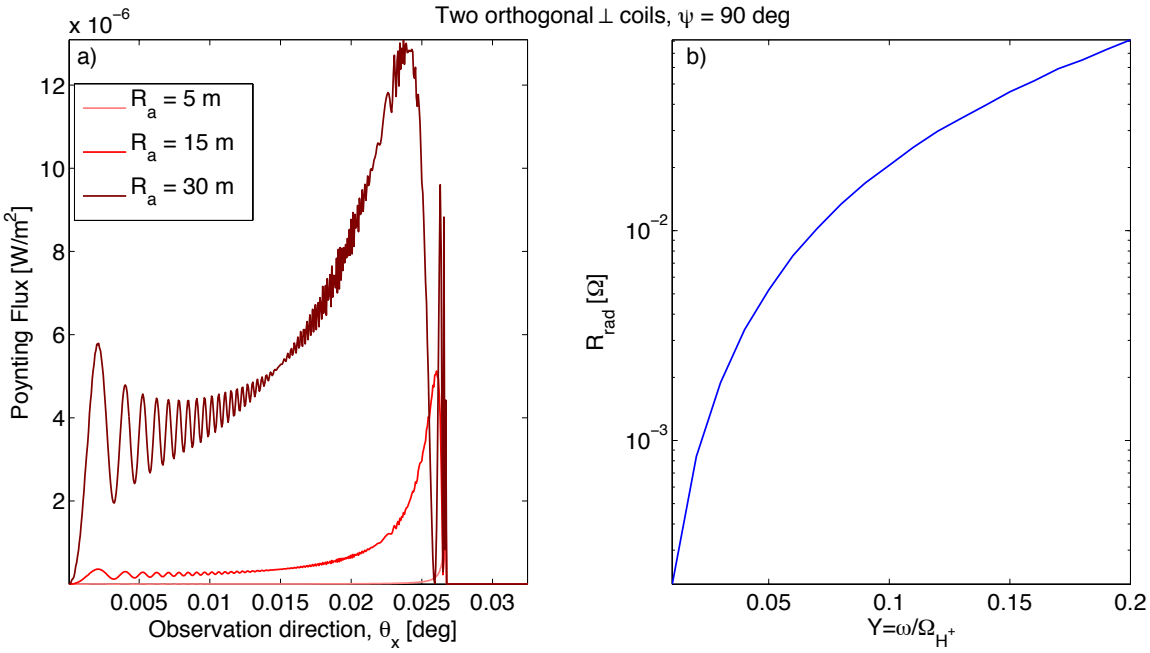


Figure 3-10: (a) Poynting flux from two orthogonal coils with axes perpendicular to the Earth's magnetic field. The plot is for the parameters in Table 3.1, a frequency of Y = 0.02, and for $\phi_x = 0°$. (b) Radiation resistance of two orthogonal loops with axes perpendicular to the Earth's magnetic field as a function of frequency.

### 3.4.7 Importance of Thermal Effects

Thermal effects could become important around the resonance cone where the Poynting flux diverges, in which case the cold-plasma approximation above would not be accurate in this region. Two different effects are not captured by cold plasma theory: Landau/cyclotron damping and finite Larmor radius effects. The inclusion of these effects would require a kinetic formulation.

Since the medium is anisotropic, the dynamics parallel and perpendicular to the Earth's magnetic field have to be considered separately. The thermal problem in this section is presented such that the condition for Landau and cyclotron damping deals with the parallel dynamics, while the finite Larmor radius effects consider the behavior in the perpendicular direction.

Landau/cyclotron damping will be important when the wave phase velocity due to the wave number vector component parallel to the Earth's magnetic field, $c_{\phi II} = \omega/k_{II}$, approaches the thermal velocity of electrons or protons. In what follows, we only consider the thermal

velocity of the electrons because it sets the most restrictive condition, which is defined as

$$v_{th} = \sqrt{\frac{2\kappa T_e}{m_e}} \tag{3.48}$$

where $\kappa$ is the Boltzmann constant and $T_e \approx 2000$ K is the temperature of the low energy electrons in the inner belt. The wave number vector of EMIC waves from space-based transmitters, however, is mostly perpendicular to $\vec{B}_0$, thus $c_{\phi\|}$ is very large up to distances extremely close to the resonance cone. If we consider that thermal effects are important whenever $c_{\phi\|} \leq 3v_{th}$, this corresponds to a cutoff $\theta_x(Y = 0.02) = 0.0256°$, which is almost the resonance value $\theta_{xres}(Y = 0.02) = 0.0267°$. For this reason, Landau/cyclotron damping have been neglected in the calculation of the radiation pattern. These non-collisional damping mechanisms, however, are further discussed and calculated in Chapter 4.

The finite Larmor radius effect could be important whenever the gyro-radius of the thermal particles is larger than the perpendicular wavelength of the waves. In the case of thermal electrons, this condition can be written as follows

$$r_{gyro} > \lambda_\perp \rightarrow \frac{\omega}{\Omega_e} v_{th} > 2\pi \frac{\omega}{\left|\vec{k}\right|} \tag{3.49}$$

where $\Omega_e$ is the cyclotron frequency of electrons. In our case, we will see in the following chapters that the selected frequencies would have Y= $\omega/\Omega_e << 1$, and cold plasma theory is therefore applicable. It must be noted, however, that the thermal effects around the resonance cone are not well understood, and the conditions above are being marginally satisfied. For this reason, the cold plasma theory is always questionable in this situation and should be carefully addressed in future efforts.

## 3.5 Conclusions

In this chapter we have investigated the effect of the plasma on the radiation pattern and radiation resistance of a space-based EMIC transmitter. The main conclusions are the following:

- Space-based transmitters are preferred to ground based antennas because they avoid inefficiencies associated with ionospheric coupling and ground effects. Additionally, space-based concepts are more flexible than ground-based ones, which operate at a fixed frequency, with no directional control and cannot be moved. Flexibility is especially important in the development of proof-of-concept or scientific missions that may enable testing specific parts of the remediation ideas.

- The magnetoplasma acts as an impedance connected in series to the physical space-based antenna. The real part of this impedance is responsible for radiation. The imaginary part contains the plasma sheath and the radiation reactance, which should be minimized.

- The accumulation of charge in the surface of a linear space-based antenna (electrical dipole) generates a plasma sheath that impedes radiation. The effect of the sheath is even more pronounced in the EMIC band compared to the whistler band, to the point that it is not feasible to use an electric dipole to radiate EMIC waves in the magnetosphere. Even a multi-km antenna would have too much reactance compared to radiation resistance in the EMIC regime.

- Magnetic dipoles have been identified as a promising solution to the sheath problem. A DC rotating coil is the best candidate to radiate EMIC waves in the magnetosphere, since it avoids the large self-inductance associated with AC operation. Instead of an alternating current circulating around a static coil, we propose a direct current driven around a rotating coil. Both AC and DC options, however, can be equivalently modeled in terms of radiation impedance characteristics.

- The dipole component of a DC coil rotating at the EMIC frequency is equivalent to two AC static orthogonal coils. The radiation pattern of the two orthogonal coils can be easily calculated from the expressions for a single coil antenna by superposing the fields of both coils.

- The radiation resistance of magnetic loops is several orders of magnitude smaller than the one of electric dipoles. For this reason, multiple turn arrangements and large coil radius are required to increase the radiation resistance of magnetic dipoles. Additionally, superconductors will be used to minimize ohmic losses and drive large

currents along the transmitter with the purpose of increasing the radiated power.

- The radiation resistance of magnetic dipoles scales with the cube of the loop radius and the square of the frequency. Contrarily, the radiation reactance is mostly linear with both radius and frequency. Additionally, the radiation resistance decreases with increasing $L$-shell of operation.

- The antenna axis should be oriented perpendicular to the geomagnetic field lines because it maximizes its radiation resistance.

- We have developed a full-wave model of a coil antenna in the EMIC regime immersed in a cold magnetized plasma. The model uses the Stationary Phase Method and Cauchy's residue theorem to calculate the fields and power in the far-field region radiated by the antenna. The simulations show that the power only propagates inside a very small cone (resonance cone) around the geomagnetic field direction. The beam is very focused along the magnetic field lines and illuminates a very small range of $L$-shells, which will translate into very short encounters between particles and waves; the corresponding wave normal angles are close to perpendicular to the geomagnetic field lines.

- The radiation resistance calculated with our full-wave model is in very good agreement with the quasi-static analytical approximation provided by previous authors.

- The Poynting flux and the radiation resistance of a two orthogonal coil configuration present the same features as the ones of a single coil antenna; the values of the radiation resistance of the two orthogonal loops are slightly higher than the single coil configuration, but by no more than a factor of 3.

- In our simulations we have assumed cold plasma theory. We have argued that thermal effects are small because the antenna driving frequency is very low compared to the proton cyclotron frequency and the condition for Landau/cyclotron damping is not satisfied. Thermal effects, however, should be reconsidered in more detail in future efforts.

# Chapter 4

# Propagation of EMIC Waves

This chapter presents the methodologies used to calculate the propagation and damping of EMIC waves radiated from the space-based antenna described in the previous chapter. The transmitter radiation pattern provides the wave properties at the starting point, which corresponds to the location of the source. These properties are propagated all along the waves' ray path. The results of these calculations are presented and analyzed next.

## 4.1 Model Inputs

The Earth's magnetic field is assumed dipolar, which is an accurate representation in the inner belt region. The magnetic field model is presented in Figure 4-1 (b). The electron cold plasma density background is taken from the Global Core Plasma Model (GCPM) [*Gallagher et al.*, 2000], which is an empirical model that provides plasma density as a function of solar activity and geomagnetic conditions. A 3-D mesh of densities is constructed using the GCPM with $K_p = 4^*$, which covers all Magnetic Local Times (MLT) and radial distances up to $L = 2.2$. Figure 4-1 (a) shows a cut of the cold plasma density model at MLT = 0. The plasmaspheric density at different MLTs was also analyzed by *Comfort* [1996], which shows that it is fairly stable with MLT in the inner belt.

* The $K_p$ index quantifies disturbances in the horizontal component of Earth's magnetic field, and it is used to summarize the global level of geomagnetic activity. $K_p$ is an integer that ranges from 0-9, with 1 being calm and >5 indicating a geomagnetic storm. It is calculated from the maximum fluctuations of the fields' horizontal component observed on a network of geomagnetic observatories during a three-hour interval.

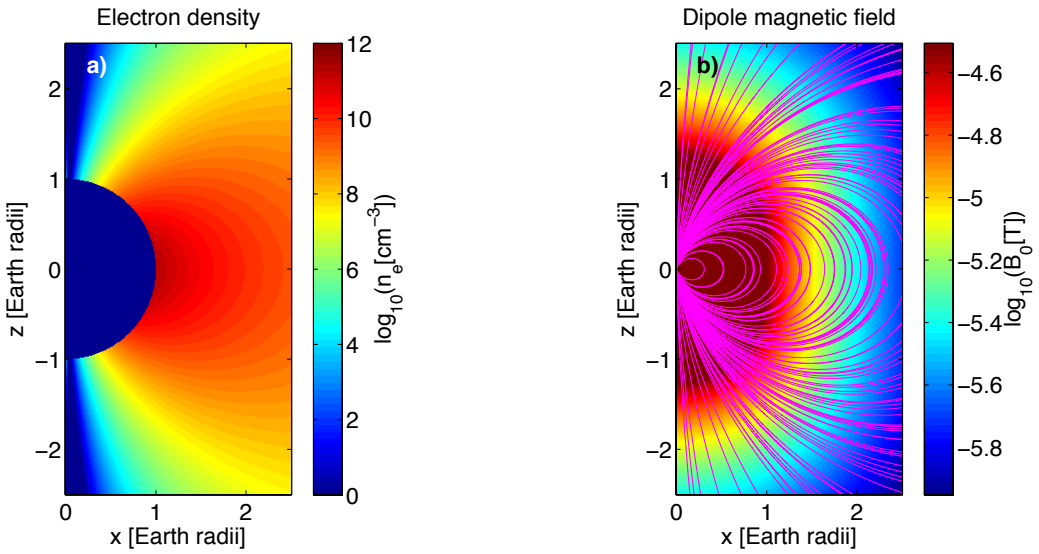


Figure 4-1: (a) GCPM electron density. (b) Dipole magnetic field model

The nominal ion composition is taken to be 90% $H^+$, 8% $He^+$ and 2% $O^+$. At the end of the chapter we also analyze the behavior during storm time conditions given by 70% $H^+$, 20% $He^+$ and 10% $O^+$ [*Horwitz*, 1987; *Meredith et al.*, 2003] and compare it to the nominal situation. It must be noted, however, that the measurement of the thermal ion concentration is difficult due to the high spacecraft potentials, which may lead to inaccurate measurements [*Horwitz*, 1987]. Thermal electrons, $H^+$, $O^+$ and $He^+$ are assumed to be Maxwellian with a temperature of 0.4 eV [*Comfort*, 1996; *Serbu and Maier*, 1966], which is used for Landau and cyclotron damping calculations.

## 4.2 Description of the Simulation

The Stanford VLF 3-D ray tracer [*Golden et al.*, 2010] adapted for EMIC waves is used together with path-integrated linear growth calculations. Ray tracing uses the geometric optics approximation to determine the trajectory of the ray path (Section 2.2.1); this approximation assumes that the properties of the medium vary slowly within one wavelength and that the plasma is cold, i.e. the thermal velocity of both electrons and protons is much smaller than the wave phase velocity [*Haselgrove*, 1955]. Ray tracing using the cold plasma dispersion relation provides wave normal vectors and plasma properties along the ray path, which are inputs to the local convective growth rate. Landau (m=0) and the first three

cyclotron resonances (m=±1, ±2, ±3) are considered in the integration of the convective growth rate described in equation (2.27). The code was originally written by Forrest Foust from the VLF Group at Stanford, and it is used here to determine the damping of the waves. The path-integrated gain is finally calculated by integrating the linear growth rate along the ray path (equation (2.30)).

Ray tracing does not directly capture the power flux divergence of the waves. This change in wave power density is associated with the change in geometric cross-sectional area as the wave propagates along its energy corridor. We define this corridor using (1) the ray paths of two parallel rays launched from adjacent injection points in the same meridional plane, and (2) the longitudinal wedge defined by an adjacent meridional plane containing identical pair of rays. The geometry is schematized in Figure 4-2. *Lauben* [1998] used the same approach to compute the power flux divergence of lightning-generated whistler waves. The scaling factor, $S^w$, affecting the power flux at time $t_1 > t_0$ can then be expressed as the ratio between the area of the corridor at the reference time $t_0$, $A_{t_0}$, and the area of the corridor at $t_1$, $A_{t_1}$,

$$P_{t_1}[W/m^2] = S^w_{t_1} \cdot P_{t_0}[W/m^2] \tag{4.1}$$

where

$$S^w_{t_1} = \frac{A_{t_0}}{A_{t_1}} \tag{4.2}$$

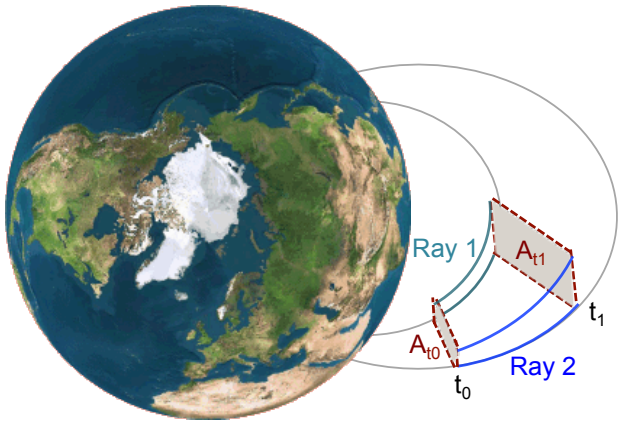


Figure 4-2: Calculation of power flux divergence

## 4.3 Propagation Results

### 4.3.1 Propagation Characteristics of Man-made EMIC Waves

L-mode EMIC waves capable of propagating through the magnetosphere have to be away from stop bands and polarization reversals (Figure 2-1). Figure 4-3 shows the latitude dependence of the different ion cyclotron frequencies. A driving frequency of ∼3 Hz is also plotted (within the EMIC oxygen band). Due to damping, wave-particle interactions and antenna design considerations, we will see throughout this dissertation that the preferred frequencies to precipitate energetic protons lay within the EMIC oxygen band. In the figure we observe that the driving frequency is always below the ion cyclotron frequencies, thus avoiding absorption or polarization reversals at any point along the ray path.

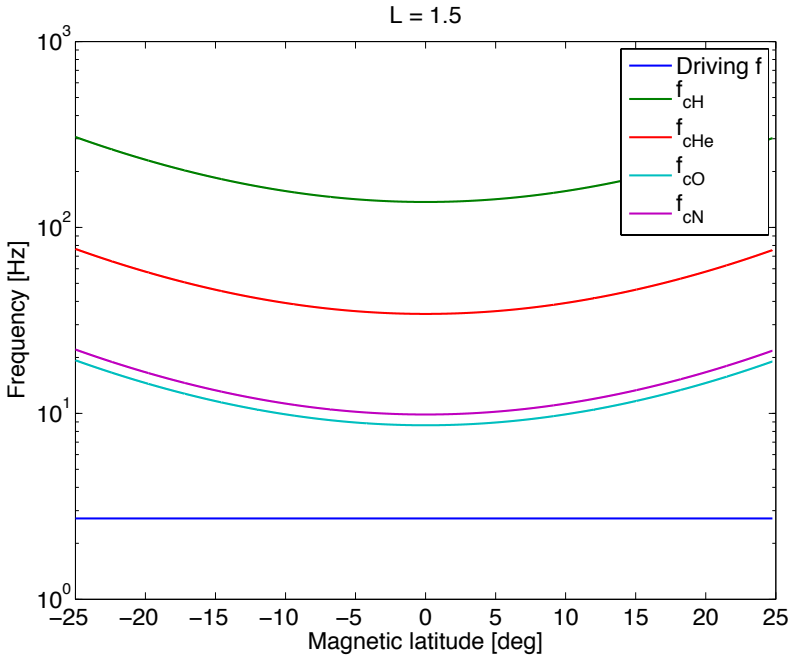


Figure 4-3: Antenna driving frequency (3 Hz) and ion cyclotron frequencies as a function of latitude at $L$=1.5

In Section 3.4 we calculated the radiation pattern from an EMIC antenna and we showed that the phase velocity of radiated waves is mostly perpendicular, along the direction of the resonance cone (equation 2.20). The gradient and curvature of the Earth's magnetic field have the capability of changing the wave normal angle of the waves during propagation in the magnetosphere. The group velocity, however, typically stays aligned with the external

magnetic field direction due to the shape of the EMIC dispersion relationship.

There is no observational evidence showing that EMIC waves are capable of bouncing back from high latitudes [*Loto'aniu et al.*, 2005; *Thorne and Horne*, 1993]. For this reason, in this thesis we take a conservative approach by not considering any bouncing of the waves. The wave-particle interactions will be therefore based on single-pass encounters between energetic protons and EMIC waves. The bouncing of EMIC waves at lower $L$-shells, however, would certainly improve the capabilities of the mission presented in this dissertation, and should be carefully addressed in future studies. Moreover, a scientific mission like the one discussed in Chapter 7 could also help answering this unresolved issue.

### 4.3.2 Wave Propagation and Wave Spreading

Space-based EMIC transmitters radiate waves with close to perpendicular wave normal angles. Ray tracing studies, however, show that the wave normal angle at equatorial heights is sensitive to the latitude of injection of the waves (i.e. inclination of the spacecraft orbit). Figures 4-4 (a) and (b) show ray tracing results of a spacecraft operating at a latitude of $\lambda_0 = 25^\circ$ at $L$=1.5. The yellow lines represent the ray paths or group velocity direction, while the light pink lines represent the Earth's dipole field. The orange and blue arrows correspond to the wave number vectors launched in a meridional plane towards and away from the Earth, respectively. The waves are initially radiated with a wave normal angle of $\theta_0 = 89.9^\circ$ and a wave frequency of Y=0.02. It can be observed that the power follows the geomagnetic lines very closely, while the wave number vectors remain close to perpendicular to the Earth's magnetic field. Figure 4-4 (b) shows that wave normals undergo a small rotation as they approach the equator. This guiding effect is due to the curvature and gradient of the Earth's magnetic field, which slightly rotates the wave normal angle towards the geomagnetic field direction as the wave approaches the equator, and it is beneficial for wave-particle interactions. On the other hand, Figures 4-4 (c) and (d) show ray tracing results of a spacecraft located at the equator at $L$=1.5. In this case, the curvature and gradient of the Earth's field only push wave normal angles towards larger values as they propagate away from the source. Moreover, it can be observed that the wave normal results from the equatorial case in Figure 4-4 (d) present the same shape and trend (but not the same values) as half of the plot of the higher latitude case in Figure 4-4 (b).

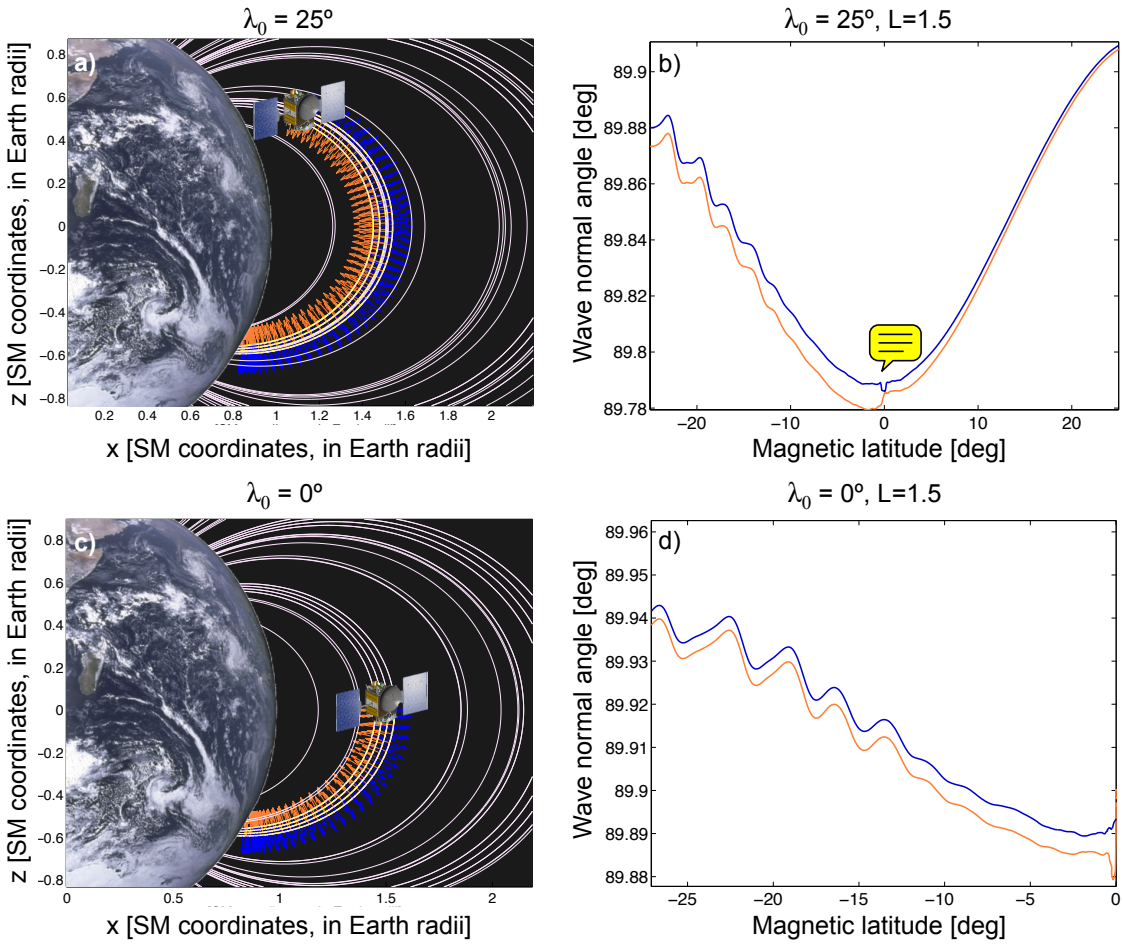


Figure 4-4: (a) Ray tracing results of a spacecraft at $\lambda = 25°$ and $L$=1.5, with frequency Y = 0.02. The waves are launched with $\theta_0 = 89.9°$. The yellow lines are ray paths. The light pink lines are the Earth's dipole field. The orange and blue arrows are the wave normal vectors towards and away from the Earth, respectively. (b) Wave normal angles as a function of latitude for the case in (a). (c) Ray tracing results of an equatorial spacecraft at $L$=1.5. (d) Wave normal angles as a function of latitude for the case in (c).

The next step consists of determining the spreading of these rays with respect to the original $L$-line of the launch point as they propagate through the inner belt region. In order to do that, we launch eight rays from the same location and with the same frequency but with different wave normal directions (all of them around a cone angle with $\theta_0 = 89.9°$). Figure 4-5 (a) shows the eight wave number vectors with respect to the geomagnetic field direction. Vectors $k_1$ and $k_2$ are contained in a meridional plane with directions towards and away from the Earth, respectively; vectors $k_3$ and $k_4$ are contained in a plane perpendicular to the radial direction from the Earth's center, and $k_5$ to $k_8$ are composition of the previous vectors. Figure 4-5 (b) shows the evolution of the wave normal angle as a function of latitude

for a source located at a latitude of $\lambda_0 = 25^\circ$ at $L$=1.5, and for a frequency of Y = 0.02. We can observe again that all the rays suffer a small alignment effect due to the curvature and gradient of the Earth's magnetic field. For these same rays, Figure 4-5 (c) and (d) shows the spatial extent of the illuminated region, i.e. the rays' azimuthal (y-coordinate) and radial spreadings with respect to the original geomagnetic line, respectively. The maximum spreading when the rays reach equatorial latitudes is 800 meters both azimuthally and radially, which corresponds to an illuminated cross sectional area of 64 $\text{hm}^2$. These are indeed very small spreadings, consistent with the fact that EMIC power radiated from space-based transmitters is confined along the geomagnetic field direction. This propagation signature will generate short wave-particle interactions with the energetic protons drifting around the Earth.

More generally, Figure 4-6 presents the spreading at the equator as a function of $L$-shell for three different frequencies in the oxygen band. Again, eight different rays close to the resonance cone ($\theta = 89.9^\circ$) have been considered per case (Figure 4-5 (a)). All the rays have been launched from a latitude of 15°, and the figure shows their spreading when they reach the equator. It can be observed that the spreading is practically independent of $L$-shell but dependent on frequency. This fact can be explained using the dispersion relationship of EMIC waves: the lower the frequency the flatter the dispersion surface, i.e. the more field-aligned the group velocity and the more perpendicular the wave number vector. For this reason, the lower frequencies spread less, because their group velocity is more field-aligned than the higher frequency cases. In the following chapters we will use the cross-sectional areas in Figure 4-6 together with the geometric change in the cross section of the energy corridor to calculate the required radiated power.

According to the results above, a *near* but *off*-equatorial orbit (i.e. low inclination orbit) is preferred because (1) it maximizes the spacecraft residence time inside the inner belt region and (2) the rays suffer a small guiding of their wave normal angle as they propagate to the equator, which increases the efficiency of wave-particle interactions. A good latitude to operate could be close to the turning point of drift loss cone particles, that is, $\lambda_0 = 12^\circ$ at $L = 1.2$, $\lambda_0 = 25^\circ$ at $L = 1.5$ and $\lambda_0 = 38^\circ$ at $L = 2$. Since we assume no bouncing of the waves, these launch points maximize the residence time of each wave packet in the magnetosphere, which still correspond to latitudes close to the equator.

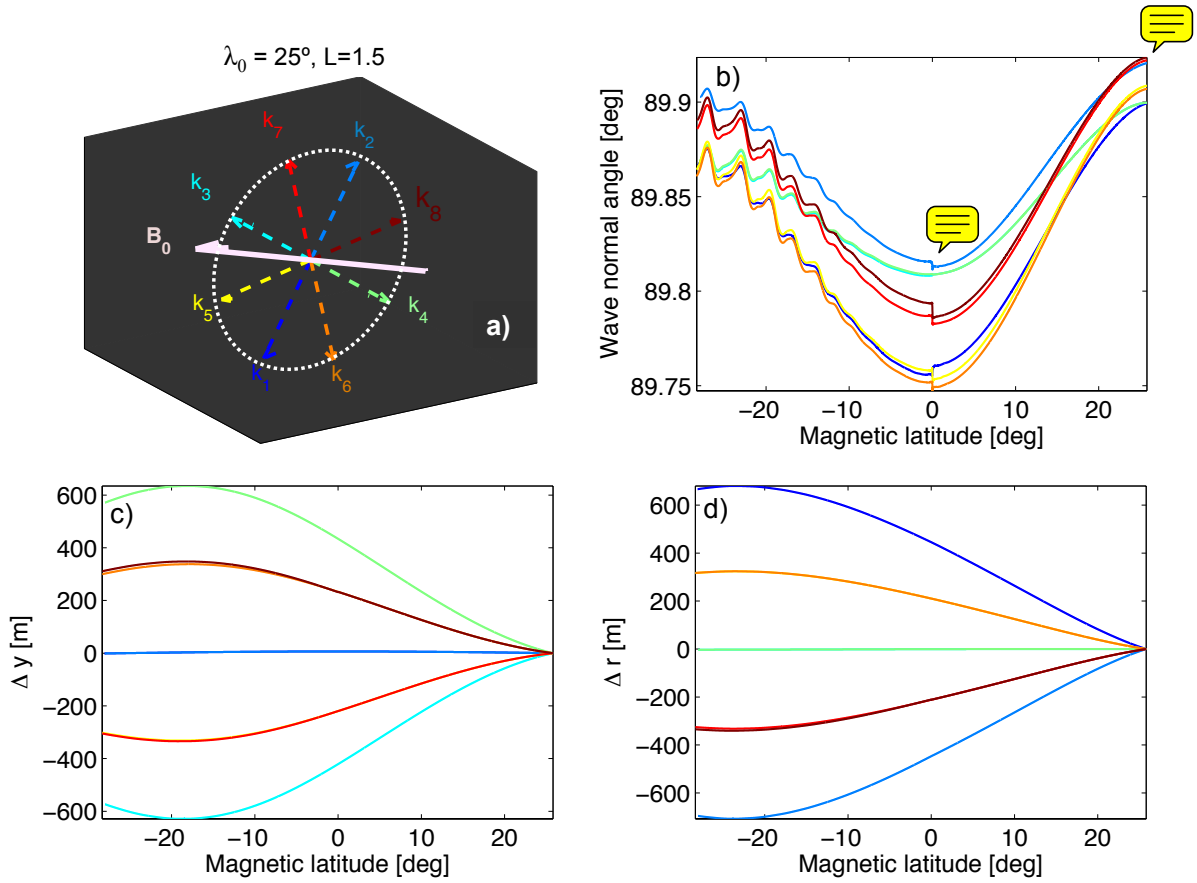


Figure 4-5: (a) Wave number vectors with respect to the geomagnetic field direction at the source location (25° latitude, $L$=1.5). Vectors $k_1$ and $k_2$ are contained in a meridional plane with directions towards and away from the Earth, respectively; vectors $k_3$ and $k_4$ are contained in a plane perpendicular to the radial direction from the Earth's center, and $k_5$ to $k_8$ are composition of the previous vectors. (b) Wave normal angle as a function of latitude for the rays in (a). (c) Azimuthal (y-coordinate) spreading as a function of latitude. (d) Radial spreading as a function of latitude. The plots are for a frequency of Y = 0.02 and an initial wave normal angle of $\theta_0 = 89.9°$.

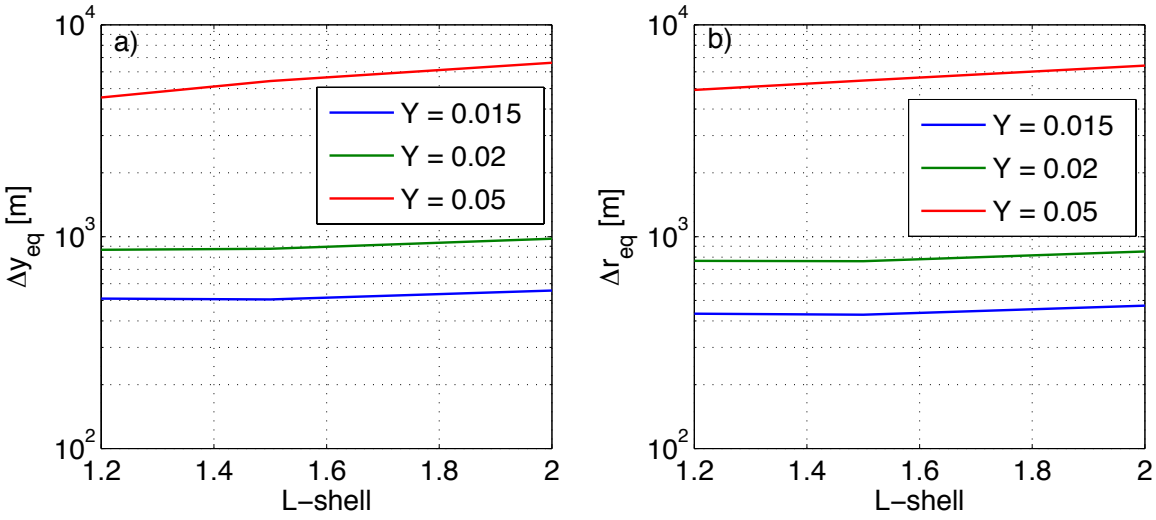


Figure 4-6: (a) Azimuthal (y-coordinate) and (b) radial spreadings at the equator as a function of $L$-shell for three different frequencies. All the rays have been launched from $\lambda = 15°$.

### 4.3.3 Landau and Cyclotron Damping Results

Landau and cyclotron damping calculations are a post-process of the ray tracing results. Their formulation was described in Section 2.2.2, and we next use the code from Forrest Foust from Stanford University to calculate the effect of these non-collisional damping mechanisms on the propagation of EMIC waves in the magnetosphere. The code takes the wave and plasma properties along the ray paths, which have been calculated using the ray tracer. Figure 4-7 presents the path-integrated damping in equation (2.30) versus $Y = \omega/\Omega_{H^+}$ and $L$-shell. The integration has been started at a source latitude of $\lambda_0 = 15°$, with an initial wave normal angle of $\theta_0 = 89°$. The figure shows two main ranges of frequencies where damping dominates. The range between $\mathrm{Y}_{res_{He^+}} = 0.25$ and $\mathrm{Y}_{cf_{He^+}} = 0.31$ corresponds to the stop band between the $He^+$ resonant and cutoff frequencies, while the damped area above Y = 0.5 is due to the proximity of the hydrogen resonant frequency, where the phase speed of the wave becomes comparable to the thermal velocity of the particles. Table 4.1 summarizes the critical frequencies at the equator normalized with the equatorial proton cyclotron frequency, $\Omega_{H^+}$. These characteristic normalized frequencies do not depend on the $L$-shell because the ion composition has been taken to be fixed in the inner belt. Landau is the dominant damping in the band around the Helium characteristic

Table 4.1: Characteristic normalized frequencies at the equator for an ion composition of 90% $H^+$, 8% $He^+$ and 2% $O^+$.

| $Y_{res_{O+}}$ | $Y_{cf_{O+}}$ | $Y_{cr_{O+}}$ | $Y_{res_{He+}}$ | $Y_{cf_{He+}}$ | $Y_{cr_{He+}}$ | $Y_{res_{H+}}$ |
|---|---|---|---|---|---|---|
| 0.07 | 0.08 | 0.11 | 0.25 | 0.31 | 0.39 | 1 |

frequencies as well as for frequencies above Y = 0.7; the lighter blue/green damped region between Y = 0.5-0.7, however, is not due to Landau but to cyclotron damping.

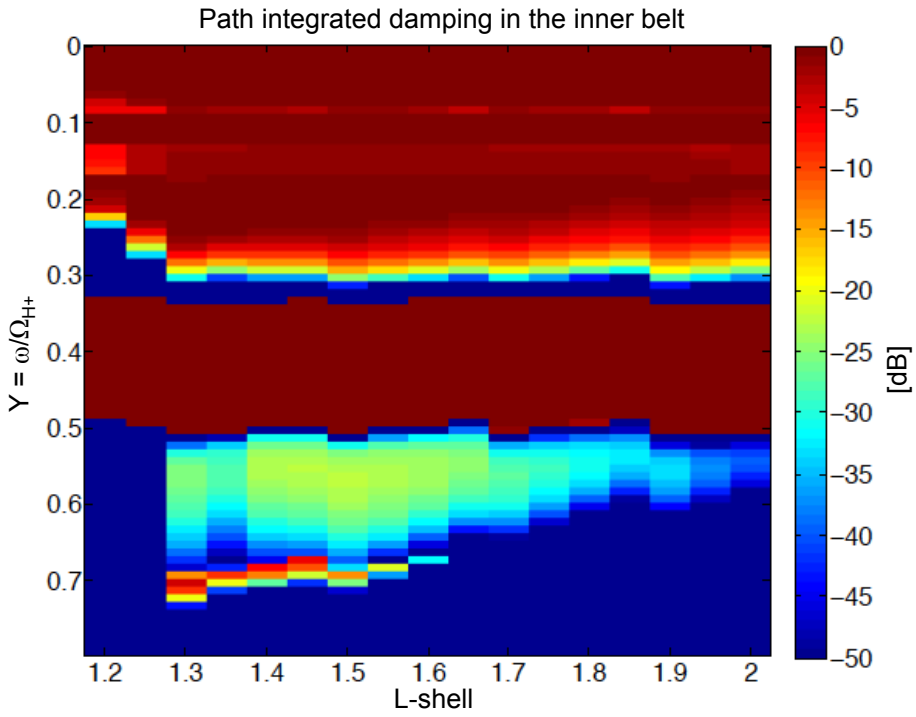


Figure 4-7: Path integrated damping as a function of $L$-shell and normalized frequency

Figure 4-8 depicts three specific mesh points in Figure 4-7. The plot represents the evolution of the wave power normalized to the initial radiated power after computing the damping due to non-collisional mechanisms. The three rays plotted in the figure are: Y=0.3 at $L$=1.2, Y=0.02 at $L$=1.5 and Y=0.8 at $L$=2. The first ray does not propagate very far because it finds the $He^+$ stop band. Similarly, the third ray is also strongly damped due to the proximity of the hydrogen gyrofrequency. On the other hand, the ray launched from $L$ = 1.5, in the oxygen band, propagates freely in the magnetosphere without suffering any damping. Landau and cyclotron damping are negligible in the oxygen band and for the very oblique wave normal angles under consideration because the resonance condition with the

thermal population is not satisfied; there is no exchange of energy or momentum between thermal particles and waves in the oxygen band. This fact suggest that, if wave-particle interactions allow, the oxygen band is a desirable range for antenna operation due to wave propagation considerations.

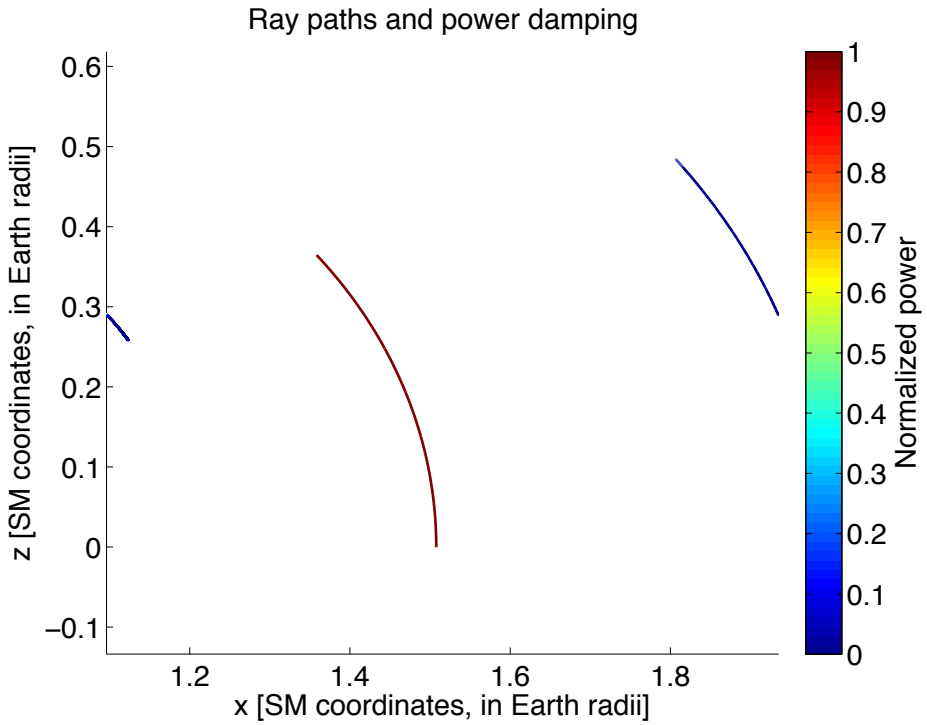


Figure 4-8: Local damping of three specific rays in Figure 4-7: Y=0.3 at $L$=1.2, Y=0.02 at $L$=1.5 and Y=0.8 at $L$=2. The colormap represents the normalized power after Landau and cyclotron damping calculations.

### 4.3.4 Power Density Divergence Results

The scaling power density divergence factor, $S^w$, was described in Section 4.2 and characterizes the power density divergence. This factor is represented in Figure 4-9 for three different $L$-shells. The behavior of the power density is associated with the change in geometric cross-sectional area as the wave propagates along its energy corridor. At the equator this cross-sectional area is maximum, i.e. the power density is minimum. The rays closer to the Earth have smaller change in cross-sectional area with respect to the injection location, thus the power divergence factor is larger than at outer $L$-shells.

It is the combination of both, ray tracing spreading results and power density geometric

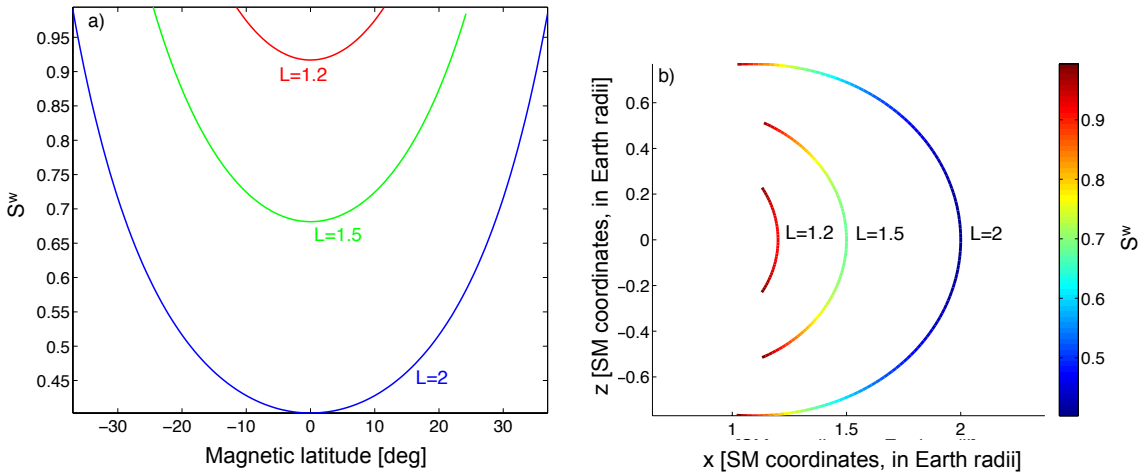


Figure 4-9: (a) $S^w$ as a function of latitude. (b) Colormap of $S^w$ as a function of solar magnetic coordinates.

divergence, that gives the total extension of the area illuminated by the transmitter. We saw that the spreading of the rays with respect to the original magnetic line (ray tracing results) is not very sensitive to $L$-shell; the power density divergence factor, however, is very sensitive to this parameter. Table 4.2 summarizes the cross-sectional area of the region illuminated at the equator resulting from ray tracing and power flux divergence calculations, which is a function of both $L$-shell and frequency. The rays have been launched from a latitude close to the turning point of drift loss cone particles, that is, $\lambda_0 = 12^\circ$ at $L = 1.2$, $\lambda_0 = 25^\circ$ at $L = 1.5$ and $\lambda_0 = 38^\circ$ at $L = 2$. Since we assume no bouncing of the waves, these launch points maximize the residence time of each wave packet in the magnetosphere, which still correspond to latitudes very close to the equator. For a fixed $L$-shell, lower frequencies spread less due to the shape of the dispersion relation; for a fixed frequency, lower $L$-shells spread less due to the smaller change in geometric cross-sectional area of the energy corridor. It must be emphasized, however, that the power density changes but the total power remains constant, since it has been shown in the previous section that, in the oxygen band, Landau and cyclotron damping mechanisms are negligible.

Table 4.2: Cross-sectional area illuminated by the transmitter at the equator

| | $L = 1.2$ ($\lambda_0 = 12°$) | $L = 1.5$ ($\lambda_0 = 25°$) | $L = 2$ ($\lambda_0 = 38°$) |
|---|---|---|---|
| Y = 0.0005 | 0.7 $hm^2$ | 0.9 $hm^2$ | 1.2 $hm^2$ |
| Y = 0.001 | 0.8 $hm^2$ | 1.0 $hm^2$ | 1.1 $hm^2$ |
| Y = 0.005 | 3.7 $hm^2$ | 4.4 $hm^2$ | 4.7 $hm^2$ |
| Y = 0.015 | 28 $hm^2$ | 30 $hm^2$ | 31 $hm^2$ |
| Y = 0.02 | 69 $hm^2$ | 71 $hm^2$ | 73 $hm^2$ |
| Y = 0.05 | 36.4 $km^2$ | 36.5 $km^2$ | 36.6 $km^2$ |

### 4.3.5 Sensitivity to Background Ion Composition

The results above were based on a nominal background (thermal) ion composition given by 90% $H^+$, 8% $He^+$ and 2% $O^+$. In this section we repeat the ray tracing and damping simulations for a composition characteristic of storm time conditions given by 70% $H^+$, 20% $He^+$ and 10% $O^+$ [*Horwitz*, 1987; *Meredith et al.*, 2003] and compare the results to those from the nominal situation.

Figure 4-10 shows the refractive index, wave normal angle and extension of the illuminated region as a function of latitude for storm time conditions at $L$=1.5 and Y=0.02. The rays have been launched with an initial wave normal angle of $\theta_0 = 89.9°$ at $\lambda_0 = 25°$. The color-code corresponds to the rays in Figure 4-5 (a), and the grey dashed lines are the results during (nominal) quiet times. We can observe that the magnitude of the refractive index is slightly increased compared to the nominal scenario, but the overall behavior of the wave normal angle and wave spreading remain practically unchanged. The reason for this negligible dependence on ion composition is the small driving frequency required by our particular application, very low into the oxygen band; this frequency is much below any ion characteristic frequencies. For this reason, the wave propagation characteristics are practically insensitive to changes in the ion composition. Similarly to the nominal case results, we have checked that Landau and cyclotron damping mechanisms are also negligible during storm time conditions, i.e. the resonance condition with the thermal population is not satisfied.

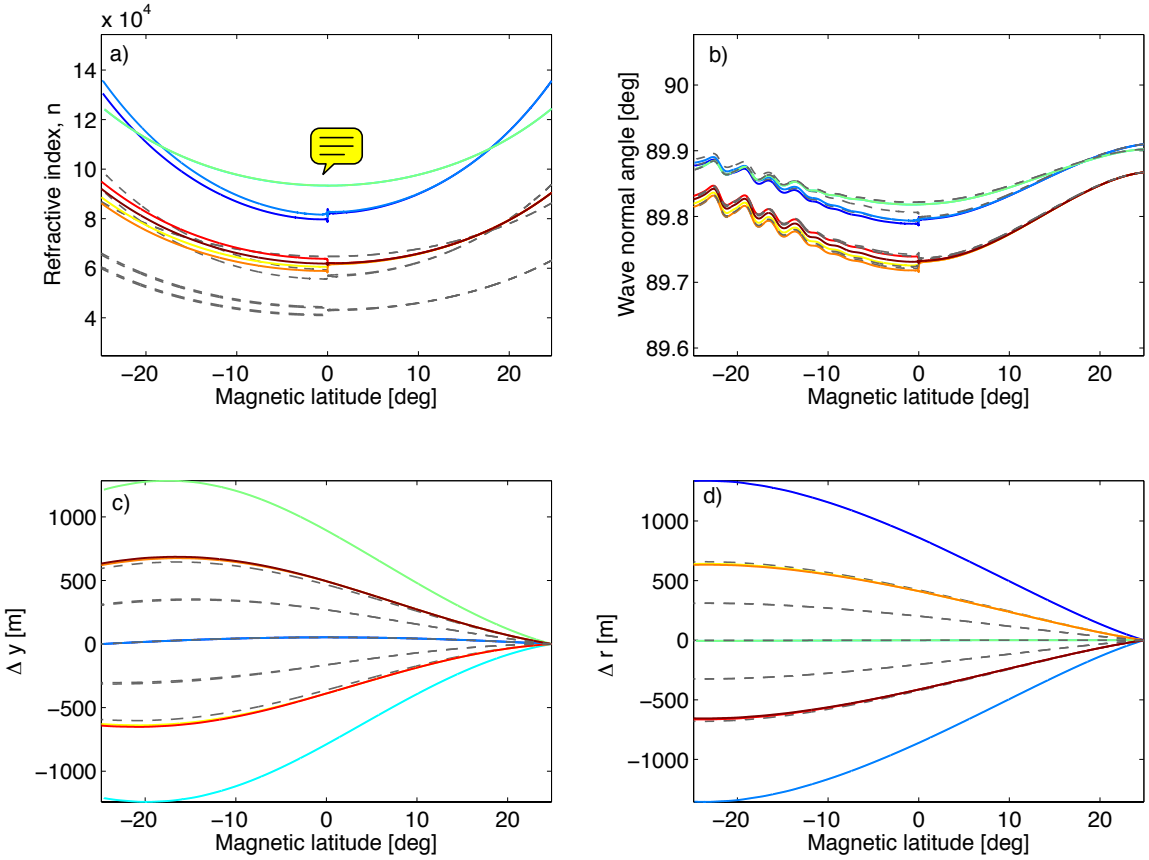


Figure 4-10: (b) Refractive index as a function of latitude for storm time thermal ion composition. The grey dashed lines correspond to the solution during nominal conditions. (b) Wave normal angle as a function of latitude. (c) Azimuthal (y-coordinate) spreading as a function of latitude. (d) Radial spreading as a function of latitude. The plots are for $L$=1.5 and Y=0.02.

## 4.4 Conclusions

In this chapter we have analyzed the propagation and damping in the magnetosphere of EMIC waves radiated from a space-based transmitter. The main conclusions are the following:

- The curvature and gradient of the Earth's magnetic field can have a guiding effect, which slightly rotates the wave normal angle of EMIC waves towards the geomagnetic field direction as they approach the equator.

- Wave spreading across $L$-shells is very small. The waves are confined along the geomagnetic field direction. This propagation signature will generate short wave-particle

interactions with the energetic protons drifting around the Earth.

- The spreading of the rays with respect to the original magnetic line is practically independent of $L$-shell but dependent on frequency due to the shape of the dispersion relationship of EMIC waves: the group velocity of lower frequency waves is more field-aligned.

- A low inclination orbit is preferred because (1) it maximizes the spacecraft residence time inside the inner belt region and (2) the rays suffer a small guiding of their wave normal angle as they propagate to the equator, which increases the efficiency of wave-particle interactions. A good latitude to operate could be close to the turning point of drift loss cone particles; since we assume no bouncing of the waves, this launch point maximizes the residence time of each wave packet in the magnetosphere, which still corresponds to latitudes close to the equator.

- Waves in the stop bands and above $Y > 0.5$ do not propagate through the equator due to Landau and cyclotron damping mechanisms. Operation in the oxygen band is preferred in terms of wave propagation.

- The greater the $L$-shell the larger the power density divergence along the ray path because there is a larger change of cross-sectional area along this path. It is the combination of both, ray tracing spreading results and power density geometric divergence, that gives the total extension of the area illuminated by the transmitter. Power density changes but the total power remains constant as far as there is no Landau or cyclotron damping.

- The propagation and damping of very low frequency EMIC waves in the oxygen band has a negligible dependence on ion composition.

# Chapter 5

# Controlled Precipitation of Inner Belt Protons

In the following sections we calculate the wave-particle interaction between energetic inner belt protons and the EMIC waves from the previous chapter. We first study the sensitivity of individual particle trajectories to wave power, wave normal angle, particle's energy and pitch angle. Following the characterization of the individual behavior, we next analyze the interaction with the whole population of particles and calculate precipitating fluxes and time evolution of their distribution. These results determine the radiated power required to effectively remediate the inner proton belt, which should be provided by the space-based antenna.

## 5.1 Model Inputs

The magnetospheric models used in the calculation of wave-particle interactions are the same as described in Section 4.1. Similarly to the propagation analyses, the nominal ion composition is taken to be 90% $H^+$, 8% $He^+$ and 2% $O^+$, and the behavior during storm time conditions (70% $H^+$, 20% $He^+$ and 10% $O^+$) is analyzed in Section 5.4.2 and compared to nominal values. In addition, the unperturbed phase-space distribution of energetic protons in velocity and pitch angle needs to be specified, which has been obtained from AP-9 [*Ginet et al.*, 2013]. AP(E)-9 is the successor of the NASA AE-8/AP-8 trapped radiation

belt models. Compared to previous models, AP(E)-9 extends the energy range, time and location of trapped energetic particles and includes new capabilities like quantification of uncertainty due to both instrument and space weather errors. Figure 5-1 presents the distribution function of energetic protons at $L = 1.5$ as a function of energy and pitch angle as given by AP-9. The figure clearly shows the loss cone, and the decrease of the distribution function with increasing energy.

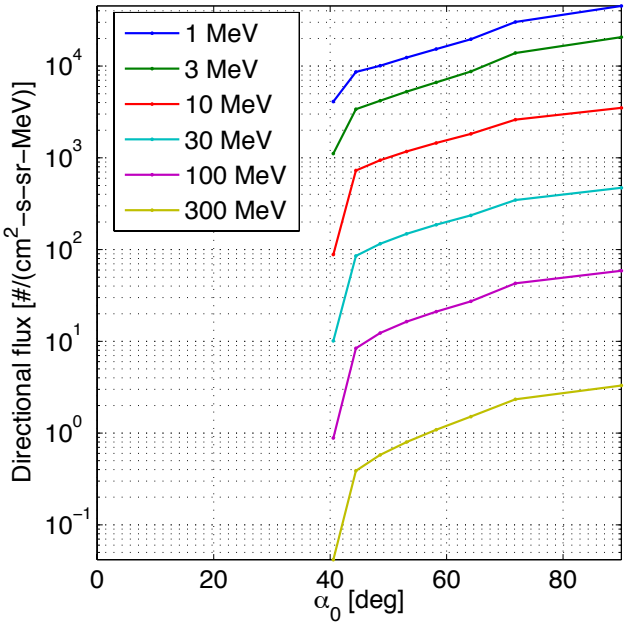


Figure 5-1: AP-9 distribution function of energetic trapped protons at $L = 1.5$

The loss cone observed in Figure 5-1 is the so called *drift* loss cone. The difference between *bounce* and *drift* loss cones arises from the fact that the Earth's magnetic field is tilted by 11.5° from its rotational axis and it is slightly off-center. For an off-center field, the particles' mirror point along their drift motion is symmetric with respect to the geomagnetic field, but it is not with respect to the atomsphere. The *bounce* loss cone assumes a centered dipole field, and it is the pitch angle for which particles have $\alpha = 90°$ at the border of the sensible atmosphere (∼100 km). On the other hand, the *drift* loss cone considers an off-centered dipole field, which is responsible for larger loss cone angles than what we would expect from a simple centered dipole model. In the offset model the particles' motions are still symmetric with respect to the geomagnetic field, but not relative to the Earth's atmosphere, i.e. particles precipitate over a wider range of pitch angles. For this reason, the more realistic drift loss cones are always larger than bounce loss cones. Drift loss cones

are considered in our simulations, which are in agreement with the data from the AP-9 empirical model.

## 5.2 The Nature of the Interaction between Inner Belt Protons and EMIC Waves

In Chapter 4 we showed that the spreading of EMIC waves across field lines is very small due to the shape of their dispersion relation. The antenna illuminates a very narrow region of space, which is confined along geomagnetic field lines. Additionally, energetic inner belt protons move very rapidly; particles cross the illuminated region in a fraction of their gyroperiod, where they are instantly scattered by the waves.

The characteristic proton periods as a function of energy together with the time it takes protons to cross the illuminated region are presented in Figure 5-2 (a). The plot is for equatorial loss cone particles at $L = 1.5$, and the extension of the waves used to determine the interaction time was taken from Table 4.2 for $L = 1.5$ and Y = 0.02 (i.e. 845 m). As seen in Section 1.2.3, the proton drift period is very fast, between 10 to 100 seconds depending on the energy. The interaction time is presented in Figure 5-2 (a), which is more than one order of magnitude shorter than the proton's gyroperiod. Similarly, Figure 5-2 (b) compares the proton gyroradius with the azimuthal wave spreading at the equator. From the figure we observe that the gyroradius is always much larger than the spatial extension of the waves. Additionally, we also plot the wavelength of an EMIC plane wave with $\theta = 89.5°$, which is also smaller than the protons' gyroradius. It must be emphasized here that the gyroradius in the figure is the one of the energetic inner belt protons. On the other hand, the gyroradius of the background (thermal) protons is only about 8 meters, much smaller than the wavelength of the waves, which was one of the reasons used to justify cold plasma theory in Section 3.4.7.

It must be noted that in this thesis we have approximated the interaction time with the guiding center motion, that is, we have calculated this time using the drift velocity of the particles. The interaction region is small while the gyroradius is big, thus the particle crosses the illuminated area many times per drift orbit, as illustrated in Figure 5-3. The blue oscillations represent the motion of the the particle, while the red lines mark off the

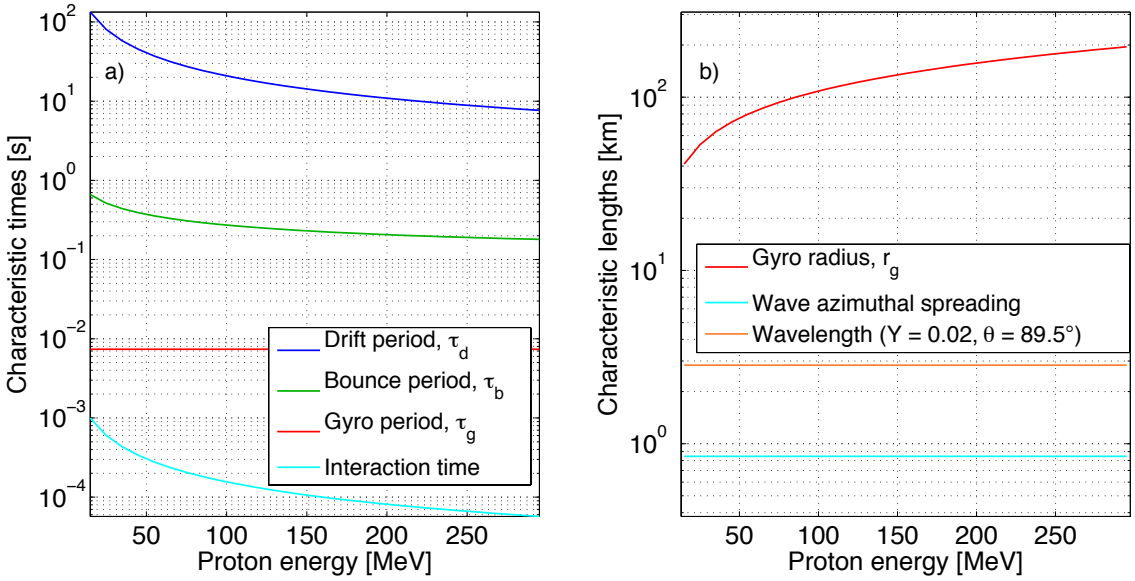


Figure 5-2: (a) Characteristic periods as a function of particle's energy together with the one-pass interaction time between these protons and man-made EMIC waves. (b) Proton gyroradius as a function of particle's energy together with the EMIC azimuthal spreading. The figure is for loss cone inner belt protons at the equator at $L = 1.5$.

region illuminated by the waves. The figure is for 20 MeV protons and an illuminated region of 845 m. In the figure we can observe that the particle goes through the illuminated region many times, back and forth during its gyro-motion, which is superimposed to the drift motion. It can be easily shown that the total interaction time per drift orbit is of the order of the illuminated ~~area~~ over the drift velocity, which agrees with our approximation. In other words, the projection along the longitudinal direction of every of the gyro-passes in Figure 5-3 is of the same order as the drift motion of the particle through the illuminated area. This approximation assumes, however, that the multiple short passes per drift orbit are equivalent to a single longer pass, which should be reconsidered in future research efforts.

The nature of the interaction described above casts doubt upon the validity of the gyroaveraged equations of motion in (2.72)-(2.74) for our particular application. The gyroaveraged solution reproduces the cumulative resonant interaction but averages out (to zero) the non-resonant effect during many gyro-cycles. This off-resonant scattering is therefore not captured by the gyroaveraged equations, but could be important for interactions shorter than a gyroperiod. The gyroaveraged description, however, is widely used for wave-particle interactions in the magnetosphere between naturally generated waves and electrons [*Inan*

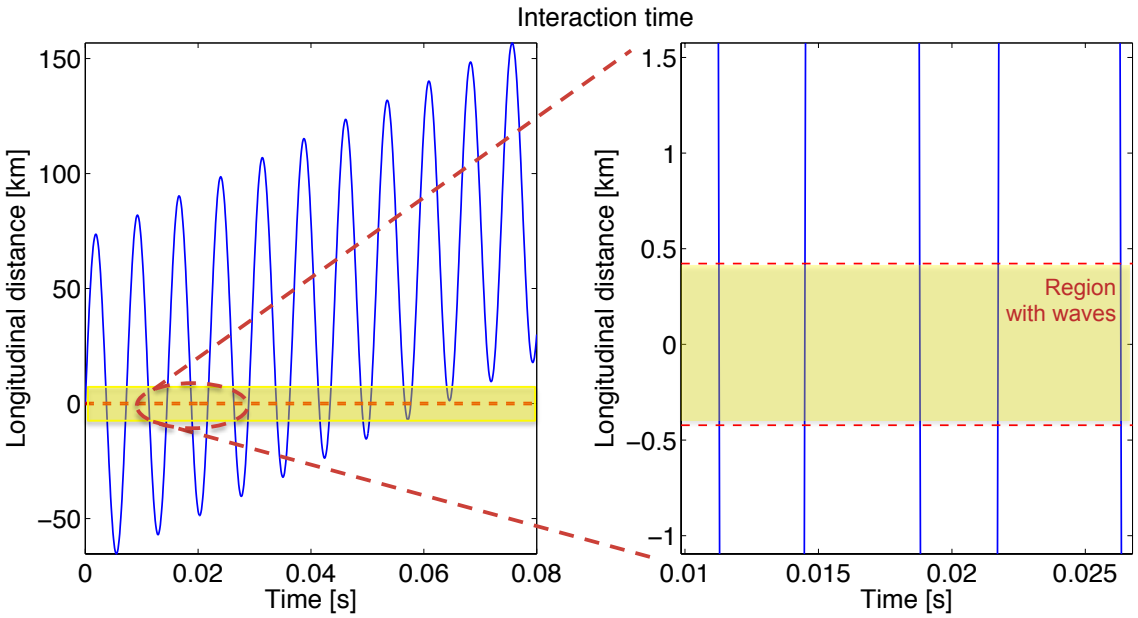


Figure 5-3: Illustration of the nature of the interaction time

*et al.*, 1978; *Albert and Bortnik*, 2009; *Tao and Bortnik*, 2010], but it has never been addressed for the case of inner belt protons interacting with EMIC waves. For these reasons, in this chapter we analyze both the solution of the non-gyroaveraged as well as the gyroaveraged equations of motion, the latter also of interest to the scientific community since it could be important for future applications.

A last point to note is the relative importance of the electric versus the magnetic wave forces. From the Faraday's law we can write that

$$\nabla \times \vec{E^w} = \frac{\partial \vec{B^w}}{\partial t} \quad \rightarrow \quad \vec{k} \times \hat{\vec{E^w}} = \omega \hat{\vec{B^w}} \quad \rightarrow \quad k\hat{E^w} \approx \omega \hat{B^w} \tag{5.1}$$

The wave number vector can be expressed as follows

$$k = \frac{\omega}{c_\phi} \tag{5.2}$$

where $c_\phi$ is the wave phase velocity. The wave electric field is then

$$\hat{E^w} = \hat{B^w} c_\phi \tag{5.3}$$

The magnetic and electric forces scale as follows

$$F_E = qE^w, \qquad F_M \approx q\left\{v_z,\, v_\perp\right\} B^w \tag{5.4}$$

and their ratio is then

$$\frac{F_E}{F_M} \approx \frac{c_\phi}{\left\{v_z,\, v_\perp\right\}} \lll 1 \tag{5.5}$$

which is much smaller than one because the protons under consideration are relativistic, i.e. their velocity is much larger than the phase velocity of the wave. The scaling above shows that the magnetic force dominates, which is not capable of changing the energy of the particles but can definitely change their momentum, thus causing pitch angle scattering and precipitation.

## 5.3 Description of the Simulation

Ray tracing, wave damping and power divergence results together with the proton distribution function previously described are inputs to the wave-particle interaction simulations.

Space-based transmitters radiate at very oblique wave normal angles with respect to the Earth's magnetic field direction (Section 3.4). The phase velocity of radiated EMIC waves is mostly perpendicular, along the direction of the resonance cone, while the group velocity typically stays aligned with the external magnetic field direction. For this reason, a single ray is used for wave-particle interaction calculations, with initial wave normal angle close to perpendicular to the geomagnetic field, and evolution and wave spreading given by the ray tracer and power flux divergence results.

No bouncing of the waves is considered. The wave normal angle equals $\theta = 90^\circ$ at the bouncing point, the parallel group velocity is zero and the wave could be reflected, which is analogous to the reflection of whisters at the lower hybrid frequency [*Thorne and Kennel*, 1967]. There is no observational evidence, however, showing that EMIC waves are capable of bouncing back from high latitudes [*Loto'aniu et al.*, 2005]. For this reason, our calculations are based on single wave-pass interactions. The bouncing of EMIC waves at lower $L$-shells,

however, would certainly improve the results of this thesis, and should be carefully addressed in future studies. Moreover, a scientific mission could also help to answer this unresolved issue.

We use two main approaches to address different aspects of the interaction:

- **Test particle simulation of the non-linear equations of motion:** used to characterize single particle behavior for the gyroaveraged and non-gyroaveraged cases, as well as to determine initial precipitation fluxes at the edge of the loss cone that could be detected by a scientific spacecraft. This formulation is also used to estimate pitch angle diffusion coefficients of energetic inner belt protons interacting with oblique EMIC waves. Test particle simulations, however, are very computationally intensive and cannot provide the time evolution of the distribution or the particles' lifetime.

- **Diffusion simulation:** diffusion coefficients estimated from test particle simulations are used to solve the pitch angle diffusion (Fokker-Planck) equation. This approach is CPU-efficient and it is applied to calculate the time evolution of distribution function of energetic protons as well as the particles' lifetime as a function of pitch angle.

We next proceed to describe each of these simulations as well as their outcomes.

### 5.3.1 Test Particle Simulation of the Non-linear Equations of Motion

Test particle simulations are used to analyze the effect of an EMIC space-based transmitter on individual energetic test protons. Both gyroaveraged (equations (2.72)-(2.74)) and non-gyroaveraged (equations (2.50)-(2.57)) cases are studied and discussed.

Test particle simulations are very computationally intensive. For this reason, they only consider protons close to their loss cone and are based on single pass encounters between waves and particles. This set-up allows to compute initial precipitating fluxes at the edge of the loss cone, which may be detected by a particle instrument onboard a scientific mission. In order to calculate initial precipitating fluxes of energetic protons we solve the equations of motion for each test particle in the AP-9 proton distribution given by $f(v_{\parallel eq}, \alpha_{eq})$ [protons/(m$^3$(m/s)$^3$)], where the subscript $eq$ refers to their equatorial value and will be

dropped from now on. At any other latitude, the pitch angle and parallel velocity of the particle can be adiabatically referred to their equatorial values as follows

$$\sin\alpha_{eq} = \sqrt{\frac{B_{0eq}}{B_0(\lambda)}}\sin\alpha(\lambda) \tag{5.6}$$

$$v_{\parallel eq} = \sqrt{\frac{B_{0eq}}{B_0(\lambda)}}\frac{\tan\alpha(\lambda)}{\tan\alpha_{eq}}v_{\parallel}(\lambda) \tag{5.7}$$

An initial coarse uniform mesh of 96 wave-particle (Larmor) phases × 150 parallel velocities × 500 pitch angles between 15-300 MeV and ~~0.5°~~ around the drift loss cone is used to solve the non-linear equations of motion. The distribution function is next discretized to be able to capture the smaller change in pitch angle and parallel velocity given by the coarse mesh. The coarse mesh is used to interpolate the points of the distribution, which is updated by weighting the neighboring cells that surround the final location of the scattered particles. As an example, Figure 5-4 represents a particle that has been scattered from its initial location $(v_{\parallel 0}, \alpha_0)$ to a lower pitch angle and parallel velocity $(v_{\parallel f}, \alpha_f)$. The updated distribution in this case would be

$$\begin{aligned}
f_{new}(v_{\parallel 0},\alpha_0) &= f_{old}(v_{\parallel 0},\alpha_0) - \frac{1}{12}f_{old}(v_{\parallel 0},\alpha_0)\\
f_{new}(v_{\parallel j},\alpha_j) &= f_{old}(v_{\parallel j},\alpha_j) + \frac{w_0}{12}f_{old}(v_{\parallel 0},\alpha_0)\frac{v_{\parallel 0}^2\frac{\sin\alpha_0}{\cos^3\alpha_0}}{v_{\parallel f}^2\frac{\sin\alpha_f}{\cos^3\alpha_f}}\\
f_{new}(v_{\parallel j-1},\alpha_j) &= f_{old}(v_{\parallel j-1},\alpha_j) + \frac{w_{left}}{12}f_{old}(v_{\parallel 0},\alpha_0)\frac{v_{\parallel 0}^2\frac{\sin\alpha_0}{\cos^3\alpha_0}}{v_{\parallel f}^2\frac{\sin\alpha_f}{\cos^3\alpha_f}}\\
f_{new}(v_{\parallel j},\alpha_{j-1}) &= f_{old}(v_{\parallel j},\alpha_{j-1}) + \frac{w_{down}}{12}f_{old}(v_{\parallel 0},\alpha_0)\frac{v_{\parallel 0}^2\frac{\sin\alpha_0}{\cos^3\alpha_0}}{v_{\parallel f}^2\frac{\sin\alpha_f}{\cos^3\alpha_f}}\\
f_{new}(v_{\parallel j-1},\alpha_{j-1}) &= f_{old}(v_{\parallel j-1},\alpha_{j-1}) + \frac{w_{diag}}{12}f_{old}(v_{\parallel 0},\alpha_0)\frac{v_{\parallel 0}^2\frac{\sin\alpha_0}{\cos^3\alpha_0}}{v_{\parallel f}^2\frac{\sin\alpha_f}{\cos^3\alpha_f}}
\end{aligned} \tag{5.8}$$

where $(v_{\parallel j}, \alpha_j)$ is the closest mesh point to $(v_{\parallel f}, \alpha_f)$ and $w_0$, $w_{left}$, $w_{down}$ and $w_{diag}$ are the weights of the neighboring cells represented in Figure 5-4. Note that $w_0 + w_{left} + w_{down} + w_{diag} = 1$. The updated distribution function conserves the total number density

of particles [*Inan et al.*, 1978].

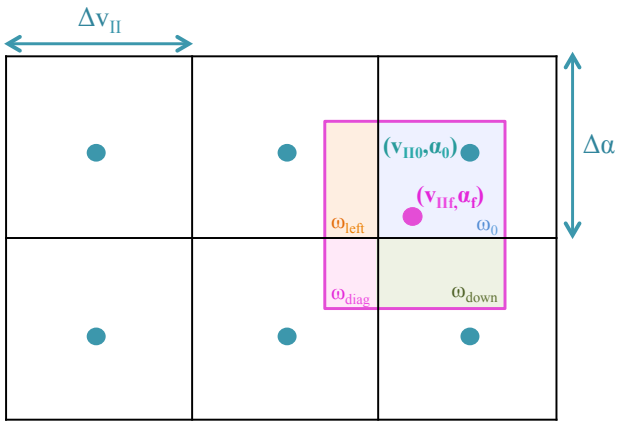


Figure 5-4: Schematics of the calculation of the perturbed distribution function

We usually don't refer to the distribution function but to the differential energy spectrum, $\Phi_{E_{diff}}(v_\parallel, \alpha)$ [protons/(m$^2$ s J ster)] [*Chang*, 1983]. The quantity $\Phi_{E_{diff}}(v_\parallel, \alpha)\, dA\, d\Omega\, dE\, dt$ is the number of particles with energy $dE$ that in a time $dt$ traverse a solid angle $d\Omega$ around the normal to the area $dA$. From conservation of particles it is possible to find a relationship between $\Phi_{E_{diff}}$ and the distribution function $f(v_\parallel, \alpha)$

$$\Phi_{E_{diff}}(v_\parallel, \alpha)\, dA\, d\Omega\, dE\, dt = f(v_\parallel, \alpha)\, v^2\, dv\, d\Omega\, v dt\, dA \tag{5.9}$$

The volume element $v^2\, dv\, d\Omega$ in velocity space represents the particles with motion along the solid angle $d\Omega$ and energy $dE$, while the element $v\, dt\, dA$ is the volume in space that these particles go through. The relationship between $dE$ and $dv$ can be easily found as follows

$$dE = d\left[mc^2\left(\frac{1}{\sqrt{1 - v^2/c^2}} - 1\right)\right] = mc^2\gamma^3\frac{v\, dv}{c^2} \tag{5.10}$$

Substituting into equation (5.9) we find that

$$\Phi_{E_{diff}}(v_\parallel, \alpha) = f(v_\parallel, \alpha)\frac{v_\parallel^2}{\cos^2\alpha}\frac{1}{m_H}\left(\sqrt{1 - \frac{v_\parallel^2}{c^2\cos^2\alpha}}\right)^3 \tag{5.11}$$

The initial precipitated differential energy spectrum at the equator, $\Phi_{E_{prec}}$ [protons/(m$^2$ s J)], can be found by integrating over all pitch angles inside the loss cone

$$\Phi_{E_{prec}}(E) = 2\pi \int_{\alpha=0}^{\alpha_{lc}} \Phi_{E_{diff}}(v_{\parallel}, \alpha) \cos\alpha \, \sin\alpha \, d\alpha \tag{5.12}$$

and the initial precipitated energy flux, $Q$ [J/(m$^2$ s)], can then be calculated as follows

$$Q = \int_{E} E \, \Phi_{E_{prec}}(E) \, dE = 2\pi \int_{v_{\parallel}} \int_{\alpha=0}^{\alpha_{lc}} E f(v_{\parallel}, \alpha) \, v_{\parallel}^3 \, \frac{\sin\alpha}{\cos^3\alpha} d\alpha \, dv_{\parallel} \tag{5.13}$$

### 5.3.2 Diffusion Simulation

Test particle simulations also allow us to estimate diffusion coefficients at all pitch angles, which can be used to efficiently solve the pitch angle diffusion equation for the time evolution of the entire proton distribution. Due to the nature of the interaction, protons will encounter the wave beam ~~once per drift orbit~~. The diffusion coefficient averaged in Magnetic Local Time (MLT) can then be estimated from test particles as follows

$$\langle D_{\alpha\alpha}(E, \alpha) \rangle = \frac{<\Delta\alpha^2>}{2 \, \tau_d(E, \alpha)} \tag{5.14}$$

where $\tau_d$ is the drift period given in equation (1.10), $\Delta\alpha^2$ is an average value of all possible short interactions that can take place at different latitudes per drift orbit, and the brackets denote the average over initial Larmor phase. It must be noted that we do not use quasi-linear theory [*Kennel and Engelmann*, 1966] to find pitch angle diffusion coefficients because is not capable of capturing non-resonant interactions, which will dominate the scattering during realistic non-gyroaveraged short encounters. For code validation purposes, however, Section 5.4.3 will explore the quasi-linear solution and compare it to bounce-averaged diffusion coefficients estimated from gyroaveraged test particle simulations.

The MLT-averaged diffusion coefficients described above are next used to solve the pitch angle diffusion equation. Ignoring energy and radial diffusion, the Fokker-Planck equation for a fixed $L$-shell and energy may be written to represent the 1D pitch angle diffusion of

the proton distribution, $f$ [*Schulz and Lanzerotti*, 1974; *Subbotin and Shprits*, 2009]

$$\frac{\partial f}{\partial t} = \frac{1}{T(\alpha)\sin(2\alpha)} \left.\frac{\partial}{\partial \alpha}\right|_{p,L} T(\alpha)\sin(2\alpha)\langle D_{\alpha\alpha}\rangle \left.\frac{\partial f}{\partial \alpha}\right|_{p,L} \tag{5.15}$$

where $\langle D_{\alpha\alpha}\rangle$ are the MLT-averaged diffusion coefficients calculated from test particles. $T(\alpha)$ is a function of the bounce period, and in a dipole magnetic field it can be expressed as follows

$$T(\alpha) = \int_0^{\lambda_m} \frac{\cos\lambda\sqrt{1+3\sin^2\lambda}}{\left[1-\frac{\sin^2\alpha_{eq}}{\cos^6\lambda}\sqrt{1+3\sin^2\lambda}\right]^{1/2}} d\lambda \tag{5.16}$$

where $\lambda_m$ is the magnetic latitude of the mirror point. *Lenchek et al.* [1961] provided a good estimation to $T(\alpha)$, given by

$$T(\alpha) = 1.3802 - 0.3198\left(\sin\alpha + \sqrt{\sin\alpha}\right) \tag{5.17}$$

The Fokker Plank equation above is solved using the 1D-VERB code described by *Subbotin and Shprits* [2009], with boundary conditions $f(\alpha = 0°) = 0$ and $\partial f/\partial\alpha(\alpha = 90°) = 0$.

The exponential decay time of the distribution, $\tau$, at each time step as a function of equatorial pitch angle can be calculated as follows [*Shprits et al.*, 2006a]

$$\tau(\alpha) = \frac{\left[f^{n+1}(\alpha) + f^n(\alpha)\right] * dt}{2\left[f^n(\alpha) - f^{n+1}(\alpha)\right]} \tag{5.18}$$

where $dt$ is the time step and $n$ refers to the iteration index. In our calculations, we consider that the equilibrium distribution is reached when the following condition is satisfied

$$\frac{\max(\tau(\alpha)) - \min(\tau(\alpha))}{\langle\tau(\alpha)\rangle} < 0.1 \tag{5.19}$$

which provides an estimation of the *lifetime* of the distribution, $\tau_L$. This is the value of $\tau$ after which the entire distribution decays at the same rate, which corresponds to the first eigenmode. The higher modes represent the faster decay of the $\alpha$-gradients, especially if

the initial condition is discontinuous ($f = 0$ for $\alpha < \alpha_{lc}$).

## 5.4 Gyroaveraged Test Particle Simulations

This section analyzes the solution of the gyroaveraged equations of motion in (2.72)-(2.74). However, we must emphasize again ~~than~~ the interactions between man-made EMIC waves and energetic inner belt protons are far from gyroaveraged. This section is included here because it is of interest to the scientific community since it could be important for future applications. Nevertheless, the reader can skip to Section 5.5 if he is only interested in the interaction between man-made EMIC waves and energetic inner belt protons.

If you decided to stay, we next analyze the effect of oblique EMIC waves on a sheet of energetic test protons with the same energy and pitch angle but uniformly distributed in Larmor phase. The particles are started at their turning point in the southern hemisphere while the waves are taken to travel in the opposite direction. In the following, we solve the gyroaveraged equations of motion in (2.72)-(2.74) to characterize the single-pass continuous interaction between EMIC waves and inner belt protons along half of their bouncing period. The gyroaveraged expressions are valid when the particle's gyroperiod is short compared to the time scale for wave-particle interactions. Firstly, we analyze the gyroaveraged resonance condition and scattering trajectories of energetic protons due to their interaction with these hypothetical waves, which are assumed to cover a broad region in Magnetic Local Time (MLT) in the inner belt (thus allowing phase trapping of the rapidly drifting protons) with a representative wave normal angle of $\theta = 87°$. Secondly, we assume field-aligned waves ($\theta = 0°$) to analyze the comparison between gyroaveraged test particle and quasi-linear diffusion simulations.

### 5.4.1 Driving Frequency based on Cyclotron Resonance Considerations

The resonance condition in equation (2.33) determines the parallel velocity of the particles that are capable of resonating with the wave as a function of latitude of interaction and wave frequency. The solution to the resonance condition is presented in Figure 5-5 (a) and (b), which shows equatorial proton energies for resonant interaction with the oblique EMIC waves described above as a function of latitude and driving frequency, and for two different

$L$-shells in the inner belt. Only the solution for the 1st-harmonic ($l = 1$) is represented. For inner belt conditions, we observe that interaction between EMIC waves and <300 MeV protons can only be achieved within the oxygen band (below the oxygen gyrofrequency). These very low EMIC frequencies are always below the $O^+$ cyclotron frequency, which ensures propagation through the interaction region (Figure 2-1). At $L = 1.2$, a 14 Hz (Y = 0.05) wave would then be capable of scattering the hazardous range of proton energies. At $L = 1.5$, the frequency would be approximately 3 Hz (Y = 0.02), or 1 Hz (Y = 0.015) at $L = 2$.

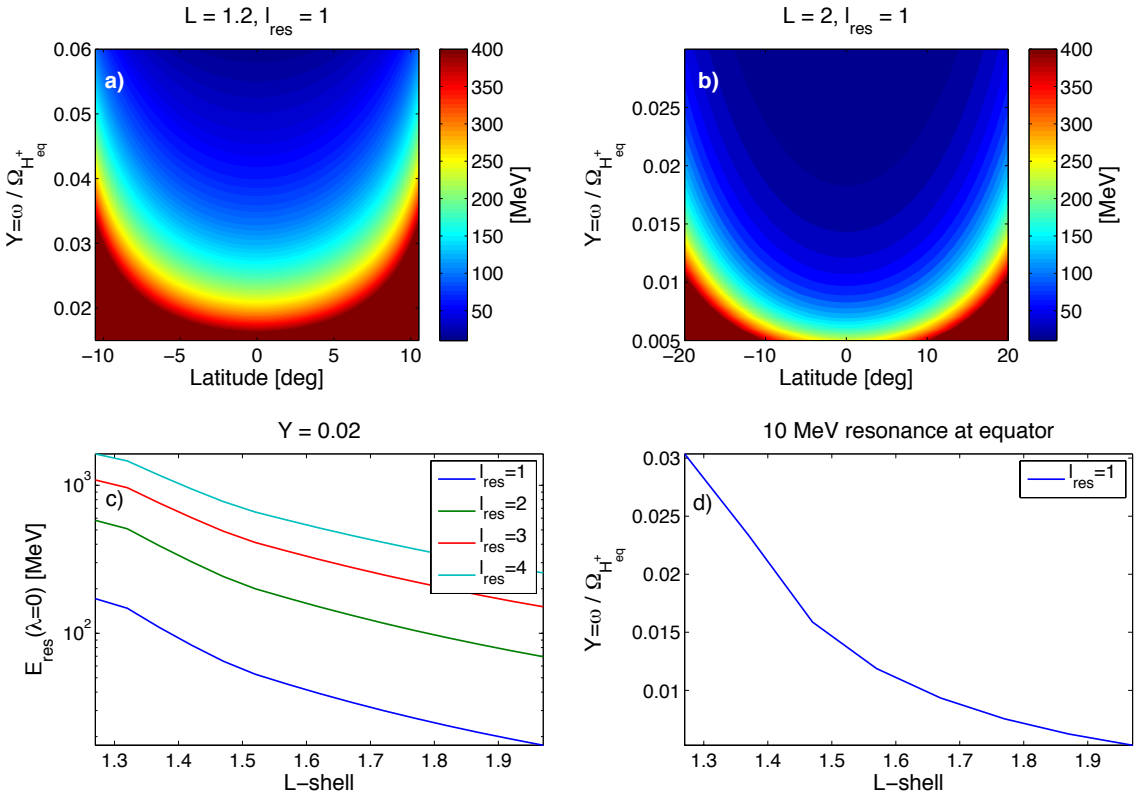


Figure 5-5: (a) Resonant energies referred to the equator as a function of latitude of interaction and normalized frequency, $Y = \omega/\Omega_{H^+}$, at $L = 1.2$; the wave normal angle equals $\theta = 87°$ and only the 1st-harmonic is considered. (b) Same as (a) but at $L = 2$. (c) Energies for equatorial resonant interaction as a function of $L$-shell for the first four harmonic numbers. (d) Non-dimensional frequency as a function of $L$-shell for 1st harmonic equatorial interaction with 10 MeV protons.

The equator is the preferred resonance location because the Earth's magnetic field gradients are smaller there, which leads to stronger and more efficient wave-particle interactions. For this reason, it is important to carefully analyze and consider all the contributing processes

around the equator. The effect of higher resonant harmonics is definitely one of these processes, which produces equatorial scattering of higher energy particles compared to the 1st-harmonic. Figure 5-5 (c) presents the resonant energy for interaction at the equator for the first four harmonics as a function of the $L$-shell for Y = 0.02. The equatorial resonant energy monotonically decreases with increasing $L$-shell for a given harmonic number, and higher harmonics lead to higher equatorial resonant energies at a specific location. At $L$ = 1.5, the 1st-harmonic most efficiently scatters 17 MeV particles at the equator, while this energy is 67 MeV for the second resonant harmonic, and 145 MeV for the 3rd-harmonic. Figure 5-5 (d) shows the non-dimensional frequency as a function of $L$-shell for equatorial resonant interaction (1st harmonic) with 10 MeV protons; higher order harmonics will equatorially scatter higher proton energies.

### 5.4.2 Gyroaveraged Test Particle Trajectories: Sensitivity Analyses

The protons' gyroaveraged response is characterized next by studying the sensitivity of the scattering to the different wave and particle parameters.

#### Scattering Trajectories

Protons' scattering dependence on latitude and initial Larmor phase, $\phi_0$, is presented in Figure 5-6, which corresponds to a power flux of 1 $\mu$W/m$^2$ at $L$ = 1.5. Figure 5-6 (a)-(c) shows the 1st-harmonic resonant interaction between equatorially resonant loss cone protons ($\alpha_{lc}$ = 40.54°, $E_{eq}$ = 17 MeV) and oblique EMIC waves ($\theta$ = 87°, Y = 0.02); the color code represents a uniform distribution in Larmor phase. The maximum scattering is $\Delta\alpha_{max} \approx 0.004°$ and the corresponding change in parallel velocity is $\Delta v_{\parallel max} \approx 2 \cdot 10^5$ m/s. The oscillations observed away from the equator are generated by the particle's off-resonant interaction with the wave fields. These oscillations are not seen during the resonant interaction because the wave-particle phase, $\eta$ (equation (2.72)), remains locked for a significant amount of time. The observed scattering as well as the initial Larmor phase dependence represented in Figure 5-6 (c) characterize linear interaction processes because $p_z$ is close to unperturbed by the wave and the pitch angle varies sinusoidally with varying initial Larmor phase. Similarly, Figure 5-6 (d)-(f) shows the 1st-harmonic resonant interaction of off-equatorially resonant particles ($E_{eq}$ = 145 MeV). This off-equatorial resonance results

in smaller scattering compared to interaction with 17 MeV particles at $\lambda = 0$. For the 3rd-harmonic (Figure 5-6 (g)-(i)), however, 145 MeV interaction happens at the equator and leads to stronger scattering compared to the off-equatorial effect of the 1st-harmonic. In addition, we observe that the scattering is strongly dependent on initial Larmor phase, which was also the case for whistlers interacting with electrons [*Inan et al.*, 1978].

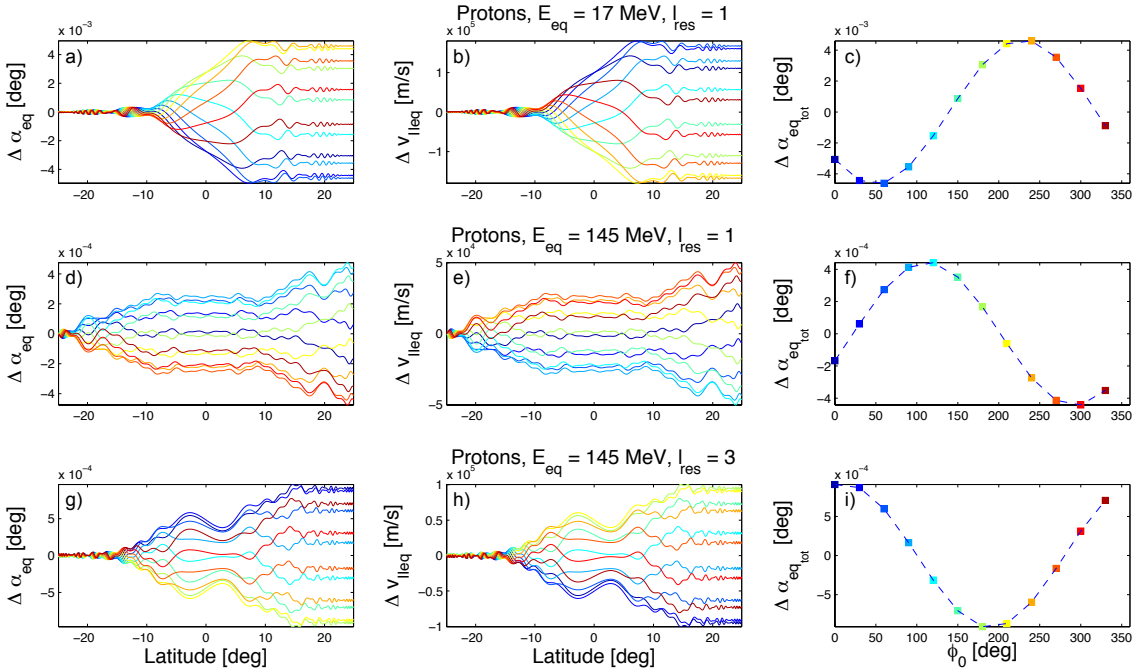


Figure 5-6: (a) Scattering of 1st-harmonic equatorially resonant protons ($E_{eq}$ = 17 MeV) as a function of latitude. (b) Change in $v_{\parallel}$ of 1st-harmonic equatorially resonant protons ($E_{eq}$ = 17 MeV) as a function of latitude. (c) Total scattering of 1st-harmonic equatorially resonant protons ($E_{eq}$ = 17 MeV) as a function of initial Larmor phase. (d) Scattering of 1st-harmonic off-equatorially resonant protons ($E_{eq}$ = 145 MeV) as a function of latitude. (e) Change in $v_{\parallel}$ of 1st-harmonic off-equatorially resonant protons ($E_{eq}$ = 145 MeV) as a function of latitude. (f) Total scattering of 1st-harmonic off-equatorially resonant protons ($E_{eq}$ = 145 MeV) as a function of initial Larmor phase. (g) Scattering of 3rd-harmonic equatorially resonant protons ($E_{eq}$ = 145 MeV) as a function of latitude. (h) Change in $v_{\parallel}$ of 3rd-harmonic equatorially resonant protons ($E_{eq}$ = 145 MeV) as a function of latitude. (i) Total scattering of 3rd-harmonic equatorially resonant protons ($E_{eq}$ = 145 MeV) as a function of initial Larmor phase.

Protons' scattering is linear for all the cases considered; particles perform a random walk in velocity space in a similar way to diffusion processes. For this reason, we may estimate bounce-averaged diffusion coefficients from our test particle solution, which can be approximated as $\langle D_{\alpha\alpha} \rangle = <\Delta\alpha^2>/2\tau_b$, where $\Delta\alpha$ is calculated between mirror points, $\tau_b$ is given in equation (5.16) and the brackets denote the average over initial Larmor phase.

Using this expression, the diffusion coefficients corresponding to the three cases analyzed above are $\langle D_{\alpha\alpha} \rangle = 0.821$ deg$^2$/day for 1st-harmonic equatorial resonance (Figure 5-6 (a)), $\langle D_{\alpha\alpha} \rangle = 0.008$ deg$^2$/day for 1st-harmonic off-equatorial resonance (Figure 5-6 (d)) and $\langle D_{\alpha\alpha} \rangle = 0.083$ deg$^2$/day for 3rd-harmonic equatorial resonance (Figure 5-6 (g)).

A brief comparison of the EMIC effect on protons and electrons seems mandatory at this point. Figure 5-7 shows the equatorial resonant interaction between loss cone electrons ($E_{eq}$ = 1.75 MeV) and oblique L-mode EMIC waves ($\theta = 87°$, Y = 0.85) at $L = 1.5$. Figure 5-7 (a)-(c) corresponds to a power flux of 1 $\mu$W/m$^2$, while Figure 5-7 (d)-(f) is for 0.1 mW/m$^2$. For a given wave field, electron's scattering is much larger than protons' scattering, which is basically due to their different masses. What is more, the interaction with electrons is strongly non-linear for power levels of >1 $\mu$W/m$^2$. Energetic protons are harder to scatter than relativistic electrons because for a given wave, the change in momentum is inversely proportional to the mass of the particle. In contrast to electrons, however, trapped protons have residence times up to several thousand years (Section 5.7).

It must be noted that interaction between EMIC waves and energetic inner belt protons significantly changes the particles' momentum but does not modify their energy. From the reference frame of the wave there is no electric field and the energy is conserved, i.e. $(v_{\parallel} - c_{\phi})^2 + v_{\perp}^2 = C$, where $c_{\phi}$ is the wave phase velocity. If $c_{\phi}$ is much smaller than the particle's parallel energy then $v_{\parallel}^2 + v_{\perp}^2 \approx C$ and the particle's energy is conserved. Acceleration/deceleration is only possible when the wave phase speed is comparable to the parallel velocity of the particle. In the case under consideration, particles are relativistic and their parallel velocity is always larger than the wave phase velocity, thus the interaction conserves energy. This explanation also relates to the lack of thermal effects detailed in Section 3.4.7.

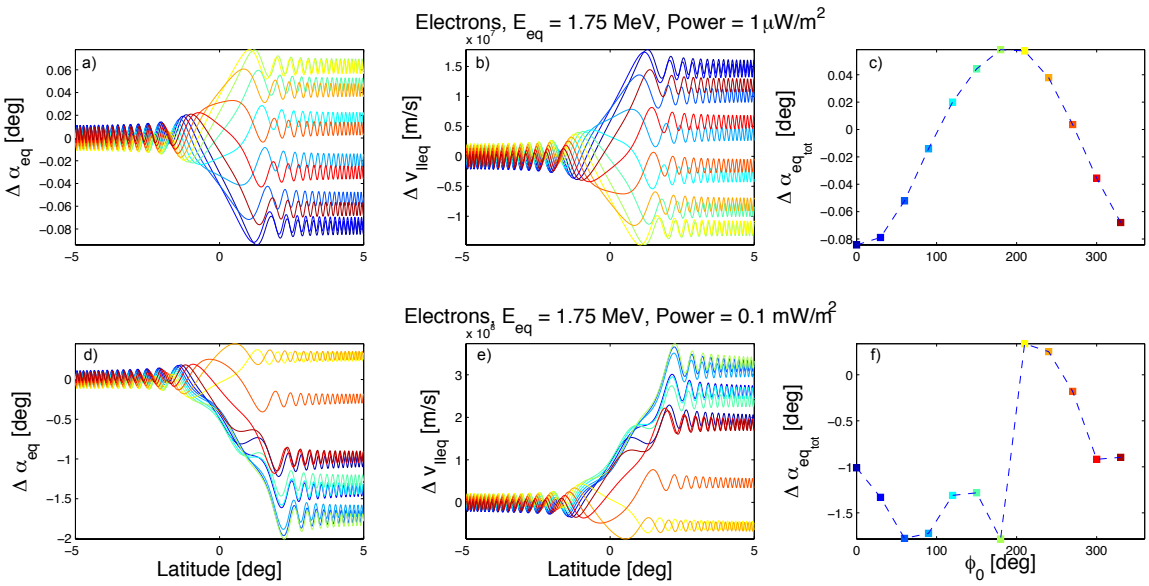


Figure 5-7: (a) Scattering of 1st-harmonic equatorially resonant electrons ($E_{eq} = 1.75$ MeV) for a power flux of 1 $\mu$W/m$^2$ as a function of latitude. (b) Change in $v_{||}$ of 1st-harmonic equatorially resonant electrons for a power flux of 1 $\mu$W/m$^2$ as a function of latitude. (c) Total scattering of 1st-harmonic equatorially resonant electrons for a power flux of 1 $\mu$W/m$^2$ as a function of initial Larmor phase. (d) Scattering of 1st-harmonic equatorially resonant electrons for a power flux of 0.1 mW/m$^2$ as a function of latitude. (e) Change in $v_{||}$ of 1st-harmonic equatorially resonant electrons for a power flux of 0.1 mW/m$^2$ as a function of latitude. (f) Total scattering of 1st-harmonic equatorially resonant electrons for a power flux of 0.1 mW/m$^2$ as a function of initial Larmor phase.

### Sensitivity to $B^w$

The effect of the wave field amplitude of a 3 Hz (Y = 0.02) wave on individual test particles at $L = 1.5$ is analyzed next. The wave normal angle is assumed constant ($\theta = 87°$), and only drift loss cone particles are considered. Figure 5-8 presents the RMS scattering of equatorially resonant protons versus the magnitude of the radiated wave field. These results have been calculated by integrating equations (2.72)-(2.74). The figure shows that protons' scattering scales linearly with the wave field amplitude for all the harmonics.

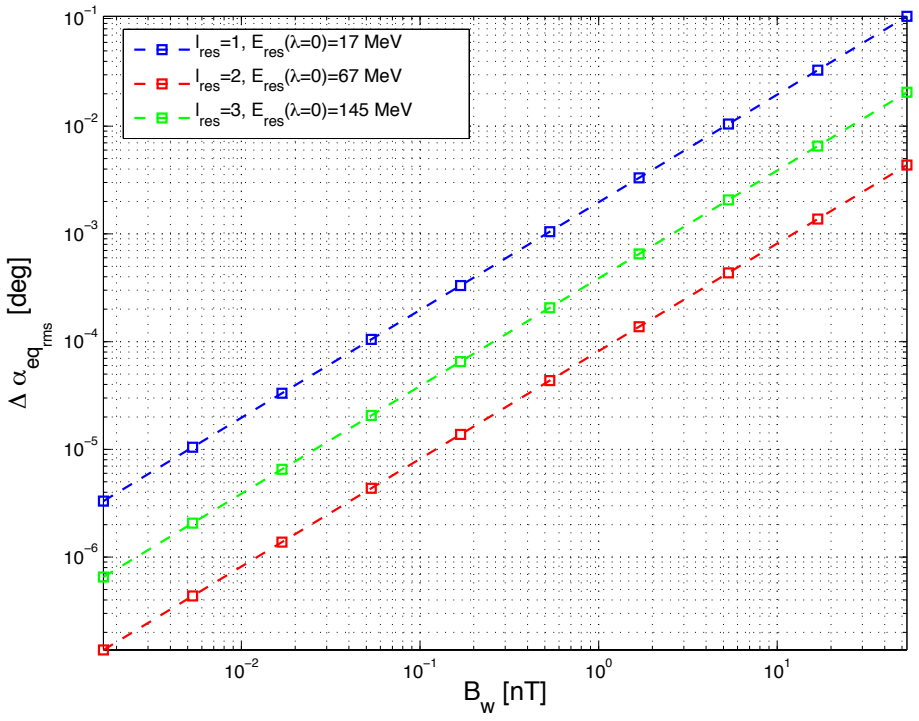


Figure 5-8: RMS scattering as a function of the wave magnetic field for the first three resonant harmonics at $L = 1.5$ and Y = 0.02.

### Dependence on $\alpha_{eq0}$ and $\mathbf{E}_{eq0}$

Figure 5-9 (a) shows the RMS scattering versus the initial equatorial pitch angle at $L = 1.5$ and for a wave with Y = 0.02, $\theta = 87°$ and a power flux of 1 $\mu$W/m$^2$. The plot is for 17 MeV protons, whose equatorial resonance corresponds to a pitch angle of $\alpha_{0eq}$=40.54°. The particle's scattering presents a periodic dependence on initial pitch angle, which is due to the phase coherence between the two resonance points at both sides of the equator. The parallel velocity of the particle decreases with increasing pitch angle. This reduced velocity implies that the total change in wave-particle phase between interaction regions increases with increasing initial pitch angle, which results in addition or subtraction (periodic behavior) of the two resonant effects at both sides of the equator. Figure 5-9 (b) corresponds to the maximum in (a) for $\alpha_{0eq}$=46° where the scattering at the two resonant regions adds up. Contrarily, Figure 5-9 (c) corresponds to the minimum in (a) for $\alpha_{0eq} = 48°$ where the two resonances produce scattering in opposite directions and partially cancel out.

Similarly, the scattering also has a periodic dependence on the particle's energy due to

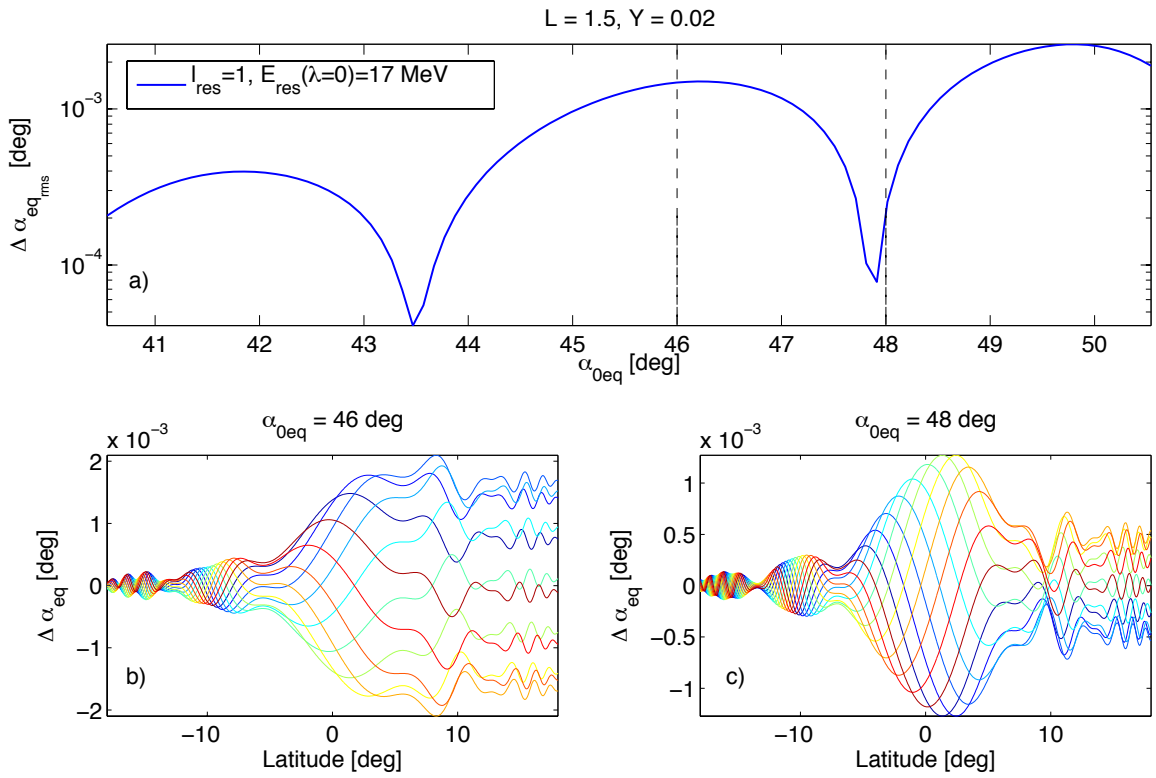


Figure 5-9: (a) RMS scattering due to 1st order resonant interaction with 17 MeV protons versus initial equatorial pitch angle. $L = 1.5$ for a wave with Y = 0.02 and $\theta = 87°$. (b) Scattering as a function of latitude of the particles in (a) corresponding to $\alpha_{0eq}$=46°. (c) Scattering as a function of latitude of the particles in (a) corresponding to $\alpha_{0eq}$=48°.

the phase coherence between the two resonances at each side of the equator. Figure 5-10 presents the RMS scattering of loss cone particles versus energy for the first four harmonics. The figure clearly shows the periodic dependence as well as the importance of higher order harmonics. While first order interaction dominates the lower energy range, higher order harmonics govern the interaction at higher energies.

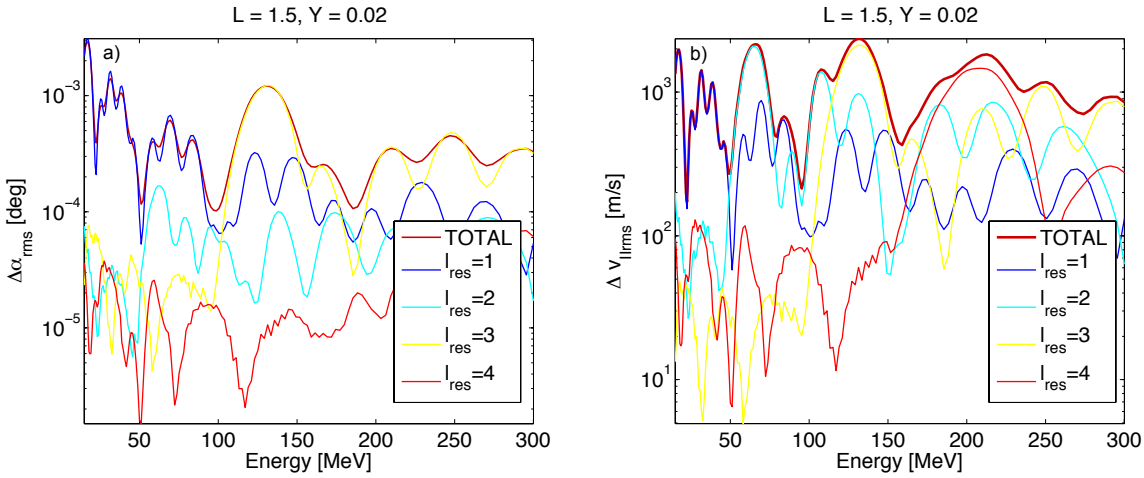


Figure 5-10: (a) RMS scattering of drift loss cone particles as a function of proton's energy. $L = 1.5$ for a wave with Y = 0.02, $\theta = 87°$ and 1 $\mu$W/m$^2$. (b) RMS change in parallel velocity of drift loss cone particles as a function of proton's energy.

### Sensitivity to Wave Normal Angle

In this section we analyze the sensitivity of the proton scattering to the wave normal angle. Field-aligned wave normal vectors are desired in terms of wave-particle interactions because their perpendicular wave fields are stronger, which increases the efficiency of the interaction with particles. The radiation pattern results in Section 3.4, however, revealed that the wave power radiated from space-based transmitters is injected at the EMIC resonance cone, which corresponds to almost perpendicular wave normal vectors. In Section 4.3.2 we also showed that, for non-equatorial spacecraft orbits, the curvature and gradient of the Earth's magnetic field can slightly rotate the wave normal angle towards the geomagnetic field direction as the wave approaches the equator, which is beneficial for wave-particle interactions.

Figure 5-11 shows the contribution of the first five resonant harmonics to the scattering of loss cone protons at $L = 1.5$ as a function of wave normal angle and particle energy. Waves with Y = 0.02 and a power flux of 1 $\mu$W/m$^2$ have been considered. The scattering at $\theta \approx 60°$ is up to three orders of magnitude larger than the scattering at $\theta \approx 90°$. This is the reason why we want off-equatorial orbits, because any magnetospheric guiding significantly improves the efficiency of the interaction. In addition, the plot presents several striations along specific wave normal angles; these structures are characteristic of wave-particle interactions and are due to the Bessel functions in equations (2.73)-(2.74).

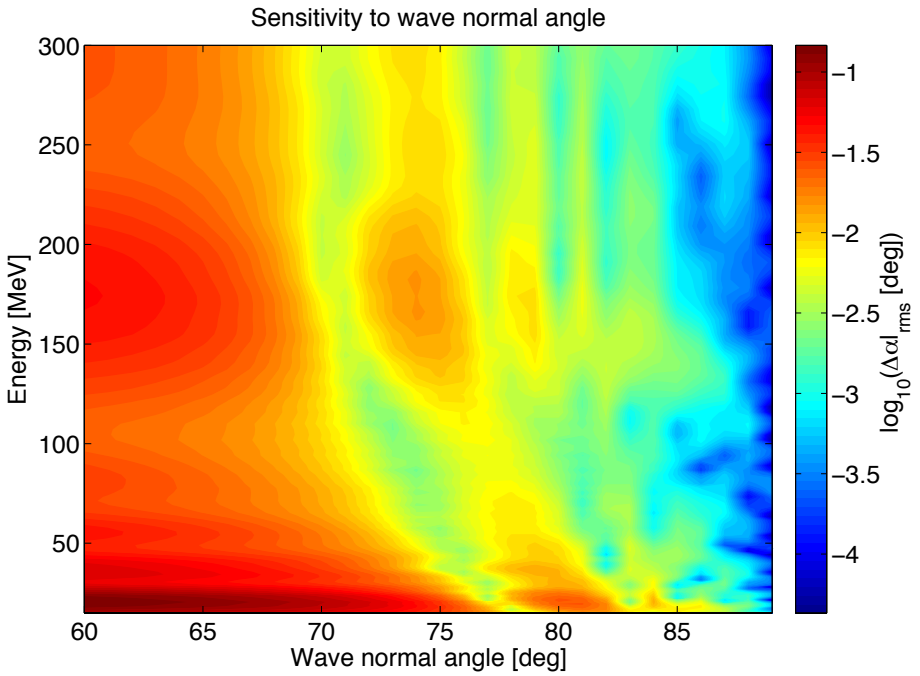


Figure 5-11: Scattering of loss cone protons at $L = 1.5$ as a function of wave normal angle and particle energy for the first five resonant harmonics. A wave with Y = 0.02 and a power flux of 1 $\mu$W/m$^2$ has been considered.

### Sensitivity to Background Ion Composition

Similarly to Section 4.3.5, we next analyze the sensitivity of the interaction to the thermal ion composition. The results above were calculated for quiet time conditions characterized by 90% $H^+$, 8% $He^+$ and 2% $O^+$. In this section we repeat the interaction simulations for a composition characteristic of storm times given by 70% $H^+$, 20% $He^+$ and 10% $O^+$ [*Horwitz*, 1987; *Meredith et al.*, 2003], and we compare the results to those from the nominal situation. Figure 5-12 (a) presents equatorial resonant energies (Y = 0.02) as a function of $L$-shell during storm times (solid lines) and nominal conditions (dashed lines). We observe that, for a fixed frequency, increasing the heavy ion concentration translates into slightly lower resonant energies, or in other words, the frequency required for equatorial interaction with a given particle's energy and pitch angle is reduced compared to the nominal scenario (Figure 5-12 (b)). This fact is due to the change in refractive index previously noticed in Figure 4-10, which modifies the resonance condition.

But do these small changes in the resonance condition really affect the particle's scattering? Figure 5-13 presents the RMS scattering at $L = 1.5$ as a function of particle's energy for

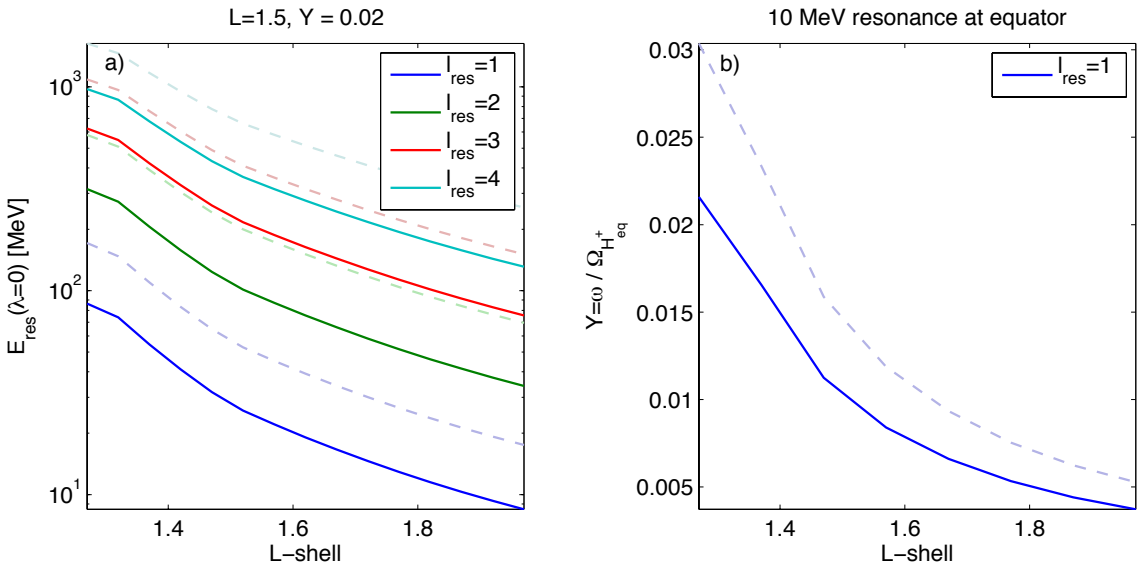


Figure 5-12: (c) Energies for equatorial resonant interaction as a function of $L$-shell for the first four harmonic numbers during storm time (solid lines) and nominal conditions (dashed lines). (d) Non-dimensional frequency as a function of $L$-shell for 1st harmonic equatorial interaction with 10 MeV protons during storm time (solid line) and nominal conditions (dashed line).

storm and nominal conditions calculated with a fixed frequency of Y = 0.02; this frequency was originally stablished as *optimal* for quiet time composition, but we also use it here for storm conditions to check the sensitivity of the scattering to the resonance condition. The first four harmonics have been considered in the calculation. The figure shows that the efficiency of the scattering during storm times is not reduced compared to the nominal scenario, i.e. the efficiency of the interaction is not sensitive to small variations in the resonance condition. This fact could also be inferred from the particle's scattering in Figure 5-6 (a), where it can be observed that the interaction happens along a wide latitude range up to $\pm 10^{\circ}$ around the equator. This width of interaction can be thought of as a width in the resonance condition itself, which is the reason why the pitch angle scattering is not sensitive to small changes in frequency.

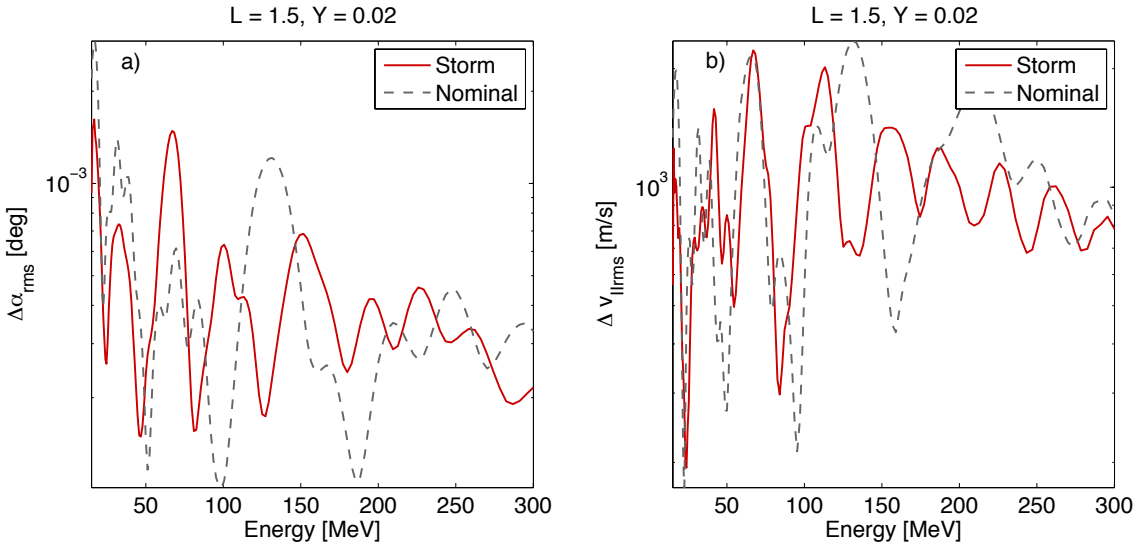


Figure 5-13: (a) Comparison between the total RMS scattering of drift loss cone particles as a function of proton's energy during storm and nominal conditions. $L = 1.5$ for a wave with Y = 0.02, $\theta = 87°$ and 1 $\mu$W/m$^2$. (b) Comparison between the RMS change in parallel velocity of drift loss cone particles as a function of proton's energy during storm and nominal conditions.

### 5.4.3 Comparison between Gyroaveraged Test Particle and Quasi-linear Diffusion Simulations

*The work in this section has been recently published by de Soria-Santacruz et al. [2013b].*

We have shown that the non-linear gyroaveraged formulation results in a random walk in velocity space of the inner belt protons. This fact suggests the utilization of a CPU-efficient model based on a diffusion approach, which is commonly used for broadband incoherent signals. In this section we compute bounce-averaged pitch angle diffusion rates from a test particle simulation and compare them to those of quasi-linear theory. The analysis serves as a validation of the test particle formulation developed in the previous section. The interaction between EMIC waves and energetic protons is calculated at $L = 1.5$. A dipole model is used to represent the magnetic field of the Earth, which is an accurate approximation in the inner belt region. The cold plasma background is assumed to be in diffusive equilibrium with an equatorial electron density of $n_e = 3.05 \cdot 10^4$ cm$^{-3}$ and a composition given by 85% $H^+$, 10% $He^+$ and 5% $O^+$. The waves are considered field-aligned with the Earth's magnetic field ($\vec{k}$ along $\vec{B}_0$), with a mean amplitude of 2 nT and a frequency of 4 Hz, which corresponds to an equatorial proton resonant energy of 3.77 MeV

for loss cone particles.

For field-aligned waves, an inhomogeneity parameter, $R$, is commonly used to characterize the competition between adiabatic and wave-induced motions [*Omura et al.*, 2008; *Albert and Bortnik*, 2009]

$$R = \left| \frac{B_0}{B^w} \frac{n^2}{n^2 - 1} \frac{c}{v_\perp} \frac{1}{k} \left( \gamma \frac{\omega}{\Omega_{H^+}} \frac{v_\parallel^2}{c^2} \frac{\partial n}{\partial s} + \frac{1}{B_0} \frac{\partial B_0}{\partial s} \left( \frac{v_\parallel}{c} - \frac{n\gamma}{2} \frac{\omega}{\Omega_{H^+}} \frac{v_\perp^2}{c^2} \right) \right) \right| \tag{5.20}$$

where $n$ is the refractive index and $s$ is the direction along the field line. The expression is evaluated at the resonance point. $R \gg 1$ means that the interaction behaves linearly, while $R \ll 1$ implies that non-linear effects dominate. Figure 5-14 shows that $R$ is always larger than one, i.e. non-linear effects are negligible and it is then legitimate to estimate bounce-averaged diffusion coefficients from the test particle solution. Furthermore, $R$ would increase even more with increasing wave normal angle because the wave perpendicular fields would be smaller, the interaction weaker.

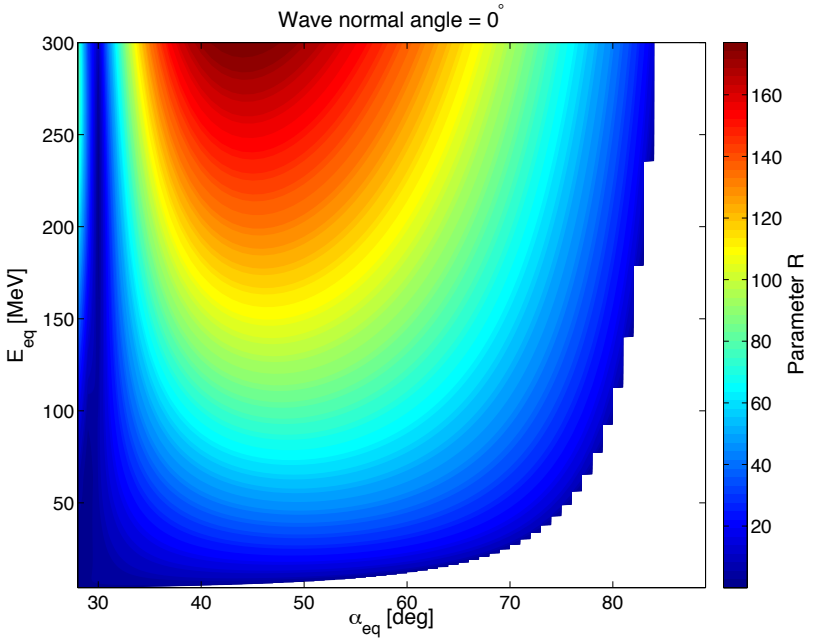


Figure 5-14: Non-dimensional inhomogeneity parameter, $R$, for 2 nT field-aligned waves as a function of particles' energy and equatorial pitch angle

According to these results, we can estimate bounce-averaged diffusion coefficients, $\langle D_{\alpha\alpha} \rangle$, from the test particle simulation as follows [*Inan*, 1987]

$$\langle D_{\alpha\alpha} \rangle = \frac{<\Delta\alpha^2>}{2\tau_{bounce}} \tag{5.21}$$

where $\Delta\alpha^2$ is calculated between mirror points, $\tau_{bounce}$ is the bounce period given in equation (5.16) and the brackets denote the average over initial Larmor phase.

For comparison with quasi-linear theory we use the code of *Shprits et al.* [2006b] that follows the formulation of *Summers* [2005] to estimate local pitch angle diffusion coefficients, $D_{\alpha\alpha}$, reduced by a factor of 2 due to *Albert* [2007]. The bounce averaging is performed using the approach from *Lyons et al.* [1972]. The waves are assumed to have a Gaussian spectral density given by

$$W(\omega) = \frac{(B^w)^2}{8\pi} \frac{1}{\rho} \frac{1}{\delta\omega} exp\left[ -\left( \frac{\omega - \omega_m}{\delta\omega} \right)^2 \right] \tag{5.22}$$

inside the range of frequencies from 1 to 100 rad/s. $\omega_m$ and $\delta\omega$ are the frequency of maximum wave power and bandwidth, respectively. $B^w$ is the wave mean amplitude, and $\rho$ is a normalization factor.

In our test particle simulations we consider monochromatic waves. Comparison with quasi-linear bounce-averaged diffusion coefficients, therefore, requires a narrow $\delta\omega$ of the Gaussian wave frequency distribution in equation (5.22). Figure 5-15 presents a sensitivity analysis of the quasi-linear $\langle D_{\alpha\alpha} \rangle$ on bandwidth, $\delta\omega$, where $\delta\omega = \text{Coefficient} \cdot \omega_m$. Diffusion coefficients are calculated for three different energies, $E = 4$, 50, and 200 MeV. It can be observed that the quasi-linear $\langle D_{\alpha\alpha} \rangle$ is independent of bandwidth for Coefficient $\leq 10^{-2}$. Quasi-linear scattering rates, therefore, will not be sensitive to this parameter for narrow distributions like the ones approaching the monochromatic case.

The comparison of bounce-averaged diffusion coefficients calculated using both gyroaveraged test particle and diffusion approaches is finally presented in Figure 5-16. The Gaussian wave frequency distribution used in quasi-linear theory is taken to be narrow with $\omega_m = 8\pi$ rad/s (= 4 Hz) and $\delta\omega = 0.01 \cdot \omega_m$. Figure 5-16 (a) presents $\langle D_{\alpha\alpha} \rangle$ of loss cone protons as a function of energy, where it can be observed that test particle and quasi-linear formulations give the same result. The oscillating behavior of the test particle solution is due to the phase coherence between the two resonance points at both sides of the equator. Figure

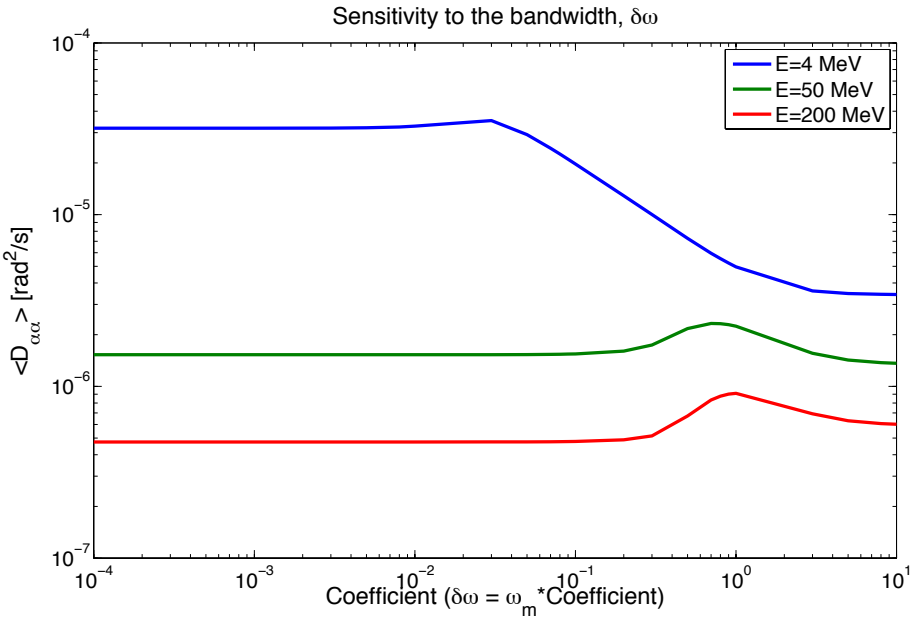


Figure 5-15: Sensitivity of quasi-linear $<D_{\alpha\alpha}>$ on bandwidth of the Gaussian wave frequency distribution for three energies $E = 4$, 50, and 200 MeV

5-16 (b) presents $\langle D_{\alpha\alpha} \rangle$ of 100 MeV protons as a function of equatorial pitch angle. In this case, test particle and quasi-linear formulations give the same result for $\alpha_{eq} < 80°$; protons with $\alpha_{eq} > 80°$ have minimum resonant energies larger than 100 MeV, and are therefore out of resonance at any point along their bouncing motion. The quasi-linear approach does not allow to quantify diffusion coefficients for non-resonant particles with $\alpha_{eq} > 80°$. These particles are out of resonance with the waves and can only be scattered due to non-resonant interactions. The test particle solution of the equations of motion is capable of capturing this weak off-resonant scattering, which results in a smooth transition to zero diffusion at large pitch angles. Overall, bounce-averaged diffusion coefficients estimated using a quasi-linear code accurately match the test particle simulations for all energies and pitch angles. Despite the fact that the waves under consideration are monochromatic, the analysis above shows that quasi-linear theory with a narrow frequency distribution can accurately reproduce the results from test particle narrowband gyroaveraged simulations, and significantly reduce the required computational time.

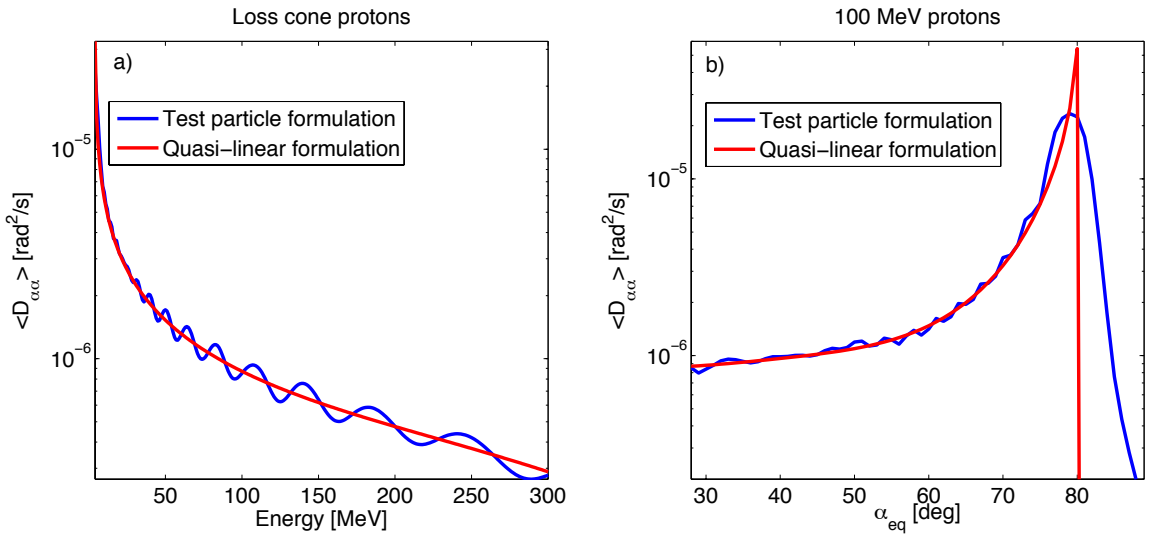


Figure 5-16: Gyroaveraged test particle and quasi-linear solutions of the bounce-averaged diffusion coefficient for 4 Hz field-aligned waves with an amplitude of 2 nT at $L = 1.5$ versus (a) energy of loss cone protons and (b) equatorial pitch angle of 100 MeV protons.

## 5.5 Non-gyroaveraged Test Particle Simulations: Short Interaction

In Section 5.4 we analyzed the gyroaveraged motion of test protons using equations (2.72)-(2.74). The gyroaveraged solution had never been studied before in the case of inner belt protons interacting with EMIC waves, and it is of interest to the scientific community. The nature of the interaction with EMIC waves radiated from a space-based transmitter, however, is far from gyroaveraged (Section 5.2). The antenna illuminates a very narrow region of space. Additionally, energetic inner belt protons drift very rapidly around the Earth. Particles cross the illuminated region in a fraction of their gyroperiod, where they are instantly scattered by the waves. For this reason, and in order to correctly capture the process, we now solve the non-gyroaveraged equations presented in (2.50)-(2.57), except for the adiabatic terms that have been gyroaveraged. The averaging of adiabatic terms neglects any geomagnetic field line curvature (FLC) scattering. This curvature can cause break down of the first adiabatic invariant if the particle's gyroradius is comparable to the radius of curvature of the geomagnetic lines [*Delcourt et al.*, 1996; *Young et al.*, 2008; *Selesnick et al.*, 2010]. FLC scattering, however, is outside the scope of this thesis.

The non-gyroaveraged expressions in equations (2.50)-(2.52) can then be rewritten as follows

$$\dot{p}_z = -q\hat{E}_z^w sin\Phi - \frac{1}{\gamma}\omega_1 p_\perp sin\left(\phi - \Phi\right) - \frac{1}{\gamma}\omega_2 p_\perp sin\left(\phi + \Phi\right) + \underline{C_2} \tag{5.23}$$

$$\dot{p}_\perp = \omega_1\left(\frac{p_z}{\gamma} + R_1 m_H\right) sin\left(\phi - \Phi\right) + \omega_2\left(\frac{p_z}{\gamma} - R_2 m_H\right) sin\left(\phi + \Phi\right) + \underline{C_3} \tag{5.24}$$

$$\dot{\Phi} = \omega - \vec{k}\cdot\vec{v} \tag{5.25}$$

$$\dot{\phi} = -\frac{\Omega_{cH^+}}{\gamma} \tag{5.26}$$

where $\phi$ is the particle's Larmor phase, $\Phi$ is the wave phase and the rest of the parameters were defined in Section 2.3. In the following section we study the differences between non-gyroaveraged and gyroaveraged solutions, and we carefully analyze the non-gyroaveraged scattering during short encounters characteristic of man-made EMIC waves interacting with inner belt energetic protons.

### 5.5.1 Non-gyroaveraged Test Particle Trajectories: General Behavior

The differences between the gyro and non-gyroaveraged formulations are presented in Figure 5-17. The plots are for 17 MeV loss cone protons at $L = 1.5$. Following the example in Figure 5-6, we consider waves with frequency Y = 0.02 and wavenormal angle $\theta = 87°$. The power flux has been assumed constant in both plots, equal to 1 $\mu$W/m$^2$. This assumption seems adequate for the short non-gyroaveraged case of Figure 5-17 (a), since the interaction is mostly local; in the gyroaveraged scenario of Figure 5-17 (b), however, the assumption may overestimate the scattering. Nevertheless, we have decided to keep the power flux constant in both simulations for comparison purposes.

Figure 5-17 (a) presents the scattering resulting from the non-gyroaveraged equations of motion. The colored lines represent the continuous non-gyroaveraged interaction along the bounce motion of 12 protons uniformly distributed in Larmor phase. The black markers in the same plot are the result of a short non-gyroaveraged interaction at 5 different latitudes and consider 12 uniformly distributed particle's Larmor phases and 8 different initial wave

phases. The interaction time has been calculated based on the time it takes to the protons to drift through the area illuminated by the transmitter (from ray tracing) at each latitude, which is a fraction of their gyroperiod. Each of the five short interactions at different latitudes are meant to represent five independent encounters between particles and waves, one per particle's drift period. On the other hand, Figure 5-17 (b) presents the scattering resulting from the gyroaveraged equations of motion. The colored lines represent the continuous gyroaveraged interaction along the bounce motion of 12 protons uniformly distributed in Larmor phase, and the black markers are the result of a short gyroaveraged interaction at 5 different latitudes. Although the formulation of short interactions (black markers) using gyroaveraged equations is not accurate, we have represented it here for comparison with the non-gyroaveraged case.

In the following we compare the non-gyroaveraged and the gyroaveraged analyses. The gyroaveraged continuous interaction (colored lines) of Figure 5-17 (b) correctly reproduces the cumulative resonant interaction ($\Delta\alpha_{res}$) but cancels out the rapidly oscillating non-resonant effect ($\Delta\alpha_{non-res}$) that can be observed in the non-gyroaveraged case of Figure 5-17 (a). This off-resonant scattering is important for encounters shorter than a gyroperiod, as shown by the short interaction results represented by the black markers. In the gyroaveraged case, the short interaction scattering is only due to the resonant contribution, which gives very small changes in pitch angle and small standard deviation. The non-gyroaveraged short interaction, however, has larger pitch angle change and standard deviation due to the off-resonant contribution. Moreover, the off-resonant scattering of a short interaction is of the same order of magnitude as the hypothetical resonant cumulative effect during a long interaction. Overall, the gyroaveraged formulation gives pessimistic estimations of the scattering because it is does not capture the off-resonant scattering that dominates short interactions: the non-gyroaveraged approach should be used for wave-particle encounters shorter than a gyroperiod.

The short non-resonant interaction is capable of changing the particles' equatorial pitch angle and violating the fist adiabatic invariant. The particles see a variation of the wave amplitude in a time much shorter than their gyroperiod. This sudden change in wave field modifies the velocity vector of the particle, i.e. introduces scattering and changes the first adiabatic invariant. Once the particles are outside the wave field and adiabatically drifting

around the Earth, their gyro-phase remains random but the change in equatorial pitch angle (change of the distribution in velocity space) is a non-reversible process that persists along the adiabatic drift motion. After one drift period, the particles encounter the wave-field again with a uniform distribution in gyro-phase but with the velocities modified by the previous kick. The particles will be scattered again by the wave, and the same process repeats every drift period. The result of these non-resonant interactions, once per orbit, generates a random walk in velocity space of the particles. Due to the gradient of their phase space density, this random walk translates into diffusion of the particles' distribution in velocity space, which is analyzed in Section 5.6.

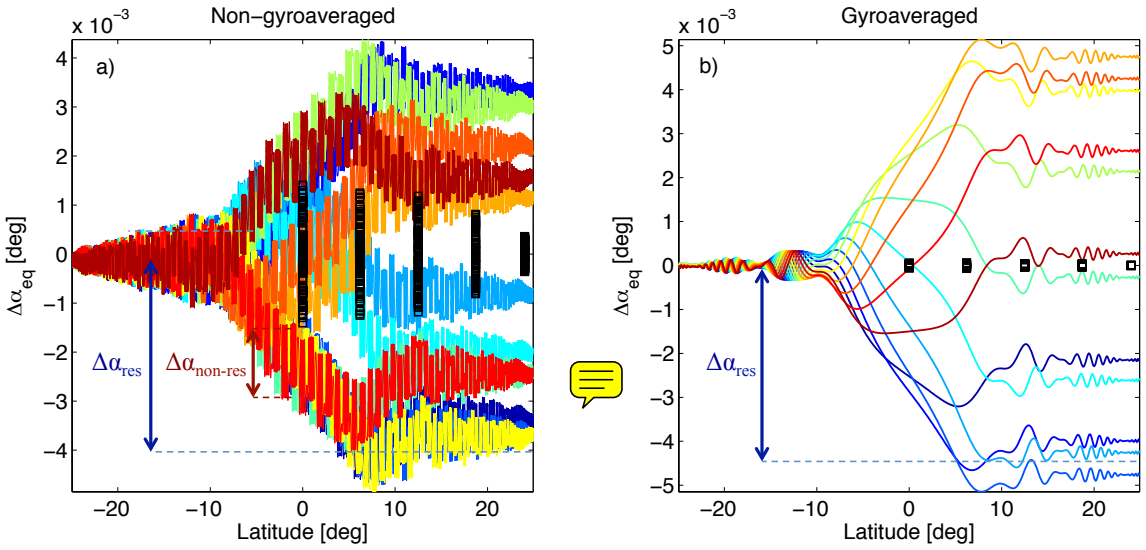


Figure 5-17: (a) Non-gyroaveraged and (b) gyroaveraged scattering as a function of latitude for the same wave and particle parameters as in Figure 5-6 (a). The power flux has been assumed constant in both plots, equal to 1 $\mu$W. The colored lines represent the continuous interaction along the bounce motion of 12 protons uniformly distributed in Larmor phase. The black squares are the result of a short interaction at 5 different latitudes.

We next analyze the sensitivity of a short equatorial non-gyroaveraged interaction to different wave and particle parameters. These analyses are presented in Figure 5-18, for L = 1.5 and Y = 0.02. It must be noted that, in the non-gyroaveraged case, there is no need to compute multiple resonant harmonics. Figure 5-18 (a) shows that the non-gyroaveraged RMS scattering scales linearly with the wave amplitude, which was also the case in the gyroaveraged solution. Figure 5-18 (b) and (c) present the scattering dependence on equatorial pitch angle and particle energy for a wave power flux of 1 $\mu$W/m$^2$, respectively. The scattering decreases with increasing pitch angle as well as increasing energy. This behav-

ior is caused by the larger drift velocity of large pitch angle and/or large energy particles. These higher energy particles, however, will cross the illuminated region more frequently than the slower ones, which will level up the long term scattering at all energies and pitch angles (i.e. will level up diffusion in velocity space).

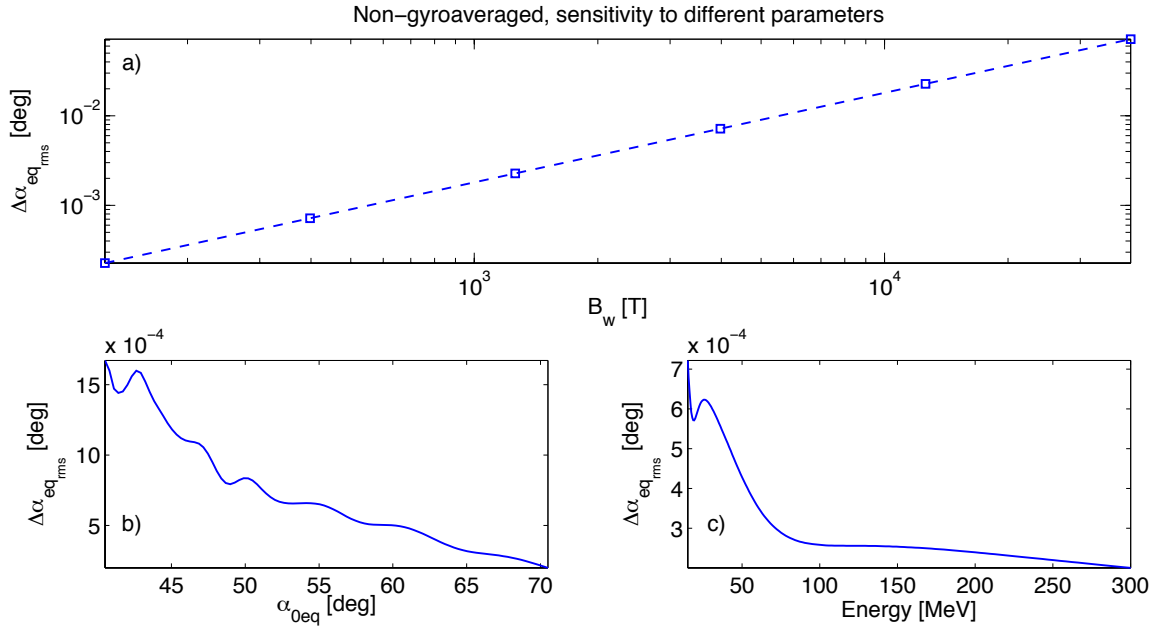


Figure 5-18: (a) Non-gyroaveraged RMS scattering as a function of wave amplitude of 17 MeV loss cone protons. (b) Non-gyroaveraged RMS scattering as a function of initial pitch angle of 17 MeV protons and a wave amplitude of 1 $\mu$W/m$^2$. (c) Non-gyroaveraged RMS scattering as a function of particle's energy of loss cone protons and a wave amplitude of 1 $\mu$W/m$^2$. The plots are for a short duration equatorial interaction at $L = 1.5$, with Y = 0.02 and a wave normal angle of $\theta = 87°$.

### 5.5.2 The Transmitter Driving Frequency: Not an Easy Choice

As seen in Section 5.2, the interaction between man-made EMIC waves and inner belt energetic protons is shorter than the particle's gyroperiod. The plots above show that this type of encounters are dominated by off-resonant scattering, which casts doubt on the selection of the wave frequency based on resonance considerations (Section 5.4.1). The resonance condition does not play a role anymore in the interaction, which is not dominated by resonant phase trapping but by rapidly oscillating non-resonant effects. Figure 5-19 analyzes the role of the frequency in the non-resonant formulation during a short equatorial encounter between protons and EMIC waves. The encounter lasts ~0.66 ms, which represents

a small fraction of the particle's gyroperiod. Wave and particle parameters are the same as in Figure 5-17 but with varying frequency. It must be noted that in this plot the spreading of the waves in Figure 5-19 has been assumed constant and independent of frequency, that is, constant interaction time and constant total power. We know, however, that different frequencies spread differently in the magnetosphere, which will be taken into account in the following section. Figure 5-19 (a) presents the total pitch angle change adiabatically referred to the equator as a function of the normalized frequency. The color code represents different non-gyroaveraged wave-particle phases. The plot reveals that the scattering favors small frequencies. The gaps in the plot correspond to the oxygen and helium stop bands. Similary, Figure 5-19 (b) shows the corresponding RMS scattering, which presents the same features as the accompanying subplot.

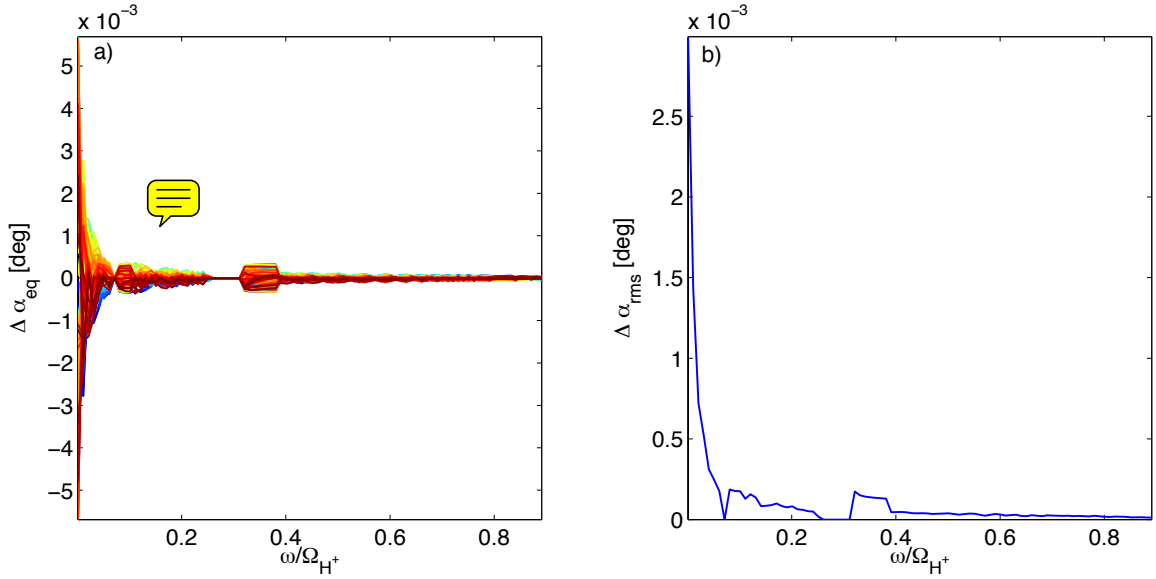


Figure 5-19: (a) Non-gyroaveraged total scattering as a function of normalized frequency for the same parameters as in Figure 5-17 (a). The color code represents different initial wave-particle phases. (b) RMS value of the different phases in (a) as a function of frequency.

The question is now, why does the non-gyroaveraged scattering increase with decreasing frequency? The answer lays on the wave variability as seen by the particle during its fast motion across the interaction region. The wave frequency is smaller that the particle's gyrofrequency; its wavelength, however, is also very small due to the large perpendicular wave normal vector of the waves. Man-made EMIC waves are very oblique, that is, $\vec{k}_\perp \cdot \vec{v}_\perp$ is very large (and $k_\perp$ depends on the frequency). In other words, the wave variability as seen by the particle is due to its Doppler shift. The scattering dependence on the frequency

remains even for extremely short interactions times, since the Doppler shift introduced by the particle is very large. The wave has a very small frequency but also a very small wavelength; decreasing the frequency decreases $k_\perp$, which in turn increases the wavelength. Figure 5-20 aims at explaining this behavior with frequency. Figure 5-20 (a) shows the sine of the particle-wave phase along a short encounter that extends between $\lambda$ = 0-0.153° (0.66 ms). The oscillating functions $\sin(\phi \pm \Phi)$ and $\cos(\phi \pm \Phi)$ dictate the behavior of the differential equations in (5.23)-(5.26). For Y = 0.01 the sine function does not have the time to complete a single cycle, while the higher frequency case (Y = 0.5) does many oscillations in the timeframe of the short interaction. These functions, when integrated over time, give different results. At high frequencies, the integration of the sine and cosine functions cancels out. Contrarily, the integration accumulates in the low frequency case, which is the explanation why the lower the frequency the larger the scattering. Figure 5-20 (b) shows the result of the integration of equation (5.23), where we have subtracted the initial parallel velocity in order to only show the changes due to the presence of the wave. In this plot we can clearly observe the effect of the frequency: larger changes in the amplitude of the velocity develop in the lower frequency case compared to higher frequencies due to the integration of the sine and cosine functions.

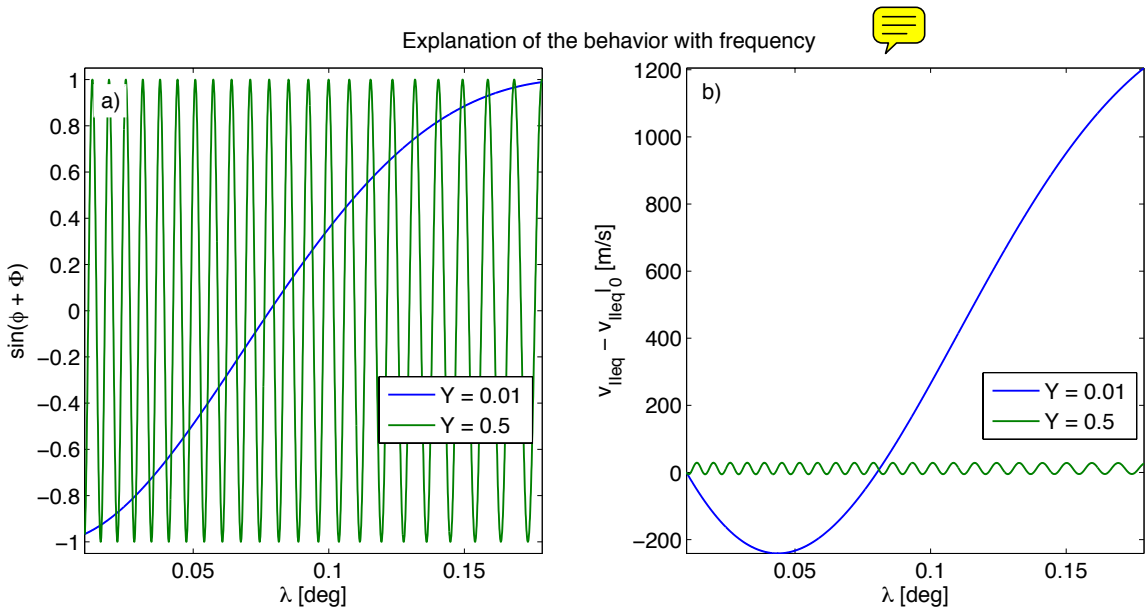


Figure 5-20: (a) $\sin(\phi + \Phi)$ and (b) parallel velocity referred to the equator relative to the initial parallel velocity as a function of latitude during a 66 ms interaction and for two different normalized frequencies.

Additionally, Section 4.3.3 revealed that Landau and cyclotron damping can introduce significant attenuation of the waves above the oxygen gyrofrequency, where large stop bands exist. Therefore, operation below the $\Omega_{O^+}$ is desired in order to ensure propagation along the geomagnetic field lines.

But not all the parameters favor the lower EMIC frequencies. Section 3.3 showed that the radiation resistance of a loop antenna scales with the square of the frequency, and so does the radiated power. A tradeoff exists, therefore, between radiated power and particle's scattering. The fixed parameter in the analysis are the superconductor capabilities (i.e. the current density that the wire is capable of handling), and we want to minimize the particle's lifetime as a function of frequency for a given wire performance. The analysis of this frequency tradeoff requires the knowledge of the transmitter specifications, which are presented in Section 6.6. Meanwhile, the following section analyzes different frequencies within the oxygen band. Moreover, a scientific RBR mission should ideally be capable of sweeping a broad range of frequencies to test the models proposed here and better understand the physics of wave radiation, propagation and interaction with energetic protons.

## 5.6 Analysis of the Full Distribution: Precipitating Fluxes and Lifetimes

Ray tracing (with an initial wave normal angle of $\theta_0 = 89.9°$) and power divergence results are next inputted to the simulation of the interaction between the AP-9 distribution of energetic inner belt protons and EMIC waves. Test particle simulations are used to determine initial precipitation fluxes at the edge of the loss cone as described in Section 5.3.1. These fluxes are interesting because they would set the instrument detectability requirements of a scientific mission (Section 7.2). Test particle simulations, however, are very computationally intensive and cannot be used to calculate the evolution of the distribution in time and the particles' lifetimes, which are required in order to determine the feasibility of the remediation concept. In the previous sections, however, we showed that inner belt protons perform a random walk in velocity space due to non-resonant interactions, thus it is justified to use a diffusion approach to solve for the particle's long term behavior. For this reason, we estimate diffusion coefficients from test particle simulations and we use them to solve the

Table 5.1: Initial equatorial particle and energy fluxes at $L = 1.5$. The values are for a wave power flux of 1 mW/m$^2$ and a wave frequency of Y = 0.02.

| | |
|---|---|
| $\Phi_{prec}$(E > 50 MeV) [#/(cm$^2$ s)] | 0.0018 |
| $\Phi_{prec}$(E > 100 MeV) [#/(cm$^2$ s)] | $4.15{\cdot}10^{-4}$ |
| $Q$(E > 50 MeV) [MeV/(cm$^2$ s)] | 0.158 |
| $Q$(E > 100 MeV) [MeV/(cm$^2$ s)] | 0.062 |

pitch angle diffusion (Fokker-Planck) equation. This diffusion simulation is CPU-efficient and it is applied to calculate the time evolution of the distribution function of energetic protons as well as the particles' lifetime as described in Section 5.3.2. It must be noted that we do not use quasi-linear theory [*Kennel and Engelmann*, 1966] to find pitch angle diffusion coefficients because it is not capable of capturing non-resonant interactions, which dominate the scattering during realistic non-gyroaveraged short encounters.

The differential energy spectrum around the loss cone, $\Phi_{E_{diff}}(\alpha, E)$, after a single-pass short interaction with EMIC waves is presented in Figure 5-21 (a) for different proton energies. The results are for a proton distribution and ray traced waves at $L = 1.5$, a wave frequency of Y = 0.02 and a power flux of 1 mW/m$^2$ at $\lambda_0 = 25°$. These results, however, are easily scalable with the square root of the wave power and they will set the detectability requirements of a particle instrument onboard a potential spacecraft (Section 7.2). The perturbed distribution has been calculated by solving the non-gyroaveraged equations of motion for every test particle that represents the AP-9 distribution. It can be observed that the loss cone ($\alpha_{lc} = 40.54°$) has partially filled up as a result of the interaction. Using equation (5.12) we can obtain the corresponding initial precipitated differential energy spectrum at the equator, $\Phi_{E_{prec}}(E)$, which is presented in Figure 5-21 (b). Similarly, Table 5.1 provides $\Phi_{prec}$ and the initial precipitated energy flux at the equator, $Q$, which have been integrated over E > 50 MeV and E > 100 MeV.

The calculation of the particles' lifetime is presented in Figure 5-22 for protons at $L = 1.5$ and a wave frequency of Y = 0.02. The wave propagation pattern used in these calculations was previously described in Figure 4-5. The first step in the lifetimes' calculation consists of evaluating diffusion coefficients as a function of energy and pitch angle, which are presented in Figure 5-22 (a) for a power flux of 1 mW/m$^2$ at the source location ($\lambda_0 = 25°$), which corresponds to a cross-sectional area of 71 hm$^2$ at equatorial heights (Table 4.2). These

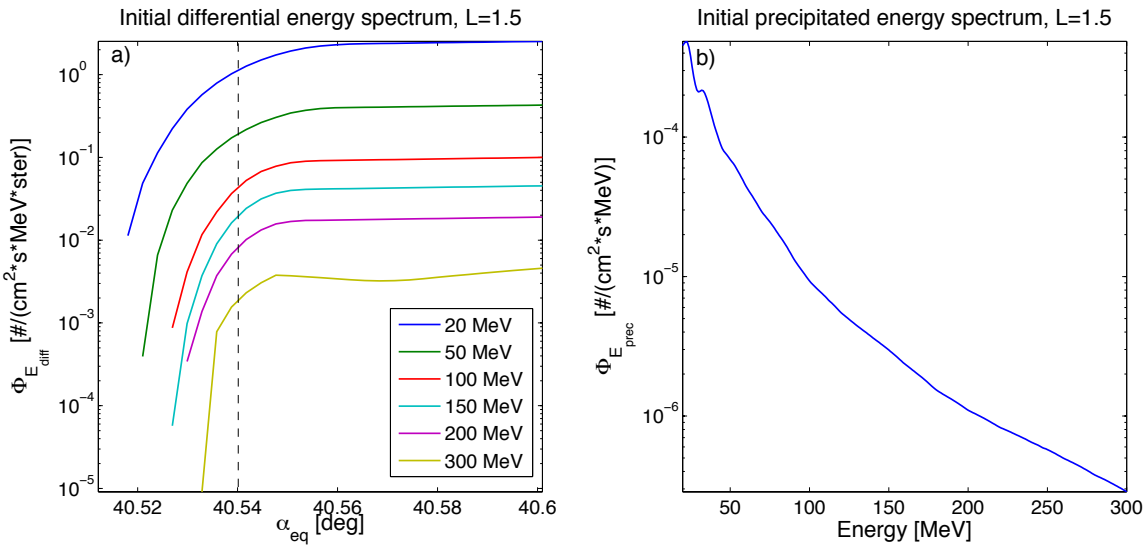


Figure 5-21: (a) Perturbed distribution of energetic trapped protons at $L = 1.5$. (b) Non-gyroaveraged initial precipitated differential energy spectrum at the equator as a function of proton energy. The plots are for a wave power flux of 1 mW/m$^2$ and a wave frequency of Y = 0.02.

diffusion coefficients have been calculated from test particle simulations using equation (5.14), which is averaged over Magnetic Local Time (MLT) and therefore takes into account the nature of the interaction. In the figure we clearly observe that the gyroaveraged solution greatly underestimates diffusion rates, by about three orders of magnitude compared to the more realistic non-gyroaveraged simulation. Additionally, we observe that the non-gyroaveraged diffusion coefficients are practically independent of pitch angle and energy, i.e. $\langle D_{\alpha\alpha}(E,\alpha)\rangle \approx 5 \cdot 10^{-12}$ rad$^2$/s $\approx$ const. The higher energy particles go through the illuminated region more often and faster, which levels up diffusion in velocity space. These diffusion coefficients are used in Figure 5-22 (b) to calculate the time evolution of the AP-9 distribution of 100 MeV protons, where the colorbar represents time. In this simulation the 1D-VERB code has been used to solve the Fokker-Planck equation in (5.15). Additionally, Figure 5-22 (c) presents the exponential decay time of the distribution given by equation (5.18) at each time step as a function of equatorial pitch angle. We can only talk about lifetime when the distribution decays at the same rate for every pitch angle. The actual particles' *lifetime*, $\tau_L$, as a function of radiated power is presented in Figure 5-22 (d), which is the time it takes to the distribution to decay by 1/e and corresponds to the first eigenmode given by equation (5.19). The power in Figure 5-22 (d) goes through a cross-sectional area of 71 hm$^2$ at the equator. As we would expect form the shape of the diffusion coefficients,

the particle's lifetime is independent of energy, while it decreases inversely with increasing radiated power. A lifetime of $\tau_L = 10$ years requires a radiated power of 60 kW for Y = 0.02, which corresponds to a power flux of 0.08 W/m$^2$ at the equator. This is the power required to precipitate the energetic protons contained in a volume given by a radial thickness of 845 m centered at $L = 1.5$. In Chapter 7 we scale these results and analyze the power required to clean up the entire inner belt region; based on these numbers, however, we can anticipate that the remediation of the proton belt is going to be a pretty difficult task.

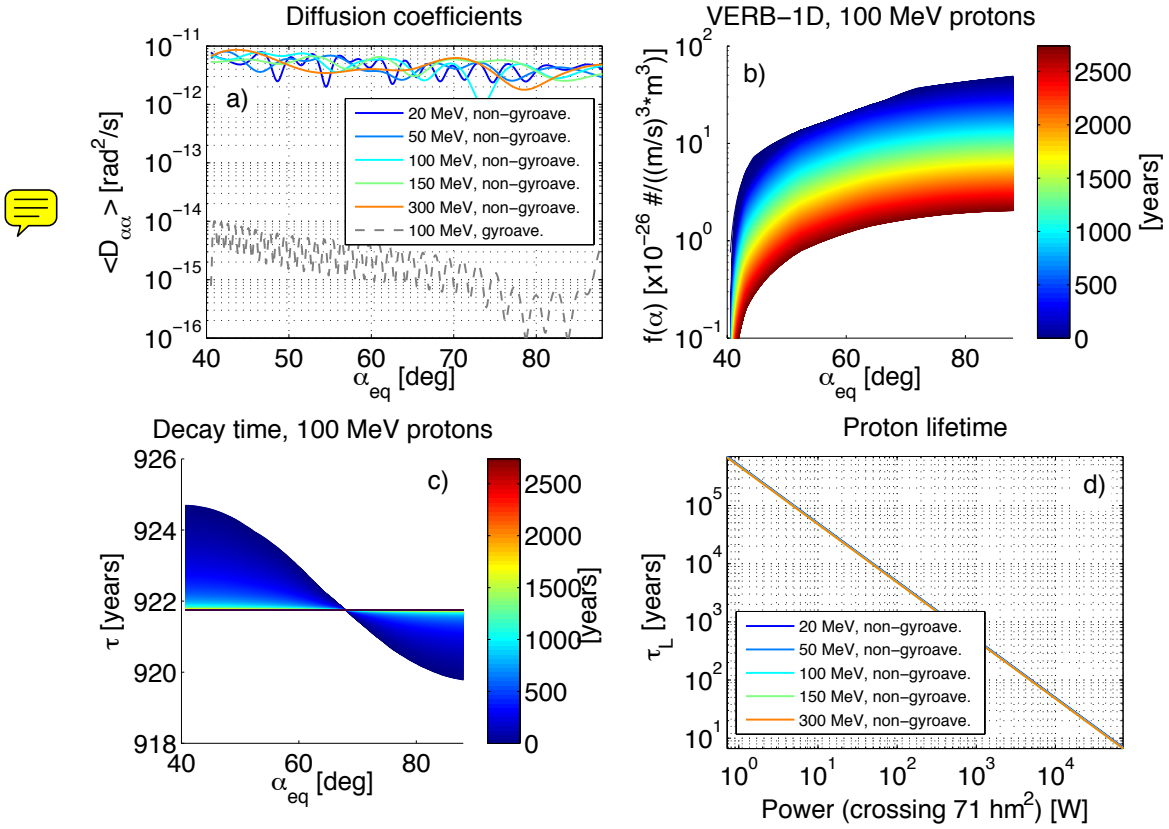


Figure 5-22: (a) MLT-averaged diffusion coefficients for different energies as a function of equatorial pitch angle for non-gyroaveraged (solid lines) and gyroaveraged (dashed line) particle trajectories. (b) Time evolution of the AP-9 distribution of the 100 MeV protons in (a) at each time step as a function of equatorial pitch angle. (c) Exponential decay time of the distribution in (b) at each time step as a function of equatorial pitch angle. (d) Particles' lifetime as a function of required radiated power for different proton energies. All the plots are for a wave frequency of Y = 0.02 at $L = 1.5$. Waves have been launched from $\lambda_0 = 25°$, which corresponds to an illuminated area of 71 hm$^2$ at the equator. Plots (a)-(c) are for a power flux of 1 mW/m$^2$ at the location of the source.

Similarly, Figure 5-23 presents diffusion coefficients and lifetimes of 100 MeV protons at different $L$-shells and for different normalized frequencies (within the EMIC oxygen band),

which are the result of non-gyroaveraged calculations. Figure 5-23 (a) shows the diffusion coefficients for a power flux of 1 mW/m$^2$ (power flux at the source location, as wide as the antenna); the wave spreading as a function of $L$-shell and frequency is given by the ray tracer and power divergence results (Table 4.2). Therefore, the different frequencies in Figure 5-23 (a) correspond to different total power, since they have the same power flux but through different cross-sectional area (which is dependent on frequency but not as much on $L$-shell). In the figure, we observe that it is easier to scatter particles from the higher $L$-shells; the scattering is weaker closer to the Earth because the geomagnetic field is stronger there, i.e. weaker wave fields relative to the Earth's magnetic field. The different cutoffs in the coefficients correspond to the drift loss cone angle of the particles. In Figure 5-23 (b) we analyze the particle's lifetime as a function of power for different $L$-shells and frequencies. Again, we observe that for a fixed frequency and power, protons at lower $L$-shells are harder to scatter compared to higher $L$-shells, which translates into longer lifetimes of the particles. Additionally, for a fixed power, the lower frequencies are capable of reducing the most the lifetime of the particles. From the figure, we need 30 kW of radiated power at a frequency of Y = 0.015 to precipitate an 845 meter-thick layer of protons at $L = 1.5$ in less than 10 years; for the same power and frequency, it takes more than 30 years at $L = 1.2$ for a layer of 833 m, and only 110 days at $L = 2$ for 856 m. These results suggest that a practical approach would then be to clean up first the upper reaches of the belt, then tackle the lower regions gradually. This technique is also reinforced by the behavior of the natural residence times presented in the following section.

The lifetimes above are the result of human intervention and are to be compared with the natural precipitation mechanisms, which are analyzed next. Additionally, the power levels above refer to remediation of a thin layer of a couple hundred meters, as wide as the area illuminated by the antenna. However, if we want to precipitate the entire proton population in the inner Van Allen belt we have to scale the power in Figure 5-23 (b) with the size of this belt. This scaling is presented in Chapter 7.

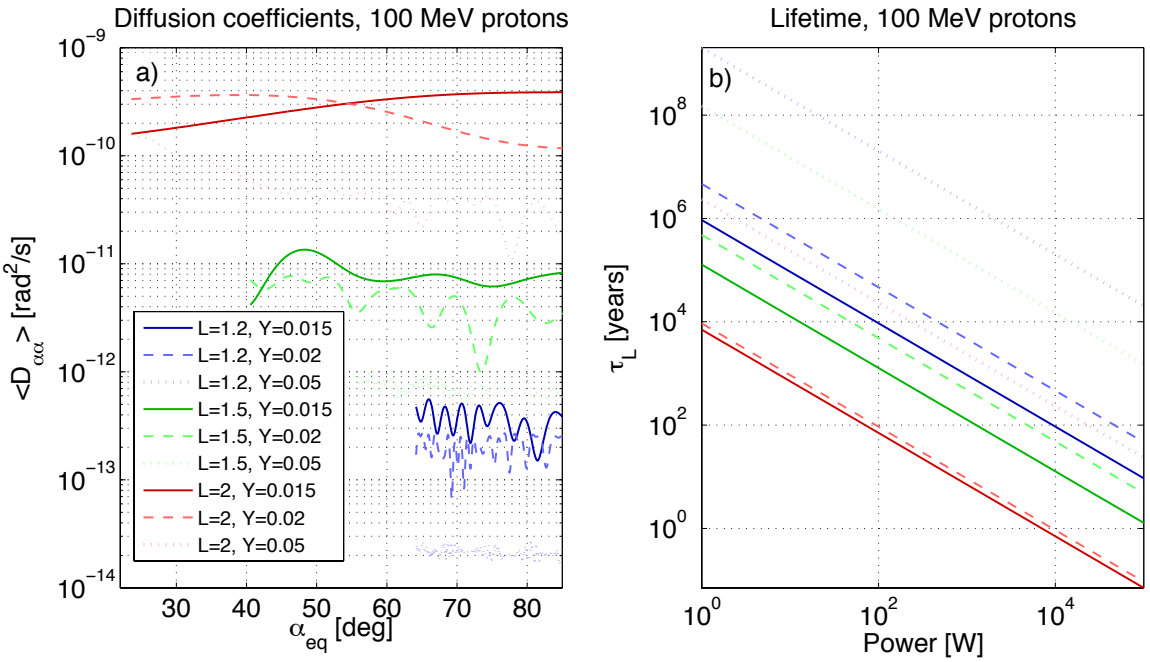


Figure 5-23: (a) MLT-averaged diffusion coefficients of 100 MeV protons as a function of equatorial pitch angle at different $L$-shells, for different frequencies and for a power flux of 1 mW/m$^2$. (b) Particles' lifetime as a function of radiated power of 100 MeV protons at different $L$-shells and for different frequencies.

## 5.7 Comparison with Natural Precipitation Mechanisms

*Selesnick et al.* [2007] developed a theoretical model of the inner proton belt and provided proton intensities as a function of time and the three adiabatic invariants. The authors suggested that Cosmic Ray Albedo Neutron Decay (CRAND) is the major source of >100 MeV protons, while <100 MeV protons are solar energetic protons (SEP). CRAND is the product of radioactive decay of albedo neutrons, which are themselves the result of cosmic ray collisions with atmospheric nuclei. On the other hand, inner belt proton losses are dominated by slowing down due to excitation and ionization of O, N, He and H neutral atoms at different altitudes.

Proton natural residence times range from less than a year to more than 4000 years. *Dragt et al.* [1966] provided a good fit to the data on proton lifetimes in the inner radiation belt

$$\tau_{natural} \approx 2 \cdot 10^4 \frac{(E\,[MeV])^{1.3}}{<\rho>\,[cm^{-3}]} \quad years \tag{5.27}$$

where $<\rho>$ is the electron density averaged over the proton orbit. The expression above is therefore a function of the $L$-shell and particles' energy. Figure 5-24 (a) presents the natural lifetimes as a function of proton energy for three $L$-shells in the inner belt. Particles at the lower $L$-shell values decay faster because they are closer to the Earth, which increases collisions with neutrals and reduces the protons' residence time. This behavior is opposite to the wave-particle interaction dependence on $L$-shell described in Figure 5-23. In previous sections we saw that wave-particle interactions are weaker closer to the Earth because the geomagnetic field is stronger there, which translates into weaker wave fields relative to the Earth's magnetic field. This opposite trend with $L$-shell between natural and man-made behavior reinforces the idea of targeting the upper reaches of the inner belt first, and gradually tackling the lower regions as more power becomes available.

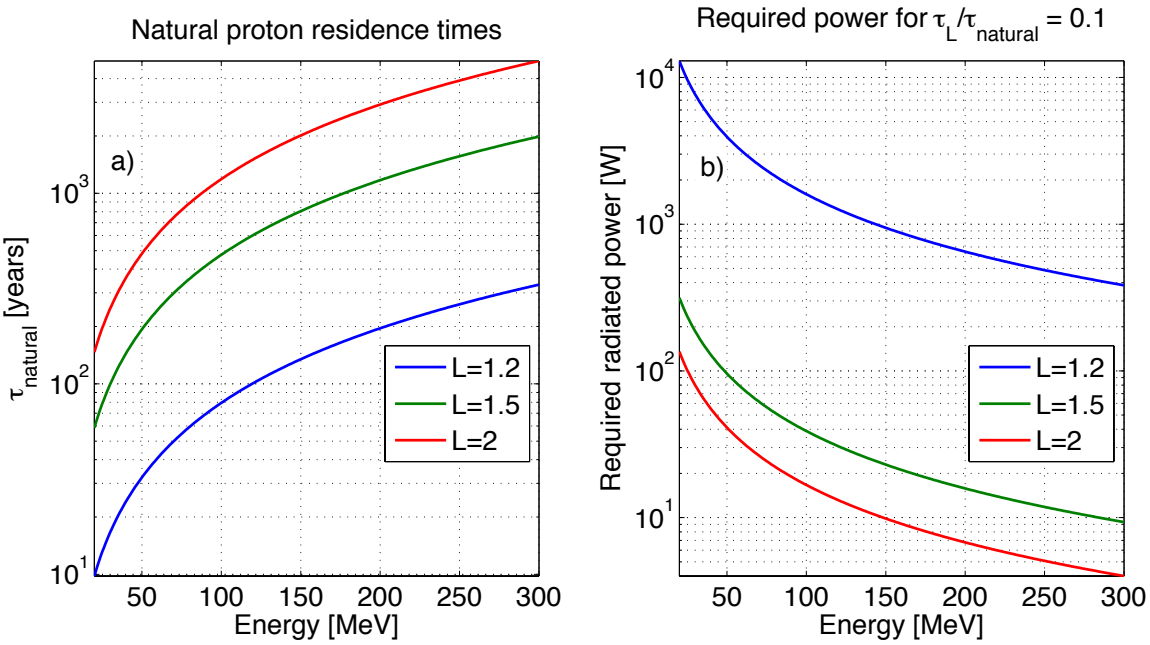


Figure 5-24: (a) Natural lifetimes of inner belt protons as a function of particles' energy at three different $L$-shells. (b) Radiated power required to reduce the natural proton residence times by a factor of 10, as a function of proton energy and $L$-shell. A frequency of Y = 0.005 has been considered.

The natural proton residence times are to be compared with the lifetimes induced by wave-particle interactions described in the previous section. Figure 5-24 (b) presents the required radiated power as a function of proton energy required to reduce the natural residence times by one order of magnitude ($\tau_L/\tau_{natural} = 0.1$), and for a frequency of Y = 0.005. We must reiterate that this is the power required to precipitate a $L$-shell surface of thickness given by

the illuminated area from a single transmitter. The power required to remediate the entire inner Van Allen belt will be analyzed in Chapter 7, but based on the numbers in Figure 5-24 (b) we can expect that it will be excessively large. Again, we observe that it takes less power to precipitate particles from the outer regions of the inner belt. Additionally, it also takes less power to reduce the higher energy protons' lifetime below their natural value because the absolute time is longer compared to the one of the lower energy particles.

## 5.8 Conclusions

In this chapter we have characterized and calculated the wave-particle interactions between energetic inner belt protons and man-made EMIC waves, and compared them to natural precipitation mechanisms. The wave-particle interaction calculations presented above take as input the wave properties in the magnetosphere calculated in Chapter 4. The main conclusions from this chapter are the following:

- Each encounter between energetic inner belt protons and man-made EMIC waves is more than one order of magnitude shorter than the protons' gyroperiod. This fact is due to the small spreading of the waves across field lines together with the fast motion of the energetic protons. The nature of this interaction reveals that the commonly used gyroaveraged formulation is not applicable to our case, but the non-gyroaveraged equations have to be considered.

- The magnetic wave force dominates the interaction between energetic protons and EMIC waves, which does not modify the energy of the particles but is capable of introducing pitch angle scattering and precipitation.

- Non-gyroaveraged test particle simulations are used to determine the behavior of individual test protons during one pass interaction, the initial precipitation fluxes at the edge of the loss cone, as well as the MLT-averaged pitch angle diffusion coefficients of all the particles in the distribution. Test particle simulations, however, are very computationally intensive and cannot be used to calculate the evolution of the distribution in time and the particles' lifetime. For this reason, we estimate diffusion coefficients from test particles and use them to solve the pitch angle diffusion equation, which is

CPU-efficient and allows exploration of parameter space.

- The gyroaveraged formulation should not be used because it cancels out the off-resonant scattering that dominates short interactions, which is captured by the non-gyroaveraged formulation. These off-resonant interactions, once per particles' drift period, generate a random walk and diffusion of the particles in velocity space.

- The non-gyroaveraged scattering scales linearly with the wave amplitude. For a fixed wave amplitude, the scattering decreases with increasing pitch angle and increasing energy. This behavior is caused by the larger drift velocity of large pitch angle and/or large energy particles. These more energetic particles, however, cross the illuminated region more frequently than the slower ones, which levels up the long term scattering at all energies and pitch angles.

- The selection of the wave frequency is not based on resonance considerations but on the behavior of the off-resonant scattering, which tends to increase with decreasing frequency. Landau and cyclotron damping also favor the lower frequencies. The radiation resistance of a loop antenna, however, scales with the square of the frequency, and so does the radiated power. A tradeoff exists, therefore, between radiated power and particle's scattering, which will be analyzed in Section 6.6.

- The AP-9 model is used to describe the unperturbed distribution of energetic inner belt protons. Using test particle simulations we have calculated the initial precipitating fluxes due to a single-pass short interaction, which partially fills up the drift loss cone and sets the detectability requirements of a potential particle instrument.

- The gyroaveraged solution underestimates diffusion rates by three orders of magnitude compared to the more realistic non-gyroaveraged simulation. For this reason, quasi-linear theory cannot be used to find pitch angle diffusion coefficients since it is not capable of capturing off-resonant interactions that dominate short encounters.

- Non-gyroaveraged diffusion coefficients are practically independent of pitch angle and energy. The particle's lifetime is therefore independent of energy and decreases inversely with increasing radiated power.

- For a fixed frequency and power, protons at lower $L$-shells are harder to scatter compared to higher $L$-shells, which translates into longer lifetimes of the particles. The scattering is weaker closer to the Earth because the geomagnetic field is stronger there, i.e. weaker wave fields relative to the Earth's magnetic field. For a fixed $L$-shell and power, the lower frequencies tend to generate more scattering, which decreases the particles' lifetime.

- A radiated power of 30 kW at a frequency of Y = 0.015 is required to precipitate an 845 meter-thick layer of protons at $L = 1.5$ in less than 10 years; for the same power and frequency, it takes 30 years at $L = 1.2$ for a layer of 833 m, and only 110 days at $L = 2$ for 856 m. A practical approach could then be to clean up first the upper reaches of the belt, then tackle the lower regions gradually. These numbers suggest, however, that the remediation of the entire proton Van Allen belt is going to require an excessively large amount of power.

- Proton natural residence times range from less than a year to more than 4000 years, and they are a function of the $L$-shell and particles' energy. Inner belt proton losses are dominated by slowing down due to excitation and ionization of O, N, He and H neutral atoms at different altitudes. For this reason, particles at lower $L$-shell values decay faster because they suffer more collisions with neutrals. This behavior is opposite to the wave-particle interaction dependence on $L$-shell.

- Finally, mentioning that we have also analyzed the gyroaveraged interaction between inner belt protons and oblique EMIC waves. This formulation is not applicable to our particular problem but it could be of interest in future applications where EMIC waves extend over a broad region in Magnetic Local Time (MLT) in the inner belt, thus allowing phase trapping of the rapidly drifting protons. According to the gyroaveraged formulation, the resonant frequency to interact with energetic inner belt protons lies within the EMIC oxygen band, and the higher order harmonics of the interaction play an important role in scattering the most energetic particles in the distribution. These resonant interactions are always linear, and we have proved that quasi-linear theory with a narrow frequency distribution is capable of accurately reproducing the results from test particle narrowband gyroaveraged simulations, and significantly reduce the required computational time.

# Chapter 6

# Electrical, Mechanical and Thermal Implications of a Magnetic Coil Antenna

In Chapter 3 we argued that, based on the plasma response, in-situ magnetic dipoles are the best candidates to radiate EMIC waves in the magnetosphere. The most promising solution involves a DC rotating coil, since a plasma sheath will most likely appear around a static AC coil due to its excessive self-inductance introduced by the large dimensions and circulating current required by the system, as we will see below. Because of these effects, we continue the analysis assuming a rotating coil driven with direct current. We also saw that both options can be equivalently modeled in terms of radiation characteristics, since the dipole component of the rotating DC antenna is equivalent to two AC static orthogonal coils. This chapter analyzes the green box of Figure 3-2, i.e. the physical antenna. More specifically, we discuss the electrical, mechanical and thermal implications of such a transmitter, including a preliminary sizing of the superconducting coil antenna, its thermal control system and an estimation of its performance. The controlled removal of energetic Van Allen belt protons requires a huge amount of radiated power. Consequently, we will be dealing with the largest coil dimensions that can be reasonably launched. A scientific mission scaled down to detectability of the precipitating fluxes is analyzed later on in Chapter 7.

We must also note that, although not applicable to our DC design, a little research was

done as part of this dissertation about AC operation of superconductors. This investigation could be relevant to future applications, and for this reason it is detailed in Appendix B.

## 6.1 Electrical Considerations: A DC Rotating Coil Antenna

In the previous chapter we showed that the controlled removal of energetic Van Allen belt protons requires a very large amount of radiated power. Consequently, we will be dealing with the largest coil dimensions that can be reasonably launched. This coil structure, with very high currents circulating around it, also has a very large self-inductance. This self-inductance is the reason why we require a rotating DC coil instead of a static AC antenna.

The self-inductance of a coil transmitter operating in AC, $L_{ind}$, is given by

$$L_{ind} = \frac{N_{turn}\Phi_B}{I} = \frac{N_{turn}^2 \mu_0 \pi R_a^2}{H} \tag{6.1}$$

where $\Phi_B$ is the magnetic flux through the loop, $I$ is the current per turn, $N_{turn}$ is the number of turns, $R_a$ is the radius of the coil, $H = N_{turn}(t + l)$ is the total thickness of the coil, and $t$ and $l$ are the superconducting wire and insulation thicknesses, respectively (detailed in the following sections). Take $N_{turn} = 106$, $R_a = 15$ m and $H = 0.021$ m, then the self-inductance of the coil is

$$L_{ind} = \frac{106^2 * 15^2 * \mu_0 \pi}{0.021} \approx 470\ H$$

which is indeed very large. In an AC system, this inductance would have to be compensated in order to increase the radiation efficiency, and in such a way to reduce the voltage drop across the coil. But is this compensation possible? A conceivable circuit for this purpose is represented in Figure 6-1 (a), where the compensating capacitor is in series with the coil inductance. The corresponding circuit equations can be written as follows

$$L_{ind}\frac{dI}{dt} = V_a \tag{6.2}$$

$$C\frac{dV_c}{dt} = I \tag{6.3}$$

and

$$V = V_a + V_c \tag{6.4}$$

where $V_a$ and $V_c$ are voltages across the coil and capacitor, respectively. Taking $I = I_0 \sin \omega t$ and $V = V_0 \sin(\omega t + \phi)$ we find that

$$V_0 = \frac{I_0}{\omega C}\left(1 - \omega^2 L_{ind} C\right) \tag{6.5}$$

This voltage tends to zero at the circuit resonance ($C = C_{comp} = 1/\omega^2 L_{ind}$), which is the purpose of compensation. The voltage at resonance across the loop (and across the capacitor), however, is not zero

$$V_a = -V_c = \omega L_{ind} I_0 \cos \omega t \tag{6.6}$$

which may induce a plasma sheath around the coil and should be minimized. Moreover, not only the compensating capacitor(s) has to have the right capacitance but it has to be able to handle the voltage across the coil. Figure 6-1 shows the compensated parameters as a function of the number of turns of a coil with $R_a = 15$ m operating at $f = 2$ Hz. The rest of the parameters are taken from Table 6.2. It can be observed that even for a single turn loop the voltage induced across it (and across the capacitor) is around 10 kV, unacceptable in terms of arcing and sheath formation. Although the capacitance required for compensation is very small the component should be able to handle very large voltages, which dramatically increases its mass. In Section 3.2 we dismissed the option of a linear antenna due to the large capacitive reactance of the antenna-plasma system, which involved the formation of a thick oscillatory sheath around the transmitter. We have revealed above, however, that a plasma sheath will most likely also appear around the AC coil transmitter but due to different reasons than in electrical dipoles. In the case of a magnetic dipole, it is the large self-inductance of the coil that induces a large potential difference across its turns.

The non-linear effects generated by this voltage drop are outside the scope of this thesis, but we believe that it will attract charged particles and generate a plasma sheath due to the different response time of electrons and protons. According to Figure 6-1, not even a sequential compensation of every loop around the coil seems feasible. A way of lowering the voltage to acceptable levels would be to add a capacitor every couple meters of wire. This option, however, will increase the complexity of the design and will add joints and losses to the system.

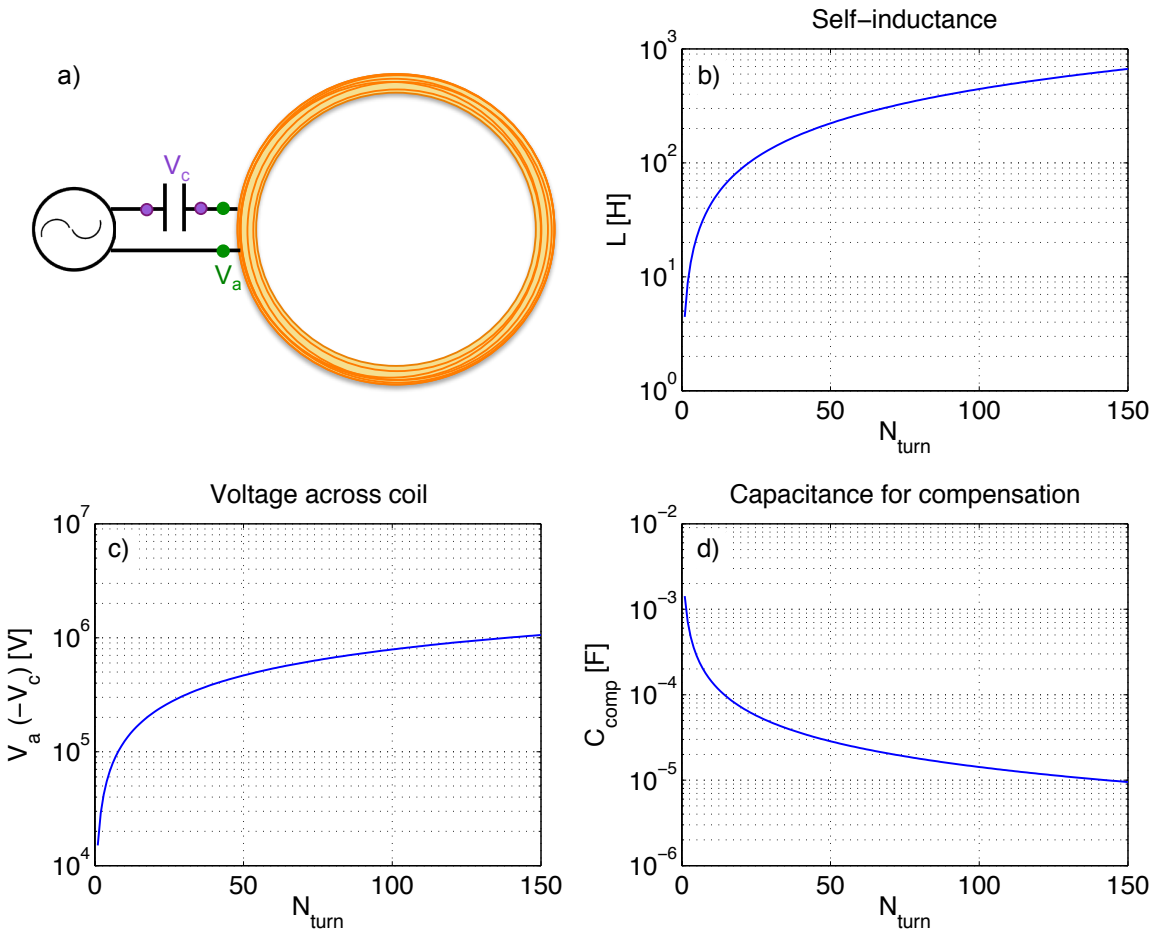


Figure 6-1: (a) LC circuit of an AC transmitter. (b) Self-inductance, (c) voltage across the loop and (d) capacitance required for compensation as a function of the number of turns. The plots are for $R_a = 15$ m, $T_c = 77$ K (critical temperature of the superconductor) and $f = 2$ Hz.

The solution to the problem involves DC operation: instead of an alternating current circulating around a static coil, we propose a direct current driven around a rotating coil. The rotation rate would have to match the desired wave frequency, which is unacceptably high

in the case of whistler waves but reasonable in the EMIC regime ($< 2$ Hz). The dipole component of this current distribution is equivalent to two orthogonally mounted static coils driven by a phased alternating current, as described in Section 3.4.5. Laboratory experiments developed at the UCLA Large Plasma Device (LAPD) tested a phased orthogonal two-loop antenna immersed in a magnetized plasma [*Gigliotti et al.*, 2009; *Karavaev et al.*, 2011], and they showed that it is capable of radiating Alfvén waves. Additionally, *Karavaev* [2010] also proposed a space-based rotating magnet with the purpose of radiating Alfvén waves, which is equivalent to the DC rotating coil idea.

The engineering implications of a rotating coil for radiation of EMIC waves are being analyzed in this dissertation for the first time and should be addressed in more detail in the future work given their relevance to the controlled removal of energetic Van Allen belt protons. The difficulty of implementing a DC rotating coil is primarily mechanical. Spinning a very large coil in space is not an easy task. In addition, Section 3.4.6 revealed that, in terms of radiation resistance, it is desirable to keep the axis of the loop perpendicular to the geomagnetic field lines, that is, to keep the rotation axis parallel to the angular velocity of the orbit. We showed in Figure 3-3, however, that the performance of the antenna is not very sensitive to the orientation for angles around this perpendicular orientation, which allows relaxation of the attitude requirements. This spin direction may introduce external torques to the system. Additionally, we believe that the *radiation drag* will impart a steady torque on the coil, which would have to be compensated, thus adding complexity to the Attitude Determination and Control System (ADCS). The dynamics of the antenna are currently being addressed by Gwendolyn Gettliffe [*Gettliffe et al.*, 2012], a Ph.D. candidate in the Space Systems Laboratory, and are briefly discussed at the end of the chapter. The following sections analyze the mechanical and thermal implications of a DC rotating coil transmitter, which involves superconductor technology and therefore active control of the antenna temperature.

## 6.2 Superconducting Materials: Wire Selection

The previous chapters revealed that superconducting materials are required to increase the radiated power from a space-based ULF magnetic coil antenna. As discussed in the previ-

ous section, a DC rotating coil antenna is the best candidate for our application, which is equivalent to a phased orthogonal two-loop configuration. Their radiation resistance, however, is several orders of magnitude smaller compared to electric dipoles, which is the reason why we need superconducting materials, large coil radius and multiple turn arrangements. Superconductors can carry very large current densities with minimal ohmic losses, which dramatically increase the total radiated power compared to regular conductors like copper wires. Two types of superconductors exist: low and high temperature superconductors. The difference between them is their critical temperature, which is the highest temperature possible for which they remain in a superconductive, non-resistive state. Low temperature superconductors (LTS) have a critical temperature below the boiling point of nitrogen (77 K), while those with critical temperatures above 77 K are classified as high temperature superconductors (HTS). Most LTS, however, are commonly found to have critical temperatures around 10 K or lower. The critical temperature of a superconducting material is related to the maximum current density and magnetic field that the wire can support before transitioning to a resistive state. The tremendous currents carried by these wires generate magnetic fields that limit the capability of neighboring wires to carry current. As the current increases the magnetic field also increases, which in turn decreases the maximum current density until the critical field is reached; increasing the current even further will cause a phenomenon referred to as quenching, whereby the superconductor turns resistive. The relationship between these three critical variables (temperature, current density and magnetic field) defines what is commonly known as the critical surface of a superconductor. LTS typically have higher critical current densities than HTS because at lower temperatures, the intrinsic pinning within the compounds is much stronger. A new 2nd generation (2G) of HTS, however, is capable of reaching critical current densities up to 1000 kA/cm$^2$ (per cross-sectional area of superconductor), larger than most low temperature superconductors. Furthermore, HTS materials are not confined to high temperature ranges, but they can be cooled down below 77 K with corresponding increase in current density. An example of a 2nd generation HTS wire is the superconducting tape presented in Figure 6-2 and commercialized by SuperPower. The SuperPower (RE)BCO-based 2G HTS consists of a flexible and high strength metal alloy tape as the base material, a ceramic-based superconductor, buffer layers and protective overlayers. The Surround Copper Stabilizer (SCS) encases the wire and is designed to prevent quenching from happening. Commercially available tapes

vary in width, ranging from 4 to 12 mm with a total thickness of 0.1 mm or less.

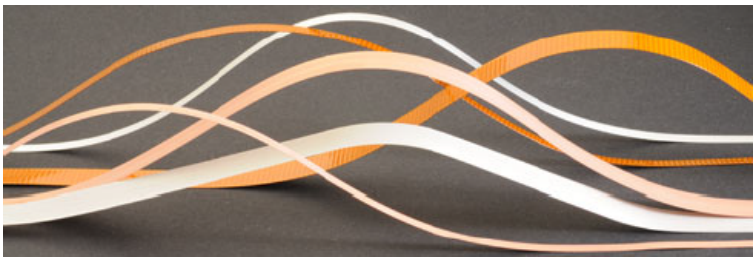

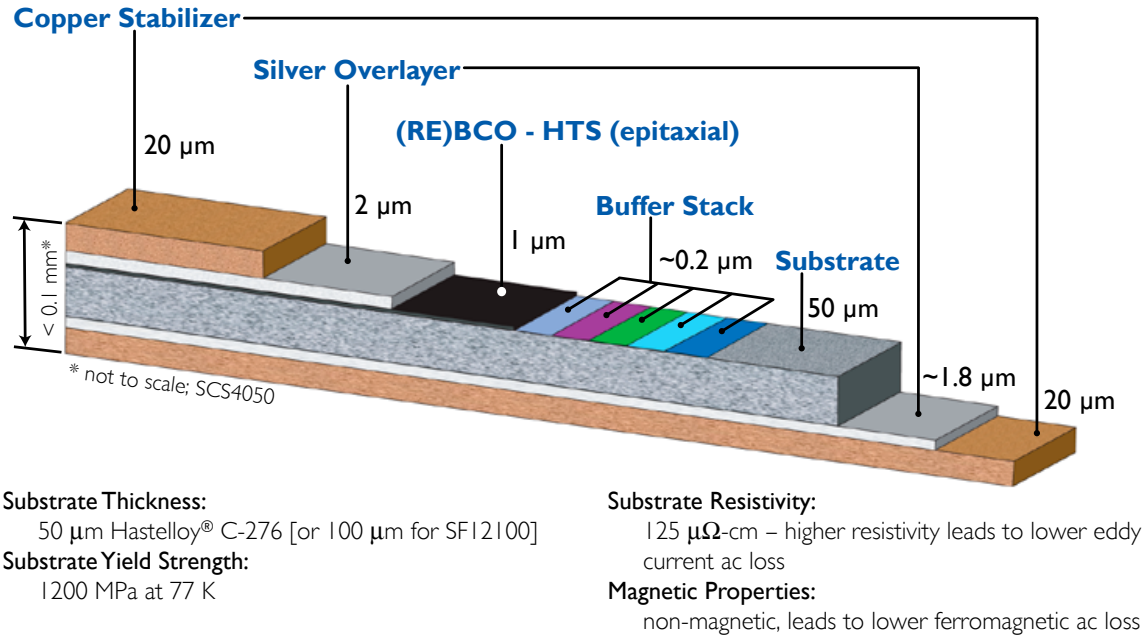


Figure 6-2: SuperPower (RE)BCO-based 2G HTS tape [*Hazelton*, 2012]

One of the most challenging aspects of using superconductors in space is the design of the cooling system. Even for HTS, the antenna has to be kept below 77 K, which requires active thermal control means in the case of spacecraft orbiting the Earth. In the case of LTS, the antenna would have to be maintained below 10 K, which translates into very large input power required by the cooling system. The demanding thermal requirements imposed by LTS need tremendous amounts of input power, to the point that the use of this type of superconductors is unfeasible for space applications. Details about the unattainable conditions required by LTS technology are provided in the following sections. The transmitter design presented below, however, builds upon the high temperature superconducting tape commercialized by SuperPower.

HTS have been used and proposed for different space applications. The Variable Specific

Impulse Magnetoplasma Rocket (VASIMR) [*Rey et al.*, 2002] and a concept called Magnetized Beamed Plasma Propulsion (MagBeam) [*Winglee et al.*, 2005] are two examples of propulsion systems that use HTS technology to generate magnetic nozzles and confine the plasma plumes. Other uses involve torque coils to de-saturate reaction wheels or control moment gyros, magnetic shielding for astronaut radiation protection [*Hoffman and Batishchev*, 2005] or Electromagnetic Formation Flight (EMFF). EMFF uses electromagnets coupled with reaction wheels to provide a propellant-less method for formation flight propulsion. More specifically, *Kwon* [2005] characterized the performance of HTS wires for EMFF applications; in a later work [*Kwon*, 2009], he studied consumable-free methods of maintaining isothermalization of a large HTS coil, which will be referenced throughout the chapter.

## 6.3 HTS Performance Characterization

In the following section we present a preliminary sizing of a single coil antenna as well as the characterization of its HTS critical variables. The maximum current in the superconductor is limited by the technology, while the coil size is set by mass and volume constraints. The sizing presented in this section is based on the largest dimensions of a single coil that can be reasonably launched. The remediation requirements in terms of number of coils of the nature described below will be analyzed in Chapter 7.

### 6.3.1 Preliminary Sizing

In this chapter we discuss the thermal and mechanical design of a DC coil antenna. The controlled removal of energetic Van Allen belt protons requires a huge amount of radiated power. For this reason, we will be dealing with the largest coil dimensions that can be reasonably launched. A scientific mission scaled down to detectability of the precipitating fluxes is analyzed later on in Chapter 7. The total wire length is a flexible parameter, only limited by the total mass and the torques on the antenna; a reference value of 10 km is considered in this chapter, and we discuss the scaling of the results with this parameter. Other wire lengths are also explored in Section 7.2 when outlining a scientific mission. The 10 km value came originally from an AC analysis, since in an AC case the wire length

is actually limited by the sheath formation onset, which would appear for wires longer than the wavelength of the waves (derivation detailed in Appendix B). In our DC rotating antenna, however, this limitation disappears. A reference coil radius is taken to be 15 meters due to deployment considerations based on standard launch vehicle fairing dimensions; the sensitivity of the loop performance to the coil radius is analyzed in the following sections. Innovative deployment techniques based on flexible concepts may allow the use of even larger coil radii, which should also be explored in future efforts. It must be noted that the deployment and dynamics of the system are outside the scope of this thesis and are currently being addressed by Gwendolyn Gettliffe [*Gettliffe et al.*, 2012] in the Space Systems Laboratory.

From the wire length and loop radius, the number of turns can be easily calculated as follows

$$N_{turn} = \frac{l_{wire}}{2\pi R_a} \tag{6.7}$$

where $l_{wire}$ and $R_a$ are the wire length and antenna radius, respectively. For $l_{wire} = 10$ km and $R_a = 15$ m, then $N_{turn} \approx 106$ turns.

The mass and dimensions of the HTS tape are taken from SuperPower specifications [*Hazelton*, 2012]. Commercially available HTS tape varies in width from 4 to 12 mm. Unless otherwise specified, we consider a width of 12 mm and thickness of 0.1 mm of the whole tape as given by SuperPower, which is the design capable of carrying the highest current. The mass density and proportion of the different layers in Figure 6-2 are summarized in Table 6.1.

The mass of wire in the coil can then be estimated as follows

$$\begin{aligned} m_{tape} &= l_{wire} * d * t * (\lambda_{Cu} * \rho_{Cu} + \lambda_{(RE)BCO} * \rho_{(RE)BCO} + \lambda_{Ag} * \rho_{Ag} + \lambda_{C276} * \rho_{C276} \\ &\quad + \lambda_{LaMnO_3} * \rho_{LaMnO_3} + \lambda_{MgO} * \rho_{MgO} + \lambda_{Y_2O_3} * \rho_{Y_2O_3} + \lambda_{Al_2O_3} * \rho_{Al_2O_3}) \end{aligned} \tag{6.8}$$

where $d$ and $t$ are the tape width and thickness, respectively. It must be noted that Table 6.1, as estimated from SuperPower data, is missing a %5 of material, which has been taken

Table 6.1: Mass density and area proportionality factors of SuperPower (RE)BCO-based 2G HTS tape

| | Mass density, $\rho_x$ [kg/m$^3$] | Area proportionality factor, $\lambda_x$ |
|---|---|---|
| Copper | 9080 | 40% |
| (RE)BCO | 6300 | 1% |
| Silver | 10490 | 3.8% |
| Hastelloy C-276 | 8890 | 50% |
| $LaMnO_3$ | 6570 | 0.05% |
| MgO | 3580 | 0.05% |
| $Y_2O_3$ | 5010 | 0.05% |
| $Al_2O_3$ | 3950 | 0.05% |

Table 6.2: Nominal sizing of the HTS tape coil

| | |
|---|---|
| Tape length, $l_{wire}$ [km] | 10 |
| Coil radius, $R_a$ [m] | 15 |
| # turns, $N_{turn}$ | 106 |
| Tape width, $d$ [mm] | 12 |
| Total tape thickness, $t$ [mm] | 0.1 |
| Superconductor thickness, $t_{sup}$ [$\mu$m] | 1 |
| Average tape density, $\langle\rho\rangle$ [$kg/m^3$] | 8548.2 |
| Total tape mass, $m_{tape}$ [$kg$] | 103 |

into account in the mass estimates below by multiplying by a correction factor. The average tape density follows immediately from the equation above

$$\langle\rho\rangle = \frac{m_{tape}}{l_{wire} * d * t} = 8548.2\ kg/m^3 \tag{6.9}$$

The nominal coil and tape dimensions described above together with the corresponding mass estimates are summarized in Table 6.2.

### 6.3.2 Critical Magnetic Field, Temperature and Current Density

The critical current density of the HTS tape is controlled by the self-induced magnetic field and operating temperature across the wire. Figure 6-3 [*Selvamanickam et al.*, 2012] shows the critical current of a single HTS tape as a function of the magnetic field for different wire temperatures. Figure 6-3 (a) presents the dependence on the parallel magnetic field, where

the parallel direction is defined in Figure 6-3 (c). Similarly, the current density dependence on the perpendicular field is presented in Figure 6-3 (b). From the figure it can be observed that the current density is more sensitive to the perpendicular than to the parallel field.

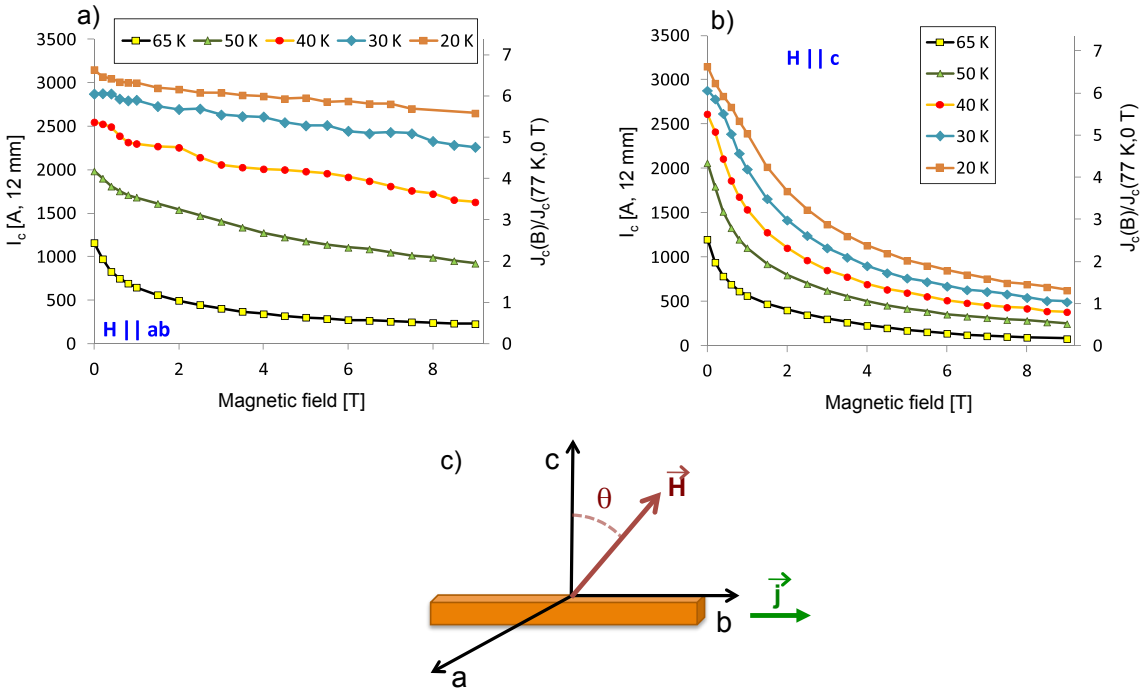


Figure 6-3: Critical current, $I_c$ of 75% Zr-added (Gd, Y)BCO superconducting tape for various temperatures as a function of (a) magnetic field parallel to the tape surface (B ∥ a-b), and (b) magnetic field perpendicular to the tape surface (B ∥ c) [*Selvamanickam et al.*, 2012]. (c) Coordinates relative to the superconducting HTS tape.

The normalized critical current dependence on temperature for different perpendicular magnetic fields is presented in Figure 6-4 (a)*. The curves are for a single HTS tape. It can be observed that the current starts to saturate as we go below 20 K. For this reason, it is strongly desired to operate below the nominal 77 K, since small temperature reductions produce large performance improvements. Section 6.4 will discuss the thermal implications of operating at these reduced temperatures. Figure 6-4 (b) shows again the normalized critical current as a function of the perpendicular magnetic field for a broader range of temperatures. Table 6.3 also presents the critical current at 77 K and 0 T along a single 2G HTS tape as a function of its width.

In our calculations we will treat each wire as a line current. The magnetic field generated

* SuperPower Inc.: www.superpower-inc.com. Last checked: June, 2013

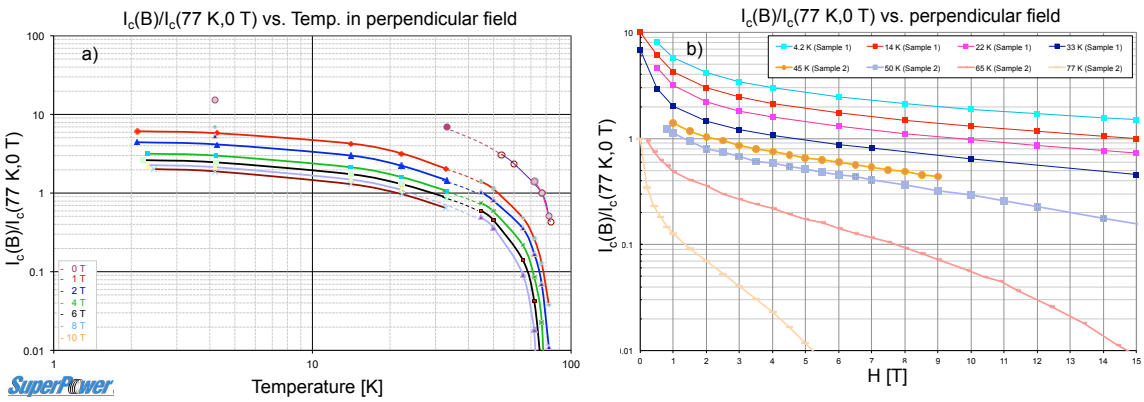


Figure 6-4: (a) Critical current, $I_c$, normalized to $I_c$(77K, 0T) as a function of temperature for different values of applied perpendicular magnetic field. (b) Critical current, $I_c$, normalized to $I_c$(77K, 0T) as a function of applied perpendicular magnetic field for different temperatures from SuperPower specifications.

Table 6.3: Critical current for different tape thicknesses

| $d$ [mm] | $I_c$(77 K, 0 T) [A] |
|---|---|
| 4 | 100 |
| 6 | 150 |
| 12 | 300 |

by a line current, $I$, at a distance $r$ can be estimated as follows

$$B = \frac{\mu_0 I}{2\pi r} \tag{6.10}$$

which is generated by each wire in the stack of $N_{turn}$ turns. This stack is presented in Figure 6-5. The superconducting tape appears in gray, and we have added 0.1 mm of insulator between each turn.

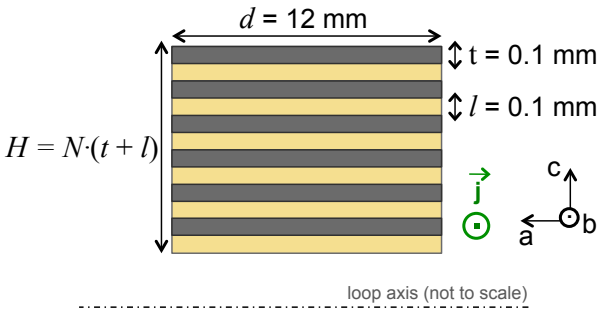


Figure 6-5: Coil cross section with $N_{turn}$ turns and insulator between each turn.

Each tape sees the magnetic field induced by the neighboring wires in the stack. The wires that see the maximum parallel magnetic field are the ones at the end of the stack, where all the contributions add up. For a stack with $N_{turn}$ turns, the maximum parallel magnetic field is

$$B_{\parallel_{max}} = \frac{\mu_0}{2\pi} \sum_{j=2}^{N_{turn}} \frac{I_j}{(j-1)(t+l)} \tag{6.11}$$

where $t$ and $l$ are the tape and insulator thicknesses, respectively.

According to Figure 6-3, however, the perpendicular field dominates the coil behavior. The stronger perpendicular field is reached at the edges of the inner radius of the loop. Since the loop has a very large radius of curvature the contribution to the perpendicular field will be mostly local. This field can be estimated by assuming an equivalent circular cross section with the same area as the stack of tapes

$$r_{eq} = \sqrt{\frac{dN_{turn}(t+l)}{\pi}} \tag{6.12}$$

where $d$ is the tape width. The maximum perpendicular field can then be found as follows

$$B_{\perp_{max}} = \frac{\mu_0 N_{turn} I_1}{2\pi r_{eq}} = \sqrt{\frac{N_{turn}}{\pi}} \frac{\mu_0 I_1}{4\sqrt{d(t+l)}} \tag{6.13}$$

where $I_1$ is the current in each tape.

Using the SuperPower single-tape data in Figures 6-3 and 6-4 we have constructed the critical surface of the HTS tape. This critical surface together with equations (6.11)-(6.13) allow us to calculate the critical variables as a function of the number of turns. These variables are presented in Figure 6-6 for three different temperatures and for the stack dimensions specified in Figure 6-5. The perpendicular field dominates the coil behavior, while the parallel field remains subcritical. The critical current of a 100-turn coil at 50 K increases by more than a factor of 2 compared to the case at 77 K, and by a factor of 3 when operating at 20 K. These results reaffirm the importance of working at low temperatures.

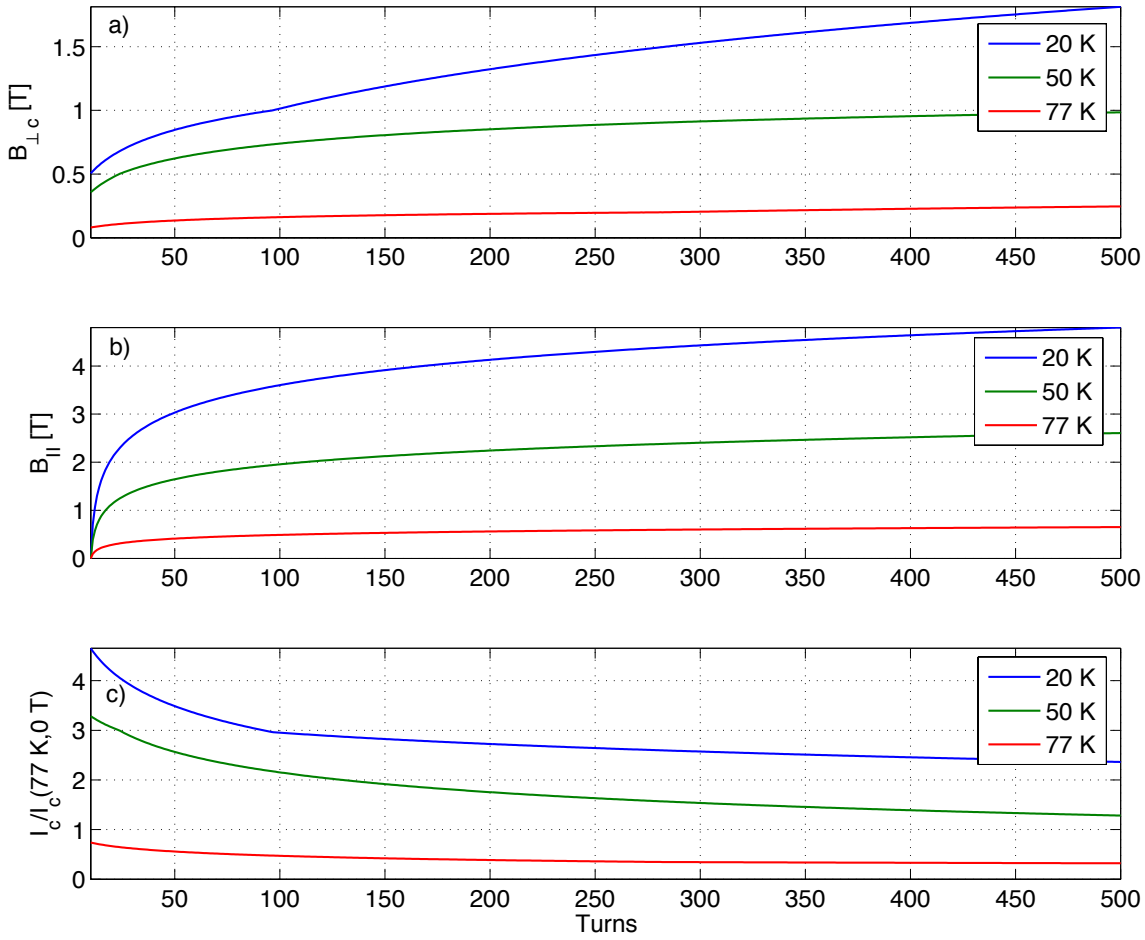


Figure 6-6: (a) Critical perpendicular magnetic field as a function of number of turns. (b) Parallel magnetic field (subcritical) as a function of number of turns. (c) Critical current, $I_c$, normalized to $I_c$(77K, 0T) as a function of number of turns. The dimensions of the stack have been taken from Figure 6-5.

### 6.3.3 Quench Failsafe System

A superconductor quenches when it goes from having no resistance (superconducting state) to being resistive (normal state). This change can be generated by a too large magnetic field inside the superconductor (above the critical value), a too large change of field (which generates eddy currents and heating), or a combination of both. The quenching process is accompanied by an increase in the rate of volumetric generation of heat, which may damage the transmitter. The copper in the HTS tape by SuperPower is a risk mitigation technique, designed to protect the wire in the event of a quench. At low temperatures, the copper is much less conductive than the superconductor. If quenching happens, the temperature will

rise, the superconductor will become resistive and the current will flow through the copper instead. The copper layer must be able to absorb all the stored magnetic energy, which is given by

$$E_M = \frac{L_{ind} I^2}{2} \tag{6.14}$$

where $I$ is the current and $L_{ind}$ is the self-inductance of the coil that was previously calculated in Section 6.1.

The copper must be able to absorb the stored magnetic energy, or in other words

$$E_M = \frac{L_{ind} I^2}{2} = m_{Cu} \int_{T_0}^{T_{melt}} c_{p,Cu}(T) dT \tag{6.15}$$

The mass of copper, $m_{Cu}$, can then be expressed as follows

$$m_{Cu} = \frac{E_M}{\int_{T_0}^{T_{melt}} c_{p,Cu}(T) dT} \tag{6.16}$$

where $c_{p,Cu}$(T) is the copper specific heat at constant pressure, $T_0$ is the operating temperature of the superconductor and $T_{melt}$ is the copper melting temperature. Typically, $T_{melt}$ = 1375.8 K, and $c_{p,Cu}$(T) is taken from tables [*White and Collocott*, 1984; *Manfreda*, 2011].

For the coil in Table 6.2 with an insulation between tapes of $l$ = 0.1 mm, operation at $T_0$ = 77 K, $I_c/I_c(77\ K, 0\ T) = 0.5$ and $I_c(77\ K, 0\ T, 12\ mm) = 300\ A$, the magnetic energy stored by the coil can be calculated as follows

$$E_M(77\ K) = \frac{470 * (300 * 0.5)^2}{2} \approx 5.3\ MJ$$

and the required mass of copper is

$$m_{Cu}(77\ K) = \frac{5.3 \cdot 10^6}{\int_{77}^{1375.8} c_{p,Cu}(T) dT} \approx 10\ kg$$

The mass of copper in the HTS tape is $l_{wire} * d * t * \lambda_{Cu} * \rho_{Cu}$ = 43.6 kg, which represents

a factor of safety of more than 4 according to the calculation above. It must be noted, however, that a detailed analysis should also consider the maximum temperature that the insulating material can support, which will probably be lower than the melting temperature of the copper.

If we operate at $T_0 = 50$ K, then the current can be higher because $I_c(50\ K)/I_c(77\ K, 0\ T) \approx 2$, which gives a stored magnetic energy of $E_M(50\ \text{K}) = 85$ MJ. The required copper mass in this case is

$$m_{Cu}(50\ K) = \frac{85 \cdot 10^6}{\int_{50}^{1375.8} c_{p,Cu}(T)dT} \approx 156\ kg$$

Similarly, for operation at $T_0 = 20$ K, the critical current goes up to $I_c(20\ K)/I_c(77\ K, 0\ T) = 3$, which gives $E_M(20\ \text{K}) = 190$ MJ and a copper mass of $m_{Cu}(20\ K) \approx 350$ kg.

We see above that operation at temperatures below 77 K requires a mass of copper larger than the one included the HTS tape arrangement, which could lead to damage of the superconductor in the event of a quench. Low temperatures, however, are desired since they have larger critical current that translate into larger radiated power. A possibility could be to accept more risk in the mission by keeping the SuperPower proportions of copper and relying on the thermal subsystem to cool down the superconductor. This option will be considered in the following sections.

In the case of low temperature superconductors (LTS), the copper involved to absorb the magnetic energy stored in our system would be several hundreds of tons, out of realm of what can be reasonably launched into space. Quenching management and thermal control are the main reasons why LTS are not used for space applications. On the ground, however, LTS are commonly used to generate large magnetic fields. One example of ground-based application is the CERN Large Hadron Collider (LHC) in Switzerland, which is the world's most powerful particle accelerator and consists of a 27-km ring of superconducting magnets. The LHC has enough copper to provide 1 s to dump heat away from the magnet; after that, the local hot-spot would overheat and eventually melt (L. Bottura, CERN Division LHC, personal communication, May 2013). The purpose of the copper is to provide a reaction time, but in a LTS high current density application it will never be enough to absorb the magnetic energy. In order to do that, LTS ground systems make sure that the

quench propagates to the whole system so that the complete mass (heat capacity) absorbs the magnetic energy (converted to heat through Joule heating). Another option used on the ground consists of extracting the energy from the system by dumping the circuit on an external resistance. All this complexity makes LTS unfeasible for space applications. For these reasons, our design is based on HTS superconductors, which have manageable quenching and thermal requirements.

## 6.4 Cooling Requirements and Thermal Control

The greatest challenge of working with superconductors in space is the design of the thermal control system. The environmental heat fluxes from the Sun and the Earth have to be rejected in order to keep the temperature of the superconductor below its critical value. In this section we find these fluxes and provide requirements and a preliminary design of the thermal system capable of maintaining good operational conditions.

### 6.4.1 Thermal Balance and Passive Control Means

The antenna will be subjected to environmental thermal loads from the Sun and the Earth. Figure 6-7 presents a schematic representation of the different fluxes and parameters relevant to the thermal balance in LEO/MEO (inner Van Allen belt), which will be used throughout this section.

The heat balance in steady state of a control volume that encloses the external coil surface can be written as follows

$$Q_a = Q_e + Q_t \tag{6.17}$$

where $Q_a$ [W] is the heat arriving to the antenna, $Q_e$ [W] is the emitted heat and $Q_t$ [W] is the heat that has to be removed by the cooling system to keep the desired HTS wire temperature. Both, $Q_t$ and the input power to the active thermal control system, will have to be evacuated to space using the spacecraft radiators. It must be noted that we have neglected any internal heat dissipation as well as ohmic losses from the superconductor, which should be carefully addressed in the future work. $Q_a$ has Sun, Earth and albedo

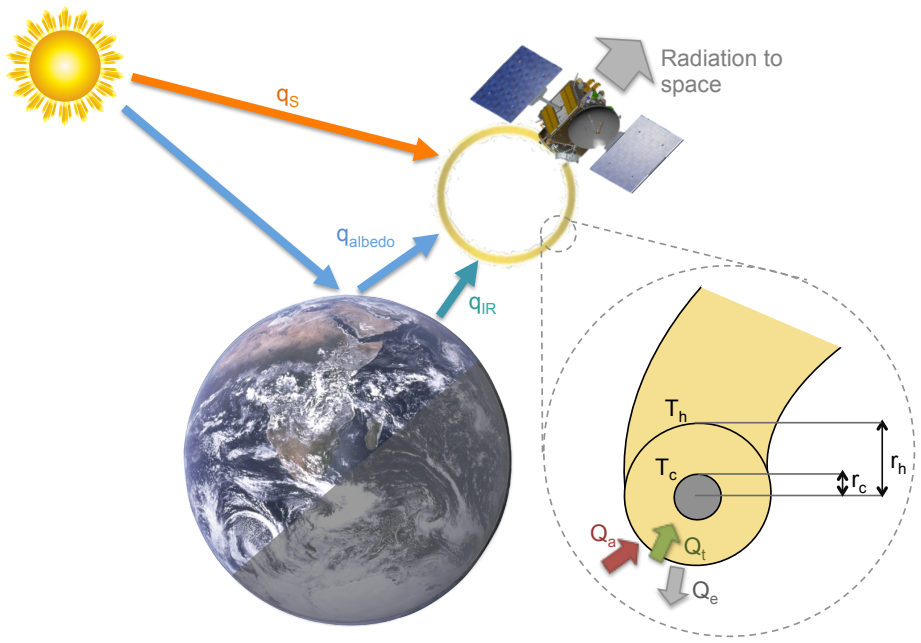


Figure 6-7: Schematic representation of the heat fluxes involved in the thermal balance of the superconducting coil antenna. The circular-equivalent cross section dimensions of the coil used in the thermal modeling are also shown. $r_h$ ($h$ for *hot*) represents the coil cross section radius, including all the tape turns (grey area) as well as the insulation and active thermal control around the coil (yellow area). $r_c$ ($c$ for *cold*) corresponds to the equivalent circular cross section of all the turns of HTS tape.

contributions, and it can be written as follows

$$Q_a = Q_{Sun} + Q_{Earth} + Q_{albedo} \tag{6.18}$$

where

$$Q_{Sun} = q_S \alpha A_S \tag{6.19}$$

$$Q_{Earth} = q_{IR} \varepsilon_h \sin^2(\rho) A_{IR} \tag{6.20}$$

$$Q_{albedo} = q_S \alpha a K_a \sin^2(\rho) A_a \tag{6.21}$$

where $q_S = 1367$ W/m$^2$ is the Sun's heat flux, $q_{IR} = 232$-$261$ W/m$^2$ is the Earth's infrared heat flux at equatorial orbit, and $\alpha$ and $\varepsilon_h$ are the coil's coating absorptivity and emissivity, respectively. $K_a$ accounts for the collimation of the energy reflected from the Earth, $a$ is the albedo factor and $\rho$ is the angular Earth radius. These parameters are given by

$$\sin(\rho) = \frac{R_E}{h + R_E} \tag{6.22}$$

$$K_a = 0.664 + 0.521\rho - 0.203\rho^2 \tag{6.23}$$

where $h$ is the orbit altitude, which in our case is taken to be circular and equatorial at $L = 1.5$, that is $h = 0.5R_E$.

$A_S$, $A_{IR}$ and $A_a$ are the areas of the coil receiving the Sun, Earth and albedo heat fluxes, respectively. These areas are taken to be the same, equal to a conservative value given by

$$A_S = A_{IR} = A_a = \pi\left[(R_a + r_h)^2 - (R_a - r_h)^2\right] = 4\pi R_a r_h \tag{6.24}$$

which considers a coil with an equivalent circular cross section as represented in Figure 6-7. $r_h$ corresponds to the coil cross section radius, including all the tape turns as well as the insulation and thermal control around the coil.

The heat emitted to space can be expressed as follows

$$Q_e = \sigma\varepsilon_h\left(T_h^4 - T_e^4\right)A_h \tag{6.25}$$

where $\sigma$ is the Stefan-Boltzmann constant, $\varepsilon_h$ is the emissivity of the coating, $T_e = 4$ K is the approximate temperature of the near-vacuum of space, $A_h$ is the coil surface area at $r_h$, and $T_h$ is the temperature of that surface, which we want to find.

Based on *Kwon* [2009], the best combination of passive thermal control means consists of Multi Layer Insulator (MLI) together with Quartz over Silver Optical Solar Reflector (OSR) coating. OSR minimizes the solar absorptivity ($\alpha$) and maximizes the infrared emissivity ($\varepsilon_h$). MLI blankets are a common method of insulating spacecraft, which consist of layers

of low emittance silvered film of aluminized Mylar with low conductance spacers like silk netting, fiberglass paper, or other polyester materials. Radiation is the main method of heat transfer within the MLI; gaseous conduction is negligible for operation in space, and solid conduction is commonly reduced by crinkling the Mylar layers, thus minimizing the contact between them. A schematic of an MLI blanket is represented in Figure 6-8 on the left [*Wertz and Larson*, 2007, Sec. 11.5].

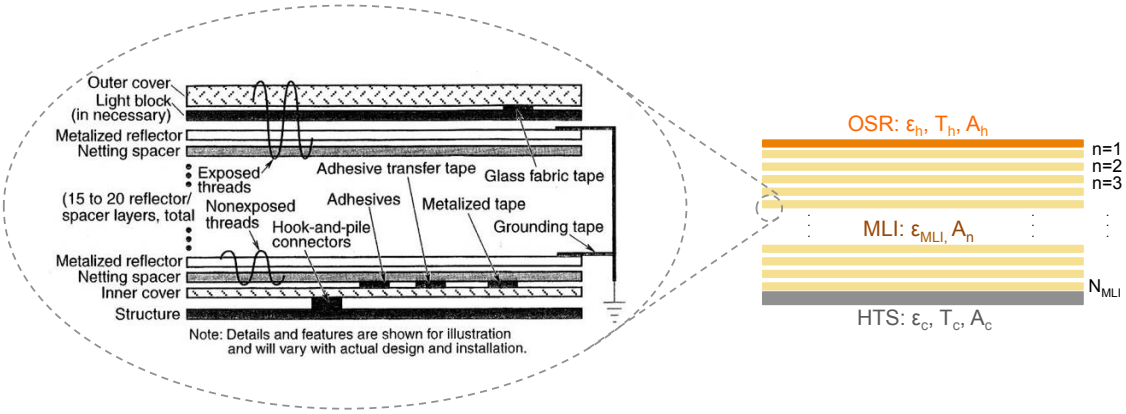


Figure 6-8: Schematic representation of an individual MLI blanket [*Wertz and Larson*, 2007, Sec. 11.5] (left) and the arrangement of $N_{MLI}$ layers of superconductor with an OSR coating (right).

Following [*Siegel and Howell*, 2002, Sec. 8.2], each layer of MLI can be modeled as a non-contacting vacuum gap, which assumes that radiation is the only form of heat transport in the insulator. An effective emissivity, $\varepsilon_t$, of the $N_{MLI}$ non-contacting layers of MLI is given by

$$\varepsilon_t = \frac{1}{\frac{1}{\varepsilon_c} + \frac{A_c}{A_h}\left(\frac{1}{\varepsilon_h} - 1\right) + \sum_{n=1}^{N_{MLI}} \frac{A_c}{A_n}\left(\frac{2}{\varepsilon_{MLI}} - 1\right)} \tag{6.26}$$

where $\varepsilon_{MLI}$ is the emissivity of the MLI layers, $A_n$ is the area of each MLI layer, $\varepsilon_c$ is the emissivity of the HTS tape surface and $A_c$ is the area at the surface of the HTS arrangement at $r_c$, which is represented in Figure 6-7 and includes all turns of tape. The MLI arrangement and the different parameters listed above are illustrated in Figure 6-8 on the right. The cross-sectional radius at the surface of the superconductor arrangement, $r_c$, can be found by considering all the turns of superconducting tape

$$r_c = \sqrt{\frac{N_{turn} t d}{\pi}} \tag{6.27}$$

Similarly, the cross-sectional radius at the outside surface of the coil, $r_h$, can be found by taking a thickness of each MLI layer of $t_{Mylar}$, and assuming a gap between the surface of the superconductor and the thermal insulator of $4r_c$ (allocated to the active thermal control system)

$$r_h = r_c + 4r_c + N_{MLI} * t_{Mylar} = 5r_c + N_{MLI} * t_{Mylar} \tag{6.28}$$

The corresponding areas in equation (6.26) are

$$A_c = 4\pi^2 R_a r_c \tag{6.29}$$

$$A_h = 4\pi^2 R_a r_h \tag{6.30}$$

$$A_n = 4\pi^2 R_a \left(5r_c + n * t_{Mylar}\right) \tag{6.31}$$

where $n$ is the summation index in equation (6.26).

The mass of the MLI blanket can also be easily calculated as follows

$$m_{MLI} = 4\pi^2 * R_a * r_h * t_{Mylar} * \rho_{MLI} \tag{6.32}$$

where $\rho_{MLI}$ is the average density of the MLI blanket.

Using the definition of $\varepsilon_t$ above, the heat that has to be removed by the cooling system to keep the desired HTS wire temperature, $T_c$, is

$$Q_t = \sigma \varepsilon_t \left(T_h^4 - T_c^4\right) A_c \tag{6.33}$$

Substituting into equation (6.17) and solving for $T_h$

$$T_h^4 = \frac{1}{\sigma} \frac{\left(q_S \alpha + q_{IR} \varepsilon_h \sin^2(\rho) + q_S \alpha K_a \sin^2(\rho)\right) A_a + \sigma \varepsilon_t T_c^4 A_c + \sigma \varepsilon_h T_e^4 A_h}{\varepsilon_t A_c + \varepsilon_h A_h} \tag{6.34}$$

and substituting back into $Q_t$, we get the following expression for the heat that has to be removed from the system, $Q_{cool}$

$$Q_{cool} = Q_t = \varepsilon_t A_c \left[ \frac{\left(q_S \alpha + q_{IR} \varepsilon \sin^2(\rho) + q_S \alpha K_a \sin^2(\rho)\right) A_a + \sigma \varepsilon_h T_e^4 A_h - \sigma \varepsilon_h T_c^4 A_h}{\varepsilon_t A_c + \varepsilon_h A_h} \right] \tag{6.35}$$

The condition $Q_t = 0$ is the boundary that determines whether we should use thermal insulation. If $Q_t > 0$, the transmitted heat flows radially inwards, thus thermal insulation (MLI) is required to keep $T_c$ at the desired operating value. Contrarily, if $Q_t < 0$ (i.e. the term $-\sigma \varepsilon_h T_c^4 A_h$ dominates), then thermal insulation should be avoided because the transmitted heat wants to flow radially outwards from the superconductor. In the case under consideration, however, $Q_t > 0$ for all the cases and MLI blankets are always required.

Figure 6-9 (a) presents the transmitted heat (equal to the heat to be removed from the system, $Q_{cool}$) as a function of the number of MLI layers. The figure corresponds to the coil design in Table 6.2 together with the thermal parameters in Table 6.4. Different superconductor temperatures are presented; the heat to be removed from the system, however, is close to independent of the HTS temperature because $T_c \ll T_h$ in equation (6.33). The transmitted heat decreases with increasing MLI thickness, but more MLI layers also add noticeable mass to the design, as we see in Figure 6-9 (b). We must note that, in our simplified MLI model, the heat load is reduced as more insulation is added to the antenna. Real MLI's, however, suffer a decrease in performance after a certain number of layers are added to the system [*Gilmore*, 1994]. For this reason, the calculations in the following section limited to 30 layers of MLI.

Table 6.4: Thermal balance parameters. MLI properties are taken from *The Gund Company, Inc.* [2013].

| Orbit | Equatorial at $L = 1.5$ |
|---|---|
| Mylar sheet thickness, $t_{Mylar}$ | 225 $\mu$m |
| MLI average density, $\rho_{MLI}$ | 1.391 g/cm$^3$ |
| $q_S$ | 1367 W/m$^2$ |
| $q_{IR}$ | 261 W/m$^2$ |
| Albedo factor, $a$ | 0.26 |
| $T_e$ | 4 K |
| $\alpha$ | 0.079 |
| $\varepsilon_h$ | 0.79 |
| $\varepsilon_{MLI}$ | 0.05 |
| $\varepsilon_c$ | 0.052 |

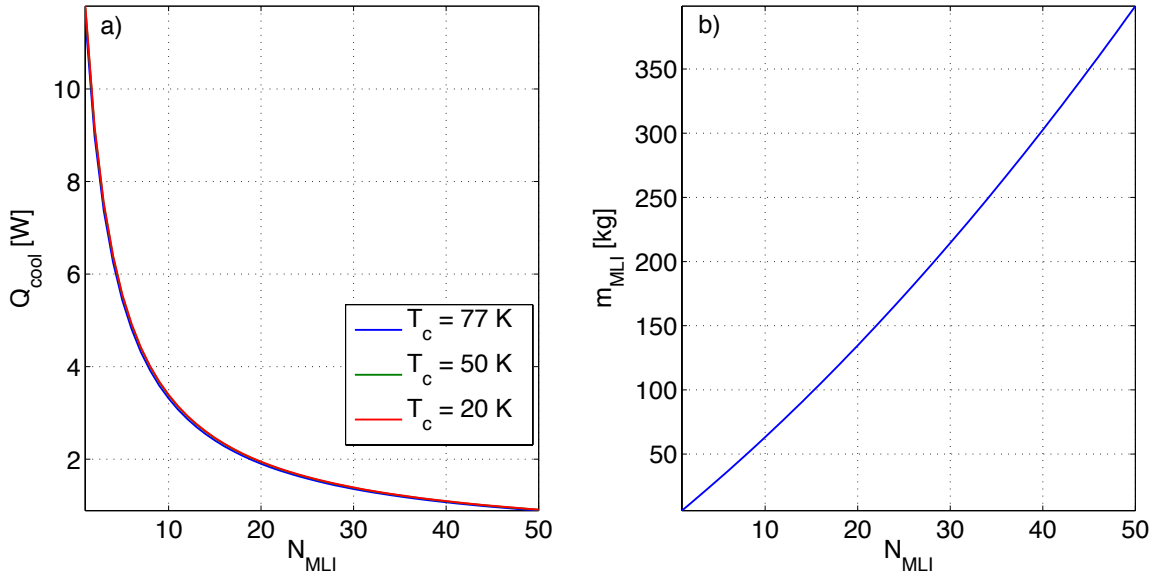


Figure 6-9: (a) Heat to be removed from the system ($Q_{cool} = Q_t$) as a function of the number of Mylar layers. (b) MLI mass as a function of the number of layers.

### 6.4.2 Active Thermal Control

The low operating temperatures of superconductors require the use of cryogenics to cool down the system. The selection of the cryogen depends on the operating temperature. Three main approaches have been commonly used to control the temperature of superconductors:

1. **Liquid cryogenic cooling:** The superconducting wires are immersed in a liquid cryogen (LN or LHe), which has to be circulated between them. The heat is extracted by evaporation of the liquid. This system ensures uniform cooling and isothermal conditions. A common example of this technique are MRI machines used in hospitals. In space, however, the evaporation of the cryogen would severely limit the lifetime of the mission.

2. **Closed cycle refrigeration:** Likewise the previous approach, superconductors are also immersed in a liquid cryogen; the heat, however, is not evacuated by evaporation of the cryogen but by taking advantage of a refrigeration cycle like Joule-Thomson coolers, Stirling coolers, Collins cycle, etc. These systems require lots of power and are capital intensive.

3. **Conduction cooling by direct contact with a cryocooler:** In this approach, the superconductor is "dry". The cryocoolers are capable of cooling down their own tips to cryogenic temperatures and removing the heat from the system via a refrigeration cycle. These devices are small and the thermal load can be divided among a multiplicity of them. However, they only provide a point of contact with the hot surface, which could lead to non-uniform temperature distributions and quenching of the superconductor.

In this thesis we propose an **hybrid thermal control system** similar to the one presented by *Kwon* [2009]. The superconducting wire is placed inside a flexible forced vapor system that ensures isothermalization, while several cryocoolers extract the heat from the vapor. The vapor (LN or LHe, depending on the required temperature) cools down at the cold tip of the cryocoolers and heats up again as it circulates through the loop antenna. This approach still requires a reservoir, but much smaller compared to the liquid cryogenic cooling because the hybrid system reuses the fluid.

*Kwon* [2009] proposed to use a heat pipe together with cryocoolers, where the circulation of the fluid around the superconductor occurs passively. However, a study developed in the Space Systems Laboratory at MIT together with the University of Maryland revealed the need for a forced vapor system. Heat pipes at cryogenic temperatures are very stiff, which will hinder the deployment of a flexible structure. This issue is made worse by the capillarity required by such passive systems. For this reason, it was decided to back out of the passive nature of the heat pipe in favor of a design based on a forced vapor flow. Raymond Sedwick at the University of Maryland is actively working on the design and testing of the forced vapor cooling approach [*Miller*, 2013]. Sedwick proposes a design where the MLI acts as the enclosure of the active cooling system. Recently, he tested the properties of Mylar at cryogenic temperatures, which remained flexible thus providing confidence on the feasibility of the concept. Sedwick's experiments also cover expansion tests of a prototype forced vapor pipe. The tested structures so far involve segmented expandable vent tubes reinforced with PVC collars glued to the vent segments. This construction technique substantially reduces the axial twisting observed during inflation in previous continuous vent tube designs. In the case of a forced vapor system, the expansion can be done by pressurization of the cooling vapor rather than by self-repulsion of the coil current, which avoids cryogenic temperatures during the deployment phase.

One or several cryocoolers would need to be placed to remove the heat from the forced vapor system. Stirling cycle cryocoolers have been successfully used in space for cold tip temperatures above 50 K, and they are efficient and reliable. The Stirling cycle has two isothermal and two constant volume processes. These devices consist of a displacer unit, a compressor pump and a regenerative heat exchanger or *regenerator*. Sunpower cryocoolers are one of those systems and they have heritage in space applications. Figure 6-10 shows one of the SunPower cryocoolers, where the different parts have been indicated. In addition to the cryocoolers, we would need to size the spacecraft radiations capable of rejecting both, the thermal load and the input power to the active system, which will be connected to the heat rejection zone of the cryocoolers. Similarly, Figure 6-11 presents the performance of the space qualified Sunpower M87N cryocooler [*Shirley et al.*, 2005]. Figure 6-11 (a) shows the cold tip temperature as a function of the thermal load for various input powers, while Figure 6-11 (b) presents the input power as a function of the cold tip temperature for different thermal loads. In this figure we can observe that it would be practically impossible

to remove heat from LTS superconductors using relatively small cryocoolers because a cold tip temperature of 4.2 K translates into huge input powers for very small thermal loads. In the case of HTS at 77 K, however, we can remove 7.5 W of heat with an input power of 150 W and a cryocooler weight of less than 3 kg.

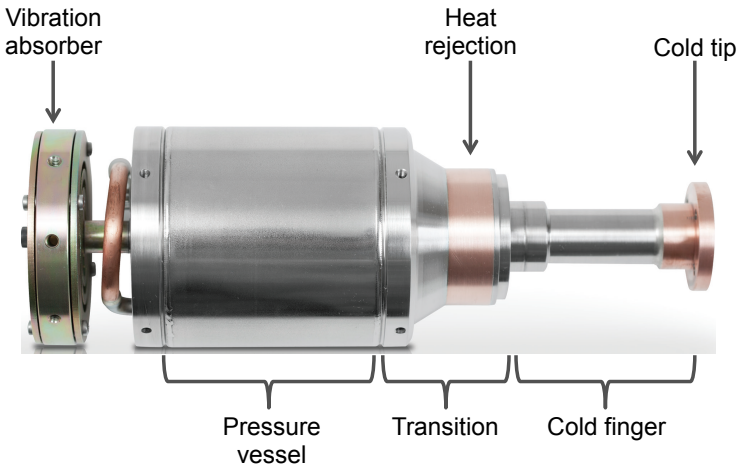


Figure 6-10: SunPower CryoTel MT [*SunPower Inc.*, 2013]

Nevertheless, we saw in Figure 6-4 that the critical current of HTS suffers a dramatic increase for operation at $T_c = 20$ K, where the curve starts to saturate. The last fifteen years of space missions have been limited to cryogenic temperatures between 55-150 K. Cooling technology for future NASA missions, however, involves the development of cryocoolers with specifications very similar to the ones of our particular application [*Ross Jr and Boyle*, 2006]. More specifically, the Jet Propulsion Laboratory (JPL) has developed and delivered two sorption LH coolers, which will be used to cool the microwave radio receivers of the Planck spacecraft of the European Space Agency (ESA). Each of these cryocoolers provides 1 W of cooling at 20 K, has a power consumption of 470 W (end of life) and weights 54 kg [*Bhandari et al.*, 2004]. In the following analysis, we use the numbers from the Planck sorption cooler to estimate the performance of the antenna at 20 K, while the Sunpower cryocoolers in Figure 6-11 are used for operation above 50 K.

For $T_c = 77$ K, 30 layers of MLI, operating at the critical current given by Figure 6-6 (c) and for the parameters in Tables 6.2 and 6.4, we found that the heat to be removed by the active cooling system is $Q_{cool} = 1.36$ W; this thermal load can be handled by a single Sunpower cryocooler with an input power of $P_{cryo} = 33$ W. Similarly, for a superconductor

temperature of $T_c = 50$ K, the thermal load is $Q_{cool} = 1.38$ W, which also requires one cryocooler with an input power of $P_{cryo} = 95$ W. For the case at $T_c = 20$ K, the thermal load is also small, $Q_{cool} = 1.39$ W, but the low cold tip temperature requires two Plank-like cryocoolers with a total input power of $P_{cryo} = 940$ W. Again, we should emphasize that not only we need the cryocoolers but also the spacecraft radiators capable of rejecting this heat away from the system. The temperature of the radiator sets the heat that it is capable of removing; the larger the temperature the more heat it can reject, but high temperatures could affect the rest of the thermal subsystem. This tradeoff should be analyzed in the future work when addressing the radiator design.

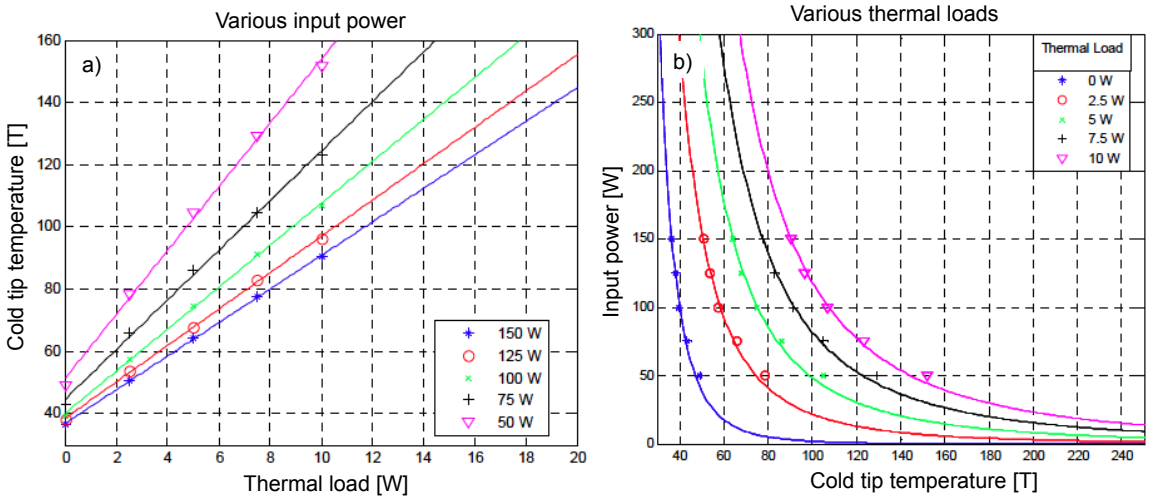


Figure 6-11: Sunpower M87N cryocooler performance characterization [*Shirley et al.*, 2005]. (a) Cold tip temperature as a function of the thermal load for different input powers. (b) Input power as a function of the cold tip temperature for different thermal loads

The mass of the active thermal control system can finally be estimated from the test experiments mentioned above as follows

$$m_{thermal} = m_{MLI} + m_{cryos} + m_{collar} + m_{active} \tag{6.36}$$

where $m_{MLI}$ was derived in equation (6.32), $m_{cryos}$ is the total mass of the cryocoolers, $m_{collar}$ accounts for the PVC collar supports of the forced vapor structure and $m_{active}$ includes the coolant, dewar and fan system. For $m_{active}$, we assume a total mass of 20 kg including the dewar, coolant and fan systems. For the PVC support collars we consider a density of $\rho_{PVC} = 1.4$ g/cm$^3$, a collar radius of $5r_c = 5.51$ cm, a width of 1 cm and a

Table 6.5: Active thermal control system power and mass estimates

| Superconductor temperature, $T_c$ [K] | 77 | 50 | 20 |
|---|---|---|---|
| Coil sizing | Table 6.2 | | |
| Thermal parameters | Table 6.4 | | |
| Number of MLI layers, $N_{MLI}$ | 30 | | |
| Thermal load, $Q_{cool}$ [W] | 1.36 | 1.38 | 1.39 |
| Number of cryocoolers, $n_{cryo}$ | 1 | 1 | 2 |
| Input power, $P_{cryo}$ [W] | 33 | 95 | 940 |
| Cryocooler mass, $m_{cryo}$ [kg] | 3 | 3 | 108 |
| MLI mass, $m_{MLI}$ [kg] | 215 | | |
| PVC support collar mass, $m_{collar}$ [kg] | 2 | | |
| Dewar/coolant/fan mass, $m_{active}$ [kg] | 20 | | |
| Total active thermal system mass, $m_{thermal}$ [kg] | 240 | 240 | 345 |

thickness of 2 mm [†]. Based on Sedwick's experiments at the University of Maryland, we place 3 collars per meter of coil, which gives a total of $n_{collar} = 283$ collars around a 15 m coil radius. The total mass of the PVC collars is then

$$m_{collar} = \rho_{PVC} * 2 * \pi * 5r_c * 0.002 * 0.01 * n_{collar} \approx 2\ kg \tag{6.37}$$

which is indeed a very small fraction of the total mass of the system. Table 6.5 summarizes the different active thermal control parameters for HTS temperatures of $T_c = 77$ K, 50 K and 20 K. The values in the table do not consider any margin in the power and mass estimates, but they will be added in Section 7.2 when outlining a scientific mission.

## 6.5 Dynamics Considerations

In this section we outline the dynamics of the DC rotating coil and present preliminary calculations. The detailed dynamics, however, are outside the scope of this thesis and should be carefully addressed in future efforts.

The DC coil is rotating at the EMIC frequencies. In addition, we saw in Section 3.3 that the coil axis should remain close to perpendicular to the Earth's magnetic field (not too sensitive according to Figure 3-3) since it maximizes the power radiated from the antenna.

[†] G. Gettliffe, personal communication, June 2013

This configuration is illustrated in Figure 6-12. Three main torques will be acting on the coil: gyroscopic, magnetic and gravity gradient torques, which are described next.

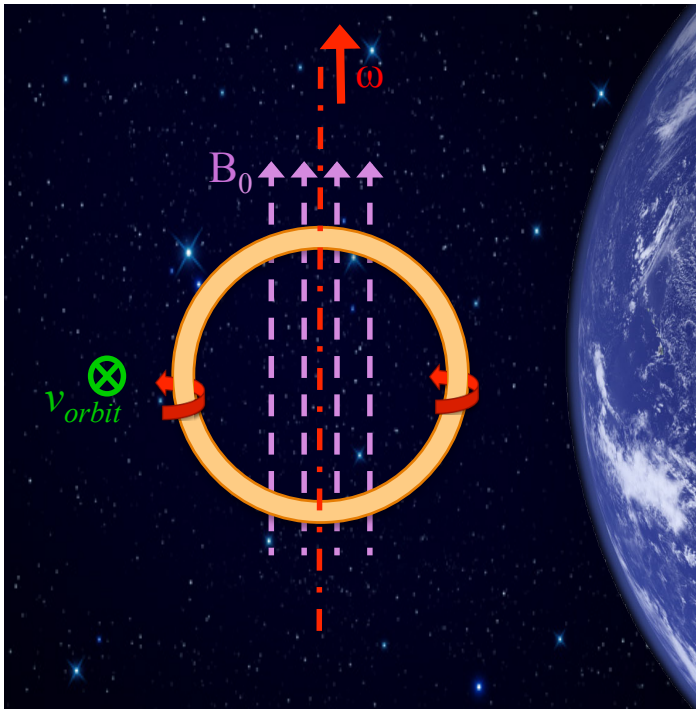


Figure 6-12: Orientation and rotation that maximizes the power radiated from the antenna. The axis of the coil (normal to the surface enclosed by the antenna) is always perpendicular to the Earth's magnetic field.

The gyroscopic torque, $\tau_{gyro}$, appears from the transformation between inertial and body-axes frames. Call $\vec{\omega}_i$ the inertial angular velocity of the antenna, and $\vec{L}$ its angular momentum. The torque on the spacecraft equals the rate of change of $\vec{L}$ in the inertial axes

$$\vec{T} = \frac{d\vec{L}}{dt}|_i \tag{6.38}$$

We can find the rate of change as seen from the body-axes using the Coriolis' Theorem as follows

$$\frac{d\vec{L}}{dt}|_i = \frac{d\vec{L}}{dt}|_b + \vec{\omega}_i \times \vec{L} \tag{6.39}$$

In orbital axes (local-vertical, local-horizontal), the inertial angular velocity can be decomposed as follows

$$\vec{\omega}_i = \vec{\Omega}_{orbit} + \vec{\omega} \tag{6.40}$$

where $\vec{\Omega}_{orbit}$ is the angular velocity of the orbit and $\vec{\omega}$ is the spin rate of the antenna or angular velocity in the orbital axes. The angular momentum can then be written as follows

$$\vec{L} = [I] \cdot \left( \vec{\Omega}_{orbit} + \vec{\omega} \right) \tag{6.41}$$

where $[I]$ is the transmitter's tensor of inertia in principal axes. Rearranging Euler's equation we get

$$[I] \frac{d\vec{\omega}}{dt}|_b + \vec{\omega} \times [I] \cdot \vec{\omega} = \vec{T} - \vec{\Omega}_{orbit} \times [I] \cdot \left( \vec{\Omega}_{orbit} + \vec{\omega} \right) - [I] \frac{d\vec{\Omega}_{orbit}}{dt}|_b \tag{6.42}$$

where everything is expressed in orbital axes. The terms in the right-side of the equation come from the transformation between inertial to body-axes frames. Taking $\vec{\Omega}_{orbit} = \text{const}$, the only remaining term is the so called gyroscopic torque

$$\vec{\tau}_{gyro} = \vec{\Omega}_{orbit} \times [I] \cdot \left( \vec{\Omega}_{orbit} + \vec{\omega} \right) \approx \vec{\Omega}_{orbit} \times [I] \cdot \vec{\omega} \tag{6.43}$$

We must emphasize that this is an internal torque and therefore does not change the angular momentum in the inertial frame, but it does in the orbital frame. This torque is zero for $\vec{\Omega}_{orbit} \parallel \vec{\omega}$, and in the presence of dissipation, it is stable to small perturbations when spinning around a major axis of inertia, as we will describe below.

An approximation to the worst-case torque (which happens when the rotation axis is in the plane of the orbit) is then

$$\tau_{gyro}|_{max} = \Omega_{orbit} * \omega * I_r \tag{6.44}$$

where $I_r = m_{coil} * R_a^2$ is the coil's polar inertia. For an equatorial orbit at $L$=1.5 then $\Omega_{orbit}$ = $6.75 \cdot 10^{-4}$ rad/s. Taking $\omega = 3.15$ rad/s (0.5 Hz), $m_{coil} = 350$ kg (for a wire length of 10 km, including HTS and thermal system) and $R_a = 15$ m, this gives a gyroscopic torque of $\tau_{gyro}|_{max} = 165$ N·m.

Another relevant torque is the magnetic torque, $\tau_{mag}$, which can be calculated as follows

$$\vec{\tau}_{mag} = \vec{\mu} \times \vec{B}_0 \tag{6.45}$$

where $\mu = N_{turn} * I * \pi R_a^2$ is the magnetic moment of the coil with direction given by the right-hand rule. The effect of this torque is to align the magnetic moment of the antenna, normal to the coil surface, with the external magnetic field direction. The worst-case magnetic torque can be approximated as follows

$$\tau_{mag}|_{max} = N_{turn} * I * \pi R_a^2 * B_0 \tag{6.46}$$

Taking $B_0 = 8 \cdot 10^{-6}$ T, $I = 300$ A, $N_{turn} = 106$ and $R_a = 15$ m, we get a magnetic torque equal to $\tau_{mag}|_{max} = 180$ N·m.

Finally, the gravity gradient torque, $\tau_{gg}$, tends to align the coil's axis of smaller inertia with the vertical direction towards the Earth's center. This torque has a complex form, but a worst-case approximation can be easily calculated as follows

$$\tau_{gg}|_{max} = 3 * \Omega_{orbit}^2 * I_r \tag{6.47}$$

which equals $\tau_{gg}|_{max} = 0.1$ N·m for the values considered above and is negligible compared to the gyroscopic and magnetic torques.

The gyroscopic and magnetic effects represent the main contribution to the torque. The gyroscopic torque cancels for $\vec{\Omega}_{orbit} \parallel \vec{\omega}$, and it is stable when spinning around a major axis of inertia; this configuration, however, corresponds to maximum magnetic torque, which also impacts the dynamics of the coil. Additionally, we would like to spin the coil as represented in Figure 6-12, since it provides the largest radiated power.

We believe that the solution to the dynamics problem described above involves a coil rotating as shown in Figure 6-12, but with the spacecraft subsystems distributed on both sides of the coil such that the body becomes a major-axis spinner. This change of inertia would provide a much larger gyroscopic stability compared to the perturbations introduced by the magnetic torque, as we will exemplify below. A spinning disc would be an equivalent

representation of our distributed system in terms of inertia, which is gyroscopically stable even in the presence of dissipation. The configuration is illustrated in Figure 6-13, where (x,y,z) and (LH,LV,$Z_o$) are the body and orbital axes, respectively.

Prof. Enrico Lorenzini from the Unversity of Pavoda has done some preliminary calculations on the dynamics problem presented here, which we summarize next. Enrico considers the dynamics of this spinning disc, which is a major-axis spinner with z-body axis perpendicular to the orbital plane. The Earth's magnetic dipole field is assumed aligned with the normal to the orbit, which is considered equatorial. The magnetic torque is therefore along the y-axis, and it is approximately constant. It must be noted, however, that in the presence of a tilted dipole the torque would have $x$ and $y$ oscillating components, but their magnitude would be bounded. For a body acted by constant magnetic torque, $\tau_{mag_y}$, perpendicular to the angular momentum $\vec{L}$ as an initial condition, it can be shown that the magnitude of this angular momentum is conserved on average, and that the vector $\vec{L}$ precesses describing a small cone if the spin rate is sufficiently large. A criterion for $\vec{L}$ precession stability is given by [*Thomson*, 1986]

$$\omega > \frac{2}{I_z}\sqrt{\tau_{mag_y} I_y} \tag{6.48}$$

which depends on the ratio $\sqrt{I_y}/I_z$. Consider a magnetic torque of magnitude $\tau_{mag_y} = 180$ N·m as calculated above, and a distributed system with $I_y$ =$10^4$ kg·m$^2$ and $I_z/I_y = 1.9$; then the minimum spin rate for stability would be $\omega > 0.14$ rad/s (0.02 Hz). Similarly, for $I_z/I_y$ = 1.2, this minimum spin rate is $\omega > 0.22$ rad/s (0.03 Hz). In other words, for a frequency of $\omega = 3.14$ rad/s (0.5 Hz), the ratio of inertias should be $I_z/I_y > 0.08$, which gives room for many design options. However, if we want the body to be a major-axis spinner the condition $I_z/I_y > 1$ will prevail over the previous one. Our frequency will therefore set the configuration of the distributed system in order to satisfy the inertia requirements, that is, the length of the trusses and location of the spacecraft subsystems.

For unbalanced initial conditions, the results from Lorenzini show that the effect of the magnetic torque just adds a small forced precession to the free gyroscopic precession of the antenna, and that these cones are small and stable as far as the spin velocity is larger than the minimum value described above. What is more, dissipation of the excess kinetic energy

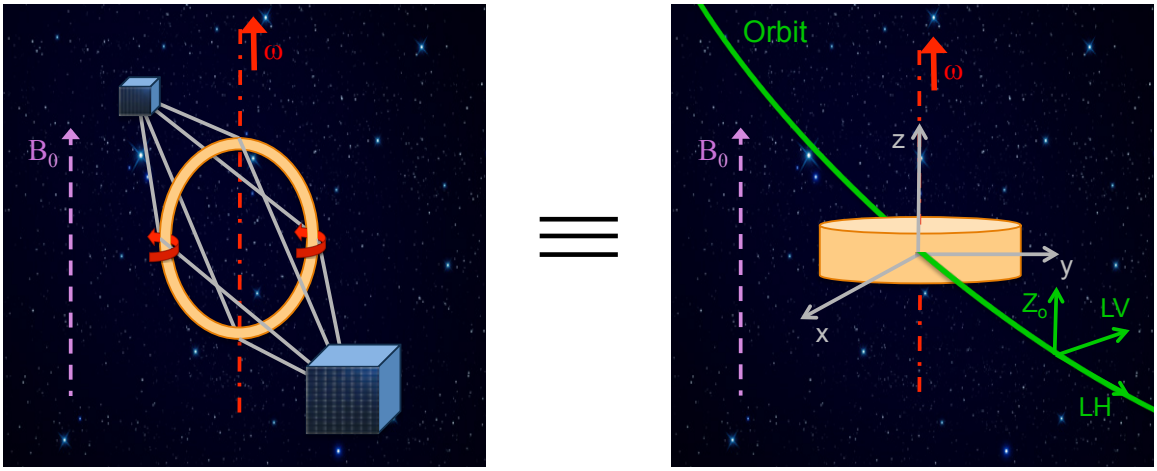


Figure 6-13: Rotating coil with distributed spacecraft subsystems, which is a major-axis spinner and equivalent to a spinning disc in terms of inertia.

with time will end up damping any free precession imposed by unbalanced initial conditions (for a major-axis spinner), and will bring the major-axis spinner to a circular precession of the angular momentum introduced by a constant external magnetic torque. Dynamics will get more complicated for a periodically varying external torque but the general behavior will still apply. The maximum semi-amplitude of the final circular precession for a constant torque can be estimated as follows

$$\nu_{max} \approx \frac{|\tau_{mag_y}|}{\omega^2(I_z - I_y)} \ [rad] \tag{6.49}$$

which is a small angle. For $I_z/I_y = 1.2$ and a frequency of 0.5 Hz, then $\nu_{max} = 0.5°$, that is, a rather small nutation angle.

Finally, we should note that in this thesis we are not addressing how the radiated power is supplied to the antenna. We believe that the *radiation drag* will impart a steady torque on the coil, which would have to be compensated. An alternative could be to supply a DC voltage to the coil to compensate this hypothetical counter electromotive force due to radiation. These concerns should be carefully studied in future efforts.

Overall, the orientation preferred in terms of science (Figure 6-12) is also favorable in terms of dynamics. The stable solution, however, implies a transformation of the system into a major-axis spinner, which could be achieved by distributing the spacecraft subsystems

around the coil. A detailed analysis of the dynamics of the antenna is needed to determine the design of the spacecraft structure, which should be addressed in future studies.

## 6.6 Magnetic Coil Performance Estimation

In this section we calculate the performance of a DC rotating coil. The rotation axis is taken parallel to the angular velocity of the orbit, while the loop axis (normal to the coil surface) is considered perpendicular to the geomagnetic field lines in order to maximize the radiation resistance (Section 3.4.6). In doing that, we ignore the misalignment between the Earth's geographic and magnetic axes in the calculation of the radiation resistance; this fact is justified by Figure 3-3, which shows that the change in the radiation resistance with angle of orientation is very small (Figure 3-3) around the direction perpendicular to the Earth's field. A schematic representation of the coil's orientation was presented in Figure 6-12. The current is DC, thus no sheath or self-inductance appear in the problem, which improves the electrical performance of the antenna compared to AC. The only reactance that remains is due to the plasma currents, which is small and cannot be compensated; the effects of this reactance, if any, should be studied in detail in the future work. We have previously explained that the radiation pattern of a DC rotating loop is equivalent to two AC static orthogonal coils, and that their radiation resistance is very close to that of a single coil antenna. For this reason, and in order to allow fast exploration of parameter space, we use equation (3.5) with $\psi = 90^\circ$ to approximate the radiation resistance of the two orthogonal coil configuration, which is a conservative estimate as described in Section 3.4.6. Additionally, the Ohmic resistance of the superconducting wire has been set to zero in the present analysis, but the details of its behavior should be analyzed in future efforts.

The radiated power is given by

$$P_{rad} = \frac{1}{2} \left( N_{turn} I_1 \right)^2 R_{rad} \tag{6.50}$$

In turn, $R_{rad}$ is proportional to the square of the frequency and the cube of the coil radius. The radiated power therefore scales as follows

$$P_{rad} \propto (N_{turn} I_1)^2 \, f^2 R_a^3 \propto (N_{turn} J \; d \; t_{sup} \; f)^2 \; R_a^3 \tag{6.51}$$

where $J$ is the current density, $d$ is the tape width and $t_{sup}$ is the thickness of the superconducting layer. It must be noted that, for a fixed wire length, the current density is also a function of the radius of the coil (or of $N_{turn}$) when selected to be the critical value or a fraction of it, i.e. $J = J_c(R_a)$. This fact was described in Section 6.3.2, and it is due to the contribution of the different turns to the critical field, which limits the current that the coil is capable of carrying.

The voltage induced with respect to the plasma is then

$$V = \frac{P_{rad}}{N_{turn} I_1} \tag{6.52}$$

The input power to the antenna includes both the radiated power and the power required by the cryocoolers to keep the system at the desired temperature

$$P_{in} = P_{rad} + P_{cryo} \tag{6.53}$$

where $P_{cryo}$ was calculated in Section 6.4.2 and it is the input power to the cryocoolers, which depends on the temperature of the superconductor and the thermal load to be removed from the antenna. The radiation efficiency of the system, therefore, can be defined as follows

$$\eta_{rad} = \frac{P_{rad}}{P_{in}} = \frac{1}{1 + P_{cryo}/P_{rad}} \tag{6.54}$$

It must be noted that $\eta_{rad}$ is not related to the capability of the system to scatter the energetic particles but it refers to the system performance in terms of useful output (radiated) power to input power.

The total mass of the system can then be calculated as follows

$$M = m_{tape} + m_{thermal} \tag{6.55}$$

where $m_{tape}$ and $m_{thermal}$ are given by equations (6.8) and (6.36), respectively.

The power radiated from a loop antenna scales with the square of the frequency, while the lifetime of the particles (and hence the natural replenish time) tends to decrease with decreasing frequency, as described in Figure 5-23. Figure 6-14 analyzes this frequency tradeoff between radiated and required power at three different $L$-shells. The plot is for 20 MeV protons, which represent the most demanding condition since they have the shorter residence time (Figure 5-24). It must be noted that the power required is the one needed to precipitate an entire $L$-shell with radial thickness given by the area illuminated by a single transmitter (Table 4.2); the implications to remediation of the entire inner belt region are discussed in the next chapter. Figure 6-14 (a) plots the power required to reduce the particles' lifetime by a factor of 10 with respect to their natural residence time ($\tau_{1/10}/\tau_{natural}$ = 0.1) as a function of normalized frequency. Similarly, Figure 6-14 (b) plots the radiated power as a function of normalized frequency, where the radiated power is the one from a coil given by the dimensions in Table 6.2 and for $T_c$ = 77 K. It must be noted that if we reduce the temperature to $T_c$ = 20 K, then the current density increases by a factor of 3 (Figure 6-6) and the radiated power by a factor of 9. Finally, Figure 6-14 (c) plots the ratio between required and radiated power, both through the same cross-sectional area at the corresponding frequency. From now on we will refer to the inverse of this ratio as *remediation efficiency*, i.e. $\eta_{RBR} = P_{rad}/P_{req}$. In this plot, we observe that there is a desirable frequency of operation where this ratio is minimum, which is $L$-shell dependent. At $L = 1.5$, the approximate optimum in Figure 6-14 (c) is Y $\approx \omega/\Omega_{H^+} = 0.005$ ($\sim$ 0.5 Hz), which will be the assumed design point when discussing this $L$-shell. It must be emphasized, however, that a scientific mission would ideally sweep a broad range of frequencies to test the proposed models and better understand the science developed in this dissertation. It is interesting to note the overall meaning of Figure 6-14, which shows that it is easier to precipitate particles at those frequencies for which one has most trouble radiating, and vice-versa. This is the reason why we are looking at the ratio between radiated and required power, because if we tried to select a frequency based on the required power alone, we would find that we can not radiate much at that frequency. The same applies to the dependency on $L$-shell: the easier layers to remediate are also those where you can radiate less, which has the behavior of a leveling principle in nature.

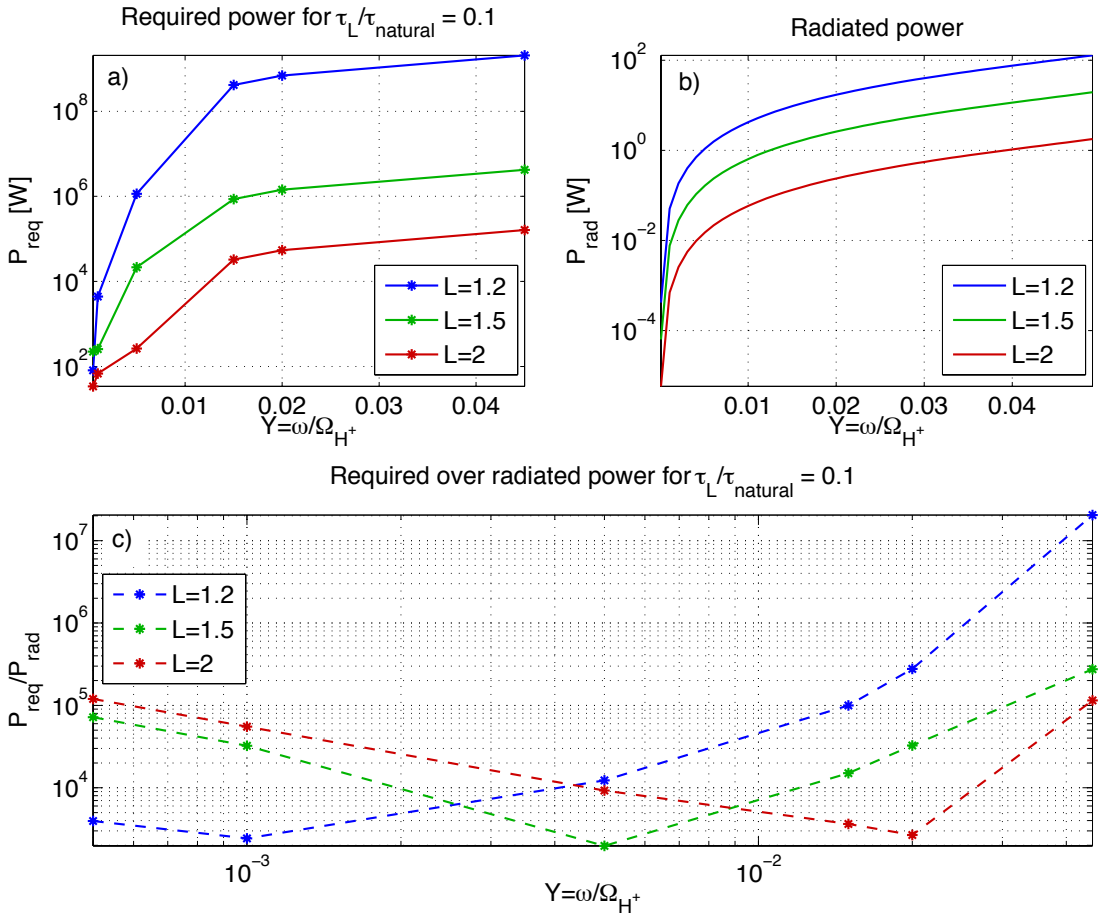


Figure 6-14: (a) Power required to reduce the residence time of 20 MeV protons by a factor of 10 as a function of normalized frequency. (b) Radiated power from a coil given by the parameters in Table 6.2 and $T_c = 77$ K as a function of normalized frequency, and carrying its maximum possible current. (c) Ratio of required power in (a) to radiated power in (b) as a function of normalized frequency. Both, radiated and required power, are considered through the same cross-sectional area at the corresponding frequency, which is given by the ray tracer.

Figures 6-15 and 6-16 characterize the behavior of an antenna at $L = 1.5$ as a function of coil radius $R_a$, for three different superconductor temperatures and a frequency of Y = 0.005. The plots are for a coil operating at its critical surface and for the parameters in Tables 6.2 and 6.4. A total wire length of 10 km has been considered here as a reference value, although this is a flexible parameter and could be scaled up if needed; for a fixed radius, the radiated power is quadratic with the wire length, while the mass is only approximately linear with this length. The radiated power per unit mass and per unit input power (efficiency) are presented in Figure 6-15 (a) and (b), respectively. These ratios are close to linear with the coil radius for $T_c = 50$-77 K; the different slopes of the 20 K case are due to the addition of heavy and

power demanding 20 K-coolers with increasing antenna radius. We saw in Figure 6-4 that a good operating temperature would be that where the critical current starts to saturate, around $T_c = 20$ K; this is the reason why reducing the operating temperature dramatically increases the slope of the radiated power per unit mass. The radiation efficiency in Figure 6-15 (b), however, decreases for operation at 20 K compared to 50 K because the former requires Planck-like cryocoolers, which are more power demanding than the Sunpower ones due to the lower cold tip temperature. It must be noted that the results above are for a mass of copper given by the SuperPower HTS tape design. Nevertheless, we saw in Section 6.3.3 that the lower temperatures require unacceptable amounts of copper in order to be able to absorb the magnetic energy in case of a quench. In these plots we are accepting more risk in the mission by keeping the SuperPower proportions of copper and relying on the thermal subsystem to cool down the superconductor. Reliability, redundancy and risk analyses will not be analyzed here but should be carefully addressed in future studies.

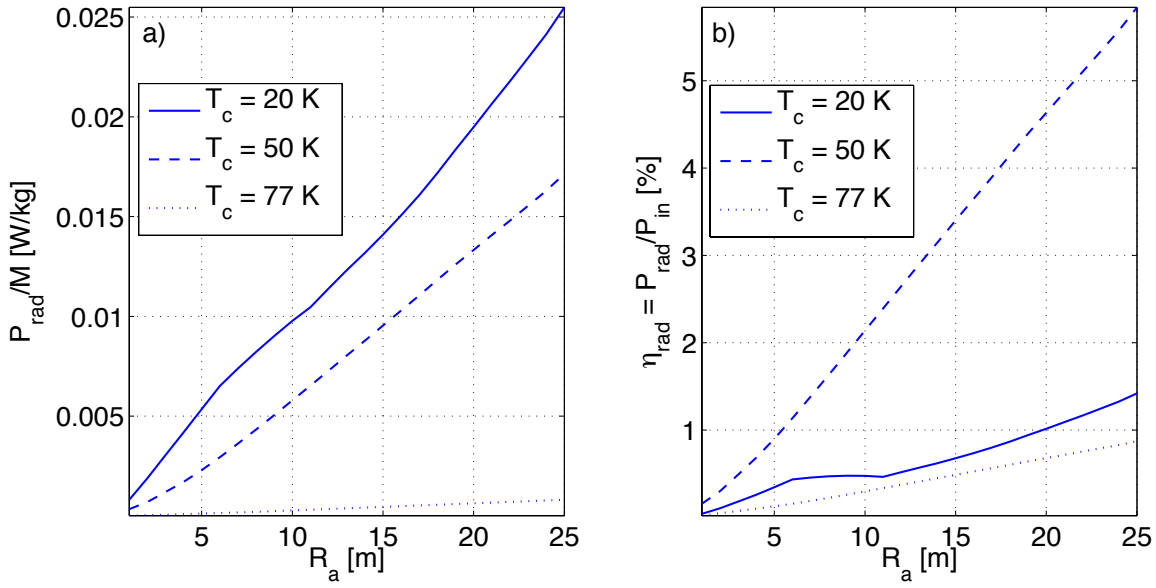


Figure 6-15: (a) Radiated power per unit mass, and (b) radiated power per unit input power (radiation efficiency) as a function of coil radius. The solid lines are for $T_c = 20$ K, the dashed lines for $T_c = 50$ K and the doted lines for $T_c = 77$ K.

Similarly, Figure 6-16 (a) presents the input power, radiated power and the thermal load to the cryocoolers as a function of the coil radius. The solid lines correspond to $T_c = 20$ K, the dashed lines to $T_c = 50$ K and the doted lines to $T_c = 77$ K. For $R_a = 15$ m and $T_c = 20$ K, the radiated power is $P_{rad} = 6.4$ W and the input power $P_{in} = 940$ W,

which corresponds to an efficiency of $\eta_{rad} = 0.7\%$. If we increase the temperature to $T_c$ = 50 K, the antenna radiates $P_{rad} = 3.3$ W but requires $P_{in} = 100$ W, i.e. $\eta_{rad} = 3.3\%$. Furthermore, in the previous sections we argued that the coil radius should be no more than 15 m due to launch vehicle dimension constraints. At MIT, however, we are studying flexible deployment options that could allow very efficient packaging of the coil and therefore could enable very large antenna radius. Therefore, if we consider the case of $R_a = 25$ m and $T_c = 20$ K, the radiated power increases to $P_{rad} = 13.5$ W and $P_{in} = 940$ W, which gives an efficiency of $\eta_{rad} = 1.4\%$; for $T_c = 50$ K, then $P_{rad} = 7.3$ W and $P_{in} = 125$ W, i.e. $\eta_{rad} = 5.8\%$. A clear tradeoff exists between radiated power and radiation efficiency: the larger the radiated power the colder the required temperature of the superconductor, which requires power demanding cryocoolers and reduces the antenna radiation efficiency as defined in equation (6.54).

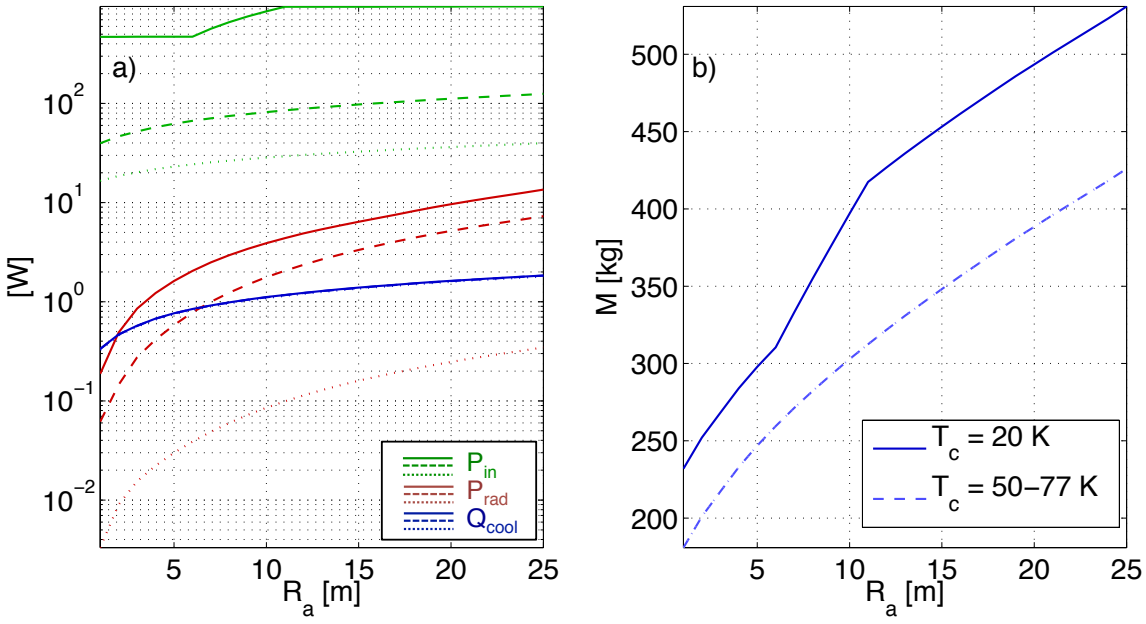


Figure 6-16: (a) Radiated power (red), input power (green) and thermal load to the cryocoolers (blue) as a function of coil radius. (b) Mass of the antenna (HTS tape and thermal) as a function of coil radius. The solid lines are for $T_c = 20$ K, the dashed lines for $T_c = 50$ K and the doted lines for $T_c = 77$ K.

The efficiencies above are indeed very small, which suggests that a true remediation mission which cleans an entire radiation belt may break down, at least using space-based transmitters. A scientific mission, however, would be of great interest to test the models presented in this thesis and demonstrate the technology involved. These topics are discussed in the

following chapter.

## 6.7 Conclusions

In this chapter we have studied the electrical, mechanical and thermal implications of a space-based transmitter capable of radiating EMIC waves. The main conclusions of the analysis are summarized next:

- An AC loop transmitter of the dimensions under consideration has a self-inductance of $\sim$ 470 H, which induces high voltages and a plasma sheath. The solution involves a DC rotating coil, which is equivalent to two AC static orthogonal coils.

- Superconductors, large coil radius and multiple turn arrangements are required to increase the power radiated from magnetic dipoles.

- We have selected the new 2nd Generation High Temperature Superconducting (HTS) tape manufactured by SuperPower. These wires are capable of reaching critical current densities up to 1000 kA/cm$^2$ (per cross-sectional area of superconductor), larger than most Low Temperature Superconductors (LTS). HTS materials can also be cooled down below the nominal 77 K, with corresponding increase in current density. Additionally, HTS and are much more flexible than the LTS designs, which makes it easier to design the deployment and thermal control system.

- Fifteen meters has been set as the nominal coil radius, limited by standard launch vehicle dimensions. In doing that, we are assuming that we have a working deployment strategy, which is currently being studied in the Space Systems Laboratory at MIT. Innovative deployment techniques based on flexible concepts may allow to use larger coil radii.

- Superconductors can carry very large current densities with minimal ohmic losses. The critical current density of the HTS tape is controlled by the self-induced magnetic field and operating temperature, which define the critical surface of the superconductor. The field perpendicular to the tape dominates the critical current density, while the parallel field remains subcritical.

- The critical current as a function of temperature starts to saturate around 20 K. For this reason, it is strongly desired to operate below the nominal 77 K, since small temperature reductions produce large performance improvements.

- The critical surface is a function of the number of turns of the coil, which we have characterized. The critical current of a 100-turn coil at 50 K increases by a factor of 2 compared to the case at 77 K, and by a factor of 3 when operating at 20 K. These results reaffirm the importance of working at temperatures below the nominal value.

- A superconductor quenches when it goes from having no resistance to being resistive due to too large magnetic fields or fast field changes. The copper layers in the HTS tape are a mitigation technique, which would absorb the stored magnetic energy in the event of a quench. For a 15 m radius coil with 106 turns, the mass of copper in the tape is 43.6 kg, which represents a factor of safety of 4 at $T_c = 77$ K. However, this copper is not enough at temperatures below $T_c = 50$ K. In this thesis we accept more risk by keeping the SuperPower proportions of copper and relying on the thermal subsystem to cool down the superconductor.

- The greatest challenge of working with superconductors in space is the thermal control system. The environmental heat fluxes from the Sun and the Earth have to be rejected in order to keep the temperature of the superconductor below its critical value.

- The selected passive thermal control means consists of 30 layers of Multi Layer Insulator (MLI) together with Quartz over Silver Optical Solar Reflector (OSR) coating. Additionally, cryogenics are required to cool down the system. A hybrid approach has been selected, consisting of a flexible forced vapor system for isothermalization and several cryocoolers that extract the heat from the vapor. Heat pipes at cryogenic temperatures are very stiff, which will hinder the deployment of a flexible structure. For this reason, it was decided to back out of the passive nature of the heat pipe in favor of a design based on a forced vapor flow.

- Cryocoolers similar to the ones in the Planck spacecraft (sorption coolers) are required for superconductor temperatures around 20 K, while Sunpower cryocoolers can be used for operation above 50 K. Planck-like coolers provide 1 W of cooling at 20 K, have a power consumption of 470 W and weight 54 kg. Sunpower cryocoolers achieve

thermal loads of 7.5 W at 77 K, with an input power of 150 W and a weight of 3 kg.

- A coil of 15 m radius and 106 turns operating at $T_c = 77$ K requires a single Sunpower cryocooler with an input power of 33 W. For $T_c = 50$ K also one cryocooler is required with an input power of 95 W. For the case at $T_c = 20$ K, two Plank-like cryocoolers should be used with a total input power of 940 W.

- A coil of 15 m radius and 106 turns operating at 50-77 K weights approximately 103 (tape) + 240 (thermal) = 343 kg. For operation at 20 K, the weight of the thermal system increases a 45% due to the cryocooler mass.

- The dynamics of the antenna have been briefly discussed. The DC coil is rotating at the EMIC frequencies ($\sim$0.5 Hz). Three main torques modify the coil's attitude: gyroscopic, magnetic and gravity gradient torques. The gyroscopic and magnetic effects represent the main contribution to the torque. The gyroscopic torque cancels for $\vec{\Omega}_{orbit} \parallel \vec{\omega}$, and it is stable when spinning around a major axis of inertia. For this reason, the solution to the dynamics problem involves a coil rotating with $\vec{\Omega}_{orbit} \parallel \vec{\omega}$ (which also maximizes the radiation resistance), but with the spacecraft subsystems distributed on both sides of the coil such that the body becomes a major-axis spinner. The magnetic torque just adds a small forced precession to the free gyroscopic precession of the antenna. In the presence of dissipation, only the circular forced precession of the angular momentum remains, which is very small ($< 0.5^\circ$ of semi-cone angle).

- The rotation rate has been selected based on the frequency tradeoff between radiated and required power. The power radiated from a loop antenna scales with the square of the frequency, while the lifetime of the particles tends to decrease with decreasing frequency. We have shown that the ratio between required and radiated power has an approximate optimum, which is $L$-shell dependent.

- A good operating temperature would be that where the critical current starts to saturate, around $T_c = 20$ K, which dramatically increases the slope of the radiated power per unit mass. The radiation efficiency, however, decreases for operation at 20 K compared to 50 K because the former requires Planck-like coolers, which are more power demanding than the Sunpower ones.

- A clear tradeoff exists between radiated power and radiation efficiency: the larger the radiated power the colder the temperature of the superconductor, which requires power demanding cryocoolers and reduces the antenna radiation efficiency. For a coil radius of 15 m at $T_c = 20$ K, the radiated power is 6.4 W and the input power 940 W, i.e. $\eta_{rad} = 0.7\%$. If we increase the temperature to $T_c = 50$ K, the antenna radiates 3.3 W but requires 100 W of input power, i.e. $\eta_{rad} = 3.3\%$. If we consider a larger radius of $R_a = 25$ m and $T_c = 20$ K, then the radiated power increases to 13.5 W and requires 940 W, which gives $\eta_{rad} = 1.4\%$; for $T_c = 50$ K, it radiates about 7.3 W and requires 125 W of input power, i.e. $\eta_{rad} = 5.8\%$.

# Chapter 7

# Space Systems Concepts and Feasibility

Finally, we have all the ingredients required to determine the feasibility of the remediation concept. Based on the science in Chapters 2 to 5 and the engineering implications in Chapter 6, we now estimate the power and number of spacecraft required to precipitate the energetic protons trapped in the inner Van Allen belt, which was already suggested to be excessive in previous sections. An outline of a scientific mission scaled down to detectability of this precipitation is also presented in this chapter, which would serve to test the theory and technology involved in the controlled removal of energetic particles.

## 7.1 Is There a Solution to the Inner Proton Belt?

We believe that the answer is *no*, it is not engineeringly feasible to clean up the proton Van Allen belt using space-based transmitters. This fact was already revealed by the analyses presented in the previous chapters, but let's take a closer look and estimate a number for remediation.

Say we call *remediation* to the fact of reducing the natural residence time of the shortest-lived proton energies (20 MeV) by a factor of 10 over the entire inner belt (therefore also of the higher energy particles). How many spacecraft would it take to remediate the inner zone based on this definition?

In Section 6.6 we saw that the *remediation efficiency* of a single transmitter, $\eta_{RBR} = P_{rad}/P_{req}$, has an optimum at a certain a frequency, which is $L$-shell dependent and equal Y = 0.005 ($\sim$ 0.5 Hz) at $L = 1.5$. The analysis was based on reducing by a factor of 10 the life of 20 MeV protons in the very thin layer illuminated by the transmitter (thickness of $\sim$200 m for Y = 0.005 at $L = 1.5$), and for an antenna temperature of $T_c = 77$ K. Figure 7-1 below repeats the results for $T_c = 20$ K and 50 K; the only difference is the critical current, which increases by a factor of 3 at 20 K compared to 77 K, or by a factor of 2 at 50 K with corresponding increase in radiated power.

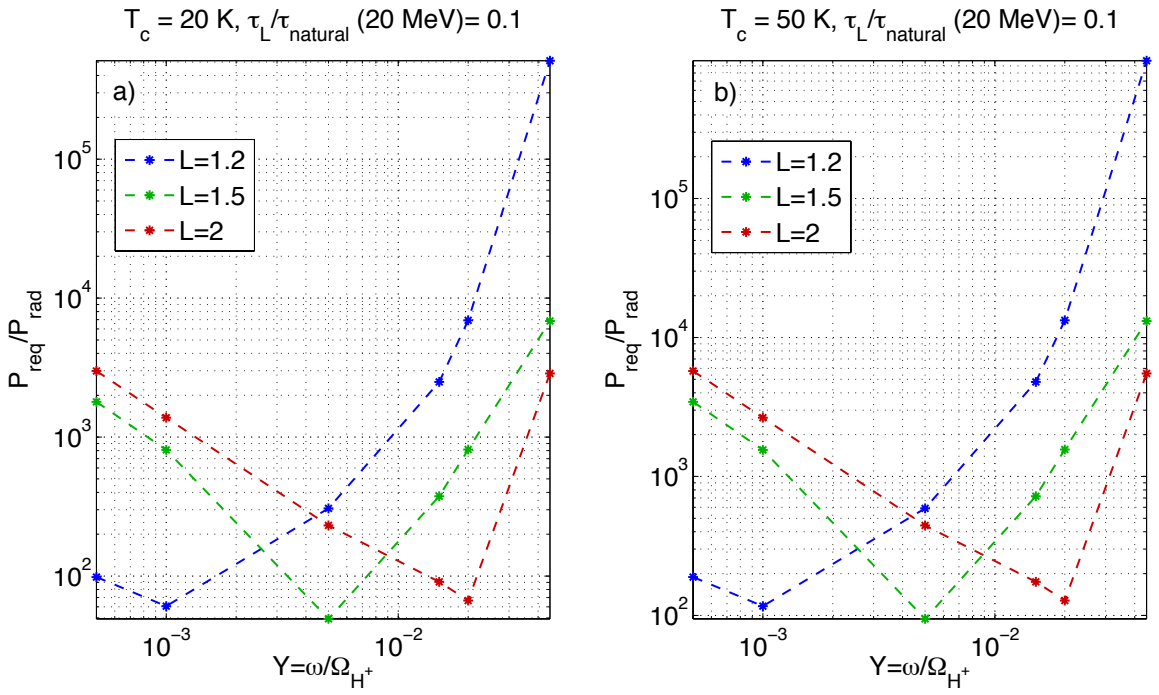


Figure 7-1: Ratio of required to radiated power for $\tau_L/\tau_{natural}(20 \text{ MeV}) = 0.1$ as a function of normalized frequency for (a) $T_c = 20$ K (b) $T_c = 50$ K.

The number of spacecraft required to clean up this thin layer, say at $L = 1.2$ and for Y = 0.001, is

$$\#S/C|_{layer} = \frac{P_{req}}{P_{rad}}(L = 1.2, \text{Y} = 0.001, T_c = 20 \text{ K})|_{max} = 60 \text{ spacecraft} \qquad (7.1)$$

where we have considered a superconductor temperature of $T_c = 20$ K and a coil radius of $R_a = 15$ m. For $T_c = 50$ K, this number would be 115 spacecraft as shown in Figure 7-1 (b), or 2430 spacecraft at $T_c = 77$ K as in Figure 6-14 (c). If we want to remediate the

entire belt, however, we have to place approximately these many spacecraft every couple hundred meters (from the ray tracer) for more than 5000 km along the equator. In other words, millions of antennas are required to clean up the inner belt region from energetic protons, which is out of the realm of what can be reasonably put into orbit with the current technology.

Another approach would be to clean up the upper reaches of the belt first, then tackle the lower regions gradually as more power becomes available. This approach was justified by the fact that particles have shorter natural residence times closer to the Earth (Figure 5-24 (a)), but the scattering is also weaker there (Figure 5-23). Similarly, let's estimate the number of spacecraft required to remediate the inner belt adopting this mode of operation. Integrating over $L$-shell, the total number of antennas required can be estimated as follows

$$\#S/C|_{belt} = \frac{1}{\Delta L\ \tau_{0.1}|_{L=1.2}} \int_{L=1.2}^{L=2} \tau_{0.1}(L) \frac{P_{req}(L)}{P_{rad}(L)} dL \tag{7.2}$$

where $\Delta L$ is the area illuminated by a single spacecraft, and $P_{req}/P_{rad}$ was provided in Figure 7-1 and represents the efficiency involved in reducing the natural residence time of 20 MeV protons by a factor of 10 in that thin layer ($\tau_{0.1}$). For $T_c = 20$ K, we would require again more than a million antennas of the ones described in Chapter 6, each one consuming 470 W of power and weighing more than 450 kg.

If we restrict ourselves to energies larger than 100 MeV, then the remediation requirements get relaxed, since the protons' natural residence time is much longer as we saw in Figure 5-24 (a). Figure 7-2 shows the ratio between required to radiated power that reduces by a factor of 10 the natural residence time of 100 MeV protons. According to the figure, we need about 7 spacecraft at $T_c = 20$ K to clean the small area illuminated by the transmitter, or 15 spacecraft at $T_c = 50$ K. If we consider again that we have to put these many satellites every couple hundred meters for more than 5000 km, then we have reduced the total number of spacecraft to $10^4$, which is still a very large number.

Overall, the combination of small radiation and remediation efficiencies negates the possibility of a controlled removal of the energetic proton population trapped in the inner Van Allen belt.

This being said, the topics of study of this thesis are of great interest to the scientific and

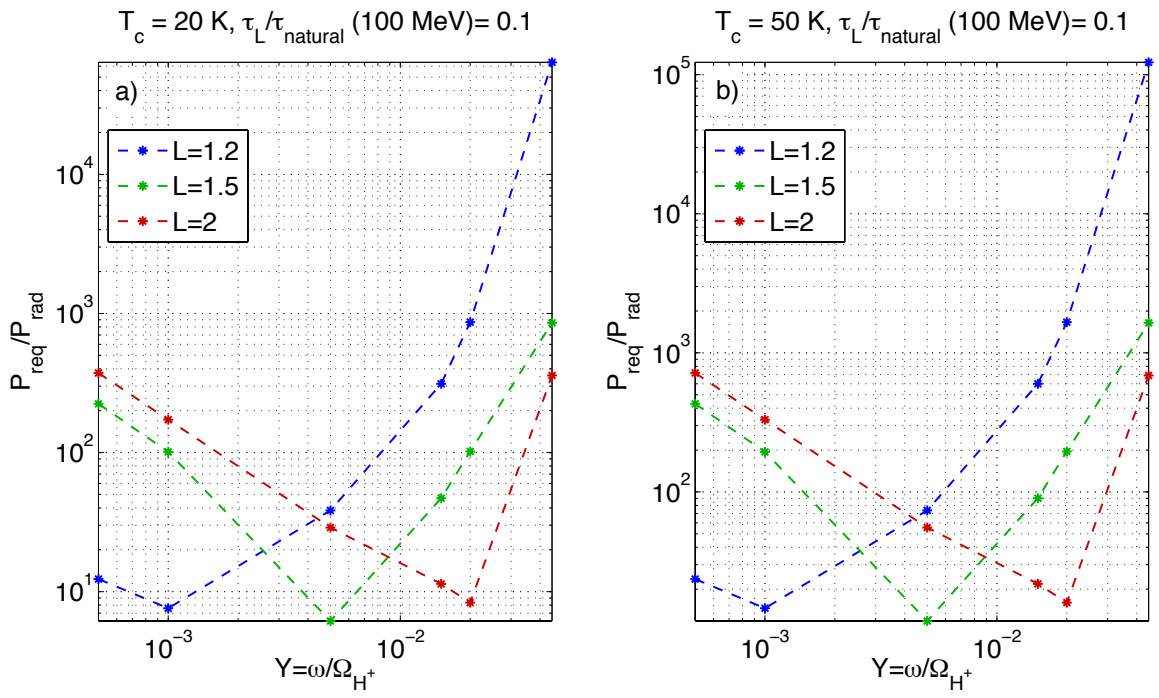


Figure 7-2: Ratio of required to radiated power for $\tau_L/\tau_{natural}(100\text{ MeV}) = 0.1$ as a function of normalized frequency for (a) $T_c = 20$ K (b) $T_c = 50$ K.

engineering communities. It would be useful to test the models developed in this thesis and maybe discover "unknown unknowns" that may impact the science. Additionally, the demonstration of large-scale superconducting structures in space will have a strong impact on future missions, with a broad range of applications. For these reasons, the next section outlines a scientific mission that would allow us to explore and understand some of the still partially unsolved problems addressed in this dissertation.

## 7.2 Outline to a Scientific Mission

Above we showed that it does not seem possible to remediate the entire Van Allen proton belt by radiating EMIC waves from space-based antennas. A scientific mission carrying a transmitter similar to the one in Chapter 6, however, would allow us to test the science and technology involved, which has applications to a broad range of areas. Some of the key advances of a scientific mission would be

- **In situ measurements to test the models in this thesis**. In this dissertation we

have developed models of the radiation and propagation of man-made EMIC waves, and their interaction with the energetic protons of the inner Van Allen belt. The only observations of EMIC waves available, however, are those of natural sources. The radiation of EMIC waves from a space-based antenna has never been tested in space; for this reason, a scientific mission would be a great opportunity to test the theory and models presented in this thesis and maybe discover new areas of research that could impact the scientific community. More specifically, this mission could allow us to characterize the interaction between energetic protons and EMIC waves from space-based antennas, as well as to determine the capability of these waves to bounce back and forth in the inner belt region.

- **Demonstration of a DC rotating coil antenna** in space, which is a completely new concept and might also be tested on the ground. This idea could have applications to areas where AC operation represents a limitation. These applications may involve operation in a plasma at frequencies below the charged particles' characteristic frequencies, or the use of superconductors since they are dissipative when driven by an AC current due to their hysteretic behavior (Appendix B).

- **Demonstration of HTS superconductor technology** in space at temperatures below 77 K, which has a broad range of applications. The Variable Specific Impulse Magnetoplasma Rocket (VASIMR) [*Rey et al.*, 2002] and a concept called Magnetized Beamed Plasma Propulsion (MagBeam) already use HTS superconductors; lower HTS temperatures, however, could allow new developments in electric propulsion. Other areas of development could be torque coils to de-saturate reaction wheels or control moment gyros, magnetic shielding for astronaut radiation protection [*Hoffman and Batishchev*, 2005] or Electromagnetic Formation Flight (EMFF). Additionally, HTS also imply the development of low temperature cryocoolers. Over the last 15 years, cryocoolers have been used for instruments at medium to high cryogenic temperatures (55-150 K) [*Ross Jr and Boyle*, 2006]. Future missions supporting studies of the origin of the Universe, distant planets and distant stars require operation at temperatures from 6-20 K. The 20 K cryocooler developed by NASA for the European Planck spacecraft, or the Mid Infrared Instrument (MIRI) on the James Webb Space Telescope (JWST) are examples of new low temperature ($< 20$ K) cryocooler technology.

There are many scientific missions that could be architected from the list above. In this thesis we are mostly interested in the first item, that is, testing the science developed in the previous chapters. Therefore, the scientific mission proposed here is based on the design presented in Chapter 6 and scaled down to demonstrate detectability of the induced proton precipitation.

The characteristic times for wave-particle interaction (interaction time, particle's bounce and drift periods, wave period) are all much shorter than the orbital period. Additionally, the interaction will most probably happen close to the spacecraft and would be mostly local. For these reasons, we believe that an on board particle instrument could detect the proton precipitation induced by the EMIC waves radiated from the antenna.

The initial precipitating fluxes at the edge of the loss cone set the detectability of the scattering induced by the transmitter. The lifetime of the entire proton population is determined by the first eigenmode of its decay, which is very slow as we saw in the previous section. The initial precipitating fluxes through the loss cone, however, correspond to higher decay modes. These higher modes have a much faster decay as well as stronger fluxes through the loss cone, which could be detected by a particle instrument.

The NOAA Polar Orbiting Environmental Satellites (POES) carry several of these instruments included in the Space Environment Monitor (SEM-2) instrument package. The Medium Energy Proton and Electron Detector (MEPED) in SEM-2 has two solid-state energetic particle telescopes capable of monitoring protons in six energy bands from 30 keV to 6.9 MeV. Our system, however, should be capable of going to proton energies of at least several tens of MeV, thus monitoring a wider range of the hazardous proton population. Protons enter through the collimator of the first detector and they are stopped and sorted into five energy bands based on their energy loss, while the sixth energy band is determined by the back detector; the telescope is illustrated in Figure 7-3 (a) [*Evans and Greer*, 2004]. The difference between the two proton telescopes onboard the POES spacecraft is their orientation; the 0°-pointing detectors have their field-of-view (FOV) centered along the local zenith and pointing outward, while the 90° detectors are approximately perpendicular to the former. Both detectors have an aperture of ±15°. In order to measure precipitating particles in the POES spacecraft it is important to select the data from the 0° detectors, since their field of view typically lies within the bounce loss cone of the particles. These

satellites are capable of determining the edge of the loss cone at the spacecraft and selecting only the measurements that fall within this cone [*Rodger et al.*, 2008; *Lam et al.*, 2010].

Another instrument design that could serve as a guideline is the Relativistic Proton Spectrometer (RPS) onboard the Van Allen Probes, which is schematized in Figure 7-3 (b)*. RPS is a particle spectrometer capable of measuring the flux, energy spectrum and angular distribution of protons from 50 MeV to 2 GeV. The RPS telescope consists of 8 silicon solid-state detectors used for energies between 50 MeV to 400 MeV, and a Chenrenkov detector for $>$ 400 MeV. The absolute flux accuracy is $dJ/J \sim 10\%$, the energy resolution is $dE/E$(@ 50 MeV) $\sim 30\%$ and $dE/E$(@ 2 GeV) $\sim 100\%$, and the angular resolution is 30° instantaneous and 5° deconvolved [*Mazur et al.*, 2012].

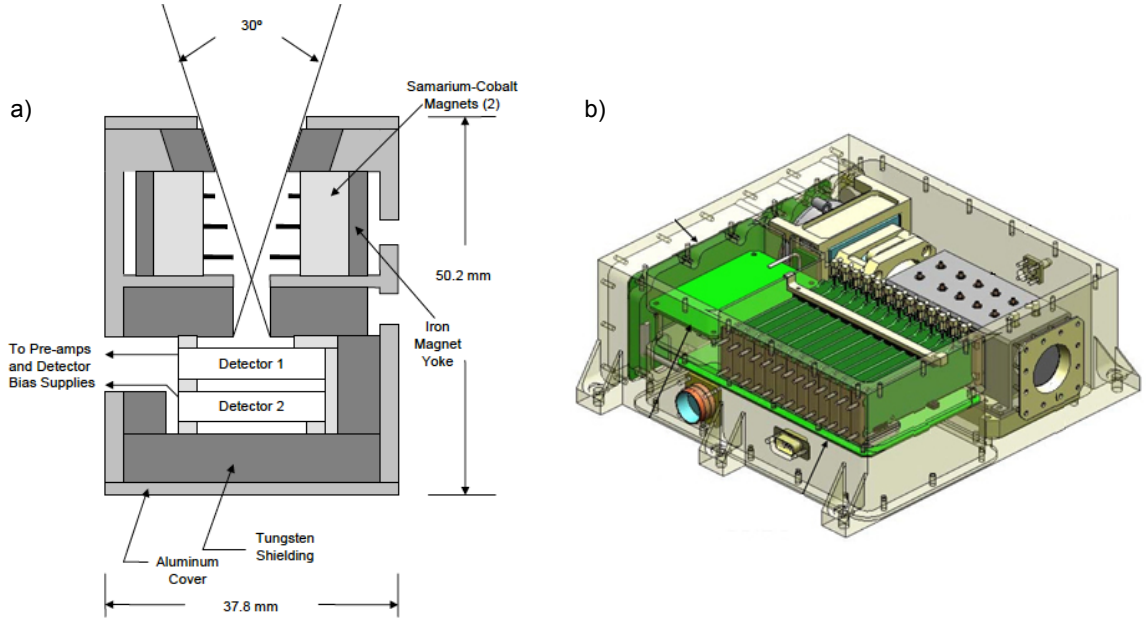


Figure 7-3: (a) Proton Solid State Detector Telescope included in the Space Environment Monitor (SEM-2) of the NOAA Polar Orbiting Environmental Satellites (POES) [*Evans and Greer*, 2004]. (b) Relativistic Proton Spectrometer (RPS) onboard the Van Allen Probes

An orbit close to the equator, say at $L = 1.5$, would maximize the residence time around the same magnetic lines in the core of the inner belt, therefore allowing us to have many observations. Consequently, the mission lifetime could be kept short, limited by the cost of radiation hardening. We expect to detect the particles streaming towards the spacecraft after they interact with the waves not very far from the antenna. For this reason, the FOV

* The Van Allen Probes: Relativistic Proton Spectrometer (RPS). Last visited October 6, 2013, from http://vanallenprobes.jhuapl.edu/spacecraft/instruments/instruments_rps.php.

of the particle telescope should be centered around the direction of the geomagnetic field lines with an aperture angle close to the edge of the loss cone of the particles. Similarly to POES, the loss cone should be determined at the location of the spacecraft in order to only select the measurements that fall within this cone. The sensor should be capable of detecting proton energies of at least several tens of MeV.

POES is in Low Earth Orbit (LEO, altitude ∼800 km), while the Van Allen Probes are in Highly Elliptical Orbit (HEO, perigee at ∼700 km, apogee at ∼30,500 km). For this reason, and in order to compare with the precipitating fluxes from our antenna, we will use data from the POES-MEPED particle detectors.

Based on POES data of precipitating proton fluxes from the field aligned detector [*Dmitrieva et al.*, 1999; *Fang et al.*, 2007; *Engebretson et al.*, 2008; *Wissing, J. M. and Bornebusch, J. P. and Kallenrode, M-B.*, 2008], we have set the detectability threshold to ∼100 $\mathrm{cm}^{-2}\mathrm{sr}^{-1}\mathrm{s}^{-1}$, which is above the background proton precipitation in most of the cases[†]. We believe that this is a conservative threshold because POES is only capable of measuring energies below 6.9 MeV; energies above 20 MeV will therefore correspond to lower background precipitating fluxes. Additionally, the transmitted signal should be modulated, which will also create a pattern in the precipitation signature, thus making its detection easier.

Using our test-particle code, we next calculate the induced proton precipitation at the edge of the loss cone, which is used to determine the radiated power required to reach a precipitated flux above the threshold value mentioned above. An equatorial orbit in the core of the inner belt ($L = 1.5$) is used in our calculations, and the precipitation is computed very close to the antenna since the detectable scattering would most probably happen locally, near the spacecraft. In what follows we analyze three different coil radii: $R_a = 15$ m, $R_a = 5$ m and $R_a = 2.5$ m. A radius of 2.5 m would fit in the launch vehicle without requiring any special folding. On the other hand, the 5 m and 15 m designs assume that we have a working deployment strategy, which is currently being studied in the Space Systems Laboratory at MIT.

Figure 7-4 shows the fluxes as a result of the local interaction between energetic protons and EMIC waves radiated from the antenna. A frequency of Y = 0.005 (0.5 Hz) has been

[†] POES geometric factor is 0.01 $\mathrm{cm}^2\mathrm{sr}$, thus the threshold flux corresponds to a count rate of 1 proton/s.

Table 7.1: Radiated power requirements for detectability

| | $R_a = 15$ m | $R_a = 5$ m | $R_a = 2.5$ m |
|---|---|---|---|
| Orbit | Near-equatorial, $L = 1.5$ | | |
| Threshold flux [protons/(cm$^2$-sr-s)] | 100 | | |
| Required radiated power [W] | 25 | 3.3 | 0.9 |

considered in the plot. The scientific mission, however, would ideally be capable of sweeping a broad range of frequencies to test the models presented in this thesis, though engineering for this capability may introduce difficulties which ultimately minimize the range of potential frequencies which may be sampled. Figure 7-4 (a) shows the directional flux of protons, $J_{prec}$ [protons/(cm$^2$-sr-s)], integrated over three energy ranges for the 15 m radius case. The dashed black line corresponds to the loss cone angle in our calculations, given by AP-9. We clearly observe that the loss cone partially fills up as a result of the interaction. The plot is for a total wave power of 25 W, which is what is required to detect precipitating protons with energies $> 20$ MeV according to Figure 7-4 (b) (the dashed black line in this plot indicates the threshold value). As expected, the fluxes corresponding to the higher energy ranges are smaller, and therefore require more radiated power to enable their detection. Similarly, Figure 7-4 (c) and (d) show the precipitating flux at the edge of the loss cone for antenna radii of $R_a = 5$ m and $R_a = 2.5$ m, respectively. The $R_a = 5$ m case requires 3.3 W of radiated power, while the $R_a = 2.5$ m case requires 0.9 W to detect energetic proton fluxes of energies $> 20$ MeV. These numbers are summarized in Table 7.1. It must be noted that the different antenna radii affect regions of different total cross-sectional area, the larger the antenna the larger the affected area; in terms of detectability, however, this is not a relevant issue (but it would be for remediation of the entire inner belt), and it is therefore desirable to go to the smaller radius, since it is easier to deploy and requires less radiated power to generate detectable precipitation.

The next step consists of determining the dimensions, mass and power requirements of a DC rotating coil antenna capable of radiating the amount of power calculated above. We would like to operate at superconducting temperatures of 50 K or higher, which allow us to use efficient and reliable space-rated cryocoolers. Based on the models developed in Chapters 3 and 6, Figure 7-5 presents the radiated power, mass and input power of the coil as a function of the number of turns for $T_c = 50$ K for the case of $R_a = 2.5$ m. The

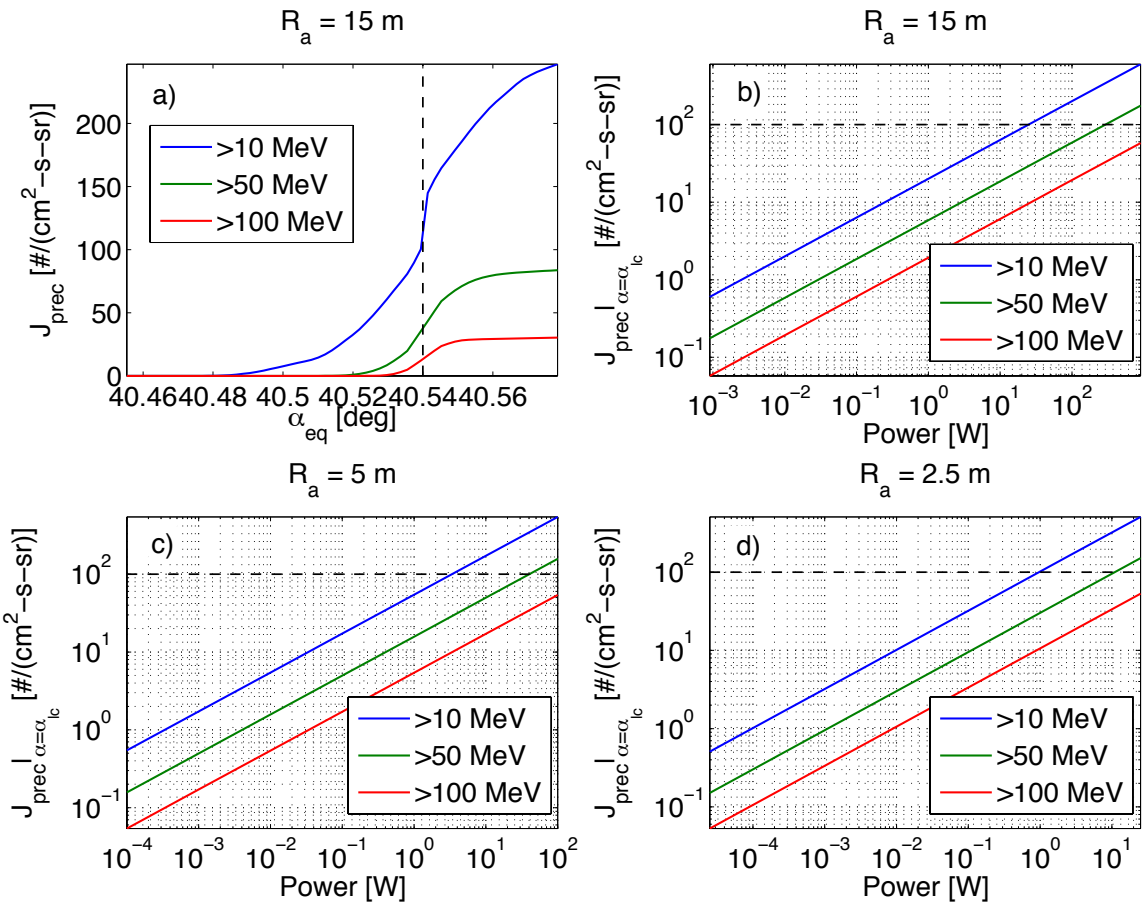


Figure 7-4: (a) Directional proton flux for three different energy ranges for an antenna of $R_a = 15$ m and a radiated power of 2.4 W. (b) Precipitated proton flux at the edge of the loss cone as a function of radiated power for an antenna of $R_a = 15$ m. (c) Same as (b) but for for an antenna of $R_a = 5$ m. (d) Same as (b) but for for an antenna of $R_a = 2.5$ m. The spacecraft is in equatorial orbit at $L = 1.5$ with a normalized frequency of Y = 0.005.

dashed lines are the actual values from the analysis, while the solid lines correspond to the values with a 50% margin in mass and thermal load, that is, the input power has been sized to remove 1.5 times more heat than expected. Similar results have been run for the other radii cases, that is, $R_a = 15$ and $R_a = 5$ m. It must be noted that the full-wave model described in Chapter 3 has been used to calculate the radiated power from the rotating DC coil, which is equivalent to two static AC coils in terms of radiation. The sizing and input power requirements of the transmitters capable of radiating the power specified in Table 7.1 are summarized in Table 7.2. It must also be mentioned that these antenna configurations still have a very large self-inductance when operated in AC, that is, the DC rotating coil idea still prevails. For example, for the $R_a = 2.5$ m case in Table 7.2, its self-inductance in

AC would be 130 H, which translates into an induced voltage of $2{\cdot}10^5$ V across the coil, i.e. sheath formation and arcing of the antenna. These problems, however, disappear in DC; the spin-up and dynamics of the DC rotating idea should be carefully addressed in future efforts.

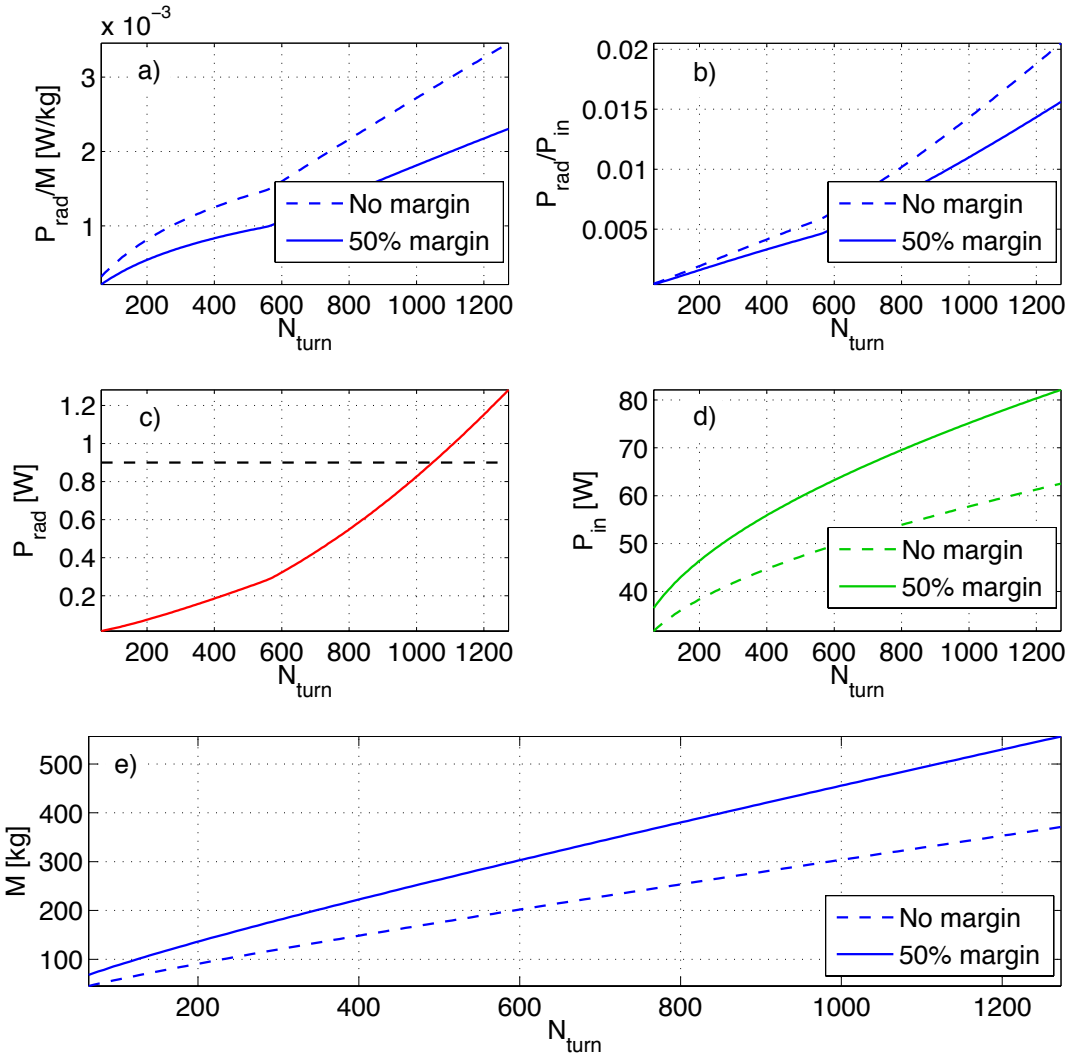


Figure 7-5: (a) Radiated power per unit mass of antenna as a function of number of turns. (b) Radiated power per unit input power as a function of number of turns. (c) Radiated power as a function of number of turns. (d) Input power as a function of number of turns. (e) Total mass (wire and thermal) as a function of number of turns. The dashed lines are the actual values from the analysis, while the solid lines correspond to a 50% margin. The plots are for a coil radius of $R_a = 2.5$ m, a HTS temperature of $T_c = 50$ K and operating in equatorial orbit at $L = 1.5$.

In addition, the capability of detecting the echoes from EMIC waves is as important as the measurements of particles' precipitation, since it could dramatically improve the remedia-

Table 7.2: Scientific mission: Mass and power estimates

| | $R_a$ = 15 m | | $R_a$ = 5 m | | $R_a$ = 2.5 m | |
|---|---|---|---|---|---|---|
| | 0% mar. | 50% mar. | 0% mar. | 50% mar. | 0% mar. | 50% mar. |
| $T_c$ [K] | 50 | | | | | |
| # cryo | 1 | | | | | |
| Tape width [mm] | 12 | | | | | |
| # turns | 255 | | 583 | | 1050 | |
| Tape mass [kg] | 262 | 393 | 200 | 300 | 180 | 270 |
| Thermal mass [kg] | 365 | 546 | 191 | 286 | 136 | 204 |
| Total mass [kg] | 627 | 940 | 391 | 586 | 316 | 474 |
| Input power [W] | 156 | 207 | 79 | 106 | 58 | 76 |

tion results. In order to do that, we should resolve the Poynting flux direction of the waves with the purpose of determining their ability to bounce back and forth in the inner belt region. The spacecraft should be able to sense electromagnetic power, that is, it should carry receivers capable of determining 3-axis electric fields, and magnetometers for 3-axis determination of the wave magnetic field. The Electric and Magnetic Field Instrument Suite and Integrated Science (EMFISIS) instrument onboard the Van Allen Probes provides highly sensitive measurements of all 6 electromagnetic components. More specifically, the EMFISIS fluxgate magnetometer (MAG) is a high-performance, wide-range triaxial fluxgate magnetometer system. The dynamic range of the instrument covers fields from <0.02 nT to 65,536 nT in three different ranges, and has a frequency range from 0-30 Hz. The RMS noise level over the 0.001-10 Hz band does not exceed 0.01 $nT^2/Hz$ [*Kletzing et al.*, 2012]. The smaller antenna described above (radius of 2.5 meters) radiates 0.9 W, that is, a power flux of 45 $mW/m^2$ in the vicinity of the coil. From the EMIC dispersion relationship, this power flux approximately corresponds to a wave magnetic field of 350 nT, which should be detectable by an instrument similar to the fluxgate magnetometer onboard the Van Allen Probes. Additionally, for a frequency of 0.5 Hz ($Y \approx 0.005$), the corresponding magnetic field spectral density is much above the instrument's noise level.

The smaller radius case ($R_a$ = 2.5 m) would be the most logical choice for a mission with the purpose of testing the interaction with particles, since our estimations say that it is capable of generating a detectable scattering on the particles, detectable waves, it does not need to be deployed, and it is the lightest and least power consuming of all the options. In case we want to test the deployment of large-scale structures at the same time, then a

larger antenna radius could be used. We suggest, however, separating the two objectives (detection and deployment) into two different scientific missions, thus reducing the risk and complexity of the spacecraft.

## 7.3 Environmental Concerns

The author has often been asked about the environmental repercussions of the remediation idea. For this reason, we have decided to briefly discuss the environmental impacts introduced by precipitating energetic particles, which main concern relates to the destruction of ozone in the atmosphere.

Energetic solar protons injected in the middle atmosphere (mesosphere and stratosphere) during intense solar storms can produce both $HO_x$ (H, OH and $HO_2$) through the generation of positive ions followed by complex chemistry, and $NO_x$ (N, NO and $NO_2$) through molecular nitrogen dissociation. The enhancement of these species could cause a decrease in ozone. The $HO_x$ constituents have a short lifetime (hours), which cause short-lived ozone reductions in the middle atmosphere. The $NO_x$ family has longer lifetimes and can impact ozone levels for longer times up to months. We next analyze two specific solar proton events (SPE), their fluxes and effects on the atmosphere, and we compare them with the fluxes induced by the scientific mission described in the previous section.

The first event corresponds to the solar storms in July 14-16, 2000, which caused large injection of solar protons into the polar cap regions. The energetic proton fluxes measured by the NOAA Geostationary Operational Environmental Satellite-8 (GOES-8) are presented in Figure 7-6 [‡]. It must be noted that these fluxes are omnidirectional, and during large proton injections they also correspond to the fluxes being precipitated into the atmosphere. The Upper Atmosphere Research Satellite (UARS) Halogen Occultation Experiment (HALOE) measured large increases in Polar Northern Hemisphere $NO_x$ as well as ozone reductions [*Jackman et al.*, 2001]. $NO_x$ values reached 50 ppbv and 200 ppbv at 0.3 hPa and 0.01 hPa, respectively, which represent a large increase compared to the background levels of 1-5 ppbv at 0.3 hPa and 20-60 ppbv at 0.01 hPa. The observed short-term decrease of middle mesospheric ozone caused by $HO_x$ reached 70%, while a longer-term reduction of up

[‡] NOAA-GOES data: http://www.swpc.noaa.gov/Data/goes.html. Last checked: 30 May, 2013

to 9% was detected in the upper stratosphere caused by $NO_x$. In addition, *Randall et al.* [2001] showed enhancements of $NO_x$ in the Southern Hemisphere using the UARS HALOE together with data from the Polar Ozone and Aerosol Measurement (POAM) III.

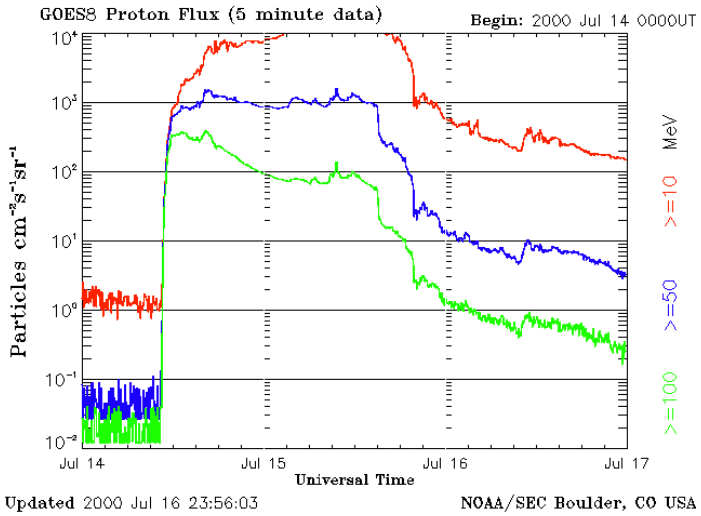


Figure 7-6: Proton fluxes measured by GOES-8 between 14-17 July, 2000

The second event corresponds to October-November, 2003. The energetic proton fluxes from GOES-11 are presented in Figure 7-7. UARS HALOE measured $NO_x$ greater than 100 ppbv at 0.03-0.006 hPa (middle to upper mesosphere) in the Polar Southern Hemisphere where the baseline values are less than 1 ppbv [*Jackman et al.*, 2005]. The short-term ozone depletions at the peak of the proton flux reached 20%-40% in the lower mesosphere probably due to an increase of $HO_x$, while day-long ozone reductions of 5%-8% were observed in the upper stratosphere.

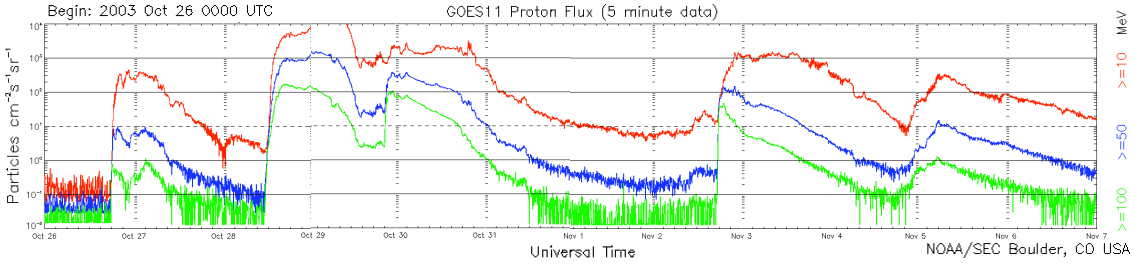


Figure 7-7: Proton fluxes measured by GOES-11 between 26 Oct-4 Nov, 2003

Figures 7-6 and 7-7 show that not only the proton injections correspond to precipitating fluxes larger than $> 100$ cm$^{-2}$sr$^{-1}$s$^{-1}$ (and at GOES altitudes), but they also span along multiple days. We saw in the previous section, however, that the precipitating fluxes in-

duced by a scientific mission would be impulse-like responses, lasting a fraction of a second. Moreover, the magnitude of these fluxes would be negligible compared to the ones recoded by GOES above. In other words, a scientific mission will not jeopardize in any way the ozone layer nor the safety of people on Earth. In the case of a full-scale clean-up mission, and assuming that one would succeed in reducing the particles' natural residence time by a factor of 10, this would also imply an enhancement of the natural aurora intensity by the same factor over all that time. The natural aurora fluxes during quiet times, however, are much smaller than the SPE fluxes in the figures above, that is, even a factor of 10 enhancement of the natural aurora would have a negligible effect on the atmosphere.

# Chapter 8

# Conclusions

In the next sections we present a summary and discussion of this dissertation, the main contributions, and the suggested future work.

## 8.1 Summary and Discussion

In this dissertation we analyzed the feasibility of a mission consisting of space-based transmitters capable of depleting the inner Van Allen belt of energetic trapped protons. These particles can rapidly damage solar panels, electronics and other components of the space systems orbiting the inner region, and represent and hindrance to development of space technologies. We studied both the physics and engineering implications involved in the concept of remediation, which include the radiation of EMIC waves from a space-based antenna, their propagation in the magnetosphere, their interaction with energetic protons, and also the mechanical, thermal and electrical implications of such an antenna. Additionally, we outlined a scientific mission scaled down to detectability of the proton precipitating fluxes.

In this thesis we have shown that it is not possible to use a linear space-based antenna (electric dipole) to radiate EMIC waves, since the accumulation of charge on its surface generates a plasma sheath that impedes radiation. Magnetic dipoles have been identified as a promising solution, which solve the capacitance problem associated with linear antennas. More specifically, we have shown that a DC rotating coil transmitter is the best candidate to

radiate these waves into space, since a large self-inductance develops for AC operation. In terms of radiation, however, the DC rotating idea is equivalent to two static AC orthogonal coils. We should note that in this thesis we did not address the origin of the radiated power; we believe that the *radiation drag* will impart a steady torque on the coil, which would have to be compensated. An alternative could be to supply a DC voltage to the coil to compensate this hypothetical counter electromotive force due to radiation. The radiation from a coil maximizes when its axis (normal to the coil's surface) is perpendicular to the Earth's magnetic field direction, although we have shown that the radiation resistance is not very sensitive to angles around this orientation. We have developed a full-wave model of the radiation pattern in the far-field region of a coil (or two orthogonal coils) in the EMIC regime immersed in a cold magnetized plasma. Our model is in very good agreement with the quasi-static analytical approximation provided by previous authors. Our simulations showed that the power only propagates inside a very small cone (resonance cone) around the geomagnetic field direction. The beam is very focused along the magnetic field lines and illuminates a very small range of $L$-shells, which will translate into very short encounters with energetic protons; the corresponding wave normal angles are close to perpendicular to the geomagnetic field lines. The radiation resistance of magnetic loops, however, is several orders of magnitude smaller than the one of electric dipoles. For this reason, superconductors, large coil radius and multiple turn arrangements are required to increase the power radiated from magnetic dipoles.

Using the properties of the waves close to the source from the full-wave model, we have determined their propagation and damping in the inner belt region. A version of the Stanford ray tracer and damping codes has been used for these calculations, adapted to the EMIC case. Our results showed that the waves propagate mostly field aligned, while the wave normal vector remains close to perpendicular; the curvature and gradient of the Earth's magnetic field have the capability of slightly rotating the wave normal angle towards the geomagnetic field direction as the waves approach the equator. The wave spreading across $L$-shells is very small and will generate short wave-particle interactions with the rapidly drifting energetic protons. Additionally, we showed that these waves are not damped in the oxygen band, while Landau damping has a strong effect near the hydrogen characteristic frequencies and around the stop bands of EMIC waves. We must also note that no bouncing of the waves was considered; there is no observational evidence showing that EMIC waves are

capable of bouncing back from high latitudes. For this reason, our calculations were based on single wave-pass interactions. The bouncing of EMIC waves at lower $L$-shells, however, would certainly improve the results of this thesis, and should be carefully addressed in future studies.

The next step consisted of calculating the interaction between these waves radiated from space-based transmitters and the energetic protons trapped in the inner belt. We showed that each of these encounters is more than one order of magnitude shorter than the protons' gyroperiod, which revealed that the commonly used gyroaveraged formulation is not applicable to our case, but the non-gyroaveraged equations had to be considered. Moreover, the gyroaveraged solution underestimates diffusion rates by three orders of magnitude compared to the more realistic non-gyroaveraged simulation. Additionally, the magnetic wave force dominates the interaction between energetic protons and EMIC waves, which does not modify the energy of the particles but is capable of introducing pitch angle scattering and precipitation. Non-gyroaveraged test particle simulations were used to determine the behavior of individual test protons during one pass interaction, the initial precipitation fluxes at the edge of the loss cone, as well as the MLT-averaged pitch angle diffusion coefficients of all the particles in the distribution. Test particle simulations, however, are very computationally intensive and cannot be used to calculate the particles' lifetime. For this reason, we estimated diffusion coefficients from test particles and used them to solve the pitch angle diffusion equation, which is CPU-efficient. We showed that the off-resonant scattering dominates short interactions, which is captured by the non-gyroaveraged formulation. These off-resonant interactions, once per particles' drift period, generate a random walk and diffusion of the particles in velocity space. We calculated non-gyroaveraged diffusion coefficients and showed that they are practically independent of pitch angle and energy. For a fixed frequency and power, protons at lower $L$-shells are harder to scatter compared to higher $L$-shells, which translates into longer lifetimes of the particles. For a fixed $L$-shell and power, the lower frequencies tend to generate more scattering, which also decreases the particles' lifetime. We estimated that a radiated power of 30 kW at a frequency of Y = 0.015 is required to precipitate an 845 meter-thick layer of protons at $L = 1.5$ in less than 10 years; for the same power and frequency, it takes 30 years at $L = 1.2$ for a layer of 833 m, and only 110 days at $L = 2$ for 856 m. These numbers already suggested that the remediation of the entire proton Van Allen belt requires an excessively large amount of

radiated power.

In order to determine the feasibility of the remediation concept we characterized the engineering implications and performance of the space-based antenna described above. High Temperature Superconducting (HTS) tapes were selected for this application, since they are capable of reaching critical current densities up to 1000 kA/cm$^2$ (larger than most Low Temperature Superconductors (LTS)), they can work at relatively high temperatures and they are much easier to pack and manipulate than the brittle LTS designs. Additionally, HTS can be cooled down below their critical temperature with corresponding increase in critical current density. Moreover, the critical current as a function of temperature starts to saturate around 20 K; for this reason, it is strongly desired to operate below the nominal 77 K, since small temperature reductions produce large performance improvements. For the HTS design of SuperPower, we characterized the performance of the superconductor as a function of the number of turns of the coil, and analyzed the passive and active thermal control required to keep the wire at operating conditions. More specifically, we selected 30 layers of Multilayer Insulator (MLI) together with Quartz over Silver Optical Solar Reflector (OSR) coating. For the active thermal control, we adopted a hybrid cooling approach consisting of a flexible forced vapor system enclosing the coil to ensure isothermalization, and Stirling-cycle cryocoolers (above 50 K) to extract the heat from the vapor. Heat pipes at cryogenic temperatures are very stiff, which will hinder the deployment of a flexible structure. For this reason, it was decided to back out of the passive nature of the heat pipe in favor of a design based on a forced vapor flow. Cryocoolers for temperatures below 50 K have been successfully used in space, and they are efficient and reliable. On the other hand, operation below 20 K, which is desirable in terms of critical current, requires heavy and power demanding cryocoolers. The dynamics of the antenna were also briefly discussed. We showed that the gyroscopic and magnetic effects represent the main contribution to the torque. The gyroscopic torque cancels for spin rate parallel to the angular velocity of the orbit, and it is stable when spinning around a major axis of inertia. For this reason, the solution to the dynamics problem involved a coil rotating around the angular velocity of the orbit (which also maximizes the radiation resistance), but with the spacecraft subsystems distributed on both sides of the coil such that the body becomes a major-axis spinner. We showed that, for this configuration, the magnetic torque just adds a small forced precession to the free gyroscopic precession of the antenna. In the presence of dissipation, only the

circular forced precession of the angular momentum remains, which is very small. The rotation rate was selected based on the frequency tradeoff between radiated and required power, which we called remediation efficiency. The power radiated from a loop antenna scales with the square of the frequency, while the lifetime of the particles tends to decrease with decreasing frequency. We showed that the ratio between required and radiated power has an approximate optimum, which is $L$-shell dependent and equals to 0.5 Hz at $L = 1.5$. For this frequency, we estimated that an antenna of 15 m radius operating at 20 K can radiate 6.4 W and requires 940 W of input power, which corresponds to a radiation efficiency of $\eta_{rad}$ = 0.7%. For operation at 50 K, the antenna radiates 3.3 W but requires 100 W of input power, that is, $\eta_{rad}$ = 3.3%. A clear tradeoff exists between radiated power and radiation efficiency: the larger the radiated power the colder the temperature of the superconductor, which requires power demanding cryocoolers and reduces the antenna radiation efficiency.

The combination of small radiation and remediation efficiencies above led us to the conclusion that, with the current technology, it is not engineeringly feasible to clean up the proton Van Allen belt using space-based transmitters. In order to remediate the entire proton belt, we would require millions of antennas to reduce by a factor of 10 the lifetime of all the particles above 20 MeV, or tens of thousands of spacecraft for the case of 100 MeV particles and above. A scientific mission scaled down to detectability of the proton precipitating fluxes, however, would allow us to test the science involved in the concept of remediation, and will offer an opportunity for maturation of some key technologies. In this thesis, we outlined a scientific mission capable of detecting the precipitating proton fluxes as well as determining the ability of EMIC waves to bounce back and forth in the inner belt region. An orbit close to the equator at $L = 1.5$ was suggested for this mission, since it maximizes the residence time in the inner belt, therefore allowing us to have many observations; the mission lifetime could be kept short, limited by the cost of radiation hardening. The interaction would be mostly local, close to the antenna; an onboard particle telescope could therefore detect the particles streaming towards the spacecraft after they interact with the waves not very far from the antenna. With this purpose, the field-of-view of the instrument should be centered around the direction of the geomagnetic field lines with an aperture angle close to the edge of the loss cone of the particles. Based on measurements from the Medium Energy Proton and Electron Detector (MEPED) onboard the NOAA Polar Orbiting Environmental Satellites (POES), we determined that a minimum

proton precipitating flux of 100 $cm^{-2}sr^{-1}s^{-1}$ is required for detection, which is above the background precipitation level. We analyzed the performance of three different coil radii: 2.5 m, 5 m and 15 m. We showed that the smaller option would be the most logical choice since it is capable of generating a detectable scattering on the particles, it does not need to be deployed, and it is the lightest (316-474 kg) and least power consuming (56-76 W) of all the options. Additionally, we showed that the fields generated by this antenna could be detected by triaxial receivers and magnetometers, which would allow us to determine the ability of EMIC waves to bounce back and forth in the inner belt region.

## 8.2 Contributions

The main contribution of this thesis can be summarized as follows:

**Assessment of the ability of space-based antennas in the EMIC band to clean up the inner Van Allen belt from energetic protons.** The mass and power estimates of a system capable of cleaning this belt are out of the realm of what can be reasonably launched into space nowadays. The models developed in this dissertation led us to the conclusion that, with the current technology, it does not seem possible to use space-based antennas to *remediate* the proton radiation belt.

Additional contributions were made on the way of producing the statement above, which are summarized below:

**Identification of a transmitter capable of radiating EMIC waves**. The analyses in this dissertation led to the dismissal of linear dipoles as well as magnetic dipoles operated in AC. A DC rotating coil was identified as the best candidate to radiate these waves from a space-based platform.

**Development of a full-wave code to solve for the radiation pattern of this antenna**. The code is a linear model capable of calculating the fields and Poynting flux in the far-field region radiated from a coil antenna (or composition of two orthogonal coils) immersed in a cold electron-proton magnetized plasma.

**Characterization of the propagation and damping of man-made EMIC waves in the inner belt region**. These analyses were performed using a modified version of the 3D ray tracer and damping codes from the VLF Group at Stanford University. These codes were previously used to calculate the propagation of whistler waves in the outer belt, and we adapted them to the EMIC case in the inner belt region. Using these models, we have shown that the waves propagate mostly field aligned; each transmitter therefore illuminates a very small region of space.

**Characterization of the off-resonant nature of the interaction between man-made EMIC waves and energetic trapped protons, and development of a non-gyroaveraged test particle code capable of resolving this process.** The behavior of these very short encounters is different from the naturally occurring processes in the magnetosphere, the latter dominated by gyroveraged resonant interactions. In the case of EMIC waves radiated from space-based transmitters, we have shown that off-resonant interactions determine the scattering of the energetic protons, and we have developed a code based on a non-gyroaveraged formulation capable of resolving this phenomena. Additionally, a gyroaveraged code was also developed to characterize the interaction between energetic protons and hypothetical EMIC waves spread over a broad range of MLTs, which could be relevant to future studies.

**Characterization of the evolution of the energetic proton distribution in the inner belt as a result of its interaction with man-made EMIC waves radiated from space-based transmitters**. Using the 1D-VERB code from UCLA together with our non-gyroaveraged code described above, we have characterized the evolution of the entire distribution of energetic protons due to its interaction with man-made EMIC waves. We have determined the new lifetime of the particles resulting from this interaction and compared it with the natural precipitation mechanisms.

**Identification and preliminary characterization of the engineering implications of a space-based antenna capable of radiating EMIC waves in the magnetosphere.** We have analyzed the electrical, mechanical and thermal implications of a space-based DC rotating coil capable of radiating EMIC waves. We have selected High Temperature Superconducting tapes as the best candidate for our application, and characterized

their performance, the requirements on the thermal subsystem and the cooling strategy. An estimation of the power radiated from the antenna as a function of its mass and required input power has also been provided.

**Characterization of a scientific mission capable of testing the science and technology involved in the concept of remediation of the proton Van Allen belt.** We have estimated the mass and power requirements of a scaled down antenna capable of detecting the proton precipitating fluxes. The specifications of the sensors capable of meeting the mission scientific requirements have also been outlined.

List of papers published during my PhD:

**de Soria-Santacruz, M.**, K. G. Orlova, M. Martinez-Sanchez, and Y. Y. Shprits (2013b), Scattering rates of inner belt protons by EMIC waves: A comparison between test particle and diffusion simulations, *Geophys. Res. Lett.*, 40, doi:10.1002/grl.50925.

**de Soria-Santacruz, M.**, M. Spasojevic, and L. Chen (2013a), EMIC waves growth and guiding in the presence of cold plasma density irregularities, *Geophys. Res. Lett.*, 40(8), 1940-1944, doi:10.1002/grl.50484.

**de Soria-Santacruz, M.**, and M. Martinez-Sanchez (2013), Electromagnetic ion cyclotron (EMIC) waves for Radiation Belt Remediation applications, *IEEE Trans. Plasma Sci.*, doi: 10.1109/TPS.2013.2260181.

E. Clements, B. Alvisio, A. Babuscia, Z. Casas, B. Coffee, S. Giblin, L. Hallock, R. Kingsbury, M. Leaman, N. Lynch, M. O'Connor, E. Quian, H. Schmidt, **M. de Soria-Santacruz**, L. Sotomayor, et al., TERSat: Trapped Energetic Radiation Satellite, in *Small Satellite Conference*, Logan, UT, August 2012.

## 8.3 Suggestions for Future Work

This dissertation brought up lots of new areas of research relevant to both scientists and engineers. These areas are related to the radiation of EMIC waves and the physics behind the concept of remediation (on the science side), as well as to the design of the antenna and

the other subsystems of a future scientific mission (on the engineering side). The description of these issues is detailed in the following paragraphs.

### Future Work on Radiation of EMIC Waves

In this dissertation we have analyzed the radiation pattern and radiation resistance of a DC rotating coil antenna. In doing that, we have assumed that the radiation energy comes form the kinetic energy of the rotating coil. Future efforts, however, should address not only the radiation of waves, but also the torque that this radiation puts on the coil and its slowing down due to the energy being taken away by the waves. These studies will also impact the dynamics, attitude control and structures design of the spacecraft.

Another relevant issue are thermal effects introduced by the low-energy background plasma, which have been considered small according to the calculations presented in this thesis. The behavior of the plasma around resonance cones like in the EMIC case, however, are not well understood; cold plasma theory is always questionable in this situation and should be studied in detail in future efforts.

The radiation reactance of a DC rotating coil could be another interesting area of research. The full wave-model presented in this thesis is only capable of calculating the radiation resistance, but not the radiation reactance since it appears as a complicated volume integral in the Poynting Theorem. What is more, it is not clear what *reactance* means in the case of a DC rotating antenna; the radiation reactance is due to plasma currents, but what is its effect on the radiation from a DC rotating transmitter? This is a very interesting topic that could also be part of futures studies.

We believe there is also a broad area of research about the non-linear effects that could happen in the vicinity of the antenna. The radiation models developed in this dissertation are linear, and therefore cover the far-field region. The near-field, however, is believed to be non-linear due to the presence of the plasma; the inhomogeneity of the plasma near the antenna, for example, could generate ducting of the waves and other effects that should be addressed in detail.

Finally, some of the ideas for future work above could be studied not only theoretically but experimentally. The Large Plasma Device (LAPD) at UCLA has heritage on holding

similar experiments. The facility is 19 m long with a 75 cm diameter plasma column, which is capable of performing experiments that require conditions not suitable for small testing facilities. This device could be used to test the near-field behavior of the antenna, the far-field characteristics of the radiation pattern and also the interaction between the radiated waves and energetic particles.

### Future Work on the Physics of Remediation

In this thesis we have showed that it is not possible to remediate the inner proton belt by radiating EMIC waves from space-based transmitters. We have reached this conclusion based on our scientific and engineering models, which contain several assumptions. These assumptions should be reconsidered in future efforts, since they tend to be pessimistic and could improve the outcomes. One of these assumptions is the *no bouncing* condition of EMIC waves, which was justified based on the lack of observational evidence showing that these waves are capable of bouncing back from high latitudes. The bouncing of EMIC waves at lower $L$-shells, however, would certainly improve the results of this thesis, and should be carefully addressed in future studies. Moreover, a scientific mission could also help to answer this unresolved issue.

Another possible area of research involves the utilization of right-hand polarized (R-mode) waves for scattering of energetic protons. This dissertation focused on L-mode EMIC waves by analogy with the ones that are naturally generated in the magnetosphere, and that have been shown to precipitate ring current protons. The progress made in this thesis on wave-particle interactions, however, shows that the nature of the encounters between waves and energetic protons could also favor other polarizations. Nevertheless, right-hand polarized EMIC waves are an unguided mode, thus their radiation and propagation would have to be carefully studied in order to address their applicability to the problem under consideration.

Finally, this thesis was based on remediation by using space-based transmitters. We can think, however, about other options that could have an impact on the energetic inner belt proton population, which could be part of future research efforts. One of these options involves electrostatic scattering of the particles using high-voltage tethers [*Hoyt and Minor*, 2005; *Zeineh*, 2005]. The electric field generated by the tether is responsible for scattering the particles into the loss cone, which also follows a diffusive process. The concept, however,

implies very long tethers covering the entire belt region and charged at voltages comparable to the particles' energies, that is, megavolts with respect to the plasma. Additionally, some of the highly energetic particles will be captured by the tether, which may severely damage the system. Even though the idea of electrostatic scattering also seems engineeringly complicated, these systems may have a large capability of precipitating hazardous trapped protons, which should be carefully reconsidered in future research efforts.

### Future Work on Design of a DC Rotating Antenna

This thesis analyzed the electrical, mechanical and thermal implications of a DC rotating coil antenna capable of radiating EMIC waves. Lots of design work and testing, however, has to be done in order to transform these implications into actual hardware that could fly in a scientific mission.

The difficulty of implementing a DC rotating coil is primarily mechanical. The detailed dynamics, deployment and spin up of the coil represent a critical part of the design, which are currently being addressed in the Space Systems Laboratory at MIT. Similarly, the design and testing of the hybrid cooling system is critical in order to keep the superconductor in good operating conditions, which is currently being addressed by Ray Sedwick at the University of Maryland in collaboration with MIT.

Additionally, a broad area of research exists around High Temperature Superconductors (HTS), which is not limited to space-based antennas but has applications to many other technologies. For the problem presented in this thesis, more work is required on the losses side. The DC antenna design allowed us to neglect hysteresis losses on superconductors. Other losses due to joints, feeds and coupling, however, should be considered in detail in order to carefully determine the performance of the system. Additionally, the packing of the coil needs to be studied carefully, since it could help minimizing these losses. Ohmic dissipation in the superconductor was neglected in this dissertation, which should also be characterized in future studies.

### Proposing A Scientific Mission

In this thesis we have presented an outline to a scientific mission, which could be useful to test the physics behind the remediation idea. Lots of systems engineering work, however, is still left to do in ~~oder~~ to transform this outline into an actual proposal. This proposal should show a good understanding of the different spacecraft subsystems, i.e. power, structures, thermal, attitude determination and control, avionics, communications, and others.

The power subsystem should be capable of managing and providing a large amount of current to the superconducting coil antenna, as well as the required input power to the cooling system and the rest of the subsystems onboard.

The structural design and configuration of the spacecraft subsystems are strongly influenced by the detailed dynamics of the antenna. We saw that the solution to the dynamics problem involved the transformation of the coil into a major-axis spinner, which could be achieved by distributing the spacecraft subsystems on both sides of the coil.

The design of the Attitude Determination and Control subsystem (ADCS) may also be impacted by the dynamics of the coil, as well as by the sensor pointing requirements like the ones imposed by the particle telescopes described in this dissertation.

Additionally, the details of the instrumentation, like receivers and particle detectors, should be carefully addressed before proposing any mission, since they are the eyes of the spacecraft and should be capable of seeing the science that we want to sense. What is more, we want to see this science too; the communications subsystem also has an important role, as it does in all the missions that fly into space.

Finally, but not less important, are the cost and risk analyses, which would actually determine the viability of the scientific mission.

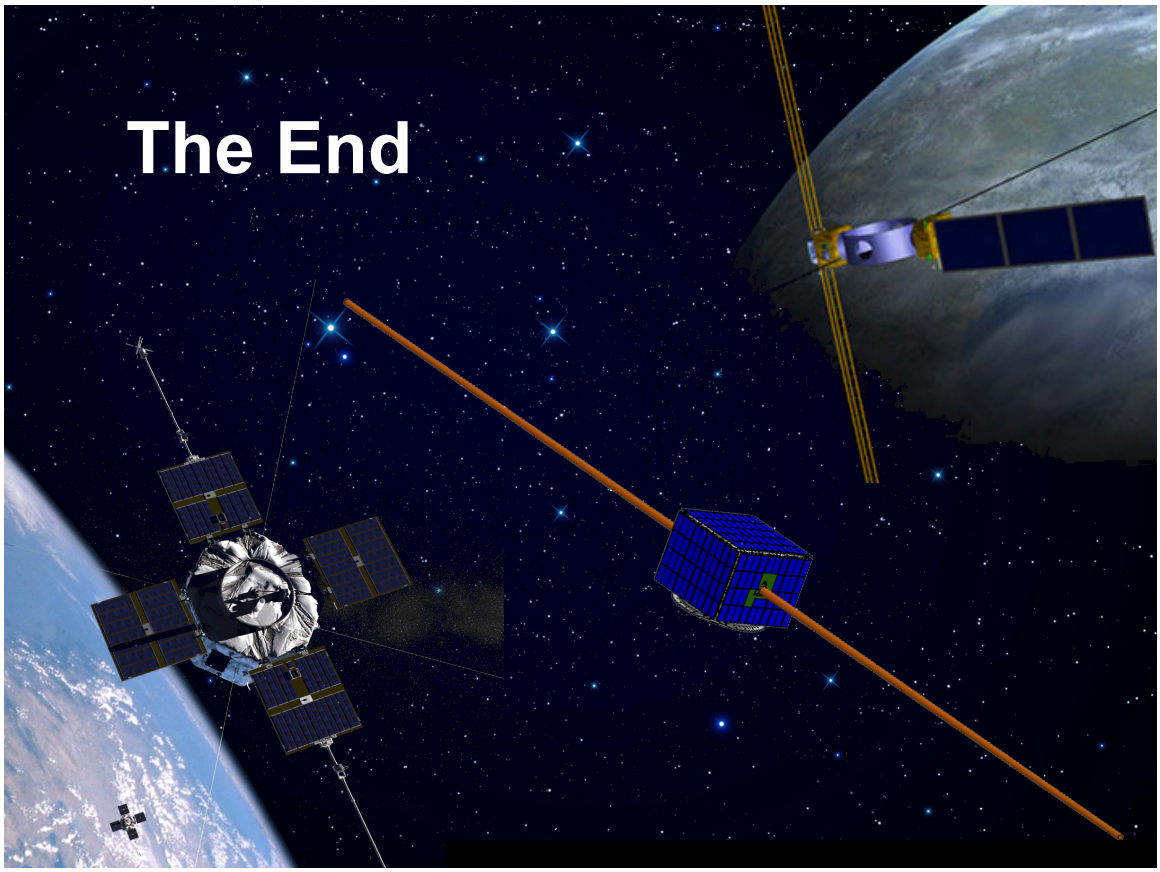


Figure 8-1: From left to right: The Van Allen Probes, Trapped Energetic Radiation Satellite (TERSat), Demonstration and Science Experiments (DSX)

# Appendix A

# Derivation of Stationary Points

The Stationary Phase Method is used in the full-wave model to integrate over $\theta$ and $\phi$ when the observation point is in the far field region. At the so called stationary points ($\theta_S$, $\phi_S$) the exponential term does not vary rapidly. Near the stationary points it is possible to take the other terms out of the integral and only integrate the exponential. Since it is only the vicinity of the stationary points that contributes, the exponent can be expanded in Taylor series about these points.

The stationary points ($\theta_S$, $\phi_S$) can be found by imposing $\frac{\partial \Phi}{\partial \phi} = 0$ and $\frac{\partial \Phi}{\partial \theta} = 0$, where the phase $\Phi$ is given by

$$\Phi(\theta, \phi, \theta_x, \phi_x) = \frac{sin\theta sin\theta_x cos(\phi - \phi_x) + cos\theta cos\theta_x}{\sqrt{\frac{1+cos^2\theta}{2} - \frac{Y^2 sin^2\theta}{2M} \pm \sqrt{\frac{sin^4\theta}{4}\left(1 + \frac{Y^2}{M}\right)^2 + Y^2 cos^2\theta}}} \tag{A.1}$$

The stationary points are then given by

$$\frac{\partial \Phi}{\partial \phi} = 0 \implies \phi_{S_j} = \begin{cases} \phi_x \\ \phi_x + \pi \end{cases} \tag{A.2}$$

$$\frac{\partial \Phi}{\partial \theta} = 0 \implies \begin{cases} \tan\left(\theta_S - \theta_x\right) = \frac{\tan\theta_S}{2}\left(1 \mp \frac{\sin^2\theta_S}{\sqrt{\sin^4\theta_S + 4Y^2\cos^2\theta_S}}\right) & \text{for } \phi_S = \phi_x \\ \tan\left(\theta_S + \theta_x\right) = \frac{\tan\theta_S}{2}\left(1 \mp \frac{\sin^2\theta_S}{\sqrt{\sin^4\theta_S + 4Y^2\cos^2\theta_S}}\right) & \text{for } \phi_S = \phi_x + \pi \end{cases} \tag{A.3}$$

where the negative and positive signs correspond to the right and left-hand polarizations of the dispersion relationship, respectively. As detailed in *de Soria-Santacruz* [2011], the expression above has two or three solutions for $\phi_S$ depending on the value of $\theta_x$, which have to be considered in the full wave solution.

# Appendix B

# Notes on AC Operation of Superconductors

Although not applicable to the DC rotating antenna design, a little research was done as part of this dissertation about AC operation of superconductors. This investigation could be relevant to future applications, and for this reason it is detailed here. The first section below presents the critical wire length for constant current on an AC coil antenna, while the second section summarizes our research on AC losses in superconductors.

## B.1 Critical Length for Constant Current on an AC Antenna

In the case of the static AC coil, the current along the antenna has to remain constant in space in order to avoid the formation of a plasma sheath around the antenna. This sheath will develop not due to the self-inductance of the coil (which is the reason why AC operation is not feasible) but to the oscillation of the current in space, which will induce large potentials across the coil. The critical length that allows a full wavelength along the wire can be expressed as follows

$$l_{crit} = \frac{c_{wire}}{\omega} \tag{B.1}$$

where $c_{wire}$ is the wave propagation velocity along the wire. A simple model to find this

propagation speed can be formulated assuming a *matrix sheath* with $n_{H^+} = n_{e\infty} = \text{constant}$. Under this assumption, Poisson's equation can be written as follows

$$\frac{1}{r}\frac{d}{dr}\left(r\frac{d\phi}{dr}\right) = \frac{en_{e\infty}}{\epsilon_0} \tag{B.2}$$

Integrating and imposing $\phi = 0$ at the sheath boundary $r = a + \delta$, and $\phi = V$ at $r = a$, where $a$ is the wire radius, $V$ is the voltage applied to the antenna and $\delta$ approximately equals the debye length $\delta \approx \delta_{debye} = \sqrt{\frac{\epsilon_0 k_B T_e}{n_{e\infty} q^2}}$, then

$$\phi = \frac{V + \frac{en_{e\infty}}{4\epsilon_0}\left[(a+\delta)^2 - a^2\right]}{Ln\left(\frac{a}{\delta+a}\right)} Ln\left(\frac{r}{\delta+a}\right) + \frac{en_{e\infty}}{4\epsilon_0}\left[r^2 - (a+\delta)^2\right] \tag{B.3}$$

Imposing $\frac{\partial\phi}{\partial r}|_{a+\delta} = 0$, the charge at the surface p.u. length can be expressed as follows

$$Q_l = 2\pi a\epsilon_0 \left.\frac{\partial\phi}{\partial r}\right|_a = 2\pi\epsilon_0 \left[\frac{2V\,(a+\delta)^2}{(a+\delta)^2\left[2Ln\left(\frac{a}{\delta+a}\right)+1\right] - a^2} + \frac{en_{e\infty}}{2\epsilon_0}a^2\right] \tag{B.4}$$

The first term on the right-hand side of the equation above corresponds to the forced sheath term, which determines the capacitance p.u. length, $C_l$, given by

$$C_l = \frac{|Q_l|}{V} = \left|\frac{4\pi\epsilon_0\,(a+\delta)^2}{(a+\delta)^2\left[2Ln\left(\frac{a}{\delta+a}\right)+1\right] - a^2}\right| \tag{B.5}$$

The inductance p.u. length of the wire can be easily expressed as follows

$$L_l = \frac{\mu_0}{2\pi} Ln\left|\frac{\delta}{a}\right| \tag{B.6}$$

Combining capacitance and inductance it is possible to get the propagation speed along the wire given by

$$c_{wire} = \frac{1}{\sqrt{C_l L_l}} \frac{\sqrt{2}c\sqrt{\left|(a+\delta)^2\left[2Ln\left(\frac{a}{\delta+a}\right)+1\right] - a^2\right|}}{2\,(a+\delta)\sqrt{Ln\,|\delta/a|}} \approx c \tag{B.7}$$

which is approximately the speed of light. This result implies that the constant current condition is easily satisfied even for very long wire lengths, i.e. a forced sheath is not going to develop around a magnetic dipole antenna due to the oscillation of the current (but it will due to the self-inductance). Figure B-1 presents the critical wire length for sheath formation onset. Figure B-1 (a) shows that $l_{crit}$ increases with $L$-shell, while the dependence on the wire radius is negligible according to Figure B-1 (b). Nevertheless, $l_{crit}$ is in the order of $10^4 - 10^5$ km and does not represent a limitation.

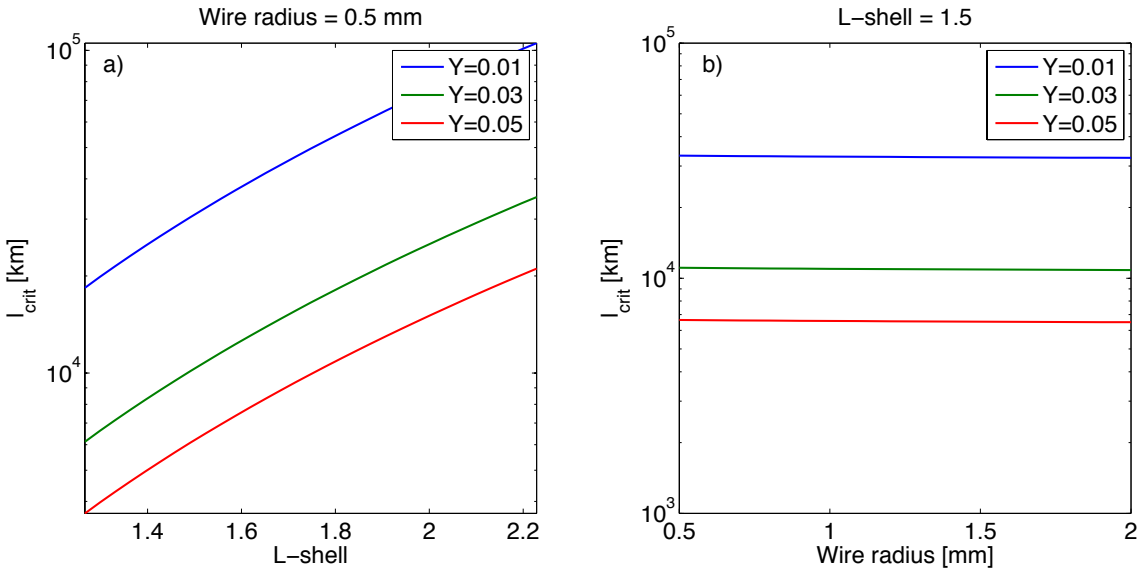


Figure B-1: (a) Critical wire length as a function of $L$-shell for a wire radius of 0.5 mm and three different frequencies. (b) Critical wire length as a function of wire radius at $L$=1.5 for three different frequencies.

## B.2 AC Losses on Superconductors

Superconductors are intrinsically dissipative under an applied transport current, time-varying magnetic field, or a combination of both. AC losses arise due to magnetization considerations and they can be of three types: hysteresis, coupling and eddy-current losses. Hysteresis power losses ($w_{hy}$) are proportional to the rate of change of the self-induced field, while coupling ($w_{cp}$) and eddy-current ($w_{ed}$) losses scale with the square of this field rate

$$w_{hy} \propto \dot{B} \tag{B.8}$$

$$w_{cp} \propto \dot{B}^2 \tag{B.9}$$

$$w_{ed} \propto \dot{B}^2 \tag{B.10}$$

The dominant AC loss in low frequency applications, therefore, will be the hysteresis loss.

Hysteresis loss occurs because most superconductors contain material impurities that can sustain a nonzero electric field. These are called Type II superconductors (or hard superconductors), which are made from alloys or oxide ceramics and include all HTS superconductors. These impurities are intentionally introduced into the superconducting material because they provide a *pinning* force that opposes the $\vec{J_c} \times \vec{H}$ Lorentz force. The balance of Lorenz and pinning forces determines the critical current $J_c$, which is dramatically increased compared to pure diamagnetic superconductors (Type I, or soft) thanks to the flux pinning effect. The flux pinning idea is schematized in Figure B-2 [*Bishop et al.*, 1993]. The superconductor corresponds to the blue box, which contains artificial and/or natural defects. The current flowing though the superconductor is disrupted by the cylinders representing an induced circulating current pinned to the impurities, which adds to the circulating current on one side but subtracts from the other. The result is a net force that pushes the cylinders at right angles to the current flow.

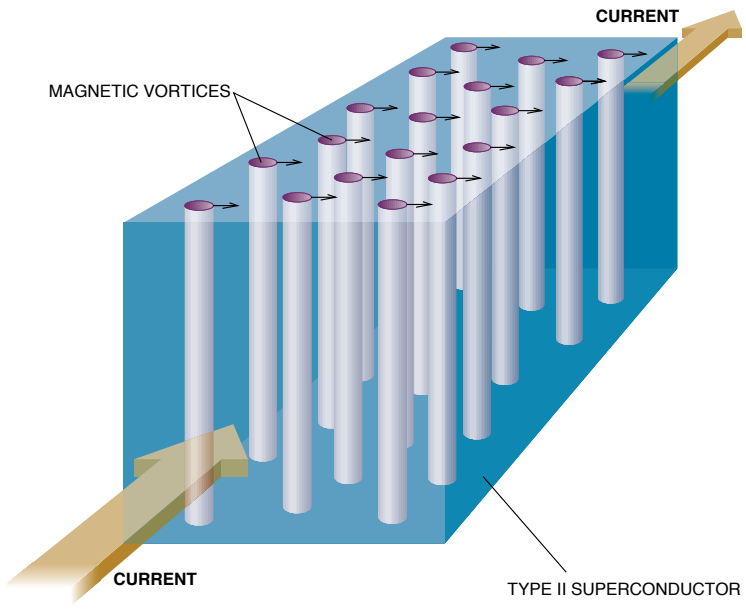


Figure B-2: Flux pinning representation in Type II superconductors [*Bishop et al.*, 1993]

The magnetic characterization of hard superconductors is commonly addressed using the Bean's Critical State model, which provides a simple but accurate approximation of the superconductor's behavior [*Iwasa*, 1994, Chap. 5]. This model assumes that the material consists of superconducting and normal layers that allow field penetration into the superconductor. It is assumed that the field experienced by each lamina induces a current density equal to its critical value, $J_c$, and that this current is field-independent. Under these assumptions, the hysteresis loss is derivable in closed analytical form. An accurate calculation of the AC losses, however, would require the numerical computation of the magnetic field distribution in time and space all over the coil cross-section [*Norris*, 1970; *Grilli et al.*, 2013], which is outside the scope of this thesis. The hysteresis energy density loss for a Bean slab, $e_{hy}$ $[J/m^3/cycle]$, with a transport current $I_t$ is given by [*Hahn*, 2011; *Pardo et al.*, 2012]

$$e_{hy} = \frac{2}{3}\mu_0 H_p^2 i^3 \tag{B.11}$$

where $i = I_t/I_c$ and $H_p$ is the penetration field given by

$$H_p = J_c * \frac{d}{2} \tag{B.12}$$

where $d$ is the tape thickness. The energy density loss, therefore, scales with the square of the tape thickness. Equation (B.11) is valid for field excitations of the type $I_t(t) = 0 \rightarrow I_t \rightarrow 0 \rightarrow -I_t \rightarrow 0$ and under the condition $0 \leq H_m \leq H_p(1-i)$. $H_m$ is the magnetic field corresponding to the maximum $B_{\perp_{max}}$ derived in Section 6.3.2. We consider that tapes in the cable act independently, and that the critical current at a given temperature and coil configuration is given by Figure 6-6 (c).

The loss per unit length of tape, $E_{hy}$ $[J/m/cycle]$, can then be calculated as follows

$$E_{hy} = e_{hy} * d * t * \lambda_{(RE)BCO} \tag{B.13}$$

The power loss per unit volume, $w_{hy}$ [W/m$^3$], can be easily found by multiplying $e_{hy}$ by the driving frequency

$$w_{hy} = e_{hy} * f \tag{B.14}$$

where $f$ is the driving frequency. The total power loss, $W_{hy}$ $[W]$, is then

$$W_{hy} = w_{hy} * d * t * \lambda_{(RE)BCO} * l_{wire} \tag{B.15}$$

As an example, consider a coil operating in AC with $d = 4$ mm, $l_{wire} = 10$ km and $R_a = 15$. The coil operates at T = 77 K with $i = I_t/I_c = 0.5$. Take critical field given by $B_{\perp_c} = 0.12$ T and $J_c = 1.5 \cdot 10^{10}$ A/m$^2$, respectively. If we assume that the losses are represented by the high field condition, the penetration field can then be calculated as follows

$$H_p(0.12\ T, 77\ K) = 1.5 \cdot 10^{10} \left[\frac{4 \cdot 10^{-3}}{2}\right] = 3 \cdot 10^7\ \frac{A}{m} \tag{B.16}$$

and the closed cycle hysteresis loss is then

$$e_{hy} = \frac{2}{3}\mu_0 \left(3 \cdot 10^7\right)^2 0.5^3 = 9.4261 \cdot 10^7\ \frac{J}{m^3 cycle} \tag{B.17}$$

or per unit length

$$E_{hy} = 9.4261 \cdot 10^7 \left[\frac{J}{m^3 cycle}\right] 4 \cdot 10^{-3}\,[m]\, 10^{-6}\,[m] = 0.3770\ \frac{J}{m\ cycle} \tag{B.18}$$

The power loss for the case above operating at a frequency of $f = 2$ Hz is

$$W_{hy} = 0.3770 \left[\frac{J}{m\ cycle}\right] 10^4\,[m]\, 2 \left[\frac{cycle}{s}\right] = 7.5\ kW \tag{B.19}$$

which corresponds to $w_{hy} = 0.1875$ W/mm$^3$.

In the following, we estimate these losses as a function of transport current, tape width and temperature. Figure B-3 (a) and (b) presents $E_{hy}$ and $W_{hy}$, respectively, as a function of the normalized transport current, for three different tape widths and a temperature of 77 K. The losses depend on the cube of $i = I_t/I_c$ and linearly on the tape thickness as it can also

be observed in the plots. Figure B-3 (c) and (d) presents the dependence on temperature for $i = 0.1$. $W_{hy}$ has been calculated based on a frequency of 2 Hz and a wire length of $l_{wire}$ = 10 km. In terms of AC losses, low $I_t$ and $d$, and high temperature are preferable. The power radiated from the coil, however, follows the opposite trends.

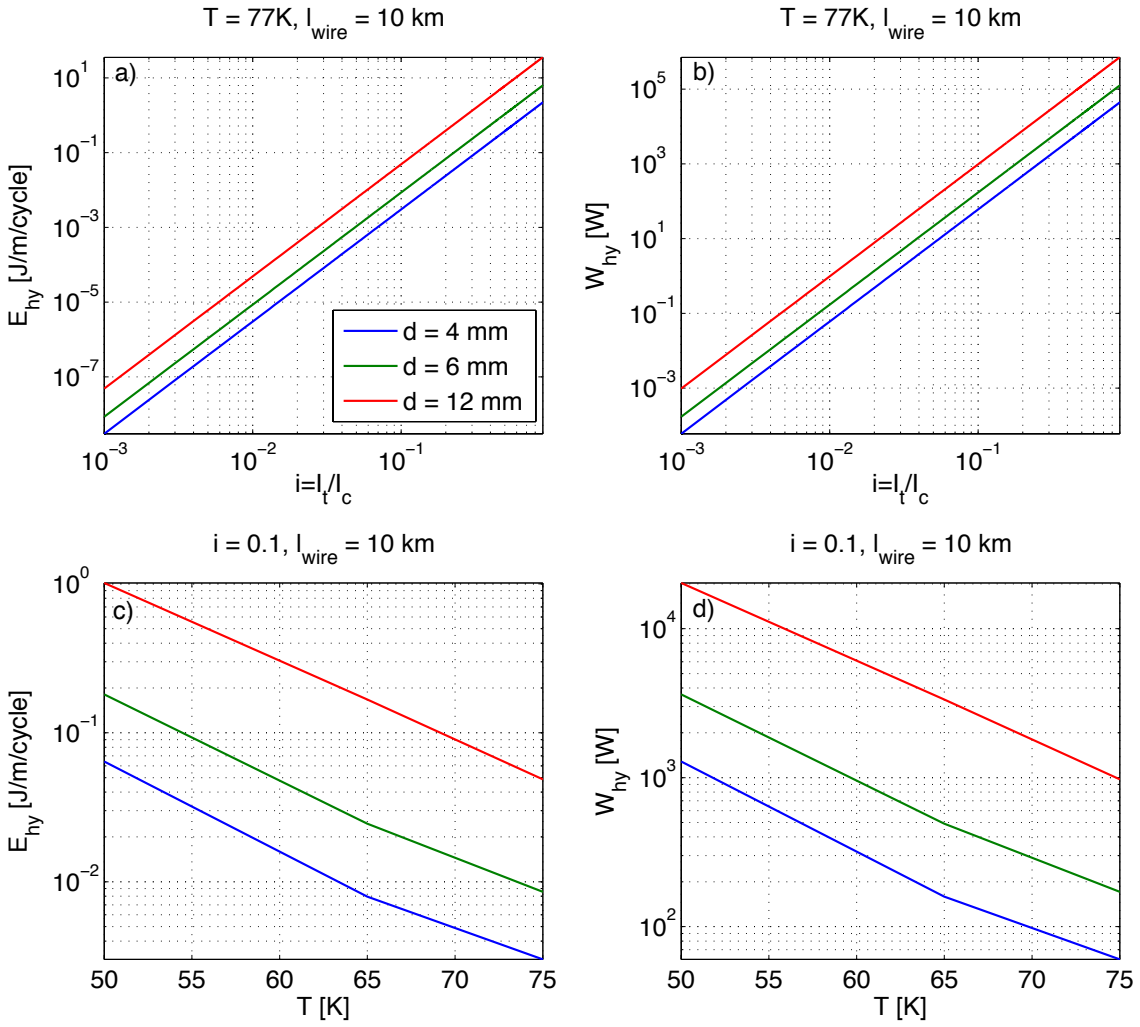


Figure B-3: (a) AC energy density loss as a function of normalized transport current for three different tape widths and T = 77 K. (b) Power loss as a function of normalized transport current for T = 77 K. The plot is for a frequency of 2 Hz and a wire length of 10 km. (c) AC energy density loss as a function of temperature for a normalized transport current of $i = 0.1$. (d) AC power loss as a function of temperature for a normalized transport current of $i = 0.1$, a frequency of 2 Hz and a wire length of 10 km.

The cases analyzed above are all unacceptable in terms of thermal control requirements. The problem lies in the architecture of HTS tapes, which is not mature enough for AC applications. HTS tapes are characterized by high aspect ratios, i.e. centimeter widths

versus micron thicknesses. In the presence of magnetic fields normal to the tape these aspect ratios lead to unacceptable hysteresis losses for AC applications. However, lots of promising research exists around improving these architectures in AC regimes. *Carr Jr and Oberly* [1999] were the first to provide a solution to these losses, which consists of subdividing the superconducting HTS layer into thin linear filaments, commonly called striations, and then twist the tape as a whole to decouple the magnetic field between the different wires in the coil. The new width of the striations would then determine the AC losses, which according to equation (B.11) would now scale with the square of this new effective width. Successful experiments showing this loss reduction due to striations are being developed in different laboratories [*Amemiya et al.*, 2004; *Schuller et al.*, 2007; *Lee et al.*, 2009, 2013], but the technology is still under development. Figure B-4 presents an example of these striations by *Cobb et al.* [2002], which has been produced using a laser ablation technique to subdivide YBCO filaments. The average width of the striations and cuts is 254 $\mu$m and 66 $\mu$m, respectively. These samples were tested at different temperatures with no transport current, and they experimentally observed a linear dependency of the losses on the striation width as predicted by the theory. In the case of a superconductor with an applied transport current, however, the losses depend on the square of the striation width (equation (B.11)); thus, we expect an even more dramatic improvement due to this new tape architecture. Although the laboratory experiments so far have only been able to test striations up to several thousands of microns, we conjecture that the same scaling will also prevail for tens of microns, which remarkably reduces the losses.

Figure B-5 analyzes the effect of the striations. The AC losses are represented as a function of the width of the striations, $d_{str}$, and for different transport currents. A tape of total width $d = 12$ mm has been considered. The total power losses are for a frequency of 2 Hz and a wire length of 10 km. Figure B-5 (a)-(b) are for $T_c = 77$ K, while (c)-(d) are for $T_c = 50$ K. Compared to Figure B-3, the striations effectively decrease the hysteresis losses, which depend on the square of their width. These values are now most probably acceptable in terms of thermal control requirements, but as mentioned above they require further maturation of the superconductor technology for AC applications.

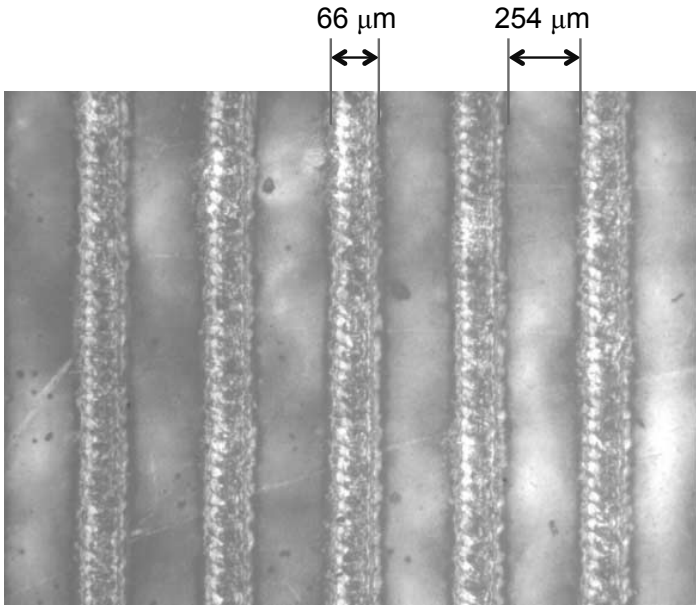


Figure B-4: Striated structure of YBCO generated with laser ablation [*Cobb et al.*, 2002]. The average width of the striations and cuts is 254 $\mu$m and 66 $\mu$m, respectively.

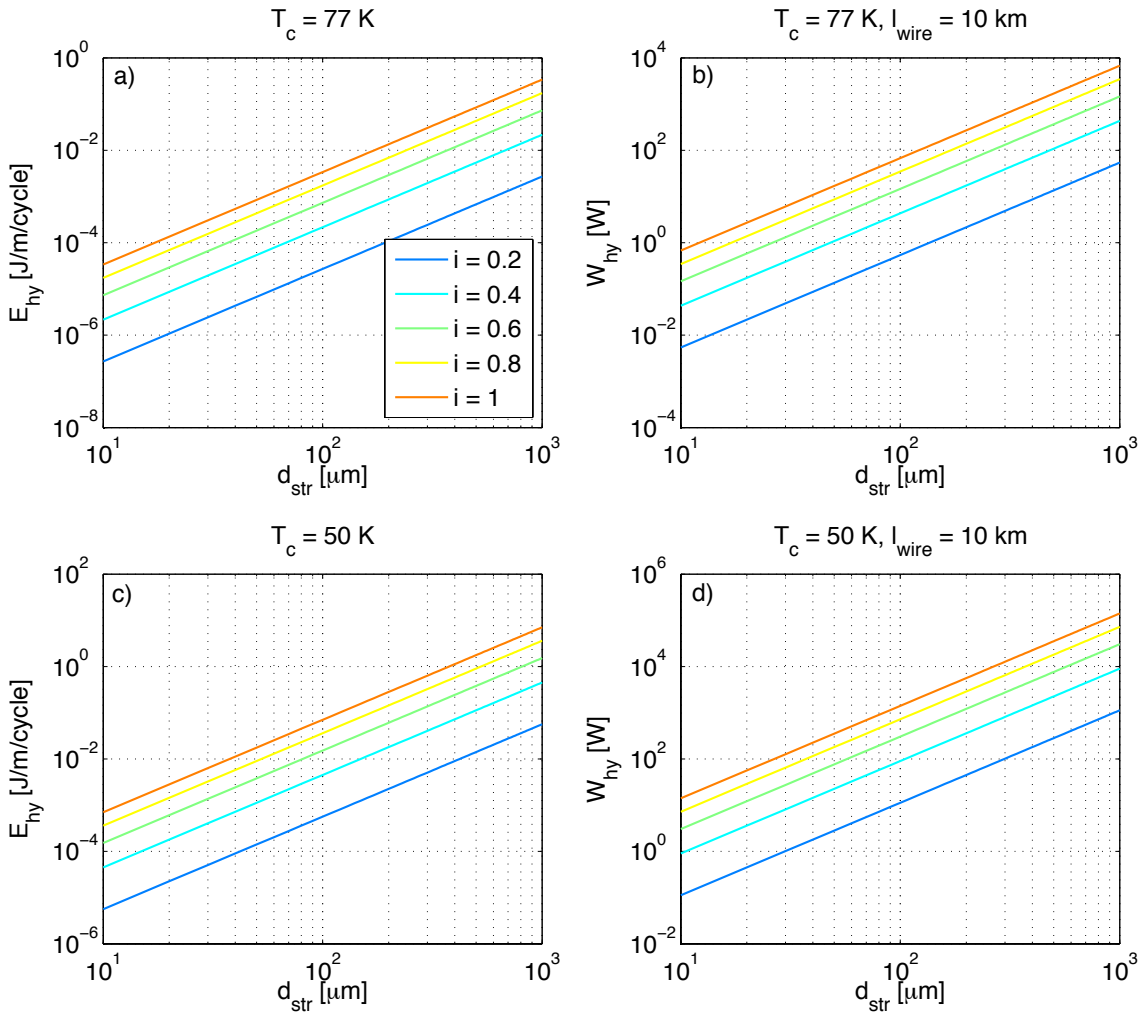


Figure B-5: a) AC energy density loss as a function of the width of the striations for different normalized transport currents at T = 77 K. (b) Power loss as a function of the width of the striations at T = 77 K. The plot is for a frequency of 2 Hz and a wire length of 10 km. (c) AC energy density loss as a function of the width of the striations at T = 50 K. (d) AC power loss as a function of the width of the striations at T = 50 K. The plot is for a frequency of 2 Hz and a wire length of 10 km.

# Appendix C

# Additional Resources

Different codes from different sources were used in this dissertation, which are listed below:

- **Full-wave radiation model:** Code written in Matlab by the author.
- **3D Ray tracer:** Code written in Fortran. Original version by Forrest Foust [*Golden et al.*, 2010] from the VLF Group at Stanford University.
- **Damping code:** Code written in Matlab. Original version by Forrest Foust [*Golden et al.*, 2010] from the VLF Group at Stanford University.
- **Test-particle codes:** Codes written in Matlab by the author.
- **VERB 1D code:** Code written in Matlab. Original version by Dmitriy Subbotin [*Subbotin and Shprits*, 2009] from UCLA.

# Bibliography


Abel, B., and R. M. Thorne (1998), Electron scattering loss in Earth's inner magnetosphere 1. Dominant physical processes, *Journal of Geophysical Research*, *103*(A2), 2385–2396, doi:10.1029/97JA02919.

Albert, J. (2007), Simple approximations of quasi-linear diffusion coefficients, *Journal of Geophysical Research: Space Physics*, *112*(A12), doi:10.1029/2007JA012551.

Albert, J. M. (1999), Analysis of quasi-linear diffusion coefficients, *Journal of Geophysical Research*, *104*(A2), 2429–2441, doi:10.1029/1998JA900113.

Albert, J. M. (2003), Evaluation of quasi-linear diffusion coefficients for EMIC waves in a multispecies plasma, *Journal of Geophysical Research*, *108*, doi:10.1029/2002JA009792.

Albert, J. M. (2005), Evaluation of quasi-linear diffusion coefficients for whistler mode waves in a plasma with arbitrary density ratio, *Tech. rep.*, DTIC Document.

Albert, J. M., and J. Bortnik (2009), Nonlinear interaction of radiation belt electrons with electromagnetic ion cyclotron waves, *Geophysical Research Letter*, *36*, doi:10.1029/2009GL038904.

Amemiya, N., S. Kasai, K. Yoda, Z. Jiang, G. A. Levin, P. N. Barnes, and C. E. Oberly (2004), AC loss reduction of YBCO coated conductors by multifilamentary structure, *Superconductor Science and Technology*, *17*(12), 1464, doi:10.1088/0953-2048/17/12/018.

Anderson, B. J. (1996), Recent observations of electromagnetic ion cyclotron waves in space, *Advances in Space Research*, *17*(10), 41–50, doi:10.1016/0273-1177(95)00693-9.

Baker, D. N. (2000), The occurrence of operational anomalies in spacecraft and their relationship to space weather, *IEEE Transactions on Plasma Science*, *28*(6), 2007–2016, doi:10.1109/27.902228.

Baker, D. N. (2001), Satellite anomalies due to space storms, in *Space Storms and Space Weather Hazards*, pp. 285–311, Springer.

Baker, D. N., S. Kanekal, V. C. Hoxie, M. G. Henderson, X. Li, H. E. Spence, S. R. Elkington, R. H. W. Friedel, J. Goldstein, M. K. Hudson, et al. (2013), A Long-Lived Relativistic Electron Storage Ring Embedded in Earth's Outer Van Allen Belt, *Science*, doi:10.1126/science.1233518.

Balmain, K. (1964), The impedance of a short dipole antenna in a magnetoplasma, *IEEE Transactions on Antennas and Propagation*, *12*(5), 605–617, doi:10.1109/TAP.1964.1138278.

Bell, T. F. (1984), The nonlinear gyroresonance interaction between energetic electrons and coherent VLF waves propagating at an arbitrary angle with respect to the Earth's magnetic field, *Journal of Geophysical Research*, *89*, 905–918, doi:10.1029/JA089iA02p00905.

Bell, T. F., and T. Wang (1971), Radiation resistance of a small filamentary loop antenna in a cold multicomponent magnetoplasma, *IEEE Transactions on Antennas and Propagation*, *19*(4), 517–522, doi:10.1109/TAP.1971.1139957.

Bell, T. F., U. S. Inan, and T. Chevalier (2006), Current distribution of a VLF electric dipole antenna in the plasmasphere, *Radio Science*, *41*(2), doi:10.1029/2005RS003260.

Bhandari, P., M. Prina, R. C. Bowman Jr, C. Paine, D. Pearson, and A. Nash (2004), Sorption coolers using a continuous cycle to produce 20 K for the Planck flight mission, *Cryogenics*, *44*(6), 395–401, doi:10.1016/j.cryogenics.2004.02.022.

Bishop, D. J., P. L. Gammel, and D. A. Huse (1993), Resistance in high-temperature superconductors, *Scientific American*, *268*, 48–55, doi:10.1038/scientificamerican0293-48.

Bortnik, J. (2004), Precipitation of Radiation Belt Electrons by Lightning-Generated Magnetospherically Reflecting Whistler Waves, Ph.D. thesis, Department of Electrical Engineering, Stanford University.

Bortnik, J., U. S. Inan, and T. F. Bell (2006), Temporal signatures of radiation belt electron precipitation induced by lightning-generated MR whistler waves: 1. Methodology, *Journal of Geophysical Research*, *111*(A2), doi:10.1029/2005JA011182.

Brown, W. L., and J. D. Gabbe (1963), The electron distribution in the Earth's radiation belts during July 1962 as measured Telstar, *Journal of Geophysical Research*, *68*(3), 607–618, doi:10.1029/JZ068i003p00607.

Budden, K. (1966), *Radio waves in the ionosphere*, Cambridge University Press.

Carr Jr, W. J., and C. E. Oberly (1999), Filamentary YBCO conductors for AC applications, *IEEE Transactions on Applied Superconductivity*, *9*(2), 1475–1478, doi:10.1109/77.784671.

Chang, H. C. (1983), Cyclotron Resonant Scattering of Energetic Electrons by Electromagnetic Waves in the Magnetosphere, Ph.D. thesis, Department of Electrical Engineering, Stanford University.

Chang, H. C., and U. S. Inan (1983), Quasi-relativistic electron precipitation due to interactions with coherent VLF waves in the magnetosphere, *Journal of Geophysical Research*, *88*, 318–328, doi:10.1029/JA088iA01p00318.

Chang, H. C., and U. S. Inan (1985a), Lightning-induced electron precipitation from the magnetosphere, *Journal of Geophysical Research*, *90*, 1531–1541, doi:10.1029/JA090iA02p01531.

Chang, H. C., and U. S. Inan (1985b), Test particle modeling of wave-induced energetic electron precipitation, *Journal of Geophysical Research*, *90*, 6409–6418, doi:10.1029/JA090iA07p06409.

Chen, L., R. M. Thorne, V. K. Jordanova, C. P. Wang, M. Gkioulidou, L. Lyons, and R. B. Horne (2010), Global simulation of EMIC wave excitation during the 21 April 2001 storm from coupled RCM-RAM-HOTRAY modeling, *Journal of Geophysical Research: Space Physics*, *115*(A7), 1978–2012, doi:10.1029/2009JA015075.

Chevalier, T. W., U. S. Inan, and T. F. Bell (2008), Terminal impedance and antenna current distribution of a VLF electric dipole in the inner magnetosphere, *IEEE Transactions on Antennas and Propagation*, *56*(8), 2454 –2468, doi:10.1109/TAP.2008.927497.

Chevalier, T. W., U. S. Inan, and T. F. Bell (2010), Fluid simulation of the collisionless plasma sheath surrounding an electric dipole antenna in the inner magnetosphere, *Radio Science*, *45*, 1010, doi:10.1029/2008RS003843.

Cobb, C. B., P. N. Barnes, T. J. Haugan, J. Tolliver, E. Lee, M. Sumption, E. Collings, and C. E. Oberly (2002), Hysteretic loss reduction in striated YBCO, *Physica C: Superconductivity*, *382*(1), 52–56, doi:10.1016/S0921-4534(02)01196-6.

Cohen, M. B. (2009), ELF/VLF phased array generation via frequency-matched steering of a continuous HF ionospheric heating beam, Ph.D. thesis, Department of Electrical Engineering, Stanford University.

Comfort, R. H. (1996), Thermal structure of the plasmasphere, *Advances in Space Research*, *17*(10), 175–184, doi:10.1016/0273-1177(95)00710-V.

Davidson, G. T. (1977), *The Trapped Radiation Handbook*, chap. The motion of charged particles in the Earth's magnetic field, DNA 25241H, Lockheed Palo Altro Research Laboratory.

de Soria-Santacruz, M. (2011), Radiation of VLF/ELF waves from a magnetospheric tether, S. M. Thesis, Department of Aeronautics and Astronautics, Massachusetts Institute of Technology.

de Soria-Santacruz, M., M. Spasojevic, and L. Chen (2013a), EMIC waves growth and guiding in the presence of cold plasma density irregularities, *Geophysical Research Letters*, *40*(8), 1940—1944, doi:10.1002/grl.50484.

de Soria-Santacruz, M., K. G. Orlova, M. Martinez-Sanchez, and Y. Y. Shprits (2013b), Scattering rates of inner belt protons by EMIC waves: A comparison between test particle and diffusion simulations, *Geophysical Research Letters*, *40*(18), 4793–4797, doi:10.1002/grl.50925.

Delcourt, D. C., J.-A. Sauvaud, R. F. Martin, and T. E. Moore (1996), On the nonadiabatic precipitation of ions from the near-Earth plasma sheet, *Journal of Geophysical Research: Space Physics*, *101*(A8), 17,409–17,418, doi:10.1029/96JA01006.

Dmitrieva, N. P., A. G. Yahnin, T. V. Miroshnikova, and I. V. Despirak (1999), Precipitation of Energetic Protons at High Latitudes: Dependence on the Interplanetary Magnetic Field, *Cosmic Research*, *37*(4), 317–325.

Dobes, K. (1970), The HM wave-particle cyclotron resonance for non-parallel propagation, *Planetary and Space Science*, *18*(3), 395 – 406, doi:10.1016/0032-0633(70)90177-7.

Dragt, A. J., M. M. Austin, and R. S. White (1966), Cosmic Ray and Solar Proton Albedo Neutron Decay Injection, *Journal of Geophysical Research*, *71*(5), 1293–1304, doi:10.1029/JZ071i005p01293.

Engebretson, M. J., M. R. Lessard, J. Bortnik, J. C. Green, R. B. Horne, D. L. Detrick, A. T. Weatherwax, J. Manninen, N. J. Petit, J. L. Posch, et al. (2008), Pc1–Pc2 waves and energetic particle precipitation during and after magnetic storms: Superposed epoch analysis and case studies, *Journal of Geophysical Research: Space Physics*, *113*(A1), doi:10.1029/2007JA012362.

Erlandson, R. E., and A. J. Ukhorskiy (2001), Observations of electromagnetic ion cyclotron waves during geomagnetic storms: Wave occurrence and pitch angle scattering, *Journal of Geophysical Research*, *106*(A3), 3883–3895, doi:10.1029/2000JA000083.

Evans, D. S., and M. S. Greer (2004), Polar Orbiting Environmental Satellite Space Environment Monitor - 2: Instrument Descriptions and Archive Data Documentation, *NOAA Technical Memorandum*, Space Environment Center, Boulder, CO.

Fang, X., M. W. Liemohn, J. U. Kozyra, D. S. Evans, A. D. DeJong, and B. A. Emery (2007), Global 30–240 keV proton precipitation in the 17–18 April 2002 geomagnetic storms: 1. Patterns, *Journal of Geophysical Research: Space Physics*, *112*(A5), doi:10.1029/2006JA011867.

Fraser, B. J., J. C. Samson, Y. D. Hu, R. L. McPherron, and C. T. Russell (1992), Electromagnetic ion cyclotron waves observed near the oxygen cyclotron frequency by ISEE 1 and 2, *Journal of Geophysical Research*, *97*(A3), 3063–3074, doi:10.1029/91JA02447.

Fraser, B. J., H. J. Singer, W. J. Hughes, J. R. Wygant, R. R. Anderson, and Y. D. Hu (1996), CRRES Poynting vector observations of electromagnetic ion cyclotron waves near the plasmapause, *Journal of Geophysical Research*, *101*(A7), 15,331–15, doi:10.1029/95JA03480.

Gallagher, D. L., P. D. Craven, and R. H. Comfort (2000), Global Core Plasma Model, *Journal of Geophysical Research: Space Physics*, *105*(A8), 18,819–18,833, doi:10.1029/1999JA000241.

Gettliffe, G., N. K. Inamdar, R. Masterson, and D. W. Miller (2012), High-temperature superconductors as electromagnetic deployment and support structures in spacecraft, *NASA NIAC Phase I Final Report*, Massachusetts Institute of Technology.

Gigliotti, A., W. Gekelman, P. Pribyl, S. Vincena, A. Karavaev, X. Shao, A. Sharma, and D. Papadopoulos (2009), Generation of polarized shear Alfvén waves by a rotating magnetic field source, *Physics of Plasmas*, *16*, 092,106.

Gilmore, D. G. (1994), *Satellite Thermal Control Handbook*, Aerospace Corporation Press, El Segundo, CA.

Ginet, G. P., T. P. O'Brien, S. L. Huston, W. R. Johnston, T. B. Guild, R. Friedel, C. D. Lindstrom, C. J. Roth, P. Whelan, R. A. Quinn, et al. (2013), AE9, AP9 and SPM: New Models for Specifying the Trapped Energetic Particle and Space Plasma Environment, *Space Science Reviews*, pp. 1–37, doi:10.1007/s11214-013-9964-y.

Glauert, S. A., and R. B. Horne (2005), Calculation of pitch angle and energy diffusion coefficients with the PADIE code, *Journal of Geophysical Research*, *110*(A4), doi: 10.1029/2004JA010851.

Golden, D. I., M. Spasojevic, F. R. Foust, N. G. Lehtinen, N. P. Meredith, and U. S. Inan (2010), Role of the plasmapause in dictating the ground accessibility of ELF/VLF chorus, *Journal of Geophysical Research*, *115*(A11), doi:10.1029/2010JA015955.

Gomberoff, L., and R. Neira (1983), Convective Growth Rate of Ion Cyclotron Waves in a $H^+$-$He^+$ and $H^+$-$He^+$-$O^+$ Plasma, *Journal of Geophysical Research*, *88*(A3), 2170–2174, doi:10.1029/JA088iA03p02170.

Grilli, F., E. Pardo, A. Stenvall, D. N. Nguyen, W. Yuan, and F. Gömöry (2013), Computation of Losses in HTS Under the Action of Varying Magnetic Fields and Currents, *IEEE Transactions on Applied Superconductivity*, doi:10.1109/TASC.2013.2259827.

Hahn, S. (2011), AC loss and other disturbances, *2.64 - Superconducting magnets: Class notes*, Massachusetts Institute of Technology.

Haselgrove, J. (1955), Ray theory and a new method for ray tracing, in *Physics of the Ionosphere*, vol. 1, p. 355.

Hazelton, D. W. (2012), 2G HTS Conductors at SuperPower, in *Low Temperature High Field Superconductor Workshop*, Napa, CA.

Hoffman, J., and O. Batishchev (2005), Use of superconducting magnet technology for astronaut radiation protection, *Final Report for NIAC Phase I Contract CP 04-01*, NASA's Institute for Advanced Concepts (NIAC).

Horne, R. B., and R. M. Thorne (1993), On the preferred source location for the convective amplification of ion cyclotron waves, *Journal of Geophysical Researchesearch*, *98*(A6), 9233–9247, doi:10.1029/92JA02972.

Horne, R. B., and R. M. Thorne (2003), Relativistic electron acceleration and precipitation during resonant interactions with whistler-mode chorus, *Geophysical Research Letters*, *30*(10), 1527, doi:10.1029/2003GL016973.

Horwitz, J. L. (1987), Core plasma in the magnetosphere, *Reviews of Geophysics*, *25*(3), 579–587, doi:10.1029/RG025i003p00579.

Hoyt, R. P., and B. M. Minor (2005), Remediation of radiation belts using electrostatic tether structures, in *IEEE Aerospace Conference*, pp. 583–594, IEEE, doi: 10.1109/AERO.2005.1559348.

Imhof, W. L., J. B. Reagan, H. D. Voss, E. E. Gaines, D. W. Datlowe, J. Mobilia, R. A. Helliwell, U. S. Inan, J. Katsufrakis, and R. Joiner (1983), Direct observation of radiation belt electrons precipitated by the controlled injection of VLF signals from a ground-based transmitter, *Geophysical Research Letters*, *10*, 361–364, doi:10.1029/GL010i004p00361.

Inan, U. S. (1987), Gyroresonant pitch angle scattering by coherent and incoherent whistler mode waves in the magnetosphere, *Journal of Geophysical Research*, *92*, 127–142, doi: 10.1029/JA092iA01p00127.

Inan, U. S., and T. F. Bell (1991), Pitch angle scattering of energetic particles by oblique whistler waves, *Geophysical Research Letters*, *18*, 49–52, doi:10.1029/90GL02476.

Inan, U. S., T. F. Bell, and R. A. Helliwell (1978), Nonlinear pitch angle scattering of energetic electrons by coherent VLF waves in the magnetosphere, *Journal of Geophysical Research*, *83*(A7), 3235–3253, doi:10.1029/JA083iA07p03235.

Inan, U. S., T. F. Bell, and H. C. Chang (1982), Particle precipitation induced by short-duration VLF waves in the magnetosphere, *Journal of Geophysical Research*, *87*, 6243–6264, doi:10.1029/JA087iA08p06243.

Inan, U. S., H. C. Chang, and R. A. Helliwell (1984), Electron precipitation zones around major ground-based VLF signal sources, *Journal of Geophysical Research*, *89*(A5), 2891–2906, doi:10.1029/JA089iA05p02891.

Inan, U. S., T. F. Bell, and J. Bortnik (2003), Controlled precipitation of radiation belt electrons, *Journal of Geophysical Research*, *108*(A5), doi:10.1029/2002JA009580.

Iwasa, Y. (1994), *Case Studies in Superconducting Magnets: Design and Operational Issues*, Selected Topics in Superconductivity, Plenum Press, New York.

Jackman, C. H., R. D. McPeters, G. J. Labow, E. L. Fleming, C. J. Praderas, and J. M. Russell (2001), Northern hemisphere atmospheric effects due to the july 2000 solar proton event, *Geophysical Research Letters*, *28*(15), 2883–2886, doi:10.1029/2001GL013221.

Jackman, C. H., M. T. DeLand, G. J. Labow, E. L. Fleming, D. K. Weisenstein, M. K. Ko, M. Sinnhuber, and J. M. Russell (2005), Neutral atmospheric influences of the solar proton events in october–november 2003, *Journal of Geophysical Research: Space Physics (1978–2012)*, *110*(A9), doi:10.1029/2004JA010888.

Jordanova, V. K., J. U. Kozyra, and A. F. Nagy (1996), Effects of heavy ions on the quasi-linear diffusion coefficients from resonant interactions with electromagnetic ion cyclotron waves, *Journal of Geophysical Research*, *101*(A9), 19,771–19,778, doi:10.1029/96JA01641.

Jordanova, V. K., J. U. Kozyra, A. F. Nagy, and G. V. Khazanov (1997), Kinetic model of the ring current-atmosphere interactions, *Journal of Geophysical Research*, *102*, doi:10.1029/96JA03699.

Jordanova, V. K., C. J. Farrugia, J. M. Quinn, R. M. Thorne, K. E. Ogilvie, R. P. Lepping, G. Lu, A. J. Lazarus, M. F. Thomsen, and R. D. Belian (1998), Effect of wave-particle interactions on ring current evolution for January 10-11, 1997: Initial results, *Geophysical Research Letter*, *25*, doi:10.1029/98GL00649.

Jordanova, V. K., C. J. Farrugia, R. M. Thorne, G. V. Khazanov, G. D. Reeves, and M. F. Thomsen (2001), Modeling ring current proton precipitation by electromagnetic ion cyclotron waves during the May 14–16, 1997, storm, *Journal of Geophysical Research*, *106*, doi:10.1029/2000JA002008.

Karavaev, A. V. (2010), Waves in plasmas generated by a rotating magnetic field and implications to radiation belts, Ph.D. thesis, University of Maryland.

Karavaev, A. V., N. A. Gumerov, K. Papadopoulos, X. Shao, A. S. Sharma, W. Gekelman, Y. Wang, B. Van Compernolle, P. Pribyl, and S. Vincena (2011), Generation of shear Alfvén waves by a rotating magnetic field source: Three-dimensional simulations, *Physics of Plasmas*, *18*, 032,113, doi:10.1063/1.3562118.

Kennel, C. F., and F. Engelmann (1966), Velocity space diffusion from weak plasma turbulence in a magnetic field, *Physics of Fluids*, *9*(12), 2377, doi:10.1063/1.1761629.

Kimura, I. (1966), Effects of ions on whistler-mode ray tracing, *Radio Science*, *1*(3), 269–283.

Kletzing, C. A., W. S. Kurth, M. Acuna, R. J. MacDowall, R. B. Torbert, T. Averkamp, D. Bodet, S. R. Bounds, M. Chutter, J. Connerney, et al. (2012), The Electric and Magnetic Field Instrument Suite and Integrated Science (EMFISIS) on RBSP, *Space Science Reviews*, pp. 1–55, doi:10.1007/s11214-013-9993-6.

Kuehl, H. H. (1962), Electromagnetic radiation from an electric dipole in a cold anisotropic plasma, *Physics of Fluids*, *5*(9), 1095–1104, doi:10.1063/1.1724479.

Kulkarni, P., U. S. Inan, and T. F. Bell (2008), Energetic electron precipitation induced by space based VLF transmitters, *Journal of Geophysical Research*, *113*, doi:10.1029/2008JA013120.

Kwon, D. W. (2005), Electromagnetic Formation Flight of Satellite Arrays, *S. M. Thesis*, Department of Aeronautics and Astronautics, Massachusetts Institute of Technology.

Kwon, D. W. (2009), Cryogenic heat pipe for cooling high temperature superconductors with application to Electromagnetic Formation Flight satellites, *Ph. D. Thesis*, Department of Aeronautics and Astronautics, Massachusetts Institute of Technology.

Lam, M. M., R. B. Horne, N. P. Meredith, S. A. Glauert, T. Moffat-Griffin, and J. C. Green (2010), Origin of energetic electron precipitation $>$ 30 keV into the atmosphere, *Journal of Geophysical Research: Space Physics*, *115*(A4), doi:10.1029/2009JA014619.

Lauben, D. S. (1998), Precipitation of radiation belt electrons by obliquely-propagating lightning-generated whistler waves, Ph. D. Thesis, Department of Electrical Engineering, Stanford University.

Lee, J. K., S. Byun, B. W. Han, W. S. Kim, S. Park, S. Choi, C. Park, and K. Choi (2009), Reduction effect on magnetization loss in the stacked conductor with striated and transposed YBCC coated conductor, *IEEE Transactions on Applied Superconductivity*, *19*(3), 3340–3343, doi:10.1109/TASC.2009.2017845.

Lee, J. K., Y. Kim, S. Lee, W. S. Kim, S. H. Park, C. Park, and K. Choi (2013), AC Loss Analysis of Striated HTS Compact Cables for Low Loss Cable Design, *IEEE Transactions on Applied Superconductivity*, doi:10.1109/TASC.2013.2239340.

Lenchek, A. M., S. F. Singer, and R. C. Wentworth (1961), Geomagnetically trapped electrons from cosmic ray albedo neutrons, *Journal of Geophysical Research*, *66*(12), 4027–4046, doi:10.1029/JZ066i012p04027.

Li, W., Y. Y. Shprits, and R. M. Thorne (2007), Dynamic evolution of energetic outer zone electrons due to wave-particle interactions during storms, *Journal of Geophysical Research*, *112*(A10), doi:10.1029/2007JA012368.

Lorentzen, K. R., M. P. McCarthy, G. K. Parks, J. E. Foat, R. P. Lin, R. M. Millan, D. M. Smith, and J. P. Treilhou (2000), Precipitation of relativistic electrons by interaction with electromagnetic ion cyclotron waves, *Journal of Geophysical Research: Space Physics*, *105*(A3), 5381–5389, doi:10.1029/1999JA000283.

Loto'aniu, T., R. Thorne, B. Fraser, and D. Summers (2006), Estimating relativistic electron pitch angle scattering rates using properties of the electromagnetic ion cyclotron wave spectrum, *Journal of Geophysical Research*, *111*(A4), A04,220, doi:10.1029/2005JA011452.

Loto'aniu, T. M., B. J. Fraser, and C. L. Waters (2005), Propagation of electromagnetic ion cyclotron wave energy in the magnetosphere, *Journal of Geophysical Research*, *110*, doi:10.1029/2004JA010816.

Ludlow, G. R. (1989), Growth of obliquely propagating ion cyclotron waves in the magnetosphere, *Journal of Geophysical Research*, *94*(A11), 15,385–15,391, doi:10.1029/JA094iA11p15385.

Lyons, L. R. (1974a), General relations for resonant particle diffusion in pitch angle and energy, *Journal of Plasma Physics*, *12*(01), 45–49, doi:10.1017/S0022377800024910.

Lyons, L. R. (1974b), Pitch angle and energy diffusion coefficients from resonant interactions with ion–cyclotron and whistler waves, *Journal of Plasma Physics*, *12*(03), 417–432, doi:10.1017/S002237780002537X.

Lyons, L. R., and R. M. Thorne (1972), Parasitic pitch angle diffusion of radiation belt particles by ion cyclotron waves, *Journal of Geophysical Research*, *77*(28), doi:10.1029/JA077i028p05608.

Lyons, L. R., R. M. Thorne, and C. F. Kennel (1972), Pitch-angle diffusion of radiation belt electrons within the plasmasphere, *Journal of Geophysical Research*, *77*(19), 3455–3474, doi:10.1029/JA077i019p03455.

Manfreda, G. (2011), Review of ROXIE's Material Properties Database for Quench Simulation, *Internal Note 2011-24*, Magnets, Supercondutors and Cryostats, TE-MSC.

Mazur, J., L. Friesen, A. Lin, D. Mabry, N. Katz, Y. Dotan, J. George, J. Blake, M. Looper, M. Redding, et al. (2012), The relativistic proton spectrometer (RPS) for the radiation belt storm probes mission, *Space Science Reviews*, pp. 1–41, doi:10.1007/s11214-012-9926-9.

Meredith, N. P., R. M. Thorne, R. B. Horne, D. Summers, B. J. Fraser, and R. R. Anderson (2003), Statistical analysis of relativistic electron energies for cyclotron resonance with EMIC waves observed on CRRES, *Journal of Geophysical Research*, *108*, doi:10.1029/2002JA009700.

Miller, D. W. (2013), Mid-term report to the NASA Shared Services Center (NSSC), *Tech. rep.*, Massachusetts Institute of Technology.

Miyoshi, Y., K. Sakaguchi, K. Shiokawa, D. Evans, J. Albert, M. Connors, and V. Jordanova (2008), Precipitation of radiation belt electrons by EMIC waves, observed from ground and space, *Geophysical Research Letter*, *35*, doi:10.1029/2008GL035727.

Mozer, F. S., D. D. Elliott, J. D. Mihalov, G. A. Paulikas, A. L. Vampola, and S. C. Freden (1963), Preliminary analysis of the fluxes and spectrums of trapped particles after the nuclear test of July 9, 1962, *Journal of Geophysical Research*, *68*(3), 641–649, doi:10.1029/JZ068i003p00641.

NASA Data Center National Space Science (2012), Intercosoms 24, http://nssdc.gsfc.nasa.gov/nmc/spacecraftDisplay.do?id=1989-080A.

Norris, W. T. (1970), Calculation of hysteresis losses in hard superconductors carrying ac: isolated conductors and edges of thin sheets, *Journal of Physics D: Applied Physics*, *3*(4), 489, doi:10.1088/0022-3727/3/4/308.

Omura, Y., Y. Katoh, and D. Summers (2008), Theory and simulation of the generation of whistler-mode chorus, *Journal of Geophysical Research: Space Physics*, *113*(A4), doi: 10.1029/2007JA012622.

Pardo, E., J. Šouc, and J. Kováč (2012), AC loss in ReBCO pancake coils and stacks of them: modelling and measurement, *Superconductor Science and Technology*, *25*(3), 035,003, doi:10.1088/0953-2048/25/3/035003.

Pieper, G. F. (1963), A second radiation belt from the July 9, 1962, nuclear detonation, *Journal of Geophysical Research*, *68*(3), 651–655, doi:10.1029/JZ068i003p00651.

Raghuram, R., R. Smith, and T. Bell (1974), VLF Antarctic antenna: Impedance and efficiency, *IEEE Transactions on Antennas and Propagation*, *22*(2), 334–338, doi: 10.1109/TAP.1974.1140777.

Randall, C., D. Siskind, and R. Bevilacqua (2001), Stratospheric $NO_x$ enhancements in the southern hemisphere vortex in winter/spring of 2000, *Geophysical Research Letters*, *28*(12), 2385–2388, doi:10.1029/2000GL012746.

Rauch, J. L., and A. Roux (1982), Ray tracing of ULF waves in a multicomponent magnetospheric plasma: Consequences for the generation mechanism of ion cyclotron waves, *Journal of Geophysical Research*, *87*(A10), 8191–8198, doi:10.1029/JA087iA10p08191.

Rey, C. M., W. C. Hoffman Jr, F. R. Chang-Diaz, A. V. Ilin, A. J. Petro, D. S. Winter, H. Mukai, and S. W. Schwenterly (2002), Design and fabrication of an HTS magnet for the VASIMR experiment, *IEEE Transactions on Applied Superconductivity*, *12*(1), 993–996, doi:10.1109/TASC.2002.1018567.

Ristic-Djurovic, J. L. (1993), Gyroresonant scattering of radiation belt electrons by oblique whistler waves, Ph.D. thesis, Department of Electrical Engineering, Stanford University.

Ristic-Djurovic, J. L., U. S. Inan, and T. F. Bell (1992), Precipitation of suprathermal (100 eV) electrons by oblique whistler waves, *Geophysical Research Letters*, *19*(16), 1639–1642, doi:10.1029/92GL01811.

Ristic-Djurovic, J. L., T. F. Bell, and U. S. Inan (1998), Precipitation of radiation belt electrons by magnetospherically reflected whistlers, *Journal of Geophysical Research*, *103*, 9249–9260, doi:10.1029/97JA03724.

Rodger, C. J., T. Raita, M. A. Clilverd, A. Seppälä, S. Dietrich, N. R. Thomson, and T. Ulich (2008), Observations of relativistic electron precipitation from the radiation belts driven by EMIC waves, *Geophysical Research Letter*, *35*, doi:10.1029/2008GL034804.

Ross Jr, R. G., and R. F. Boyle (2006), An overview of NASA space cryocooler programs—2006, *Tech. rep.*, Jet Propulsion Laboratory, National Aeronautics and Space Administration, Pasadena, CA.

Scherbarth, M., D. Smith, A. Adler, J. Stuart, and G. Ginet (2009), AFRL's Demonstration and Science Experiments (DSX) Mission, in *SPIE Optical Engineering+ Applications*, pp. 74,380B–74,380B, International Society for Optics and Photonics.

Schuller, S., W. Goldacker, A. Kling, L. Krempasky, and C. Schmidt (2007), AC-loss measurement of a DyBCO-Roebel assembled coated conductor cable (RACC), *Physica C: Superconductivity*, *463*, 761–765, doi:10.1016/j.physc.2007.01.063.

Schulz, M., and L. J. Lanzerotti (1974), *Particle diffusion in the radiation belts*, Springer-Verlag, New York.

Selesnick, R. S., M. D. Looper, and R. A. Mewaldt (2007), A theoretical model of the inner proton radiation belt, *Space Weather*, *5*(4), doi:10.1029/2006SW000275.

Selesnick, R. S., M. K. Hudson, and B. T. Kress (2010), Injection and loss of inner radiation belt protons during solar proton events and magnetic storms, *Journal of Geophysical Research: Space Physics*, *115*(A8), doi:10.1029/2010JA015247.

Selvamanickam, V., Y. Yao, Y. Chen, T. Shi, Y. Liu, N. D. Khatri, J. Liu, C. Lei, E. Galstyan, and G. Majkic (2012), The low-temperature, high-magnetic-field critical current characteristics of Zr-added (Gd, Y) $Ba_2Cu_3O_x$ superconducting tapes, *Superconductor Science and Technology*, *25*(12), 125,013, doi:10.1088/0953-2048/25/12/125013.

Serbu, G. P., and E. J. R. Maier (1966), Low-energy electrons measured on IMP 2, *Journal of Geophysical Research*, *71*(15), 3755–3766, doi:10.1029/JZ071i015p03755.

Shao, X., K. Papadopoulos, and A. S. Sharma (2009), Control of the energetic proton flux in the inner radiation belt by artificial means, *Journal of Geophysical Research*, *114*(A7), A07,214, doi:10.1029/2009JA014066.

Shirley, K., S. Banks, R. Boyle, and R. Unger (2005), Design and Qualification of the AMS-02 Flight Cryocoolers, *Space Cryogenics Workshop, Colorado Springs, CO, PowerPoint Presentation slides*, NASA Goddard Space Flight Center, Cryogenics and Fluids Branch.

Shprits, Y., W. Li, and R. Thorne (2006a), Controlling effect of the pitch angle scattering rates near the edge of the loss cone on electron lifetimes, *Journal of Geophysical Research: Space Physics*, *111*(A12), doi:10.1029/2006JA011758.

Shprits, Y. Y., R. M. Thorne, R. B. Horne, and D. Summers (2006b), Bounce-averaged diffusion coefficients for field-aligned chorus waves, *Journal of Geophysical Research*, *111*(A10), doi:10.1029/2006JA011725.

Siegel, R., and J. Howell (2002), *Thermal radiation heat transfer*, Fourth ed., Taylor and Francis.

Song, P., B. W. Reinisch, V. Paznukhov, G. Sales, D. Cooke, J. N. Tu, X. Huang, K. Bibl, and I. Galkin (2007), High-voltage antenna-plasma interaction in whistler wave transmission: Plasma sheath effects, *Journal of Geophysical Research*, *112*(A3), doi: 10.1029/2006JA011683.

Spanjers, G., J. Winter, D. Cohen, A. Adler, J. Guarnieri, M. Tolliver, G. Ginet, B. Dichter, and J. Summers (2006), The AFRL Demonstration and Science Experiments (DSX) for DoD space capability in the MEO, in *IEEE Aerospace Conference*, pp. 10–pp, IEEE, Big Sky, MA.

Stenzel, R. L. (1975), Self-ducting of large-amplitude whistler waves, *Phys. Rev. Lett.*, *35*(9), 574–577, doi:10.1103/PhysRevLett.35.574.

Stenzel, R. L. (1976), Antenna radiation patterns in the whistler wave regime measured in a large laboratory plasma, *Radio Science*, *11*(12), 1045–1056, doi: 10.1029/RS011i012p01045.

Stix, T. H. (1992), *Waves in Plasmas*, Springer-Verlag New York, Inc.

Subbotin, D. A., and Y. Y. Shprits (2009), Three-dimensional modeling of the radiation belts using the Versatile Electron Radiation Belt (VERB) code, *Space Weather*, *7*(10), S10,001, doi:10.1029/2008SW000452.

Summers, D. (2005), Quasi-linear diffusion coefficients for field-aligned electromagnetic waves with applications to the magnetosphere, *Journal of Geophysical Research*, *110*, doi:10.1029/2005JA011159.

SunPower Inc. (2013), *SunPower CryoTel MT Specifications Sheet*, Athens, OH.

Takiguchi, Y. (2009), Emission of whistler waves from an ionospheric tether, Master's thesis, Department of Aeronautics and Astronautics, Massachusetts Institute of Technology.

Tao, X., and J. Bortnik (2010), Nonlinear interactions between relativistic radiation belt electrons and oblique whistler mode waves, *Nonlinear Processes in Geophysics*, *17*, 599–604, doi:10.5194/npg-17-599-2010.

The Gund Company, Inc. (2013), Mylar* Polyester Film Type EL-21: Material data sheet.

Thomson, W. T. (1986), *Introduction to space dynamics*, Dover Publications Inc.

Thorne, R. M., and R. B. Horne (1993), Cyclotron absorption of ion-cyclotron waves at the bi-ion frequency, *Geophysical Research Letters*, *20*(4), 317–320, doi:10.1029/93GL00089.

Thorne, R. M., and C. F. Kennel (1967), Quasi-trapped VLF propagation in the outer magnetosphere, *Journal of Geophysical Research*, *72*(3), 857–870, doi: 10.1029/JZ072i003p00857.

Thorne, R. M., R. B. Horne, V. K. Jordanova, J. Bortnik, and S. Glauert (2006), Interaction of EMIC waves with thermal plasma and radiation belt particles, *Geophys. Monogr. Ser.*, *169*, 213, doi:10.1029/169GM14.

Tu, J., P. Song, and B. W. Reinisch (2008), Plasma sheath structures around a radio frequency antenna, *Journal of Geophysical Research*, *113*(A7), doi:10.1029/2008JA013097.

Van Allen, J. A., G. H. Ludwig, E. C. Ray, and C. E. McIlwain (1958), Observation of high intensity radiation by satellites 1958 Alpha and Gamma, *Jet Propulsion*, *28*(9), 588–592, doi:10.2514/8.7396.

Voss, D. L., A. Gunda, D. Carssow, T. Fritz, A. Mavretic, and J. Sullivan (2009), Overview of the loss cone imager fixed sensor head instrument, in *Proceedings of SPIE*, vol. 7438, p. 743808.

Wang, T. N. C., and T. F. Bell (1969), Radiation resistance of a short dipole immersed in a cold magnetoionic medium, *Radio Science*, *4*(2), 167–177, doi:10.1029/RS004i002p00167.

Wang, T. N. C., and T. F. Bell (1970), On VLF radiation resistance of an electric dipole in a cold magnetoplasma, *Radio Science*, *5*(3), 605–610, doi:10.1029/RS005i003p00605.

Wang, T. N. C., and T. F. Bell (1972a), Electric dipole radiation at VLF in a uniform warm magneto-plasma, *Revue de Physique Appliquee*, *7*(1), 11–20, doi:10.1051/rphysap:019720070101100.

Wang, T. N. C., and T. F. Bell (1972b), VLF/ELF Radiation Patterns of Arbitrarily Oriented Electric and Magnetic Dipoles in a Cold Lossless Multicomponent Magnetoplasma, *Journal of Geophysical Research*, *77*, 1174–1189, doi:10.1029/JA077i007p01174.

Wang, T. N. C., and T. F. Bell (1972c), VLF/ELF input impedance of an arbitrarily oriented loop antenna in a cold collisionless multicomponent magnetoplasma, *IEEE Transactions on Antennas and Propagation*, *20*(3), 394 – 398, doi:10.1109/TAP.1972.1140212.

Wang, T. N. C., and T. F. Bell (1973), On input impedance of an arbitrarily oriented small loop antenna in a cold collisionless magnetoplasma, *IEEE Transactions on Antennas and Propagation*, *21*(5), 745–746, doi:10.1109/TAP.1973.1140562.

Wertz, J. R., and W. J. Larson (Eds.) (2007), *Space Mission Analysis and Design*, Third ed., Space Technology Library.

White, G. K., and S. J. Collocott (1984), *Heat Capacity of Reference Materials, Cu and W*, American Chemical Society and the American Institute of Physics for the National Bureau of Standards.

Winglee, R., T. Ziemba, and et al. (2005), Magnetized Beamed Plasma Propulsion (MagBeam), *NIAC Fellows Meeting Presentation*, NASA's Institute for Advanced Concepts (NIAC).

Wissing, J. M. and Bornebusch, J. P. and Kallenrode, M-B. (2008), Variation of energetic particle precipitation with local magnetic time, *Advances in Space Research*, *41*(8), 1274–1278, doi:10.1016/j.asr.2007.05.063.

Young, D. T., S. Perraut, A. Roux, C. de Villedary, R. Gendrin, A. Korth, G. Kremser, and D. Jones (1981), Wave-Particle Interactions near $\Omega_{He^+}$ Observed on GEOS 1 and 2, 1. Propagation of Ion Cyclotron Waves in $He^+$-Rich Plasma, *Journal of Geophysical Research*, *86*(A8), 6755–6772, doi:10.1029/JA086iA08p06755.

Young, S. L., R. E. Denton, B. J. Anderson, and M. K. Hudson (2008), Magnetic field line curvature induced pitch angle diffusion in the inner magnetosphere, *Journal of Geophysical Research*, *113*(A3), A03,210, doi:10.1029/2006JA012133.

Zeineh, C. F. (2005), Applications of an Electrostatic High-Voltage Tether to Radiation Belt Remediation, Master's thesis, Department of Aeronautics and Astronautics, Massachusetts Institute of Technology.